

THE UNIVERSITY OF HULL

**A spectroscopic and imaging investigation of
sporopollenin-metal interactions**

Being a Thesis submitted for the Degree of Doctor of Philosophy

in

The University of Hull

By

Fatmah Mohammad Alkhatib, B.Sc., M.Sc.

August 2017

I. Abstract

The main objective has been the determination of the nature of the interaction of metal complexes and salts with the surface of sporopollenin exine capsules (SEC) and other naturally occurring spore exines. These natural materials derived from plant pollen and spores can interact with the inorganic compounds via the formation of coordination bonds and can impart unusual properties. This makes them ideal materials for investigation as they can be used in a wide variety of applications including catalysis, metal remediation, imaging and biological delivery. Although there have been many studies using brown SECs, the focus of this work has been on bleached SECs as the paler colour enables the use of a wider variety of spectroscopic techniques. The first row transition metals copper, iron, nickel, and zinc were used and a selection of spectroscopic techniques (IR, Raman, ICP-OES, UV-Vis, NMR, EPR, Mössbauer and X-ray absorption spectroscopy) were employed to characterise the complexes formed between the metals and the brown and white SECs. Metal loadings of 0.5 to 10 wt% were observed for all the metals and both the brown and bleached SECs. The higher loadings were observed for complexes derived from acetate salts for copper, nickel and zinc. IR spectroscopy of the SECs revealed the presence of aliphatic chains and hydroxyls, aliphatic carbons, carbonyls, unsaturation, ester and ether groups. For the copper, nickel and zinc complexes the IR spectra showed the presence of ν_{CO} modes indicating the mode of coordination, and in the acetate complexes there were a significant difference in the spectrum indicating the presence of bound acetate. The IR spectra of the iron complexes were different indicating the presence of a different structural motif.

The UV-vis spectra displayed the characteristic features of metal(II) for copper, nickel and zinc, with the spectra of the complexes prepared from chloride and nitrate solutions being essentially identical, but different to that from the acetate solution. There were slight differences between all the spectra of the iron-BL-SEC complexes, with the complex derived from SEC and solution of $(\text{NH}_4)\text{Fe}(\text{SO}_4)_2$ presenting the highest intensity peak.

The ^{13}C NMR solid state spectra of the brown and bleached SECs, as well as those of the zinc complexes showed peaks characteristic of aliphatic, olefinic and aromatic carbon, C-O, carboxylic acid and ester groups. For the zinc acetate with BL-SECs was different in the 35 – 10 ppm aliphatic region compared to that of zinc nitrate and zinc chloride with BL-SEC. However, the spectra were similar for all zinc salts with BR-SECs.

The metal K-edge EXAFS data from the nickel and zinc complexes were more similar to the copper data rather than the iron data, indicating the presence of mononuclear octahedral metal complexes for nickel and zinc. For copper, the EXAFS data indicated the presence of a Jahn-Teller distortion for copper, which was confirmed by EPR spectroscopy. In the case of iron the EXAFS data indicated the formation of small oxide or oxyhydroxide particles. The metal K-edge XANES data confirmed the presence of Cu(II), Ni(II) and Zn(II), but indicated that in the case of iron, this was present as Fe(III), which was also consistent with the ^{57}Fe Mössbauer data. μXRF imaging data using synchrotron radiation has shown that the metal distribution in the copper, nickel and zinc complexes is very closely associated with the underlying physical structure of the SEC.

The conclusion from all the spectroscopic data is that the most likely source of coordination of the copper, nickel and zinc metals are the carboxylate groups in the sporopollenin structure resulting in monomeric complexes on the sporopollenin surface. The structures of the chloride and nitrate complexes are very similar, but in the case of acetate there is evidence for the presence of acetate ligands in the coordination environment. The higher metal loadings observed for the acetate complexes can be explained by this as the metal does not require so many ligand groups in close proximity on the SEC surface. In the case of iron, the structures appear to be different, and are based on very small clusters of iron oxide or oxyhydroxide particles attached to the SEC surface.

II. Risk assessment

All experiments were carried out in accordance with the University of Hull's Health and Safety guidelines. A risk assessment and Control of Substances Hazardous to Health (COSHH) was applied for each new experiment, signed by the undertaking student, supervisor, (Dr N. Young) and the departmental safety officer (Dr T. McCreedy) before any practical work started.

III. Acknowledgements

Firstly, I would like to express my gratitude and thanks to my supervisors Dr Nigel Young and Prof Steve Archibald. I would like to express my deep thanks to my primary supervisor Dr Nigel for his patience, constant support, encouragement for all the knowledge he has imparted to me and opportunities to diversify my skills and he guided me through my research. I am also grateful to Prof Steve for his help and guidance in the biological study, I would like to thank Dr. Grahame Mackenzie for his help and advice throughout the project.

Moreover, I would like to thank Dr B. Burke and Dr S. Shah for their help also, Dr S. Nigam for her assistance in the biological work. Technical staff must certainly not be forgotten, thanks to C. Kennedy, B. Knight and T. Sinclair.

Finally, my sincere thanks go to my family: my great mother for her incessant backing, tender care and support, I would like to especially thank my sons (Eyad, Saeed and Anmar) for everything they have done for me throughout my life and without whom none of this would have been achieved, I love you so much for the happiness you have brought me. I would like to thank my brothers, my sisters and all my friends.

Special thanks are due to my sponsors Umm Al- Qura University and ministry of Higher Education in Saudi Arabia, for their support.

IV. Abbreviations

Ab	Antibody
BSA	Bovine serum albumin
BL-SEC	Bleached sporopollenin exine capsule
BR-SEC	Brown sporopollenin exine capsule
CHN	Carbon, Hydrogen, Nitrogen analysis
cm⁻¹	Wavenumber
CN	Coordination number
EPR	Electron paramagnetic resonance
EtOH	Ethanol
eV	Electronvolt
EXAFS	Extended X-ray absorption fine structure
FACS	Fluorescence associated cell sorting
FBS	Fetal bovine serum
FT	Fourier transform
g	<i>g</i> -values
GHz	Gigahertz
ICPMS	Inductively coupled plasma mass spectroscopy
ICP-OES	Inductively coupled plasma optical emission spectroscopy
IR	Infrared spectroscopy
KBr	Potassium bromide
LcSEC	<i>Lycopodium clavatum</i> sporopollenin exine capsule
M	Molar
mAb	Monoclonal antibody
mg	Milligram
mL	Millilitre
mmol	Millimole
MQ	Milli-Q water
NaClO	Sodium hypochlorite
NaOH	Sodium hydroxide
NMR	Nuclear magnetic resonance
OAc	Acetate
PBS	Phosphate buffer saline

ppm	Parts per million
RT	Room temperature
S	Spin
SEC	Sporopollenin exine capsule
SECs	Sporopollenin exine capsules
SEM	Scanning electron microscope
T	Transmittance
UV	Ultraviolet
UV-vis	Ultraviolet visible light
v/v	Volume/volume
w/w	Weight/weight
XANES	X-ray absorption near edge structure
XAS	X-ray absorption spectroscopy
XRF	X-ray fluorescence
Å	Ångstrom (10^{-10} m)
µl	Microlitre
µm	Micrometre
σ²	Variance

V. List of Equations

Equation 2.1 The Beer-Lambert law.....	27
Equation 2.2 The Kubelka-Munk equation.....	28
Equation 2.3 The concentration of cells.	37
Equation 3.1 The Beer-Lambert law.....	59
Equation 3.2 The Kubelka-Munk equation.....	59
Equation 4.1 The equation for determining the g-value in EPR spectroscopy.	109

VI. List of Figures

Figure 1.1 Schematic diagram of structure of spores and pollen. ⁷	3
Figure 1.2 Scanning electron microscopy (SEM) image of spores of (A) <i>Lycopodium clavatum</i> , and (B) <i>Ambrosia trifida</i> . ²⁵	4
Figure 1.3 Schematic diagram illustrating Sporomex technology. (A) original spore; (B) empty shell; and (C) refilled shell. ⁷	5
Figure 1.4 The isolation process of sunflower sporopollenin exine capsules (SECs). ³¹	6
Figure 1.5 Pyrolysis products from SECs and the β -carotene polymers.	11
Figure 1.6 Structures of phenylalanine and the phenolic acids.	12
Figure 3.1 The images of the physical structure of exine.	41
Figure 3.2 The process of extraction from <i>L. clavatum</i> . ²⁹	43
Figure 3.3 SEM images of BR-SECs.....	48
Figure 3.4 SEM images of BL-SECs.....	49
Figure 3.5 IR spectra of BR-SECs and BL-SECs.....	51
Figure 3.6 Expanded from 400 to 2000 cm^{-1} of the IR spectra of BR-SECs and BL-SECs.	51
Figure 3.7 Raman spectrum from brown SECs (BR-SECs).....	55
Figure 3.8 Raman spectrum from bleached SECs (BL-SECs).	55
Figure 3.9 NMR spectra for brown and bleached SECs.....	57
Figure 3.10 Diffuse reflectance (Kubelka-Munk) electronic absorption spectra from BL-SECs and BR-SECs.	58

Figure 3.11 Diffuse reflectance (Kubelka-Munk) electronic absorption spectra for BL-SECs with different stirring times.....	59
Figure 4.1 schematic representation of the attachment of copper complexes to SECs. ...	62
Figure 4.2 A) UV-vis-NIR spectra of copper solutions (0.1 M) before addition of BL-SECs. B) UV-vis-NIR spectra of copper solutions after addition of BL-SECs and stirred for 3 days.	69
Figure 4.3 SEM images of BL-SECs following reaction with copper(II) acetate solution. (The left-hand scale bar is 20 μm , the central and right-hand ones are 10 μm).	79
Figure 4.4 SEM images of BR-SECs following reaction with copper(II) acetate solution. (The left-hand scale bar is 20 μm , the central and right-hand ones are 10 μm).	80
Figure 4.5 SEM images of BL-SECs following reaction with copper(II) chloride solutions. (The left-hand scale bar is 20 μm , the central and right-hand ones are 10 μm).	80
Figure 4.6 SEM images of BR-SECs following reaction with copper(II) chloride solution. (The left-hand scale bar is 20 μm , the central and right-hand ones are 10 μm).	81
Figure 4.7 SEM images of BL-SECs following reaction with copper(II) nitrate solution. (The left-hand scale bar is 20 μm , the central and right-hand ones are 10 μm).	81
Figure 4.8 SEM images of BR-SECs reacted with copper(II) nitrate solution. (The left-hand scale bar is 20 μm , the central and right-hand ones are 10 μm).	81
Figure 4.9 Superposition of the UV-vis spectra of 0.1 M solution of copper (II) acetate, copper(II) chloride and copper(II) nitrate.	83
Figure 4.10 Superposition of the solid state diffuse reflectance UV-vis spectra of copper SEC complexes prepared using 2.5 mmol of metal, 100 mg of SEC and stirring for 3 days in 25 mL of water.....	84
Figure 4.11 Expanded solid state diffuse reflectance UV-vis spectra for SECs loaded with different copper complexes from 5000 to 30000 cm^{-1}	85

Figure 4.12 UV–vis spectra of different loading ratios of (A) copper chloride and (B) copper nitrate with BL-SECs stirring for 3 days.	86
Figure 4.13 UV–vis spectra of (A) different loading ratios of copper acetate with BL- SECs and (B) copper acetate (2.5 mmol:100 mg) with BL-SECs in different stirring.	86
Figure 4.14 Raman spectrum from BL-SECs reacted with copper(II) acetate solution (2.5 mmol:100 mg).....	88
Figure 4.15 IR spectroscopy results from BL-SECs and copper complexes with BL-SECs (2.5 mmol: 100 mg).	89
Figure 4. 16 IR spectroscopy results from BL-SECs and copper complexes with BL-SECs (2.5 mmol:100 mg) (A) The expanded from 4000-2500 cm^{-1} , (B) The expanded from 2000-500 cm^{-1}	90
Figure 4. 17 IR spectroscopy results from copper acetate with BL-SECs different loading.	91
Figure 4.18 (A) IR spectroscopy results from copper complexes with BR-SECs (2.5 mmol: 100 mg), and (B) expanded from 2000-500 cm^{-1} IR spectroscopy results from copper complexes with BR-SECs.....	92
Figure 4.19 Cu K-edge XANES data for $\text{Cu}(\text{OAc})_2 \cdot \text{H}_2\text{O}$, $\text{Cu}(\text{NO}_3)_2 \cdot 3\text{H}_2\text{O}$, $\text{CuCl}_2 \cdot 2\text{H}_2\text{O}$ and $\text{Cu}_2(\text{CO}_3)(\text{OH})_2$	94
Figure 4.20 Cu K-edge XANES data for copper(II) acetate, copper(II) nitrate and copper(II) chloride solutions with BL and BR-SECs.	95
Figure 4.21 Cu K-edge EXAFS analyse of $\text{Cu}(\text{OAc})_2 \cdot \text{H}_2\text{O}$	97
Figure 4.22 Cu K-edge EXAFS analyses of $\text{Cu}(\text{NO}_3)_2 \cdot 3\text{H}_2\text{O}$	97
Figure 4.23 Cu K-edge EXAFS analyses of $\text{CuCl}_2 \cdot 2\text{H}_2\text{O}$	98
Figure 4.24 Cu K-edge EXAFS analyses of $\text{Cu}_2(\text{CO}_3)(\text{OH})_2$	99

Figure 4.25 Cu K-edge EXAFS (left) and FTs (right) for (A) Cu(OAc) ₂ .H ₂ O with BL-SECs, (B) Cu(OAc) ₂ .H ₂ O with BR-SECs.	102
Figure 4.26 Cu K-edge EXAFS (left) and FTs (right) for (A) Cu(NO ₃) ₂ .3H ₂ O with BL-SECs, (B) Cu(NO ₃) ₂ .3H ₂ O with BR-SECs.	104
Figure 4.27 Cu K-edge EXAFS (left) and FTs (right) for (A) CuCl ₂ .2H ₂ O with BL-SECs, (B) CuCl ₂ .2H ₂ O with BR-SECs.	106
Figure 4.28 Cu K _α XRF images stirred three days. (A) BR-SECs with 7.5 mmol of copper(II) acetate solution. (B) BL-SECs with 7.5 mmol of copper(II) acetate solution. (C) BL-SECs with 2.5 mmol 2.5 mL of copper(II) acetate solution.	107
Figure 4.29 Cu K _α XRF images stirred three days. (A) BR-SECs with 7.5 mmol of copper(II) nitrate solution. (B) BL-SECs with 2.5 mmol of copper(II) nitrate solution. (C) BL-SECs with 7.5 mmol of copper(II) nitrate solution.	108
Figure 4.30 Cu K _α XRF images stirred three days. (A) BR-SECs with 7.5 mmol of copper(II) chloride solution. (B) BR-SECs with 2.5 mmol of copper(II) chloride solution.	108
Figure 4.31 X-band (9.87 GHz) EPR spectra of copper SEC complexes at room temperature.	112
Figure 4.32 X-band (9.87 GHz) EPR spectra of copper SEC complexes at room temperature.	113
Figure 4.33 Schematic illustrations of possible interaction of copper with SEC surface. (A) copper acetate with carboxylate on SEC surface, (B) copper chloride or nitrate with carboxylate on SEC surface and (C) copper acetate with phenolate on SEC surface. ...	116
Figure 5.1 Schematic representation of the attachment of iron complexes to SECs.	118
Figure 5.2 (A) SEM images of iron(II) chloride with BR-SECs, (B) SEM images of iron(II) chloride with BL-SECs.	125
Figure 5.3 (A) SEM images of iron(III) chloride with BR-SECs, (B) SEM images of iron(III) chloride with BL-SECs.	125

Figure 5.4 (A) SEM images of iron(II) acetate with BR-SECs, (B) SEM images of iron(II) acetate with BL-SECs.	126
Figure 5.5 (A) SEM images of ammonium iron(II) sulfate with BR-SECs, (B) SEM images of ammonium iron(II) sulfate with BL-SECs.	126
Figure 5.6 (A) SEM images of iron(III) sulfate with BR-SECs, (B) SEM images of iron(III) sulfate with BL-SECs.	127
Figure 5.7 UV-vis spectra for iron salts with bleached SECs.	128
Figure 5.8 Expanded from 5000 to 25000 cm^{-1} of the UV-vis experiment for iron salts with bleached SECs.	129
Figure 5.9 IR spectroscopy results for iron salts with BR-SECs.	130
Figure 5.10 IR spectroscopy results for iron salts with BL-SECs.	131
Figure 5.11 Fe K-edge XANES data for ammonium iron(II) sulfate and ammonium iron(III) sulfate.	132
Figure 5.12 Fe K-edge XANES data for BL-SECs and BR-SECs reacted with ammonium iron(II) sulfate, ammonium iron(III) sulfate, iron(II) chloride, iron(III) chloride and iron(II) acetate solutions.	134
Figure 5.13 Fe K-edge EXAFS (left) and FTs (right) for (A) ammonium iron(II) sulfate, (B) ammonium iron(III) sulfate.	135
Figure 5.14 Plots of R (goodness of fit) vs. CN (coordination number) for all iron samples.	136
Figure 5.15 Fe K-edge EXAFS (left) and FTs (right) for BR-SEC with (A) iron(II) chloride, (B) iron(III) chloride, (C) iron(II) acetate, (D) ammonium iron(II) sulfate, (E) ammonium iron(III) sulfate.	139
Figure 5.16 Fe K-edge EXAFS (left) and FTs (right) for BL-SEC with (A) iron(II) chloride, (B) iron(III) chloride, (C) iron(II) acetate, (D) ammonium iron(II) sulfate, (E) ammonium iron(III) sulfate.	140

Figure 5.17 Illustrative ^{57}Fe Mössbauer spectra of high- and low- spin iron (II) and iron(III) complexes at 80 K.....	143
Figure 5.18 The figures on the left show ^{57}Fe Mössbauer spectra of iron salts with BR-SEC at 80 K; the figures on the right show ^{57}Fe Mössbauer spectra of iron salts with BL-SEC in 80 K	145
Figure 6.1 The attachment of metal complexes to SECs.	149
Figure 6.2 SEM images of BL-SECs after reaction with (A) NiCl_2 solution, (B) $\text{Ni}(\text{NO}_3)_2$ solution and (C) $\text{Ni}(\text{OAc})_2$ solution.	159
Figure 6.3 SEM images of BR-SECs reacted with (A) NiCl_2 solution, (B) $\text{Ni}(\text{NO}_3)_2$ solution and (C) $\text{Ni}(\text{OAc})_2$ solution.	160
Figure 6.4 SEM images of BL-SECS after reaction with (A) ZnCl_2 solution, (B) $\text{Zn}(\text{NO}_3)_2$ solution and (C) $\text{Zn}(\text{OAc})_2$ solution.	160
Figure 6.5 SEM images of BR-SECs after reaction with (A) ZnCl_2 solution, (B) $\text{Zn}(\text{NO}_3)_2$ solution and (C) $\text{Zn}(\text{OAc})_2$ solution.	161
Figure 6.6 (A) UV–vis spectra for BL-SECs stirred with nickel acetate solution for varying times, (B) Expanded UV -vis spectra.....	162
Figure 6.7 Data of the UV–vis experiment for nickel nitrate, (B) Expanded UV -vis spectra for nickel nitrate.	163
Figure 6.8 (A) Data of the UV–vis experiment for nickel chloride, (B) Expanded UV -vis spectra for nickel chloride.....	163
Figure 6.9 (A) Data of the UV–vis experiment for nickel salts with BL-SECs, (B) Expanded UV -vis spectra for nickel salts with BL-SECs at loading 7.5mmol and three days stirring.....	164
Figure 6.10 Data of the UV–vis experiment for zinc acetate (2.5mmol:100mg) at in different stirring, (B) Expanded UV -vis spectra for zinc acetate.	164

Figure 6.11 (A) Data of the UV–vis experiment for zinc nitrate, (B) Expanded UV -vis spectra for zinc nitrate.....	165
Figure 6.12 Data of the UV–vis experiment for zinc chloride, (B) Expanded UV -vis spectra for zinc chloride.....	165
Figure 6.13 Data of the UV–vis experiment for different zinc salts (2.5mmol:100mg) at in three days stirring.....	166
Figure 6.14 IR spectroscopy results for Ni(OAc) ₂ with BL-SEC with different stirring times.....	167
Figure 6.15 IR spectroscopy results with different stirring times (A) Ni(NO ₃) ₂ with BL-SEC, (B) NiCl ₂ with BL-SEC.....	167
Figure 6.16 (A) IR spectroscopy results for nickel salts with BL-SEC, (B) Expanded IR spectroscopy for nickel salts with BL-SEC.	168
Figure 6.17 IR spectroscopy results for nickel salts with BR-SEC, (B) Expanded IR spectroscopy for nickel salts with BR-SEC.....	168
Figure 6.18 IR spectroscopy results for Zn(OAc) ₂ with BL-SEC with different stirring times.....	169
Figure 6.19 IR spectroscopy results with different stirring times (A) Zn(NO ₃) ₂ with BL-SEC, (B) ZnCl ₂ with BL-SEC.	169
Figure 6.20 (A) IR spectroscopy results for zinc salts with BL-SEC, (B) expanded IR spectroscopy results for zinc salts with BL-SEC.....	170
Figure 6.21 (A) IR spectroscopy results for zinc salts with BR-SEC, (B) expanded IR spectroscopy results for zinc salts with BR-SEC.....	170
Figure 6.22 (A) Raman spectra from Ni(OAc) ₂ with BL-SEC (2.5 mmol:100 mg), (B) Expanded Raman spectra from Ni(OAc) ₂ with BL-SEC.....	171
Figure 6.23 Raman spectra from Ni(NO ₃) ₂ with bleached SEC (2.5 mmol:100 mg), (B) Raman spectra from NiCl ₂ with bleached SEC (2.5 mmol:100 mg).	172

Figure 6.24 (A) Raman spectra from Zn(OAc) ₂ with BL-SECs (2.5 mmol:100 mg) (B) Expanded Raman spectra from Zn(OAc) ₂ with BL-SECs.....	172
Figure 6.25 Raman spectra from Zn(NO ₃) ₂ with BL-SECs (2.5 mmol:100 mg), (B) Raman spectra from ZnCl ₂ with BL-SECs (2.5 mmol:100 mg).	173
Figure 6.26 NMR data for Zinc salts with BL-SEC and BR-SEC.....	174
Figure 6.27 Ni K-edge XANES data for nickel(II) acetate, nickel(II) nitrate, nickel(II) chloride solutions with BL and BR-SECs, and nickel(II) salts solution with BL and BR-SECs.....	175
Figure 6.28 Ni K-edge EXAFS (left) and FTs (right) for (A) Ni(OAc) ₂ .4H ₂ O, (B) Ni(NO ₃) ₂ .6H ₂ O, (C) NiCl ₂ .6H ₂ O.....	177
Figure 6.29 The plots of R vs CN for all nickel samples.....	178
Figure 6.30 Ni K-edge EXAFS (left) and FTs (right) for (A) Ni(OAc) ₂ with BR-SEC, (B) Ni(NO ₃) ₂ with BR-SEC, (C) NiCl ₂ with BR-SEC.	180
Figure 6.31 Ni K-edge EXAFS (left) and FTs (right) for (A) Ni(OAc) ₂ with BL-SEC, (B) Ni(NO ₃) ₂ with BL-SEC, (C) NiCl ₂ with BL-SEC.....	181
Figure 6.32 Zn K-edge XANES data for zinc(II) acetate, zinc(II) nitrate, zinc(II) chloride solutions with BL and BR-SECs, and zinc(II) salts solutions with BL and BR-SECs...	182
Figure 6.33 Zn K-edge EXAFS (left) and FTs (right) for (A) Zn(OAc) ₂ , (B) Zn(NO ₃) ₂ .6H ₂ O.....	183
Figure 6.34 The plots of R vs CN for all zinc samples.....	184
Figure 6.35 Zn K-edge EXAFS (left) and FTs (right) for (A) Zn(OAc) ₂ with BR-SEC, (B) Zn(NO ₃) ₂ with BR-SEC, (C) ZnCl ₂ with BR-SEC.....	186
Figure 6.36 Zn K-edge EXAFS (left) and FTs (right) for (A) Zn(OAc) ₂ with BL-SEC, (B) Zn(NO ₃) ₂ with BL-SEC, (C) ZnCl ₂ with BL-SEC.....	187

Figure 6.37 Ni K_{α} XRF images stirred three days. (A) BR-SECs with 7.5 mmol: 300 mg, of nickel(II) acetate solution. (B) BL-SECs with 7.5 mmol: 300 mg of nickel(II) acetate solution.....	189
Figure 6.38 Ni K_{α} XRF images stirred three days. (A) BR-SECs with 7.5 mmol: 300 mg of nickel(II) chloride solution. (B) BL-SECs with 7.5 mmol: 300 mg of nickel(II) chloride solution.....	189
Figure 6.39 Ni K_{α} XRF images stirred three days. (A) BR-SECs with 7.5 mmol: 300 mg of nickel(II) nitrate solution. (B) BL-SECs with 7.5 mmol: 300 mg of nickel(II) nitrate solution.....	190
Figure 6.40 Zn K_{α} XRF images stirred three days. (A) BR-SECs with 7.5 mmol: 300 mg of zinc(II) acetate solution. (B) BL-SECs with 7.5 mmol: 300 mg of zinc(II) acetate solution.....	190
Figure 6.41 Zn K_{α} XRF images stirred three days. (A) BR-SECs with 7.5 mmol: 300 mg of zinc(II) chloride solution. (B) BL-SECs with 7.5 mmol: 300 mg of zinc(II) chloride solution.....	190
Figure 6.42 Zn K_{α} XRF images stirred three days. (A) BR-SECs with 7.5 mmol: 300 mg of zinc(II) nitrate solution. (B) BL-SECs with 7.5 mmol: 300 mg of zinc(II) nitrate solution.....	191
Figure 6.43 Schematic illustrations of interaction of metals (M = Ni, Zn) with SEC surface. (A) metal acetate with carboxylate on SEC surface, (B) metal chloride or nitrate with carboxylate on SEC surface and (C) metal acetate with phenolate on SEC surface.	193
Figure 7.1 A schematic diagram of the components of a flow cytometer. ²³²	197
Figure 7.2 SEM image of BL-SECs.....	199
Figure 7.3 Helical wheel (A) and serpentine (B) diagrams of the CXCR4 receptor. ²⁴⁰ .	200
Figure 7.4 Example flow cytometry plot showing negative control (purple), positive control (green) and an intermediate binding profile (pink).....	201

Figure 7.5 (A) dot plot, Forward-scattered light (FSC) is proportional to cell-surface area or size and Side-scattered light (SSC) is proportional to cell granularity or internal complexity, (B) Histogram, Purple is the negative control (cells only), green is isotype mAb (no binding should be observed), blue is cells incubated with released 12G-5 mAb and pink is cells incubated with non-encapsulated 12G-5 mAb.....202

VII. List of Schemes

Scheme 3.1 The process of the extraction BR-SEC from <i>L. clavatum</i>	45
Scheme 3.2 The process of the preparation of BL-SEC from BR-SEC.	46

VIII. List of Tables

Table 1.1. Empirical formulae of different sporopollenins. ²¹	4
Table 1.2 Information from infrared spectra of sporopollenin. ^{11, 50, 51, 108}	21
Table 1.3 The information from Raman spectra of sporopollenin. ^{111, 112}	22
Table 3.1 Results of elemental analysis of SECs.....	49
Table 3.2 IR absorptions obtained from some SECs. ^{108, 150}	53
Table 3.3 The masses of BL-SECs in different stirring.	58
Table 4.1 Concentration of copper salts used in preparation of copper loaded SECs.	63
Table 4.2 The results of metal loading from ICP-OES.....	64
Table 4.3 ICP-OES results for BL-SECs following reaction with copper(II) acetate, chloride and nitrate solutions using Cu 327.393 nm emission line and * is carried out 3 times in ICP-OES analysis.....	66
Table 4.4 Comparison of the copper loading of SECs prepared from reaction with copper(II) acetate, chloride and nitrate solutions for stirring 3 days.	67
Table 4.5 Comparison of ICP-OES results for Cu-SEC complexes prepared with different quantities of reagents (all stirred for three days).	67
Table 4.6 Comparison of ICP-OES results for Cu-SEC acetate prepared with different stirring.	68
Table 4.7 Summary of spectral features of various copper species in aqueous-acetic acid solutions. ¹⁸⁰	71
Table 4.8 Comparison of metal loading from ICP-OES and initial metal adsorption from UV-vis.....	72
Table 4.9 Copper loadings in dry Cu-SEC complexes before and after extraction in neutral pH solution.....	74

Table 4.10 complete the results for copper loading in dry Cu-SEC complexes and in solution.....	74
Table 4.11 Summary of results for copper loading in dry Cu-SEC complexes and in solution.....	75
Table 4.12 Summary of data for Cu-SEC complexes extracted in acid (pH 1.5).....	76
Table 4.13 Summary of data for Cu-SEC complexes extracted in basic condition (pH 12.5).	77
Table 4.14 Results of elemental analysis of SECs with copper salts.....	78
Table 4.15 IR absorptions obtained from some SEC with metals.	91
Table 4.16 Cu K-edge EXAFS data of $\text{Cu}(\text{OAc})_2 \cdot \text{H}_2\text{O}$, $\text{Cu}(\text{NO}_3)_2 \cdot 3\text{H}_2\text{O}$, $\text{CuCl}_2 \cdot 2\text{H}_2\text{O}$ and $\text{Cu}_2(\text{CO}_3)(\text{OH})_2$	100
Table 4.17 Cu K-edge EXAFS data of $\text{Cu}(\text{OAc})_2 \cdot \text{H}_2\text{O}$ with BL-SECs and BR-SECs. .	102
Table 4.18 Cu K-edge EXAFS data of $\text{Cu}(\text{NO}_3)_2 \cdot 3\text{H}_2\text{O}$ with BL-SECs and BR-SECs.	104
Table 4.19 Cu K-edge EXAFS data of $\text{CuCl}_2 \cdot 2\text{H}_2\text{O}$ with BL-SECs and BR-SECs.....	106
Table 5.1 Concentration of iron salts used in preparation of iron loaded SECs.	119
Table 5.2 ICP-OES results for Fe-SEC complexes.	120
Table 5.3 Iron loadings in dry SECs before and after extraction in neutral pH.....	122
Table 5.4 Complete results of all data calculations of both dry Fe-SEC complexes and in solution.....	123
Table 5.5 The results of all data calculations of both dry Fe-SEC complexes and in solution.	124
Table 5.6 Fe K-edge EXAFS data of ammonium iron(II) sulfate, ammonium iron(III) sulfate.....	135

Table 5.7 Fe K-edge EXAFS data of all iron solutions with BL and BR-SECs.....	141
Table 6.1 Concentration of metals salts used in preparation of nickel and zinc loaded SECs.	150
Table 6.2 ICP-OES results for Ni-SEC and Zn-SEC complexes for the 100 mg, 25 mL, 0.1 M solutions.....	152
Table 6.3 ICP-OES results for Ni-SEC complexes for 300 mg SEC, 75 mL and 0.1 M solution samples.....	153
Table 6.4 Nickel loadings in dry SECs before and after extraction at neutral pH.....	154
Table 6.5 Complete results of data calculations of both dry Ni-SEC complexes and in solution.....	155
Table 6.6 The results of all data calculations of both dry Ni-SEC complexes and in solution.	155
Table 6.7 ICP-OES results for Zn-SEC complexes for 300 mg SEC, 75 mL and 0.1 M solution samples.....	156
Table 6.8 Zinc loadings in dry SECs before and after extraction in neutral pH.....	157
Table 6.9 Complete results of all data calculations of both dry Zn-SEC complexes and in solution.....	158
Table 6.10 The results of all data calculations of both dry Zn-SEC complexes and in solution.....	158
Table 6.11 Ni K-edge EXAFS data of Ni(OAc) ₂ .4H ₂ O, Ni(NO ₃) ₂ .6H ₂ O and NiCl ₂ .6H ₂ O	178
Table 6.12 Ni K-edge EXAFS data of all nickel solutions with BL and BR-SECs.	182
Table 6.13 Zn K-edge EXAFS data of all zinc solutions.	184
Table 6.14 Zn K-edge EXAFS data of all zinc solutions with BL and BR-SECs.	188

IX. Table of Contents

I. Abstract	I
II. Risk assessment	III
III. Acknowledgements	IV
IV. Abbreviations	V
V. List of Equations	VII
VI. List of Figures	VIII
VII. List of Schemes	XVIII
VIII. List of Tables	XIX
IX. Table of Contents	XXII
1 Introduction	2
1.1 Pollen and spores	2
1.2 Types of spores and pollen	3
1.3 History of sporopollenin	3
1.4 Isolation of pollen and spore shells	5
1.4.1 Chemical isolation	5
1.4.2 Enzymatic isolation	7
1.5 Chemical Structure of sporopollenin	7
1.5.1 Elemental analysis	8
1.5.2 Building blocks and functional groups in sporopollenin	8

1.5.2.1 Hydroxyl groups	8
1.5.2.2 Cross linked aliphatic framework	8
1.5.2.3 Aromatic and phenolic groups	9
1.5.2.4 Ketones	10
1.5.2.5 Carboxylic acid groups	10
1.6 Carotenoids as possible precursors of sporopollenin.....	10
1.7 Inhibition and radiolabelling studies on sporopollenin biosynthesis.....	12
1.7.1 Effects of inhibitors of carotenoid synthesis on sporopollenin.....	12
1.7.2 Tracer experiments on sporopollenin biosynthesis.....	12
1.8 Physical and chemical properties of sporopollenin.....	13
1.9 The properties of sporopollenin	13
1.10 The applications of sporopollenin.....	14
1.10.1 Sporopollenin microcapsules	15
1.10.1.1 Microencapsulation of active pharmaceutical components	15
1.10.1.2 Taste masking	17
1.10.1.3 Food industry	17
1.10.1.4 Cosmetics.....	18
1.10.2 Removal of metal ions from solution.....	18
1.10.3 Metal binding to sporopollenin.....	19
1.11 Spectroscopic techniques applied to sporopollenin	19
1.11.1 Ultraviolet-visible (UV-vis) spectroscopy	19

1.11.2 ICP-OES (Inductively coupled plasma optical emission spectroscopy).....	19
1.11.3 Nuclear magnetic resonance spectroscopy (NMR).....	20
1.11.4 Infrared spectroscopy (IR)	20
1.11.5 Raman spectroscopy	21
1.11.6 X-Ray absorption spectroscopy (XAS)	22
1.11.7 Mössbauer spectroscopy	22
1.11.8 Electron paramagnetic resonance spectroscopy (EPR).....	23
1.12 Summary and aims.....	23
2 Experimental processes.....	26
2.1 Materials	26
2.2 Material evaluation	26
2.2.1 Elemental Analysis (CHN)	26
2.2.2 Inductively coupled plasma optical emission spectroscopy (ICP-OES).....	26
2.2.3 Scanning electron microscope (SEM).....	27
2.2.4 Ultraviolet-visible-near infrared (UV – visible - NIR) spectroscopy	27
2.2.5 Infrared (IR) spectroscopy	28
2.2.6 Raman spectroscopy	29
2.2.7 Nuclear Magnetic Resonance Spectroscopy	29
2.2.8 X-ray absorption spectroscopy (XAS).....	29
2.2.9 X-ray fluorescence (XRF) imaging	30
2.2.10 Mössbauer spectroscopy	30

2.2.11 Electron paramagnetic resonance (EPR) spectroscopy.....	31
2.3 Experimental methods in solid phase	31
2.3.1 Preparation of brown sporopollenin from <i>L. clavatum</i>	31
2.3.2 Preparation of bleached sporopollenin from <i>L. clavatum</i>	32
2.4 Investigation of stability of bleached sporopollenin in water	32
2.5 Preparation of brown and bleached SEC - metal complexes.....	32
2.5.1 Preparation of SEC – copper complexes	33
2.5.1.1 Bleached SEC - copper complexes	33
2.5.1.2 Brown SEC - copper complexes	33
2.5.2 Preparation of SEC –iron complexes.....	33
2.5.3 Preparation of SEC – nickel complexes.....	34
2.5.3.1 Bleached SEC – nickel complexes.....	34
2.5.3.2 Brown SEC – nickel complexes	34
2.5.4 Preparation of SEC – zinc complexes.....	34
2.5.4.1 Bleached SEC – zinc complexes.....	34
2.5.4.2 Brown SEC – zinc complexes.....	34
2.6 Investigation of extent of metal taken up by SEC with that left in solution.....	35
2.7 Investigation of stability of metal-SEC complexes in neutral, acidic and basic solutions	35
2.7.1 Neutral pH.....	35
2.7.2 Acidic (pH 1.5) conditions.....	36

2.7.3 Basic (pH 12.5) conditions.....	36
2.8 Antibody encapsulation and release from bleached <i>L. clavatum</i> sporopollenin.....	36
2.8.1 Antibody encapsulation into SECs	36
2.8.2 Antibody release from SECs.....	36
2.8.2.1 Biological experiment for determining the release of Ab.....	37
2.8.2.1.1 Cell culture.....	37
2.8.2.1.2 Aseptic techniques	37
2.8.2.1.3 Cell counting (Trypan blue test)	37
2.8.3 Analysis.....	38
2.8.3.1 FACS experiment cells	38
2.8.3.2 The protocol for FACS experiment to determine Ab release from Ab encapsulation sporopollenin.....	38
3 Sporopollenin	41
3.1 Introduction.....	41
3.2 Spores and pollen used in this research	41
3.2.1 Extraction of SECs from <i>L. clavatum</i>	42
3.2.2 Applications of SECs from <i>L. clavatum</i>	43
3.3 Preparation of SECs	44
3.3.1 Extraction of SECs from <i>L. clavatum</i> spores.....	44
3.3.1.1 Preparation of brown <i>L. clavatum</i> sporopollenin (BR-SEC).....	45
3.3.1.2 Preparation of bleached <i>L. clavatum</i> sporopollenin (BL-SEC)	46

3.3.2 Effect of the preparation method on the functional groups.	46
3.4 Characterisation of SECs	47
3.4.1 Scanning electron microscope (SEM) images	47
3.4.2 Chemical Structure of sporopollenin	49
3.4.2.1 Elemental analyses	49
3.4.2.2 Vibrational spectroscopic identification of functional groups in sporopollenin.....	50
3.4.2.2.1 Infrared spectroscopy (IR)	50
3.4.2.2.2 Raman spectroscopy	54
3.4.2.3 Nuclear magnetic resonance spectroscopy (NMR).....	56
3.4.2.4 Electronic absorption spectroscopy (UV – visible - NIR).....	57
3.5 Conclusion	60
4 Copper attached to sporopollenin	62
4.1 Introduction.....	62
4.2 Synthetic methods	63
4.2.1 Preparation of sporopollenin samples for copper loading studies	63
4.3 Elemental analyses.....	64
4.3.1 Inductively coupled plasma optical emission spectroscopy (ICP-OES).....	64
4.3.1.1 Solution UV-vis determination amount of copper extracted from solution.....	69
4.3.1.2 Extraction studies under different conditions	73

4.3.2 C, H, N analysis	78
4.4 Scanning electron microscope images (SEM)	79
4.5 Spectroscopic studies	82
4.5.1 Identification of metal coordination environment within sporopollenin using electronic absorption spectroscopy (UV – visible - NIR).....	82
4.5.2 Vibrational spectroscopic identification of functional groups in sporopollenin	87
4.5.2.1 Raman spectroscopy	87
4.5.2.2 Infrared spectroscopy (IR)	88
4.5.3 X- Ray absorption spectroscopy	92
4.5.4 XRF images	107
4.5.5 Electron paramagnetic resonance spectroscopy (EPR).....	109
4.6 Conclusion	114
5 Iron attached to sporopollenin	118
5.1 Introduction.....	118
5.2 Synthetic methods	119
5.2.1 Preparation of sporopollenin samples for iron loading.....	119
5.3 Elemental analyses by ICP-OES.....	119
5.3.1 Extraction studies in neutral pH.....	121
5.4 Scanning electron microscope images (SEM)	124
5.5 Spectroscopic studies	127

5.5.1 Identification of metal coordination environment within sporopollenin using electronic absorption spectroscopy (UV – visible - NIR).....	127
5.5.2 Vibrational spectroscopic identification of functional groups in sporopollenin	130
5.5.2.1 Infrared spectroscopy (IR)	130
5.5.3 X- Ray absorption spectroscopy	131
5.5.4 Mössbauer spectroscopy	142
5.6 Conclusion	146
6. Metals attached to sporopollenin	149
6.1 Introduction.....	149
6.2 Synthetic methods	150
6.2.1 Preparation of sporopollenin samples for nickel and zinc loading studies	150
6.3 Elemental analyses by ICP-OES.....	151
6.3.1 ICP-OES analyses for nickel-SECs	153
6.3.2 Extraction studies for nickel-SECs in neutral pH.....	153
6.3.3 ICP-OES analyses for zinc-SECs	156
6.3.4 Extraction studies for zinc-SECs in neutral pH	156
6.4 Scanning electron microscope images (SEM)	159
6.5 Spectroscopic studies	161
6.5.1 Identification of metal coordination environment within sporopollenin using electronic absorption spectroscopy (UV – visible - NIR).....	161

6.5.2 Vibrational spectroscopic identification of functional groups in sporopollenin	166
6.5.2.1 Infrared spectroscopy (IR)	166
6.5.2.2 Raman spectroscopy	171
6.5.3 Nuclear Magnetic Resonance Spectroscopy (NMR)	173
6.5.4 X-Ray absorption spectroscopy	174
6.5.4.1 X-Ray analyses for nickel salts	174
6.5.4.2 X-Ray analyses for zinc salts	182
6.5.5 XRF images	188
6.4 Conclusion	191
7 Encapsulation and release studies	195
7.1 Introduction	195
7.1.1 Encapsulation of proteins for drug delivery	195
7.1.2 Potential of microencapsulation	195
7.2 Flow cytometry	196
7.3 Aims of the biological study	198
7.4. <i>In vitro</i> biological assessment of mAb released from the sporopollenin	199
7.5 Conclusions and Further Work	202
8. Conclusion and Future Work	204
8.1 Conclusion	204
8.2 Future work	209

9. References.....210

Chapter 1

Introduction

1 Introduction

1.1 Pollen and spores

Sporomorphs (pollen and spores) typically consist of one or two types of cells (sporoplasm)¹ and are the reproductive elements and vectors of land plants.^{2, 3} They are comprised of fats, vitamins, proteins and carbohydrates.

Pollen is the male gametophyte and is found in the male sporangia (*anthers*) of flowers.⁴ Once the pollen grains are ready, they may be blown by the wind or collected by bees or other insects and transferred to the tip (*stigma*) of the female organ (*pistil*) of other flowers from the same species. Here, the pollen reaches maturity by growing through the *apertures* of exine, a *pollen tube* that enters the ovary where fecundation occurs resulting in the production of fruit.¹ The sporangia of the non-flowering seed-bearing plants (mostly conifers) are *cones*. The male pollen is transported by the wind and once ripened, it fecundates the female cones.^{3, 5}

Spores are made by the sexual organs of the plants (*sporangia*), which reside within the internal cavity (*loculus*).⁶ Spores are protected by a strong double-layered wall. The inner layer (*intine*) consists of cellulose and a few other polysaccharides.⁷ The outer shell (*exine*) is formed from sporopollenin. The exact structure of sporopollenin is unknown, but it is one of the most stable natural organic materials known as it is a highly cross-linked polymer composed of carbon, hydrogen and oxygen.^{8, 9} Kawase and Takahashi explained the structure as an aliphatic backbone cross-linked with aromatic sidechains.¹⁰ However, Dominguez *et al.* rejected aromatics as being foreign components.¹¹ Van Bergen *et al.* described the structure as an aliphatic core cross-linked by phenolic moieties.¹² In the algaean zygospore cell walls of the *Chlamydomonas monoica*, fatty acids and alcohols are cross linked to form a polymer using ether and ester bonds.¹³ It is believed that sporopollenin in plants is evolved from these algaenans in algal cyst walls.¹⁴ As well as the incorporation of phenolic moieties, which are absent from algaenans, sporopollenins have shorter alkyl chains (16-18 carbons, as opposed to 25 to 34) and are only cross-linked by ether bonds.¹ Research has also suggested that sporopollenin is an oxidative polymer of carotenoids⁷ or polyunsaturated fatty acids.^{5, 11, 15} There is also strong evidence for the presence of conjugated phenols.¹⁶ Exine shells do not produce any allergic effect due to the fact they contain no nitrogen (protein).⁷ Figure 1.1 shows the diagram of the structure

of pollen and spores. Sporopollenin makes up the exine of plant spores and pollen and when extracted it is in the form of an empty exine or microcapsule.⁹

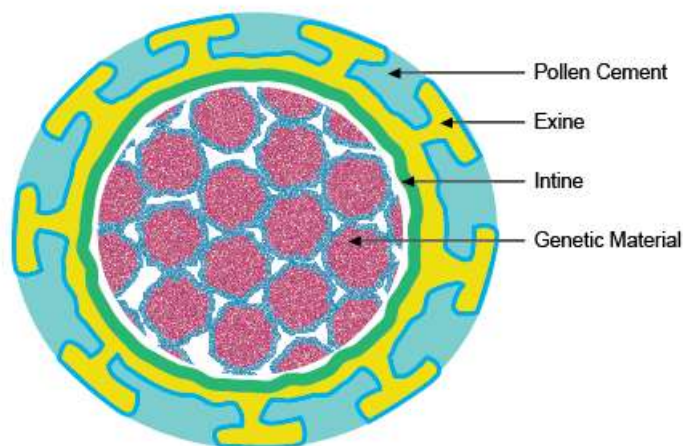


Figure 1.1 Schematic diagram of structure of spores and pollen.⁷

1.2 Types of spores and pollen

There are many types of spores and pollen. These include: *Lycopodium clavatum* (common club moss), *Chlorella vulgaris*, *Aspergillus niger*, *Helianthus annuus* (common sunflower), *Secale cereale* (rye), *Pinus* (pine pollen) and *Ambrosia trifida* (giant ragweed). These can be obtained in multi-ton quantities at a commercially viable price.⁷

1.3 History of sporopollenin

The sporopollenin exine was first observed by John and Baraconnot in 1814 and 1829, respectively.^{17, 18} Both researchers noted the inertness of the exine compared to the rest of the pollen wall. Baraconnot originally used the term “pollenin” to describe the pollen exine. In 1928, Zetzsche and Huggler used the term “sporonin” to describe exine material from *Lycopodium clavatum* spores.¹⁸ Eventually Zetzsche *et al* coined the collective name of “sporopollenin” to describe the resistant exine material from both spores and pollen grains, since they have very similar chemical character.¹⁹

Zetzsche *et al.*^{17, 19, 20} reported a method of preparing a morphologically intact pollen or spore wall devoid of any cytoplasmic contents e.g. nitrogen, fats, genetic material and proteins. The internal contents were removed by treating the spores with organic solvents

and boiling sodium hydroxide solution. The resulting nitrogen free “membranes” consisted of two layers and retained their original shape. The inner layer was stained blue with iodine in sulfuric acid. This is characteristic of cellulose when treated in these conditions. This inner layer was then removed by treatment with hot 85% *ortho*-phosphoric acid over five days.¹⁷ The remaining material was considered to be sporopollenin. After research into sporopollenin from different plant sources, Zetzsche¹⁹ deduced a general empirical formula based on a C₉₀ unit, Table 1.1.

Material	Empirical formula
<i>Lycopodium clavatum</i>	C ₉₀ H ₁₄₄ O ₂₇
<i>Equisetum arvense</i>	C ₉₀ H ₁₄₄ O ₃₁
<i>Ceratozamia mexicana</i>	C ₉₀ H ₁₄₈ O ₃₁
<i>Picea exelsa</i>	C ₉₀ H ₁₄₄ O ₂₆
<i>Picea orientalis</i>	C ₉₀ H ₁₄₄ O ₂₅
<i>Taxus baccata</i>	C ₉₀ H ₁₃₈ O ₂₆

Table 1.1. Empirical formulae of different sporopollenins.²¹

In 1968 a residue very similar to modern sporopollenin was recovered by Brooks and Shaw from sedimentary rocks that were up to a hundred million years old.²¹⁻²³ Some meteorites have also been found to contain insoluble matter that resembles modern sporopollenin.^{21, 24} These findings are significant in tracing the history of vegetation and the origins of life. See Figure 1.2 for an example of SEM images of spores from *Lycopodium clavatum* and *Ambrosia trifida*.

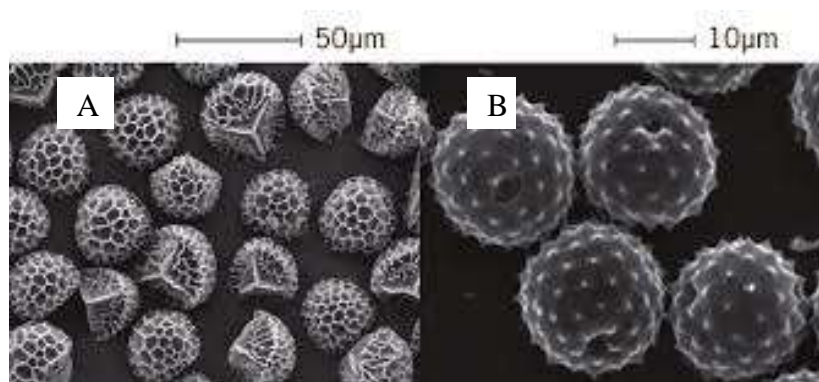


Figure 1.2 Scanning electron microscopy (SEM) image of spores of (A) *Lycopodium clavatum*, and (B) *Ambrosia trifida*.²⁵

1.4 Isolation of pollen and spore shells

Before sporopollenin can be studied it needs to be extracted from the pollen or spores. The inertness of sporopollenin aids this process due to its resistance to many biological, chemical and physical techniques. Various processes^{11, 26-29} can be applied to separate the exine shell from the other components of the cell (sporoplasm and intine). It is possible to remove the genetic content and inner layer of cellulose of the spore or pollen through the porous shell wall, resulting in an empty shell.⁷ Any protein in the original pollen and spores may be eradicated during the extraction process to produce allergen free, non-toxic shells.⁷

30

Many methods have been developed to carry out the extraction.³¹ These methods are traditionally very harsh due to the strength of the double wall structure of the spores and pollen cells.⁹ When comparing studies on sporopollenin it is important to take the extraction method used into account due to its potential impact on the chemical structure of sporopollenin. Both chemical and enzymatic extraction procedures may be used, or a combination of both.⁷ The sporopollenin content depends upon the pollen or spore source. Sources with higher levels of sporopollenin are preferred for producing intact shells.⁷ The diagram of sporopollenin exine capsule is shown in Figure 1.3.

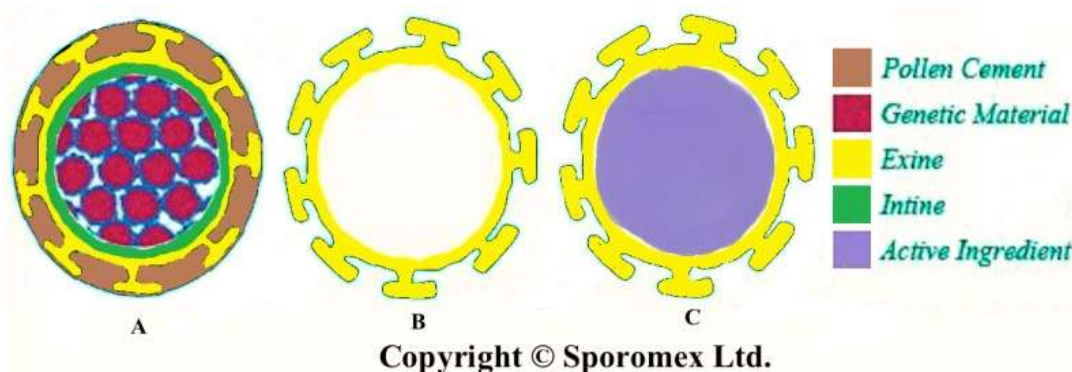


Figure 1.3 Schematic diagram illustrating Sporomex technology. (A) original spore; (B) empty shell; and (C) refilled shell.⁷

1.4.1 Chemical isolation

Zetzsche *et al.*^{7, 18, 19, 32} developed the first method of isolation of sporopollenin. Lipids in the outer layer were removed by sequential treatment with organic solvents. The genetic material from the inner cavity was then removed using alkali, before the polysaccharide

intine was removed by a final aqueous acid treatment. Different acids or bases were used to modify the original method in subsequent studies.^{7,33} Sporopollenin microcapsules have been produced for pharmaceutical applications under similar extraction conditions but using non-toxic mineral acids and alkalis.⁷ It is of note that, Shaw *et al.* found that phosphoric acid was not strong enough to completely remove the cellulose intine and added an extra treatment of 80 % sulfuric acid.³⁴ Alternative harsh methods include: the treatment of spores and pollen using acetolysis^{2, 35, 36} (a 9:1 mixture of acetic anhydride and concentrated sulfuric acid), developed by Erdtman; the use of anhydrous hydrofluoric acid in pyridine at 40 °C,^{7,37} the use of aqueous 4-methylmorpholine-*N*-oxide and sucrose under alkaline conditions at 20 °C or 70 °C for 1 h.^{7, 11, 38}

An example of an extraction process is shown in Figure 1.4, which illustrates the successful extraction of sunflower sporopollenin exine capsules (SECs) by acidolysis using phosphoric acid.³¹

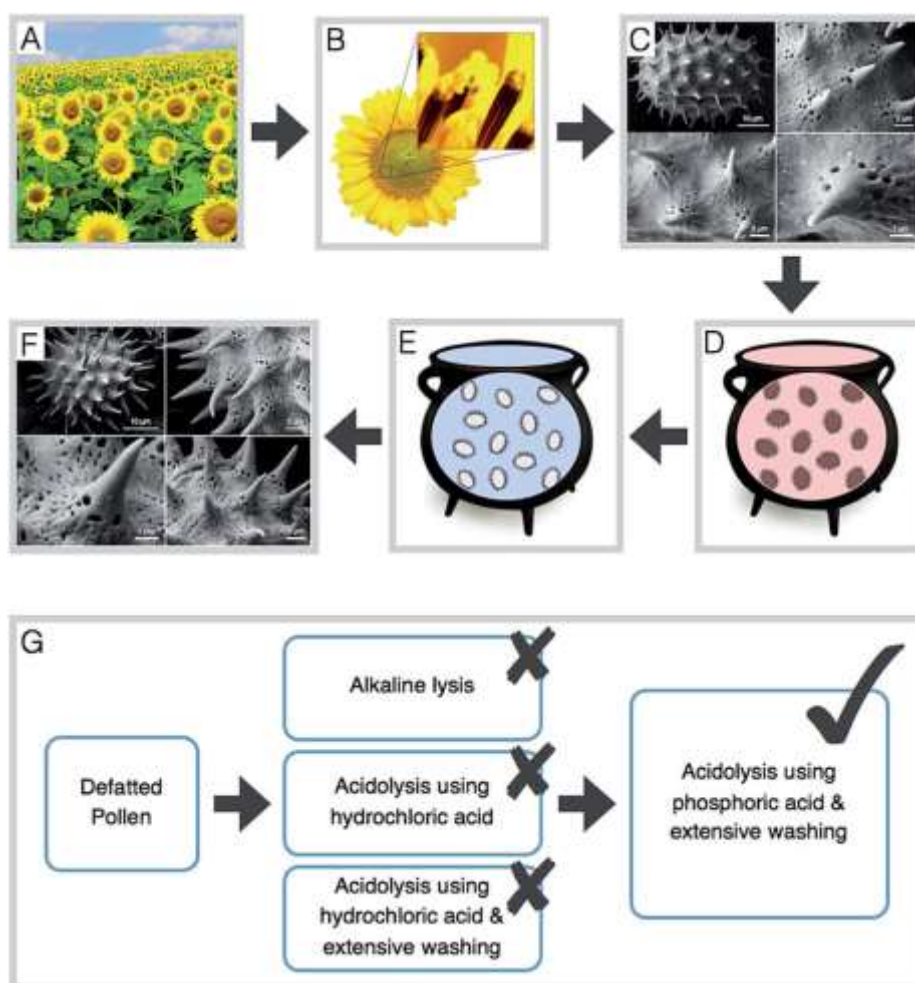


Figure 1.4 The isolation process of sunflower sporopollenin exine capsules (SECs).³¹

Mundargi *et al.*³¹ found that clean, intact sunflower SECs could be isolated and the distinct sunflower pollen morphology conserved. Sunflowers were first cultivated on a large scale (A) and the location of sunflower pollen is shown (B). The defatted pollen grains can be seen at different magnifications in the scanning electron microscopic images (C). The SECs were extracted by either alkaline lysis with potassium hydroxide, or acidolysis with hydrochloric acid or phosphoric acid, to remove all pollen constituents (D). Any residual pollen materials were removed by washing with organic solvents and dilute acids, yielding clean, intact SECs (E). The resulting SECs are shown in Figure 1.4 F at various magnifications in the final scanning electron microscopic images. Figure 1.4 G shows the various extraction approaches that were used to isolate intact sunflower SECs.

1.4.2 Enzymatic isolation

Enzymes have also been used to obtain sporopollenin, or have been incorporated into the extraction procedure as an enzymatic hydrolysis step.^{36, 39-42} The use of strong acids can be avoided by employing different enzymes in sequence. Protease, lipase, amylase, pectinase, cellulases, and hemicellulose have been used to remove both the sporoplasm and intine. Subsequent washing with hot methanol was shown to produce hollow exines from *Corylus avellana L.* (hazelnut) and *Pinus mugo Turra* (mountain pine) pollens.^{7, 39, 40, 42-44} Careful application of the extraction method appears to be necessary for repeatability and reproducibility.

1.5 Chemical Structure of sporopollenin

The structure of sporopollenin is not yet fully understood,^{45, 46} but it is believed to be a very cross-linked polymer as outlined in section 1.1. Sporopollenins from pollen grains and spores belonging to several species have been studied in order to elucidate its chemical structure.

Zetsche and co-workers (1928-1937) conducted the first experiments into the structure of sporopollenin.¹⁸ Since then, its elemental composition and functional groups have been determined and it has been found to contain no nitrogen.¹⁹ Its chemical structure has been defined as an oxidative polymer of carotenoids²⁰ or polyunsaturated fatty acids.^{7, 11, 15, 47} Oleic acid was shown to be incorporated into its structure by studies using ¹⁴C-labelled

oleic acid.⁴¹ Other unsaturated fatty acids, linoleic and linolenic, were found to be involved as precursors in its biosynthesis.¹¹

1.5.1 Elemental analysis

Several combustion elemental analysis (CHN) studies of one species, *L. clavatum*, of sporopollenin, extracted by the same method (acetone treatment, potassium hydroxide), all concluded that the sporopollenin was composed only of C, H and O.^{18, 32, 48-50} It was deduced that sporopollenin can be represented by an empirical formula based on a C₉₀ unit, which varies from species to species. For example, elemental analysis of *Lycopodium clavatum*, gave an empirical formulae of C₉₀H₁₄₄O₂₇, and other examples based on the C₉₀ nomenclature are given in Table 1.1.^{19, 20}

More recently, elemental analysis showed the bonding of carbon in sporopollenin was shared equally between CH and CH₂.⁵¹ Low intensity signals for CH₃ and quaternary carbons were found using solid-state ¹³C NMR,¹ indicating a preponderance of CH and CH₂ groups.

1.5.2 Building blocks and functional groups in sporopollenin

1.5.2.1 Hydroxyl groups

Several studies have shown the presence of hydroxyl groups in sporopollenin.^{18, 19, 40, 52} A study on sporopollenin extracted from *L. clavatum*, using acetylation with ¹⁴C-labelled acetic anhydride, followed by saponification with alkali and assaying loading of ¹⁴C on the polymer, found it contained 6.6 OH groups per C₉₀ atoms.⁵³

1.5.2.2 Cross linked aliphatic framework

Sporopollenin has an aliphatic core consisting of saturated and unsaturated oxygenated hydrocarbon building blocks.⁵ Kuhn-Roth oxidations with chromic acid carried out by Zetsche and co-workers, indicated the presence of C-CH₃ groups. The amount was shown to vary between sporopollenin extracted from different species, e.g.: 1.70 C-CH₃/mol (0.90 mmol/g) for *Pinus sylvestris*; 4.50 C-CH₃/mol (2.6 mmol/g) for *Lange sporonin*; and 2.04 C-CH₃/mol (1.2 mmol/g) for *L. clavatum*.^{17, 19}

Studies using solid- state NMR in the late 1980s,³³ revealed the presence of unsaturated units in a cross-linked aliphatic backbone with aromatic side- chains.^{42, 51} This agrees with FTIR spectra data presented by Kawase *et al.* that showed a predominance of aliphatic units, suggesting the possibility of an aliphatic core.^{10, 54}

Sporopollenin from different species all show a high proportion of aliphatic units and have similar IR spectra. This indicates that they probably share a common biosynthesis between species.^{10, 54} This means that each type of plant probably produces different aromatic side chains. This could differentiate the morphology and chemical structure of pollen grains and spores at a microscopic level.^{42, 51, 55, 56} Ether linkages have been shown in a number of pollen species to play an important role in cross linking to strengthen the polymer framework of sporopollenin.^{11, 40, 51}

In summary, Zetzsche's work demonstrated that sporopollenin is a polyunsaturated compound containing methyl and hydroxyl groups. However, the harsh conditions employed during his degradation experiments may have led to modification of the structural units, hence his work was unable to provide any conclusive insight into the monomers present in the sporopollenin structure. Therefore, Shaw and co-workers^{20, 21, 50, 57} later revisited Zetzsche's experiments and carried out additional degradative studies. These studies predominantly used sporopollenin from *L. clavatum* and *P. sylvestris* and confirmed Zetzsche's initial conclusions. After the application of various degradation methods the only effective technique found to be gentle enough to gain further insight into the structure of sporopollenin was oxidation. Treatment of sporopollenin with sodium hypochlorite, chromic acid, strong nitric acid, and ozone with KOH fusion were all investigated. The most successful technique was found to be the use of ozone and KOH fusion. The membranes of *L. clavatum* and *Pinus sylvestris* pollen were found to be very similar, containing the following: cellulose, a polysaccharide material more readily hydrolysed than cellulose, a lipid fraction resistant to chemical treatments and a lignin-like fraction.^{49, 50}

1.5.2.3 Aromatic and phenolic groups

It was initially suggested that sporopollenin contains both aromatic and oxygenated aromatic units (e.g. phenols or ethers).^{39, 44, 49, 50, 58} Shaw and Yeadon⁴⁹ found phenolic acids were produced from potassium hydroxide fusion of both *L. clavatum* and *L. Henryi*

membranes. Schulze-Osthoff and Wiermann³⁹ used nitrobenzene oxidation of sporopollenin isolated from *Pinus* pollen. This resulted in the production of a number of phenols, with *p*-coumaric acid being the main product.^{44, 58} However, it did not result in characteristic lignin degradation products, providing evidence that sporopollenin differs in structure to lignin.⁴⁰ Fusion with potassium hydroxide resulted in the production of a mixture of phenolic compounds with *p*-hydroxybenzoic acid being the main product. The large number of phenolic acids produced in these experiments suggest that phenols are an integral part of sporopollenin.

Experiments using labelled precursors,⁵⁹ tracers and NMR spectroscopy demonstrated the presence of 4-hydroxyl and 4-methoxycinnamic acids.⁶⁰ In similar studies, phenylalanine was shown to be an important precursor in the biosynthesis of sporopollenin. It produced a phenylpropane unit, which is present in the final polymer.¹⁰ The presence of phenolic groups in sporopollenin has also been shown using IR spectroscopy.⁶¹ The research shows that phenols (especially *p*-coumaric and ferulic acids) are likely to be present as both side chains and cross linking units.^{10, 42, 58, 62}

1.5.2.4 Ketones

Ketones have been detected by NMR^{7, 63} and infrared spectroscopy⁶¹ as well as cytochemical studies⁷, although it is difficult to quantify their presence.⁵

1.5.2.5 Carboxylic acid groups

The spectroscopic analysis using infrared and NMR spectroscopy by Wiermann *et al*^{40, 51} of enzymatic extracted sporopollenin showed the presence of carboxylic acid and hydroxyl groups in sporopollenin.^{40, 51}

1.6 Carotenoids as possible precursors of sporopollenin

Brooks and Shaw^{64, 65} found the development of the pollen exine in *L. henryi* plants was correlated with the development of chemical substances in its anthers. This suggests that sporopollenin is formed by the oxidative polymerisation of carotenoids and carotenoid esters.^{64, 65} By examining the structures of carotenoids and carotenoid esters it is possible to explain how these molecules could act as a precursor to sporopollenin.²⁰

An almost chemically and physically identical unsaturated polymer to sporopollenin, which contained insoluble oxygen, was produced by the polymerisation of a number of carotenoids, including β -carotene, carotenoid and carotenoid esters of *L. henryi*.⁶⁴ This polymerisation was carried out in the presence of oxygen and using trace amounts of an ionic catalyst (boron trifluoride).⁶⁴ When compared to sporopollenin, the resulting polymer exhibited a similar resistance to acetolysis. In addition, it had similar elemental analysis, infrared spectra, oxidation products and pyrolysis gas-liquid chromatograms.⁶⁵ Potassium hydroxide fusion produced *p*-hydroxybenzoic acid as the major component of both polymers.

In other studies, the pyrolysis products of sporopollenin from various sources such as modern pollen, coals and river shale was examined. These were comparable to the pyrolysis products of β -carotene and its oxidative polymer.⁵³ β -Carotene, the β -carotene oxidative polymer and sporopollenin all produced ionene and most of the samples produced naphthalene, 2,6-dimethylnaphthalene and 1-methyl and 2-methylnaphthalene.⁵³ The structures are shown in Figure 1.5.

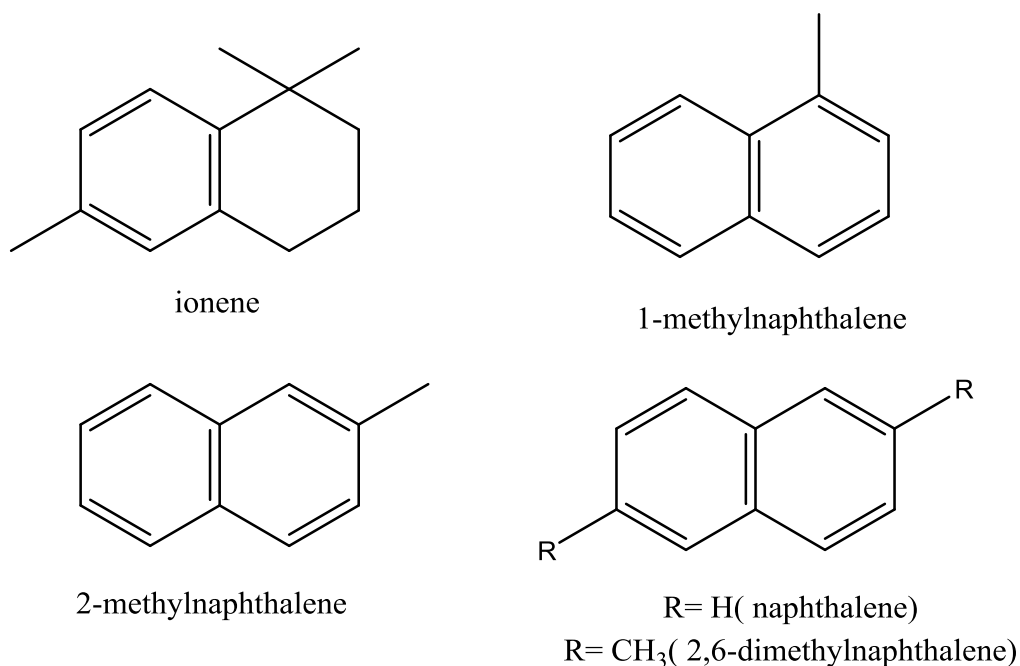


Figure 1.5 Pyrolysis products from SECs and the β -carotene polymers.

1.7 Inhibition and radiolabelling studies on sporopollenin biosynthesis

1.7.1 Effects of inhibitors of carotenoid synthesis on sporopollenin

In a possible contradiction to the evidence for carotenoids as precursors of sporopollenin, Prah *et al*⁶⁶ demonstrated that inhibiting the formation of carotenoids did not block sporopollenin biosynthesis. The application of a known inhibitor of carotenoid synthesis (Sandoz 58-035) to the plants of the *Cucuribita* (pumpkin) was shown to affect carotenoid metabolism at the site of sporopollenin synthesis. The desaturation of carotenoids was hindered leading to the accumulation of saturated precursors. Subsequent isolation of sporopollenin from the pollen revealed only a small impact on biosynthesis. However, saturated carotenoids or related molecules may still play a role in sporopollenin biosynthesis as Sandoz 58-035 only affects the final stages of the biosynthesis.

1.7.2 Tracer experiments on sporopollenin biosynthesis

Gubatz *et al.*³⁹ undertook tracer experiments on *Tulipa* and *Cucuribita* using a number of radiolabelled substances as precursors. ¹⁴C-Phenylalanine and *p*-hydroxybenzoic acid were the main labelled products following potassium hydroxide fusion, with phenylalanine being incorporated at the highest rate. However, due to the forcing condition used during formation, it was argued that these acids were unlikely to have formed part of the sporopollenin skeleton. A phenylpropyl unit such a *p*-coumaric acid was proposed as the more likely candidate. The structures of phenylalanine and the phenolic acids are shown in Figure 1.6.

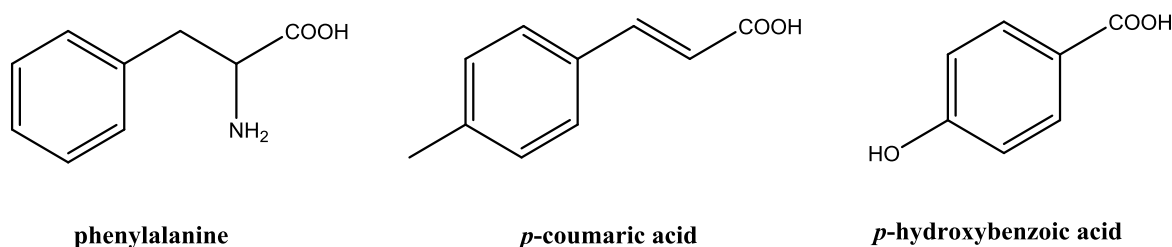


Figure 1.6 Structures of phenylalanine and the phenolic acids.

1.8 Physical and chemical properties of sporopollenin

Sporopollenin from *L. clavatum* has been successfully functionalized by previous workers and the resulting modified exines used as solid phase ‘functional materials’.^{52, 67-70} Sporopollenin has a number of advantages over commercial resins, including:

1) Constant chemical structure

Sporopollenin grains are homogeneous and have a precise and consistent morphology.^{69, 71} This should mean that sporopollenin exine shells should have the same composition when prepared by different workers on different occasions, resulting in similar loadings after functionalization. However, slight variations in the composition of sporopollenin have been observed when prepared by different methods.^{34, 72} Hence, if chemically and structurally consistent samples are to be achieved, it is essential that sporopollenin is prepared by a single method.

2) Constant spore/pollen size

Sporopollenin from *L. clavatum* has an average diameter of 20 μm , which is constant for each spore.⁷³ In contrast, most commercial resins however have a variable particle size. The diameter and consistency in size of sporopollenin from *L. clavatum* meant that columns made up of sporopollenin were free flowing, and the flow rate was unaltered over a period of use of six months.⁷³ Exine capsules from other species have also been shown to be consistent in size, ranging from between 10 and 250 μm in diameter.⁷³

1.9 The properties of sporopollenin

Sporopollenin has evolved in pollen grains or spores to protect the genetic material from light, oxidation, water, and insect damage, hence it is extremely chemically, physically and biologically stable. This stability enables pollen grains and spores to store their cytoplasm for very long periods.^{7, 52} Sporopollenin has been shown to fully retain its morphology after remaining in geological layers for millions of years.⁷⁴ It is resistant to high temperatures, pressures and extremes in pH. It is also resistant to enzymatic break down; hydrolytic decomposition in strong acids (e.g. sulfuric acid, phosphoric acid and hydrofluoric acid); and strong bases (e.g. sodium hydroxide and potassium hydroxide).

Sporopollenin in the form of exine shells is highly hydrophobic and monodispersed,⁷ which aids dispersion and optimises its role in plant reproduction.⁷ Sporopollenin exines also have an elasticity, which provides protection against impact, and are porous, which aids in the transfer of genetic content.

Within species, spores and pollen grains are of consistent size and display monodispersity. This means they form free-flowing powders and may make sporopollenin ideal as microencapsulation vessels. Microencapsulation can be used to preserve and enhance the shelf-life of an active ingredient. Sporopollenin exine shells from *L. clavatum* spores for example, have been shown to improve the stability and therefore prolong the shelf-life of omega oil over a two-month period when the oil is either encapsulated into the shells or in contact with them.¹⁶ Irradiation with UV resulted in lower values of peroxide being generated in encapsulated fish oils compared to the un-encapsulated fish oil.¹⁶ It is thought both the UV-protection capabilities of sporopollenin and its antioxidant properties facilitate this protection.¹¹ These antioxidant properties have been attributed to the presence of a mixture of conjugated phenols found within the sporopollenin.¹⁶ Coumaric and ferulic acids have both been shown to be present in sporopollenin and are both known to protect against oxidation.^{7, 62, 75} Another application where sporopollenin's UV-protection properties may be of particular benefit is in the microencapsulation of light-sensitive drugs.

The colour of the extracted exines varies from light brown/yellow to dark brown or black depending of the species involved.⁷ For some applications, such as the pharmaceutical and food industries the colour of sporopollenin is important. Hence it can be modified by bleaching with sodium hypochlorite or sodium chlorate. If desired, bleached shells can then be dyed using food colorants.⁷

1.10 The applications of sporopollenin

The resilience of sporopollenin to chemical and enzymatic attack makes it uniquely suitable for a whole range of applications. However, although there are many articles available on sporopollenin, its full potential has yet to be realised; it is not presently used in many practical applications and until recently has been more an area of academic interest. However, there are significant developments in UK by Sporomex⁷⁶ and also in Japan by Kenrico⁷⁷. Sporopollenin has a low cost and is easily prepared from widely

commercially available precursors. It is very robust and it has numerous different properties that can be potentially utilized in a number of industrial applications, as well as in the world of pharmaceuticals and chemistry. The enormous variety of sporopollenin species are chemically (at least functionally) very similar, though they vary widely in size. This fact allows for a variety of different size selective techniques to be applied on the micrometer scale to materials that have the same preparation methodology. Recently, there have been studies to develop techniques that use sporopollenin for commercial applications, a number of which are described below.

1.10.1 Sporopollenin microcapsules

The microcapsule that is derived from pollen can be used for many purposes such as those of pharmaceutical, taste masking, cosmetic industries.^{73, 78}

1.10.1.1 Microencapsulation of active pharmaceutical components

Encapsulating, transporting and selectively releasing active components, for example drugs, within the bloodstream can be achieved effectively by the use of the polymer material in the form of a microcapsule. The empty, approximately spherical nature, inertness, non-toxicity, consistent size of the SECs, and ability to be ingested orally with no ill effects and it has been reported that the SECs can pass into the blood stream *via* the digestive system, causing them to be potentially good encapsulation agents.^{73, 79} The resistance of the SECs to biological attack, but their susceptibility to controlled degradation within the bloodstream allows for the targeted release of the encapsulated components where required.⁷³

The high ability of protection to its contents from UV light as well as the chemical resistance make it of additional interest for encapsulating active ingredients, otherwise known as actives. This protecting ability means that any encapsulated actives will be less susceptible to degradation by UV light, which could potentially extend the shelf life of actives encapsulated into the sample.⁸⁰ One of the major problems with using SECs as an encapsulation agent is that controlling the uptake of the active molecules within the capsule of the sporopollenin structure and their subsequent release in a controlled manner can be very complex.

Certain methods with different encapsulating techniques often favour a specific type of active component to be used to load sporopollenin with active components. However, the limitation and the lack of commercial availability are currently affecting lots of these methods. But more effective and versatile approach of loading are under high focus of development at present, as sporopollenin is a relatively new encapsulation agent.⁸¹ There is an increased interest in the delivery of highly potent macromolecules, such as nucleic acids, proteins or peptides, to the body using sporopollenin.^{81, 82} Traditional methods of drug delivery involve the use of injections or oral formulations, such as tablets. Delivery by these methods leads to an initial rise of drug levels in the blood, before it decreases until the next administration. The high concentrations immediately after administration can create toxic side effects.⁸³ This issue could be solved by a controlled drug delivery system, which allows a drug to remain at a constant concentration in the blood for an extended period of time.⁸³

Controlled drug delivery systems make use of a polymer to support or carry a drug or bioactive agent.⁸⁴ Once inside the body, the drug is released from the polymer at a pre-determined rate. Synthetic and natural polymers have both been explored for application in drug delivery.⁸³ Ideally these polymer supports need to be both physically and mechanically stable. They should have a sufficiently high drug loading capacity and be biodegradable. Degradation of the support within the body needs to occur over an appropriate time-scale, with both the support and degradation products being non-toxic. Finally, they should be easy and cheap to prepare. Sporopollenin has been recognised as an ideal candidate for use as a drug delivery agent, and hence much research at the University of Hull has been carried out in this field. For example, Mackenzie *et al.*, demonstrated that sporopollenin could both encapsulate and release ibuprofen³⁰ in *in vitro* studies. Importantly, *in vivo* double cross-over studies in humans have shown that the exines loaded with the ethyl ester of eicosapentaenoic acid (an omega oil) enhance the bioavailability by *ca.* 10-fold by the oral route as opposed to taking the oil directly.^{7, 85} Moreover, Paunov *et al.*, demonstrated an *in-situ* (within the sporopollenin interior) preparation method for the loading of sporopollenin from *L. clavatum* with a range of inorganic and organic nanomaterials. It is a simple and robust loading technique, involving an *in-situ* chemical reaction.⁷³ Hamad *et al.*, reported the encapsulation of living cells into sporopollenin microcapsules from *L. clavatum*.⁸⁶ Finally, Harris *et al.*, reported the safe

oral delivery of 3,4-diaminopyridine for treatment of botulinum neurotoxin A intoxication using sporopollenin from *L. clavatum*.⁸⁷

1.10.1.2 Taste masking

Taste masking is very important in pharmaceutical and food industries, and arguably the most important example of sporopollenin's potential applications. Sporopollenin microcapsules can be absorbed by different means: venous, oral or cutaneous. Sporopollenin is tasteless, non-toxic, hollow and able to absorb oils because of its hydrophobic nature. Additionally, sporopollenin exine microcapsules are not allergenic because of the absence of any nitrogen groups. The microcapsules have a high loading ability and can be simply filled with certain chemical substances; for instance, drugs and vitamins. In spite of their long shelf life, sporopollenin microcapsules enter the bloodstream rapidly and once there, can be easily destroyed. The majority of the microcapsules currently used are synthetic; however, natural microcapsules obtained from pollen are potentially very attractive. The latter substances are biocompatible, renewable, biodegradable and accessible.^{26, 78} These qualities make sporopollenin microcapsules ideal candidates for taste- or odour-masking.

It was found that, due to the hydrophobic nature of sporopollenin, it could be used potentially as a taste masking agent for the ingestion of useful oils with unwelcome tastes. In the presence of water, sporopollenin absorbed oil which would remain within the sporopollenin structure.⁷ Oil absorbed into sporopollenin can also be preserved within a solid powder. Variety of traditional taste masking approaches such as, a double encapsulation with wax, or by flavouring the sporopollenin before the encapsulation of the oil, could have been used effectively to improve the taste masking ability of sporopollenin.⁷⁸ However, the ability of releasing the oil from sporopollenin into the digestive system and allowing it to be used by the body, has no clear evidence of its existence. Consequently, it is still unknown whether if full utility of sporopollenin as a helpful taste masking agent.

1.10.1.3 Food industry

Microcapsules are widely employed in the food industry, where they are primarily used to protect food ingredients.⁸⁸ Many artificial aromas, specialized oils, minerals, vitamins,

sweeteners or colouring agents are particularly sensitive to oxygen and would benefit from entrapment within a shell. It is of note that the use of sporopollenin shells from club moss is currently being considered by the European Food Standards Agency for authorisation as a novel ingredient to be added to a range of foods in the European Union. This was submitted to the UK Advisory Committee for Novel Foods and Processes as ACNFP/109/7.⁸⁹

1.10.1.4 Cosmetics

Microencapsulation could be beneficial in skin-care preparations. Creams, unguents, lotions or pomades normally have a fatty base. A number of fatty acids are also used as active ingredients. Sporopollenin has antioxidant properties and its longevity makes it particularly appealing from a cosmetic standpoint as most non-synthetic antioxidants have a short effective natural life.^{7, 26} Antioxidants are primarily used in cosmetics to slow the degradation of oxygen-sensitive components. Sporopollenin could be used to encapsulate sensitive ingredients leading to an increased protection of the product from oxidation. Furthermore, as sporopollenin is extracted from the plant pollen, the product could be marketed as having natural antioxidant properties.²⁵

1.10.2 Removal of metal ions from solution

Pollen has been used for many years as a metal removal agent in herbal medicine. Many transition metals have been shown to adsorb to sporopollenin.⁹⁰ The effect of both temperature and pH on metal ion sorption have been investigated. In general, sporopollenin was found to be less capable of adsorbing metal ions at low pH values, with pH values close to being neutral resulting in the best sorption properties.⁹⁰ This is thought to be due to the increased dissociation of carboxylic and phenolic groups within sporopollenin at higher pH values.⁹¹ A potential application of sporopollenin's metal ion sorption properties is waste water management, in order to reduce the risk of environmental damage from metals.

Sporopollenin from *L. clavatum* has been successfully used in both ion and ligand exchange chromatography for the separation of various nucleosides, nucleotides and α -amino acids.^{69, 92} Sporopollenin has also been used for the removal of transition metals such as copper(II), and heavy metal ions from aqueous solution.^{93, 94, 95}

1.10.3 Metal binding to sporopollenin

Numerous metals such as iron, copper, cobalt, nickel and zinc can be adsorbed onto sporopollenin and functionalised sporopollenin.⁹⁶⁻¹⁰¹ Initial studies have demonstrated that 95-97% of iron(II) and iron(III) continue to be attached to the sporopollenin after being exposed to either simulated gastric fluid or phosphate buffer for 60 min at 37°C.⁷ These binding properties mean that sporopollenin has great potential for use in drug delivery, chelation therapy, metal sequestration and remediation and catalysis.⁷

1.11 Spectroscopic techniques applied to sporopollenin

A range of spectroscopic techniques have been used to study sporopollenin and metal-sporopollenin complexes and their degradation products. Infrared, Raman and NMR^{11, 33} have been used to investigate the functional groups and the structure of sporopollenin; X-ray and medical imaging techniques have been applied to whole sporopollenin particles; and ICP-OES has been extensively employed to examine metal concentrations in metal-sporopollenin complexes.¹ Mössbauer spectroscopy has been used to investigate the iron oxidation state and spin state in the SECs and EPR spectroscopy has been used to study the SEC metal complexes with unpaired electrons.

1.11.1 Ultraviolet-visible (UV-vis) spectroscopy

UV-vis spectroscopy has not been commonly used to study sporopollenin and metal complexes because sporopollenin extracted by the conventional methods results in brown material due to intense transitions in the visible and UV part of the spectrum. The aim of this work is to make use of the recently developed whitened SECs obtained by a bleaching process conducted within the research group at the University of Hull to enable the use of UV-vis spectroscopy to characterise the metal complexes.

1.11.2 ICP-OES (Inductively coupled plasma optical emission spectroscopy)

The concentration of metals in sporopollenin can be determined by ICP-OES. During ICP analysis, the samples are introduced and an aerosol is generated. The sample is then ionized in an argon plasma. In ICP-OES the detection is *via* optical emission of the elements of

interest, whereas in ICP-MS the detection is *via* separation of the masses in a quadrupole mass spectrometer.¹⁰²

1.11.3 Nuclear magnetic resonance spectroscopy (NMR)

¹³C solid state NMR was first used on sporopollenin-like polymers obtained from a unicellular green alga, *Botryococcus braunii* in 1983.¹ Its initial application by Kütz to actual sporopollenins resulted in poorly resolved signals.¹ However, the spectra still showed the presence of aliphatic carbons (15-20 ppm (weak, C-CH₃) and 29-30 ppm (intense, broad, C-CH₂-C and other aliphatic C), C-O bonds (*ca.* 60-70 ppm (weak, C-O)) and olefinic and/or aromatic carbons; (*ca.* 120-130 ppm (broad, olefinic and/or aromatic C)).^{33, 47, 103-107} Since then, all of these assignments have been confirmed with better resolution in pollen and spore exines from several species (including *L. clavatum.*, *Pinus spec.*, *Ambrosia trifida* and *Typha angustifolia*).^{51, 104} Additionally peaks characteristic of phenols (140 ppm) and unsaturated carbon atoms (100 ppm and 110 ppm) have also been observed.^{34, 47, 52} Experiments by Shaw and Yeadon⁴⁹ showed variations between the structures of different sporopollenins. From the high number of aliphatic groups observed, along with the presence of COOH or COOR groups (*ca.* 172 ppm), and the low number of methyl groups, they concluded that sporopollenin was a polymerised fatty acid. This provides support to the suggestion that fatty acids are the initial precursor to sporopollenins.

1.11.4 Infrared spectroscopy (IR)

All the atoms within a molecule are vibrating continuously with respect to each other. When the frequency of a specific vibration is equal to that of the incident IR, the radiation is absorbed. Building on the work of Shaw and Yeadon,⁵⁰ Kawase¹⁰ performed infrared spectroscopy on sporopollenin. These IR studies showed that sporopollenin contained hydroxyl groups, ethers and C=O groups. The C=O groups were possibly of the structure R-CO, where R = aromatic, aliphatic or conjugated groups. Kawase *et al.* also suggested that the main structure of sporopollenin was a simple aliphatic polymer with aromatic and conjugated side groups.¹⁰ These studies suggest that sporopollenin consists of a main structure, with side chains that vary between species.

The IR work on sporopollenin exines from various plant origins (including *Pinus sylvestris* pollen and *L. clavatum* spores), is summarised in Table 1.2.

Region (cm ⁻¹)	Assignment	References
4000-3400	Hydroxyl groups (OH stretch)	11, 50, 51, 108
2930 & 2850	Methylene (CH stretch)	11, 50, 51, 108
2700	Carboxyl (O-H stretch)	1, 11, 108
1710	Ketones (C=O stretch)	11, 50, 51, 108
1640	Esters (C=O stretch)	11, 50, 51, 108
1600- 1500	Aromatic (C-H deformation)	11, 50, 51, 108
1150- 1070	Ether groups (C-O)	11, 50, 51, 108
1480- 1440	Aliphatic carbons (CH ₂ deformation)	11, 50, 51, 108

Table 1.2 Information from infrared spectra of sporopollenin.^{11, 50, 51, 108}

1.11.5 Raman spectroscopy

Infrared and Raman spectroscopy are complementary techniques and both originate from the transition in vibrational energy levels of a molecule after absorption of radiation. The intensity of IR absorption depends on the change in the dipole moment of the molecule during the vibration, whereas Raman intensity depends on the change in polarizability during the excitation. Studies on bond angles, bond lengths and other structural confirmations use Raman data in addition to IR analysis.^{109, 110}

According to the Raman effect, when a beam of intense radiation of a definite frequency is passed through a transparent substance (gas, liquid or solid), the scattered radiation has not only the original frequency, but also some other frequencies. These other frequencies are generally lower, but occasionally higher, than that of the incident radiation. This is known as Raman scattering or the Raman effect. The spectral lines whose frequencies have been modified during Raman scattering are called Raman lines. There are two types of Raman lines: the spectral lines resulting from lower frequencies than that of the incident radiation are called Stokes lines and those from higher frequencies are called anti-Stokes lines. The Raman spectra are a manifestation of the Raman effect, which is accompanied by transitions in vibrational and rotational energy levels of the molecule. Similar to IR

spectra, the position of spectral lines (or bands) in Raman spectra are also reported in wavenumbers (cm^{-1}). The results from some studies of sporopollenin using Raman spectroscopy are summarised in Table 1.3.

Band range (cm^{-1})	Assignment
3059	(C=C-H)(aromatic)
2975- 2870	CH ₂ , CH ₃ stretching
1735	C=O ester
~1600	Aromatic (C-H deformation)
1460- 1295	CH ₂ (deformation)
1085	C-O

Table 1.3 The information from Raman spectra of sporopollenin.^{111, 112}

1.11.6 X-Ray absorption spectroscopy (XAS)

X-Ray absorption spectroscopy (XAS) is a structural characterisation technique that uses X-rays to probe the structure of a system. Critically, it can provide structural data without the need for long range order.^{101, 113} Fe K-edge X-ray absorption spectroscopy has been used to study a large number of systems including geological¹¹⁴⁻¹¹⁶ and soil samples,^{117, 118} archaeological specimens,^{101, 119-121} biological tissues^{122, 123} and cometary material.^{124, 125} More recently micro-focus X-ray instrumentation has been applied to single exines, yielding both structural and chemical state imaging data.¹⁰¹ Fe K-edge XANES (X-ray absorption near edge structure), EXAFS (Extended X-Ray Absorption Fine Structure), Fe K_α X-ray fluorescence and Fe K-edge XANES imaging were used to investigate how sporopollenin reacted with iron under a variety of conditions.¹⁰¹ C K-edge (*ca.* 290 eV) spectroscopy has also been applied to sporopollenin and has identified ketonic groups on the surface of the pollen grain and aliphatic carbons throughout the whole structure.^{101, 126, 127}

1.11.7 Mössbauer spectroscopy

Mössbauer spectroscopy was discovered by Rudolf Mössbauer in 1958, and he described it as the ‘recoilless nuclear resonance absorption of gamma rays’.¹²⁸ Due to the high energy and very narrow line widths of gamma rays, it is capable of probing tiny changes in the

energy levels of an atomic nucleus in response to its environment.^{128, 129, 126} Generally, three types of nuclear interactions may be observed: isomer shift (chemical shift); quadrupole splitting; and magnetic or hyperfine splitting (Zeeman effect). The most common element studied is iron, and these three parameters give information on the oxidation state, spin state, coordination environment and magnetic properties.¹⁰¹

1.11.8 Electron paramagnetic resonance spectroscopy (EPR)

Electron paramagnetic resonance (EPR) is used to study materials with unpaired electrons.^{130, 131} In EPR spectroscopy the energy levels of the unpaired electron are split in the presence of a magnetic field, and microwave radiation of the appropriate energy is able to flip the spin of the electron. This is analogous to NMR spectroscopy, but involves the magnetic properties of the electron rather than the nucleus. EPR spectroscopy is useful for studying metal complexes with unpaired electrons.^{130, 131}

1.12 Summary and aims

In the light of the above observations, the structure of the sporopollenin is best thought of as highly cross-linked polymer containing: phenols; aliphatic and aromatic carbons; carboxylic acids and esters; ethers; aliphatic hydroxyls. Of these the metal binding sites are most likely to be carboxylate and phenolate.

The aim of this research project is to determine the nature of the interactions between a range of transition metals (Cu, Fe, Ni and Zn) and sporopollenin exine capsules. Although there is previous work on the interaction of metals with SECs that have been functionalised with organic groups, this research concerns the interaction of the metals with the sporopollenin itself.^{91, 96-101} This will give important insight into the mode of interaction, how this affects the coordination chemistry and oxidation state of the metal, as well as the functional groups available for metal binding on the surface of sporopollenin. The sporopollenin samples will include conventional 'brown' SECs extracted from *L. clavatum* using traditional methods, as well as the novel pale coloured or whitened SECs that have recently become available by bleaching the 'brown' SECs with sodium hypochlorite. The major emphasis will be on these whitened SECs because this opens up the possibility of using UV-vis spectroscopy to complement the other spectroscopic techniques, such as

infrared, Raman, NMR, EPR, X-ray absorption and Mössbauer spectroscopy, as well as microscopy and elemental analysis.

Chapter 2

Experimental processes

2 Experimental processes

This chapter provides an explanation of the materials, instrumentation, and characterisation and preparation methods used to investigate sporopollenin exine capsules and their interactions with metals.

2.1 Materials

Raw *Lycopodium clavatum*, common club moss, spores were obtained from Tibrewala International, Nepal. All the other chemicals and reagents used for the extraction of the brown and bleached sporopollenin exine capsules, and the preparation of the metal- SEC complexes were obtained from Fisher and Sigma- Aldrich and used without further purification.

2.2 Material evaluation

2.2.1 Elemental Analysis (CHN)

The elemental (CHN) analysis of SECs and the SEC-metal complexes were conducted by Carol Kennedy in the Department of Chemistry, University of Hull, using a Fisons EA 1108 CHN instrument. The analysis was carried out in duplicate for a sample and the values shown are the mean value of these analyses.

2.2.2 Inductively coupled plasma optical emission spectroscopy (ICP-OES)

ICP-OES was the analytical technique used to determine the concentration of the metals present in the extracted exines. The ICP analyses were carried out by Bob Knight, Department of Chemistry, University of Hull. The emission ICP instrument is a Perkin Elmer Optima 5300DV model. The liquid sample stream is made into an aerosol by combination with argon gas then the submicron size particles were separated from larger droplets in a spray chamber using a vortexing technique. The aerosol is then injected into the argon plasma and the light emitted is wavelength resolved by an echelle grating, and light intensities measured at those wavelengths simultaneously on a CCD detector. The plasma can be viewed almost simultaneously in axial and radial directions to the torch. Light intensities at a given wavelength are then calibrated by introducing standard

solutions diluted from certified 1000 ppm standard solutions, purchased from Romil Ltd (Cambridge, UK) and comparing intensities and concentrations. The current version of Winlab 5 software was used.

2.2.3 Scanning electron microscope (SEM)

Scanning electron microscopy (SEM) was used to image the SECs before and after extraction, and after reaction with the metals. The SEM images were obtained by Tony Sinclair, Department of Chemistry, University of Hull, using a Zeiss EVO60 SEM instrument. The operating conditions were: accelerating voltage 20 kV, probe current 100 pA. A 12 mm diameter carbon-impregnated self-adhesive disc was applied to the surface of an aluminium SEM sample mount. This mount was then gently pressed into a quantity of sample. Excess sample was removed from the mount with compressed air. This was to achieve a mono-dispersed layer of particles. The prepared mounts were then coated with gold to a thickness of 2 nm using a Polaron model 7640 Sputter Coater fitted with a Film Thickness Monitor.

2.2.4 Ultraviolet-visible-near infrared (UV – visible - NIR) spectroscopy

Electronic absorption spectroscopy in the UV-visible-near infrared (UV-vis-NIR) region was used to obtain information about the colour of the SECs, and those reacted with metals, as well as important insight into the electronic structure of the metal. The UV-vis-NIR absorption spectra of solutions and solids were recorded over the range 5000 cm^{-1} to 50000 cm^{-1} (2000 nm to 200 nm) using a Varian Cary 5E UV-VIS-NIR spectrophotometer. The solution spectra were obtained using a matched pair of quartz cells with 1 cm path length. The intensity of the colour produced by the complex ion can be used to identify the concentration of metal within a sample via the Beer-Lambert law.¹³²

$$A = \epsilon cl$$

Equation 2.1 The Beer-Lambert law.

Whereby

A = absorbance

ϵ = molar absorptivity coefficient, ($\text{dm}^3\text{ mol}^{-1}\text{ cm}^{-1}$)

c = concentration (mol dm^{-3})

l = path length (cm)

The spectra of the solids were acquired in diffuse reflectance mode using a Harrick Praying Mantis accessory utilizing BaSO_4 as the diluent. Because of the lack of the path length data in the solid state UV- vis reflectance spectra in this project, and to make them appear in the same format as conventional solution spectra, the reflectivity data from the diffuse reflectance spectra were converted to pseudo absorbance spectral function, $F(R)$, using the Kubelka-Munk equation.¹³³

$$F(R) = (1-R)^2/2R = k/s = Ac/s$$

Equation 2.2 The Kubelka-Munk equation.

Whereby

R = reflectivity

k = absorption coefficient

s = scattering coefficient

c = concentration of the absorbing species

A = absorbance

2.2.5 Infrared (IR) spectroscopy

IR spectroscopy is extensively applied to determine the composition of compounds because of its high accuracy in identifying the functional groups present. It is one of the most appropriate techniques to examine the sporopollenin structure. The region $12,500\text{--}4,000\text{ cm}^{-1}$ is referred to as the near infrared (NIR), and $4,000\text{--}400\text{ cm}^{-1}$ is known as the mid infrared (MIR). The region $400\text{--}50\text{ cm}^{-1}$ is known as the far infrared (FIR) or terahertz (THz) region. MIR spectra were used in this project and were recorded on a PerkinElmer Paragon 1000 Fourier transform infrared spectrometer or a Bruker IFS 66 spectrometer, both using KBr beamsplitters and DTGS detectors. Attenuated total reflectance (ATR) using a Pike Technologies diamond ATR accessory on the PE instrument was initially used, but the data quality was insufficient. Therefore, KBr discs were used and the samples were finely ground and pressed with anhydrous KBr (spectrosol grade), and the spectra acquired using the Bruker IFS66 instrument. During the final stages of the work, a new

diamond ATR accessory coupled to a Nicolet *IS5* FTIR instrument became available and this produced spectra of suitable quality, but was only used for a few spectra. The ATR spectra were collected over a spectral range of 4000 – 650 cm^{-1} and 4000–400 cm^{-1} was used for KBr discs. In both cases, 4 cm^{-1} resolution was used and 10 scans were co-added to give the final IR spectra.

2.2.6 Raman spectroscopy

Raman spectroscopy gives complementary vibrational spectroscopic information to IR spectroscopy. Samples were presented as neat solids and the data were collected in a 180° scattering mode on a Bruker FRA106/Raman accessory on an Equinox 55 FTIR instrument. This employed a 0.5 W 1064 nm Nd-YAG cw laser as the excitation source, a CaF_2 beamsplitter and a low temperature Ge detector.

2.2.7 Nuclear Magnetic Resonance Spectroscopy

Nuclear Magnetic Resonance Spectroscopy (NMR) technique was used to determine the structure of organic compounds.

2.2.8 X-ray absorption spectroscopy (XAS)

X-ray absorption spectroscopy (XAS) was used to investigate the local geometric and electronic structure of the metals reacted with the SECs. X-ray absorption spectroscopy (XAS) is a technique for measuring the linear X-ray absorption coefficient $\mu(E)$. The X-ray absorption spectrum is usually divided into two sections, which are XANES (X-ray Absorption Near Edge Spectroscopy) or Extended X-ray Absorption Fine Structure (EXAFS). When the X-rays hit a sample, the oscillating electric field of the electromagnetic radiation interacts with the electrons bound in an atom. Either the radiation will be scattered by these electrons resulting in diffraction or absorbed and excite the electrons to either empty orbitals, or into the continuum.

The spectra were collected at the BM26A DUBBLE facility at the European Synchrotron Radiation Facility (ESRF) in Grenoble (France) and B18 of the Diamond Light Source at Harwell (UK). The BM26A data were acquired using a double crystal Si(111) sagittal focussing monochromator in step scan mode, harmonic rejection was obtained using

mirrors, and with ion chamber detectors.¹³⁴ The B18 data were collected in QuEXAFS mode using a double crystal Si(111) monochromator and ion chambers, with plane mirrors for harmonic rejection.

The XAS spectra were calibrated using the first maximum in the first derivative spectrum of the relevant metal foil: Fe, 7112.0 eV; Co, 7709.0 eV; Ni, 8333.0 eV, Cu, 8979.0 eV; Zn 9659.0 eV. The X-ray absorption spectra were averaged using Athena,¹³⁵ which was also used to rebin the QuEXAFS spectra to make the data suitable for further analysis. Background subtraction employed Pyspline,¹³⁶ with a quadratic pre-edge function and splines for the post-edge. The edge positions in the XANES spectra were defined as the energy corresponding to a normalised absorbance of 0.5. The k^3 -weighted EXAFS spectra were modelled using curved-wave theory within Excurv98.¹³⁷

2.2.9 X-ray fluorescence (XRF) imaging

Micro-focus XRF and XANES data were used to image the location of the metal on the underlying SEC structure. The micro-focus XRF and XANES data were obtained from beamline I18 at the Diamond Light Source, Harwell (UK), using a Si(111) double crystal monochromator and Kirkpatrick-Baez (KB) mirrors to give a spot size of ca 2.5 x 2.5 μm . The fluorescence data were collected with a 9 element C-train Ge detector using the Xspress-2 data processing system. The samples were mounted between thin Mylar sheets.¹³⁸ The XRF images were processed using PyMCA.¹³⁹

2.2.10 Mössbauer spectroscopy

Mössbauer spectroscopy was used to investigate the iron oxidation state and spin state in the SECs reacted with iron. The ^{57}Fe Mössbauer spectra were recorded by Dr Sachin Shah and Prof. Dave Evans in the Chemistry Department, University of Hull, in zero magnetic field at 80 and/or 298 K on an ES-Technology MS-105 Mössbauer spectrometer with a 100 MBq ^{57}Co source in a rhodium matrix at ambient temperature. Spectra were referenced against 25 μm iron foil at 298 K, and spectral parameters were obtained by fitting with Lorentzian curves. Samples were prepared by grinding with boron nitride powder prior to mounting in the sample holder.

2.2.11 Electron paramagnetic resonance (EPR) spectroscopy

Electron paramagnetic resonance (EPR) is used to study samples with unpaired electrons. Spectra are readily obtained from samples containing one unpaired electron, and other odd numbers of unpaired electrons, although the latter can be very complex to interpret. Spectra from samples with odd numbers of unpaired electrons are much more challenging to obtain as the energy gaps between the ground and excited states are often too large to access with conventional magnet/microwave frequency combinations. However, spin triplets are sometimes accessible.

Electron paramagnetic resonance (EPR) spectroscopy has been used to study the SEC metal complexes with unpaired electrons, and in particular the copper samples. The spectra were obtained the X-band (*ca.* 9.87 GHz) EPR spectra were collected at the EPSRC National EPR service at Manchester University by Dr Adam Brookfield and Prof. David Collison using a Bruker EMX Microspectrometer equipped with a Bruker 4112SHG (super-high-Q) resonator. *ca.* 5 – 10 mg of sample (*ca.* 5 mm height) in 4 mm quartz tube at room temperature was used for the experiments. The experiments were carried out with 2 mW (20 dB attenuation) microwave power, a modulation frequency of 100 kHz, modulation amplitude 4 G, and receiver gain 40 dB. Half field measurements (1600-2000 G) were taken on the same samples with a higher gain of 60 dB. An empty tube was measured and subtracted from the raw data for each sample. The magnetic field was calibrated using a strong pitch sample with a known *g* value of 2.0028.

2.3 Experimental methods in solid phase

2.3.1 Preparation of brown sporopollenin from *L. clavatum*

There are many methods for extracting sporopollenin from natural samples such as *Lycopodium clavatum*. The sporopollenin exine microcapsules are obtained by removing the cytoplasm from within the cell, the intine. The BHS (base hydrolysed sporopollenin) methods developed in Hull over a significant period of time for *Lycopodium clavatum* were used in the extraction process in this work.^{30, 140} Firstly, the raw *L. clavatum* spores (loose powder, 20 g) were defatted by being suspended in acetone (80 mL) and stirred at 60 °C for 4 h. The spores were filtered (porosity grade 3) and air-dried overnight in the filter. The cytoplasm was extracted from the defatted spores using base hydrolysis (BHS method).

The spores were suspended in 6% (w/v) (5.4 g, 90 mL) potassium hydroxide aqueous solution and heated at 80 °C for 6 h. After filtration (porosity grade 3), the product was washed with hot water (2 × 50 mL). The operation was then repeated with fresh 6% (w/v) potassium hydroxide solution (5.4 g, 90 mL). The suspension was filtered (porosity grade 3), washed with water (6 × 50 mL) and ethanol (2 × 25 mL) and then refluxed in ethanol (90 mL) at 80 °C for 4 h. The solid was removed by filtration (porosity grade 3), washed with ethanol (2 × 25 mL) and dried until a constant mass was obtained (usually overnight) to afford *Lycopodium clavatum* sporopollenin exine capsules (SECs). The result of this method was a brown coloured SEC (**BR-SEC**). The yield of **BR-SEC** was typically 14.5 g (73%).

2.3.2 Preparation of bleached sporopollenin from *L. clavatum*

The BR-SECs prepared in the above section were further treated with sodium hypochlorite or hydrogen peroxide to bleach the SECs.

BR-SEC (20 g) was suspended in 5% NaClO aqueous solution (750 mL) and stirred at room temperature (RT) for 1 h. The suspension was filtered (porosity grade 3) and washed with water (100 mL), 2M HCl (100 mL) and water (2 × 100 mL) and dried overnight to render bleached (**BL-SEC**). The result was a white or very pale coloured SEC. The yield of **BL-SEC** was typically 15 g (75%).

2.4 Investigation of stability of bleached sporopollenin in water

BL-SEC (100 mg) SECs were added to 25 mL distilled water and stirred overnight, for three days, one week or for two weeks. The SECs were then filtered, washed with water (5 × 10 mL) and ethanol (10 mL) and dried in a desiccator for 2 days. The SECs were then examined by diffuse reflectance ultraviolet-visible (UV-vis) spectroscopy.

2.5 Preparation of brown and bleached SEC - metal complexes

Both the BL-SEC and BR-SEC samples were used to investigate the metal loading and binding to the sporopollenin surface. The preparation of these metal - SEC complexes used a similar method to that used in the preparation of iron sporopollenin complexes by Archibald *et al.*¹⁰¹

2.5.1 Preparation of SEC – copper complexes

2.5.1.1 Bleached SEC - copper complexes

Reactions between copper and bleached SEC (BL-SEC), were carried out with solutions of copper(II) chloride dihydrate, copper(II) nitrate trihydrate, and copper(II) acetate monohydrate at various loading levels, and length of reaction.

All reactions used the following the standard procedures. BL-SEC (100 mg) were added to a 25 mL solution that contained 1.0, 2.5 or 5.0 mmol of copper. The reactions were stirred overnight, for three days, one week or for two weeks; the products were filtered, washed with water (5×10 mL) and ethanol (10 mL) and dried in a desiccator for 2 days.

2.5.1.2 Brown SEC - copper complexes

For the reaction of brown SEC with copper, the same methods were used but were only stirred for three days with a metal loading of 2.5 mmol of copper to 100 mg of BR-SEC in 25 mL of water, using the following metal salts: copper(II) chloride dihydrate, copper(II) nitrate trihydrate, and copper(II) acetate monohydrate .

2.5.2 Preparation of SEC –iron complexes

Both BR-SEC and BL-SEC were reacted with the following iron salts: iron(II) chloride, iron(III) chloride, iron(II) acetate, ammonium iron(III) sulfate dodecahydrate and ammonium iron(II) sulfate hexahydrate to investigate the interaction of iron with *L. clavatum* SECs.

All reactions were carried out using Schlenk techniques using dry degassed solvents and argon as it has been shown previously that extensive air drying results in oxidation of iron(II) to iron(III).¹⁰¹ To maintain consistency, the same method was used for both iron(II) and iron(III) samples.

7.5 mmol of iron salt and 300 mg BR-SEC or BL-SEC were stirred at RT in 75 mL water for three days, filtered, washed with water (8×10 mL) and ethanol (20 mL), dried under vacuum, and stored under argon.

2.5.3 Preparation of SEC – nickel complexes

2.5.3.1 Bleached SEC – nickel complexes

First experiments were carried out with bleached SEC, BL-SEC. 2.5 mmol of nickel(II) chloride hexahydrate, nickel (II) nitrate hexahydrate, or nickel(II) acetate tetrahydrate, were added to 100 mg of bleached SEC in 25 mL of water and stirred either overnight, for three days, one week or for two weeks. The products were filtered, washed with water (5×10 mL) and ethanol (10 mL) and dried in a desiccator for 2 days.

2.5.3.2 Brown SEC – nickel complexes

For the brown SEC, BR-SEC complexes, 2.5 mmol of nickel(II) chloride hexahydrate, nickel (II) nitrate hexahydrate, or nickel(II) acetate tetrahydrate and 100 mg BR-SEC were stirred in 25 mL of water for three days, filtered, washed with water (5×10 mL) and ethanol (10 mL) and dried in a desiccator for 2 days.

2.5.4 Preparation of SEC – zinc complexes

2.5.4.1 Bleached SEC – zinc complexes

2.5 mmol of zinc(II) chloride anhydrous, zinc(II) nitrate hexahydrate, zinc(II) acetate anhydrous was added to 100 mg of bleached SEC in 25 mL of water and stirred overnight, for three days, one week or for two weeks. The product was filtered, washed with water (5×10 mL) and ethanol (10 mL) and dried in a desiccator for 2 days.

2.5.4.2 Brown SEC – zinc complexes

2.5 mmol of zinc(II) chloride anhydrous, zinc(II) nitrate hexahydrate, zinc(II) acetate anhydrous and 100 mg BR-SEC were stirred in 25 mL of water for three days, filtered, washed with water (5×10 mL) and ethanol (10 mL) and dried in a desiccator for 2 days.

2.6 Investigation of extent of metal taken up by SEC with that left in solution

These experiments were used to investigate the proportion of the metal left in solution compared with how much was removed by the SECs. UV-vis spectra of the initial solutions were compared to those of the filtrate after the solution had been stirred with the SECs for three days or one week. The SEC-metal complex was then analysed by ICP-OES to determine how much of the copper had been taken up by the SECs. As the copper solutions and solids had the most distinctive and intense features in the UV-vis spectra, these experiments were only carried out with copper.

20 mg of the Cu-SEC complex formed from the reaction of either BR-SEC or BL-SEC with solutions of copper(II) chloride dihydrate, copper(II) nitrate trihydrate, or copper(II) acetate monohydrate was added to 5 mL water and stirred for three days or one week. The solution was filtered, and the initial filtrate was analysed by both UV-vis and ICP-OES. The solid product was washed with water (7 mL) and ethanol (2 mL) and dried in a desiccator for 2 days, and the copper loading determined by ICP-OES.

2.7 Investigation of stability of metal-SEC complexes in neutral, acidic and basic solutions

To investigate the stability of the metal loaded spores under different conditions they were stirred in neutral, acidic (pH 1.5) and basic (pH 12.5) solutions. The solution and SEC were both analysed by ICP-OES.

2.7.1 Neutral pH

20.0 mg of the Cu-SEC complex (Cu-BR-SEC or Cu-BL-SEC) was added to 5 mL water and stirred for three days, and filtered. The filtrate was analysed by ICP-OES to determine how much copper had leached from the sample. The solid was then washed with water (7 mL) and ethanol (2 mL) and dried in a desiccator for 2 days. The solid was then analysed by ICP-OES to determine how much copper had remained in the solid.

2.7.2 Acidic (pH 1.5) conditions

20.0 mg of Cu-SEC complex (Cu-BR-SEC or Cu-BL-SEC) was added to 5 mL of 0.0316 M HCl solution (pH 1.5) and stirred for three days. The filtrate and solid were treated in the same way as for the neutral solution.

2.7.3 Basic (pH 12.5) conditions

20.0 mg of Cu-SEC complex (Cu-BR-SEC or Cu-BL-SEC) was added to 5 ml of 0.0316 M NaOH (pH 12.5) and stirred for three days. The filtrate and solid were treated in the same way as for the neutral solution.

2.8 Antibody encapsulation and release from bleached *L. clavatum* sporopollenin

The ability of the SEC microcapsules to encapsulate and release an antibody in a controlled manner, was investigated using Mouse IgG2A PE-conjugated Isotype Control and Human CXCR4 PE conjugated Antibody purchased from R and D system.

2.8.1 Antibody encapsulation into SECs

500 mg of BL-SECs and 500 μ l of 12 G5 –human CXCR4 PE antibody, monoclonal mouse IgG_{2A}, clone 12G5 (25 μ g of Ab in 1 mL saline with 0.5% BSA and 0.09% sodium azide solution (500 μ l contain 12.5 μ g) were well mixed well in the dark (wrapped with aluminium foil as fluorescent Ab should not exposed to light) upon ice for 10 min. The vial was transferred into a Schlenk tube and put under vacuum Schlenk line (Schlenk tube kept on ice throughout) for 30 min. After 30 min the vial was freeze–dried in liquid nitrogen and transferred to the freeze dryer. Once it was dry (~ 24 hr) it was removed from the freeze drier and the vial was sealed with Parafilm and wrapped in aluminium foil prior to transfer to the freezer. Samples were stored for 3-4 days in the freezer prior to analysis.

2.8.2 Antibody release from SECs

100 mg of mAb loaded sporopollenin exines was weighed into a vial and 10 mL of cold milliQ water added, the vial was well shaken and vortex mixed for 10 min whilst kept cold and in the dark. It was then passed through 0.45 μ m filter (the filtrate should contain the

released antibody) and recover all the trapped SECs from the filter by taking milliQ water in the syringe and pull back to remove the SECs from the filter. The released mAb solution was frozen in liquid nitrogen and transferred to the freeze dryer and transfer to a small (1.5 ml) tube. After drying the sample was removed from the freeze dryer and 100 µl PBS was added to give the samples for the FACS experiment.

2.8.2.1 Biological experiment for determining the release of Ab.

2.8.2.1.1 Cell culture

Human leukemia cell line (Jurkat) was obtained from ATCC and grown in PRMI-1640 media. Cell culture media were purchased from Lonza. Complete media was made by the addition of 10% (v/v) heat inactivated fetal bovine serum (FBS) (Biowest, France), 1% (v/v) penicillin and streptomycin (100 units/mL) antibiotics. Cell culture was maintained at 37°C in a humidified, CO₂ (5%) controlled atmosphere with sub culturing carried out every 2-3 days as appropriate.

2.8.2.1.2 Aseptic techniques

Aseptic techniques were conducted in Airstream Class II type A2 biological safety cabinets, Gen 3 fitted with a UV sterilising lamp. All glassware and heat stable solutions were autoclaved prior to use at 121°C for 10 min, disposable equipment and all solutions were of sterile tissue culture grade.

2.8.2.1.3 Cell counting (Trypan blue test)

The concentration of the cells was determined using a Neubauer hemacytometer. Cells in suspension were diluted 1:1 with 0.2% (w/v) Trypan blue stain. The diluted sample was placed onto a hemacytometer chamber and the cell density was determined using light microscopy by counting the number of cells in a set area. The following equation is used to determine the concentration of cells.

Cell concentration (cell/ml) = Averaged cell count x 2(dilution factor) x 10⁴ (volume of chamber)

Equation 2.3 The concentration of cells.

2.8.3 Analysis

Samples containing antibody encapsulation into SEC and antibody release from SEC were analysed on a FACS can flow cytometer (BD Biosciences Europe, Erembodegem, Belgium). Data were acquired and analysed with Cell Quest software (Becton Dickinson).

Analysis *via* flow cytometry detects the amount of fluorescently labelled mAb bound to each cell, of which 10,000 are counted per sample, negative and positive controls were used to set the assay limits. The negative control contains no 12G5 mAb and has no fluorescence signal. The positive control contains only 12G-5 mAb CXCR4 specific mAb producing a reading for 100 % fluorescence.

2.8.3.1 FACS experiment cells

Sample preparation by Jurkat cell concentration 5×10^5 cells/50 μ l. The reagents of the experiment are 12G-5 mAb conjugated to phycoerythrin, mouse IgG_{2A} Isotype Control Phycoerythrin and cold PBS with 0.25% BSA. During the experiment cells were kept in ice and at 4°C while being centrifuged.

2.8.3.2 The protocol for FACS experiment to determine Ab release from Ab encapsulation sporopollenin

T25 flasks containing the Jurkat cell culture were centrifuged (200 x g for 5 min), the media was decanted and cells were washed with cold PBS two times, after that cells were counted and 5×10^5 cells/50 μ l (were added into four Eppendorf tubes. In one Eppendorf tube, Jurkat cells (5×10^5 cells/50 μ l) in PBS+0.25% BSA were incubated with 30 μ l of released Ab from SECs for 1 hour on ice, in the dark (sample was covered with aluminium foil). In the second Eppendorf tube, Jurkat cells (5×10^5 cells/50 μ l) in PBS+0.25% BSA were incubated with 10 μ l of 12G-5 mAb conjugated to phycoerythrin for 1 hour on ice, in the dark (sample was covered with aluminium foil). In the third Eppendorf tube, Jurkat cells (5×10^5 cells/50 μ l) in PBS+0.25% BSA were incubated with 10 μ l of mouse IgG_{2A} Isotype Control for 1 hour on ice, in the dark (sample was covered with aluminium foil). In the fourth Eppendorf tube, Jurkat cells (5×10^5 cells/50 μ l) in PBS+0.25% BSA were incubated for 1 hour on ice, in the dark (sample was covered with aluminium foil). After 1 hr. all the Eppendorf tubes were washed three times with 1 mL of cold PBS+0.25% BSA

and centrifuged at 4°C at 1500 rpm for 5 min to remove excess of compound. The cells in each Eppendorf tube were then resuspended in 300 µL of PBS+0.25% BSA. Samples were transferred into FACS tubes and put on ice before analysis. The binding of the mAbs was analysed by flow cytometry (all of the samples were kept on ice at all times, including transfer to the FACS machine).

Chapter 3

Sporopollenin

3 Sporopollenin

3.1 Introduction

Sporopollenin is an organic polymer that makes up the external shell (the exine) of pollen grains and plants spores (Figure 3.1).⁵² Sporopollenin is known for its extreme physical, chemical and biological stability.²⁶ For example, it is resilient to high temperature and pressures, acidic and basic conditions and intact exines have been found in sedimentary rocks over 500 million years old.^{52, 96} It is also resistant to degradation by enzymes and strong chemical reagents. Sporopollenin is known to contain carbon, hydrogen and oxygen,⁴ although the exact chemical structure is not presently understood. Sporopollenin from different plants exhibit very similar properties,^{11, 30} but the chemical composition of sporopollenin does vary slightly between species.²⁶ It is believed that different pollen/spore species produce the same sporopollenin with very similar structures.

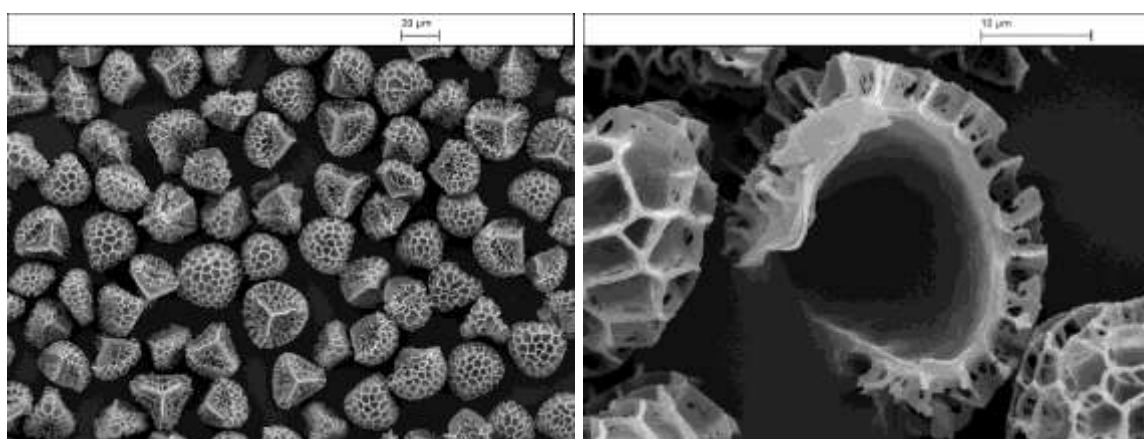


Figure 3.1 The images of the physical structure of exine.

3.2 Spores and pollen used in this research

The sporopollenin used in this research was derived from *Lycopodium clavatum* which is the most widespread species in the genus *Lycopodium* of the clubmoss family. *Lycopodiaceae*. *L. clavatum* is commonly known as running ground pine and is found in many woodland areas and rocky slopes in Europe, Central and South America, Asia and Africa.^{78, 73} It was chosen due to its low cost,⁷⁸ wide availability and chemical robustness.^{78, 73} The sporopollenin obtained from *L. clavatum* has a constant chemical structure, and is highly resistant to both biological decay and chemical attack.¹

The chemical structure of SECs is not fully understood. However, analysis of sporopollenin indicates that it is a complex polymer with a high degree of unsaturation and contains a variety of functional groups, including.¹¹ The elements composition of SECs was first measured by Zetzsche et al.^{18, 32} Sporopollenin is usually represented by an empirical formula based on a C₉₀ unit which varies from species to species as *Lycopodium clavatum* and *Ambrosia trifida*.^{20, 80} The empirical formula of *L. clavatum* determined by elemental analysis, demonstrated that the sporopollenin exine is typically composed of C₉₀H₁₄₄O₂₇, with only trace levels of N.¹⁶

3.2.1 Extraction of SECs from *L. clavatum*

Sporopollenin exine capsules (SECs) extracted from *L. clavatum* spores are an attractive biomaterial possessing a highly robust structure suitable for microencapsulation strategies. The extraction of the *L. clavatum* can be carried out chemically, with enzymes, or a combination of both.⁷ However, despite several decades of research into sporopollenin exine capsule (SEC) extraction methods, these protocols still entail harsh extraction methods in order to separate exines from other components of the spore, including proteins, lipids, nucleic acids and polysaccharides.⁷ The protocols commonly used for *L. clavatum* still entail processing with both resist strong acids and strong bases and does not dissolve into organic solvents steps at temperatures up to 180 °C and lasting up to 7 days.^{7, 29} Erdtman's acetolysis,⁵² used a mixture of glacial acetic acid and concentrated sulfuric acid. The method of Zetzsche *et al.*¹⁸ used a sequential systematic isolation method using acetone, potassium hydroxide and phosphoric acid.³⁴ These extractions resulted in hollow, uniform and biodegradable resistant microcapsules.

Mundargi *et,al.*, have very recently (2016) demonstrated a significantly streamlined processing regime, using lower temperatures and processing durations, without alkaline lysis (Figure 3.2). This method still produces SECs of equivalent quality to the traditionally harsh extraction methods.²⁹ While their process is slightly different from that described later, their illustration of the extraction process shown in Figure 3.2 summarises the important steps.

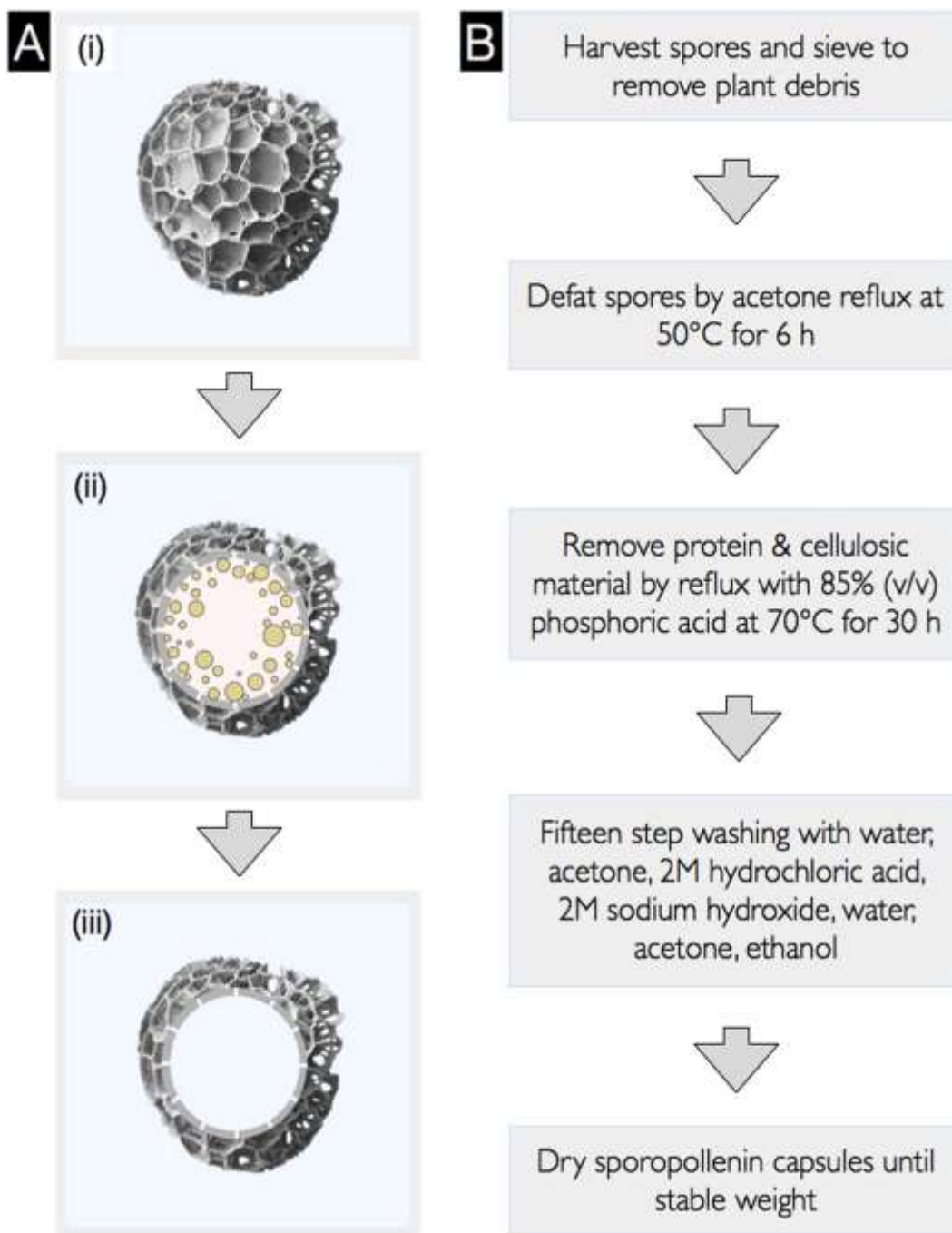


Figure 3.2 The process of extraction from *L. clavatum*.²⁹

3.2.2 Applications of SECs from *L. clavatum*

Mackenzie et al.⁷³ have developed a range of applications for sporopollenin derived from *L. clavatum*, including drug delivery and cosmetics. These are based on filling the exine with fat (Omega 3 oils), proteins, vitamins, enzymes and metals. Sporopollenin is loaded with these compounds by either physical adsorption to the surface of the sporopollenin, or penetration into its interior by diffusion through the microchannels of the exine membrane

that can be up to 40 nm in diameter.^{73, 87, 141, 142} Large proportions of oil can be encapsulated, but lower loadings can be observed with lower solubility compounds. Moreover, there are reports by other researchers who have developed techniques such as, compression, passive and vacuum loading for the encapsulation of sporopollenin from *L. clavatum*, for applications such as drug delivery.^{143, 144} Also, there are some applications in drug delivery using sporopollenin exine capsules from some natural plants as, sunflower^{31, 145} and date palm.^{140, 146}

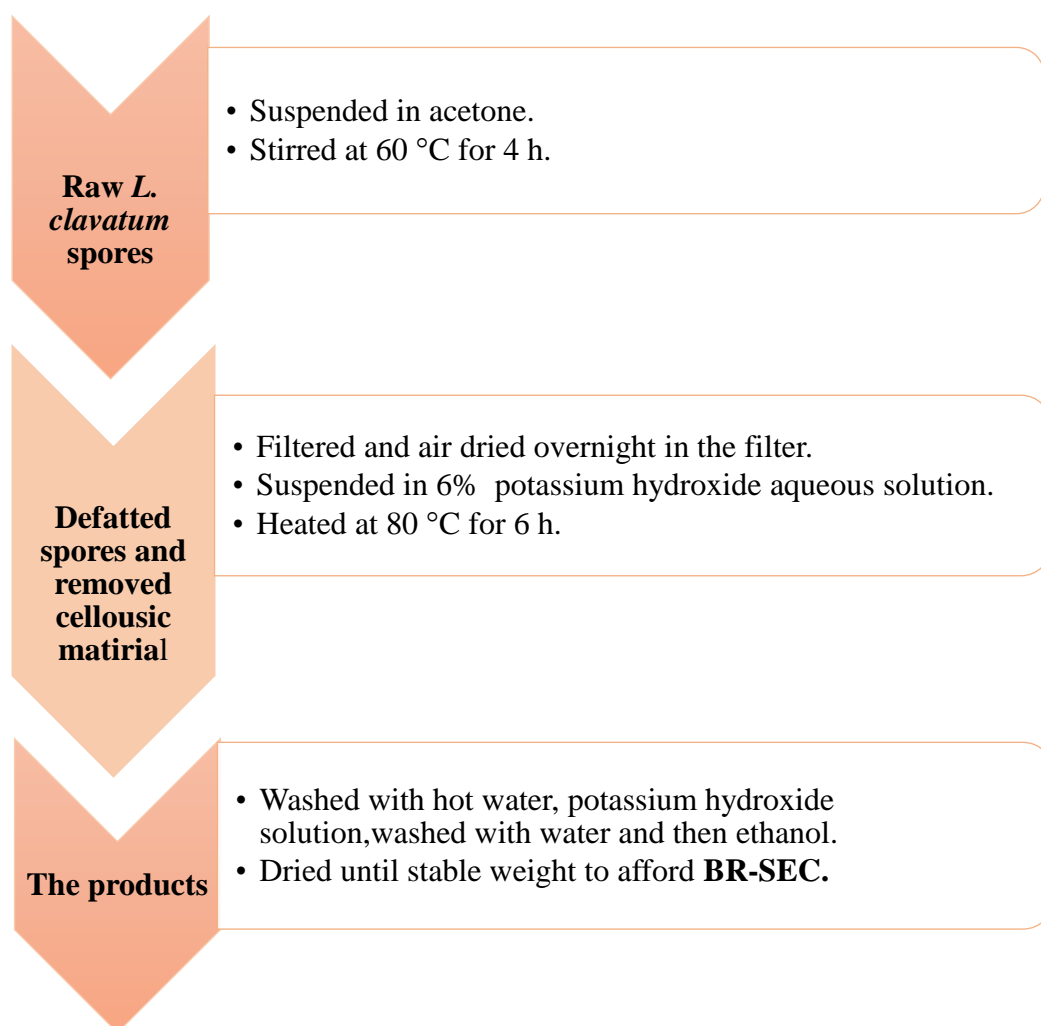
The aim of this chapter is to describe the preparation and characterisation of the brown and bleached SECs used in the later chapters.

3.3 Preparation of SECs

3.3.1 Extraction of SECs from *L. clavatum* spores

The sporoplasm and cellulose intine of *L. clavatum* were removed by an extraction protocol⁷ involving successive treatments in hot acetone and potassium hydroxide to produce brown SECs (BR-SEC) (Scheme 3.1) followed by aqueous sodium hypochlorite to produce bleached SECs (BL-SEC) (Scheme 3.2).

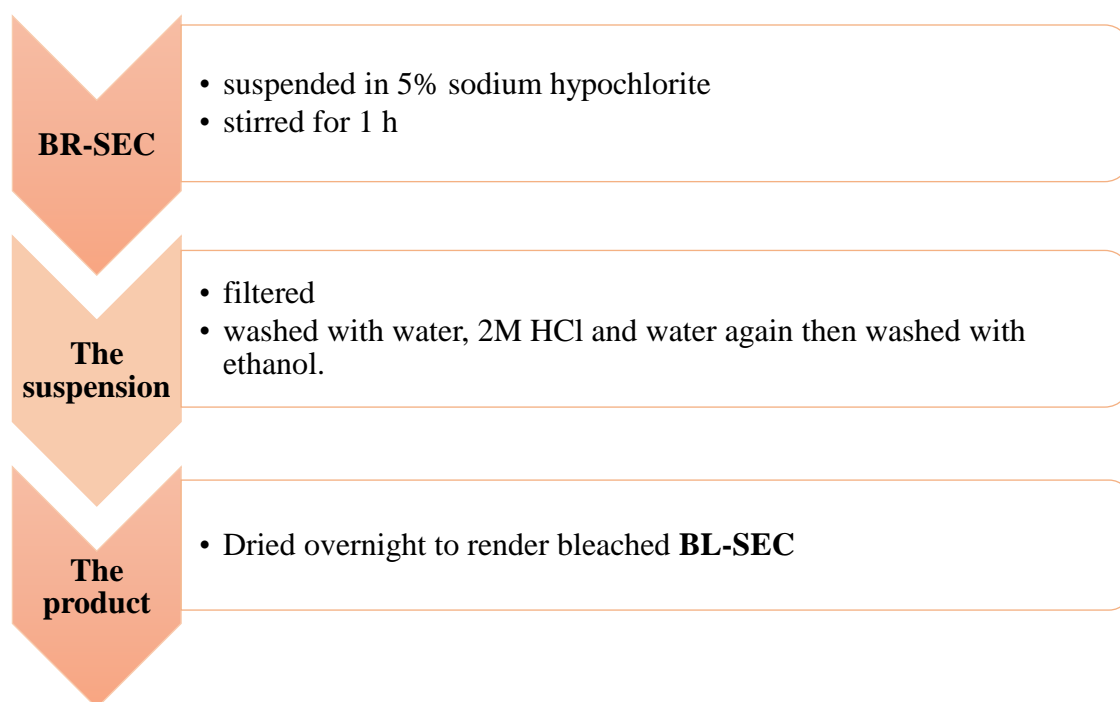
3.3.1.1 Preparation of brown *L. clavatum* sporopollenin (BR-SEC)



Scheme 3.1 The process of the extraction BR-SEC from *L. clavatum*.

The removal of sporoplasm comprises the extraction of the cytoplasm inside the intine, wherein an empty and undamaged capsule or microcapsule is obtained. The intine consists of narrow canals, hence the cytoplasm was extracted through the intine and exine. Following the procedure outlined in Scheme 3.1, the intine was removed and SECs were dried until a constant mass was obtained, leaving the sporopollenin exine microcapsule. This resulted in a brown coloured SEC (**BR-SEC**). The microcapsule could then be filled with an active substance.

3.3.1.2 Preparation of bleached *L. clavatum* sporopollenin (BL-SEC)



Scheme 3.2 The process of the preparation of BL-SEC from BR-SEC.

Bleached SECs (**BL-SEC**) were extracted by bleaching **BR-SEC** with aqueous sodium hypochlorite (NaClO) solutions as shown in Scheme 3.2. The result was a white or very pale coloured SEC.

3.3.2 Effect of the preparation method on the functional groups.

The methods of preparation of the SECs are likely to have an effect on the type of the functional groups present on the surfaces of the sporopollenin. In particular, the preparation of the brown SECs involves base (NaOH) which will result in deprotonation of the carboxylic acid and phenolic groups resulting in the formation of sodium salts of carboxylates and phenolates. In contrast, the final stages of the preparation of the bleached SECs involves washing with HCl and this will result in the protonation of the carboxylates and phenolates leading to neutral surface species. It has been shown previously sporopollenin was found to be less capable of adsorbing metal ions at low pH values, with pH values close to being neutral resulting in the best sorption properties.⁹⁰ This is thought to be due to the increased dissociation of carboxylic and phenolic groups within sporopollenin at higher pH values.⁹¹ Therefore, the carboxylates and phenolates will take

up more metal than the neutral species so the brown SECs are expected to have higher metal loading than the bleached SECs.

3.4 Characterisation of SECs

The BR-SEC and BL-SEC exines were investigated using scanning electron microscopy (SEM) to examine the structure of the SECs and by elemental analysis (ICP-OES and CHN), IR and Raman spectroscopy and UV-Vis spectroscopy to identify the chemical structure and functional groups present within them.

3.4.1 Scanning electron microscope (SEM) images

The harsh methods used in the extraction of SECs may result in the breakdown of the SEC microcapsules. SEM was used to examine the SECs for damage. The SEM images of the samples (Figure 3.3 and Figure 3.4) clearly show the almost hemi-spherical shape of the *ca.* 20 μm microcapsules, with the characteristic trilete feature on the underside, verifying that the sporopollenin particles were not damaged by the extraction process. This demonstrates that the extraction methods used in this research were not too harsh, and resulted in high quality, intact, sporopollenin exine capsules, that the quality when using quicker methods, is very similar to that when using longer times in the traditional methods.

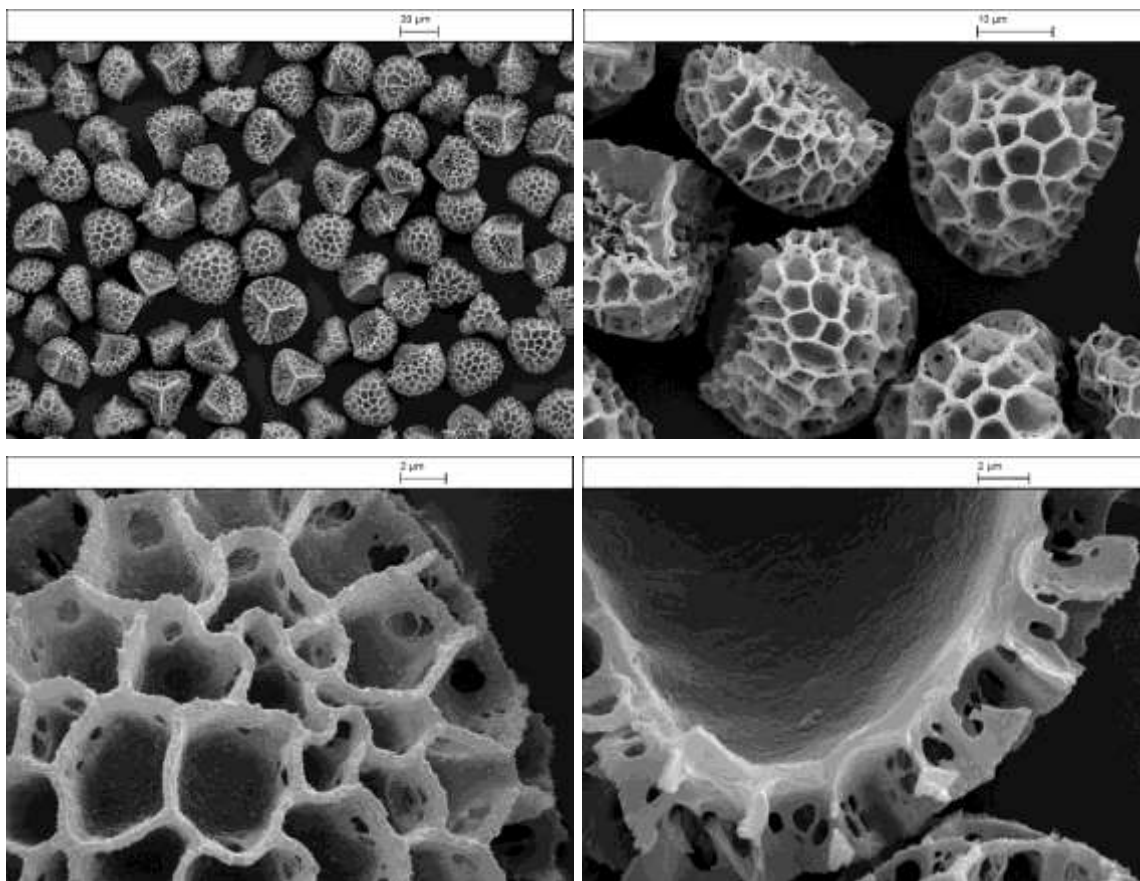


Figure 3.3 SEM images of BR-SECs.

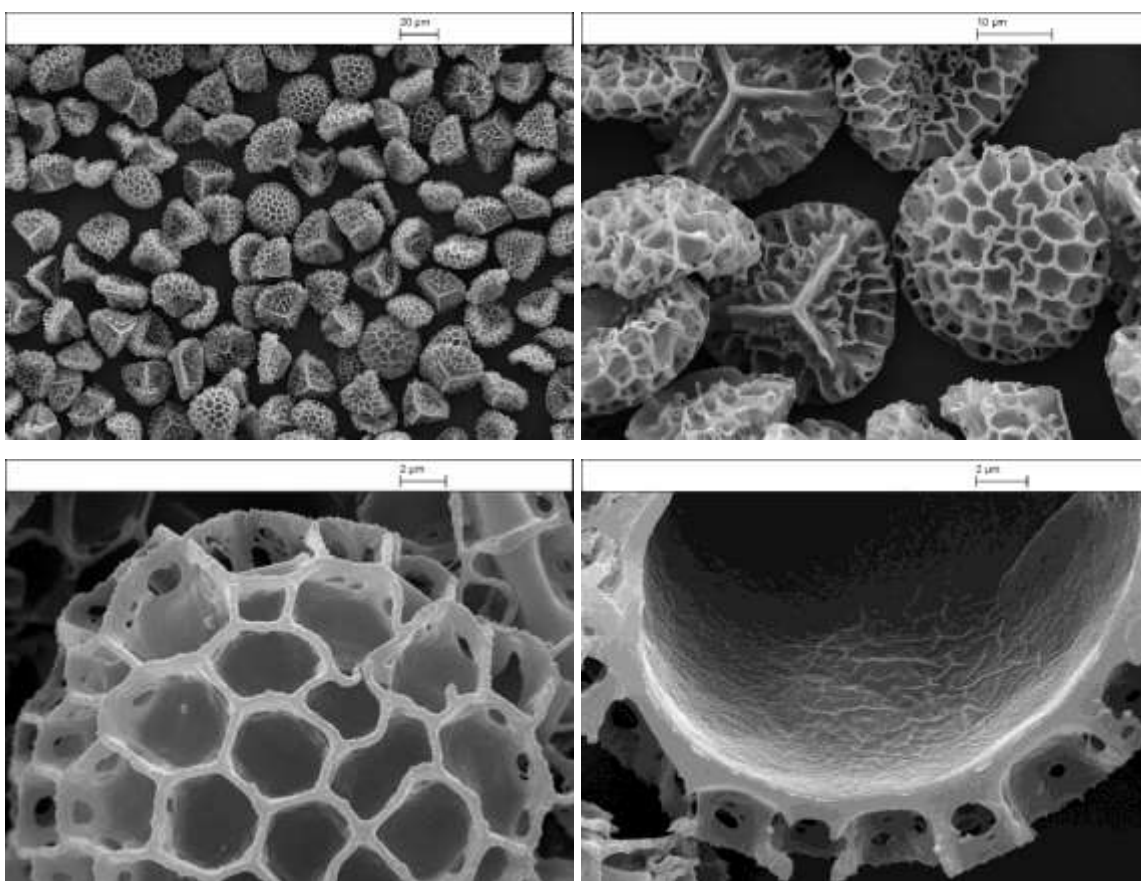


Figure 3.4 SEM images of BL-SECs.

3.4.2 Chemical Structure of sporopollenin

3.4.2.1 Elemental analyses

The C, H, N elemental analysis of different SECs are shown in Table 3.1. The empirical formula has been calculated assuming a C₉₀ base¹⁹ and that the missing mass is oxygen.³⁴

Sporopollenin sample	% Elemental analysis (C, H, N)			%O (assuming residual)	Empirical formula (assuming a C ₉₀ basis ¹⁹)
	C	H	N		
BL-SEC	56.36	8.23	0.35	35.06	C ₉₀ H ₁₅₇ O ₄₂
BR-SEC	56.24	8.00	1.44	34.32	C ₉₀ H ₁₅₃ O ₄₁

Table 3.1 Results of elemental analysis of SECs.

The C and H content of the BL-SEC and BR-SEC were similar at about 56 % and 8 % respectively. Only trace levels of N were present in all two SECs, ranging from 0.35 % to 1.4 %.

3.4.2.2 Vibrational spectroscopic identification of functional groups in sporopollenin

Raman and infrared (IR) spectroscopy were used to determine the structural units and functional groups present within sporopollenin.

3.4.2.2.1 Infrared spectroscopy (IR)

Because of the difficulties with background fluorescence experienced with Raman spectroscopy, IR spectroscopy was also used to identify the functional groups within sporopollenin. IR spectroscopy has advantages over Raman spectroscopy, rather than on the bulk properties of the compound. Some research studies conducted by Mackenzie and Barrier⁷ suggest that sporopollenin contains several functional groups, specifically alcohols, carboxylic acids, aromatics, and double bonds.⁷ IR spectroscopy can be applied to identify these functional groups from their vibrational spectra in the mid-IR region (4000–400 cm^{-1}).^{52, 10, 61, 147-149} Furthermore, it can explore the structural framework of the spore metal complex without destroying its internal structure.

A diamond ATR sampling accessory was tried in order to reduce sample preparation time, but it was found that the data were of significantly lower quality than when a potassium bromide (KBr) pellet was used.

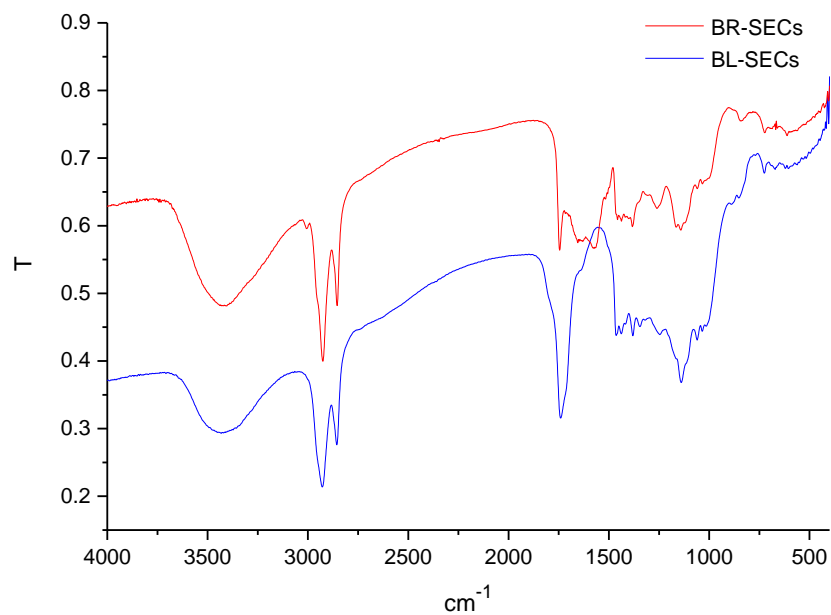


Figure 3.5 IR spectra of BR-SECs and BL-SECs.

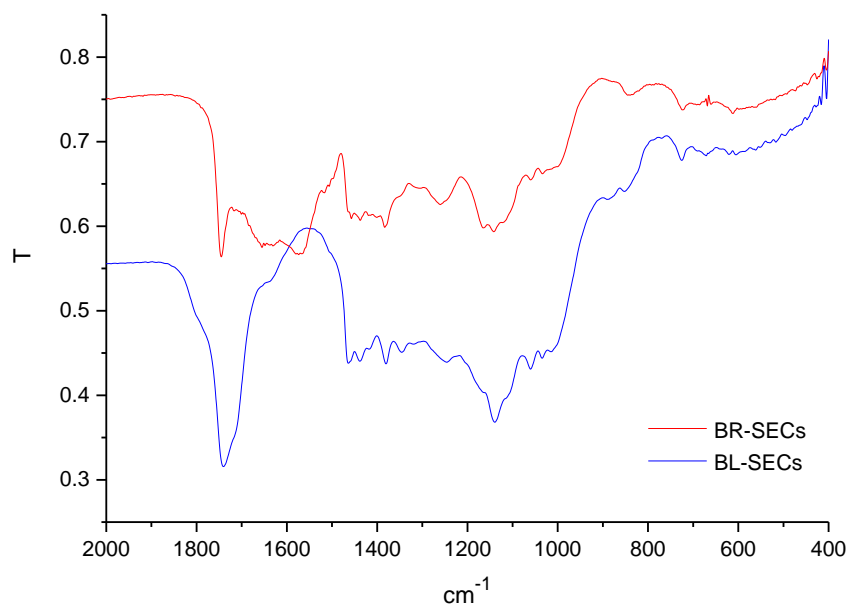


Figure 3.6 Expanded from 400 to 2000 cm^{-1} of the IR spectra of BR-SECs and BL-SECs.

The IR spectra of both the bleached and brown SECs show a broad absorption characteristic of hydrogen bonded hydroxyl groups (approximately 3430 cm^{-1}). This may be attributed to phenol O-H groups, although there might also be a contribution from water either in the KBr, or the SEC itself. Comparison between a blank KBr disc and one

containing SECs indicated that the major contribution to this feature comes from the SEC and not the KBr. On bleaching there was little change in the intensity of this band compared to the C-H modes at 3000 cm^{-1} , but the band became slightly less broad. The IR spectrum of the BR-SECs displays bands at 3006 (w) , 2957 (sh) , 2926 , 2870 (sh) and 2854 cm^{-1} . In the IR spectrum of the BR-SECs, the weak peak at 3006 cm^{-1} is no longer visible, but the other four bands are still present, but the most intense peaks have shifted to slightly higher wavenumber (2928 and 2856 cm^{-1}). These bands are characteristic of C-H stretching modes. The antisymmetric and symmetric C-H stretching modes for CH_3 groups normally occur at $2972 - 2952\text{ cm}^{-1}$ and $2882-2862\text{ cm}^{-1}$, respectively.^{150, 108} For CH_2 groups the antisymmetric and symmetric C-H stretching modes are usually found at $2936 - 2916\text{ cm}^{-1}$ and $2863-2843\text{ cm}^{-1}$, respectively. Therefore, these bands are evidence for the presence of an aliphatic (CH_2) backbone in both BR-SECs and BL-SECs. The absence of the weak peak at 3006 cm^{-1} in the spectrum of the BR-SECs implies the loss of aromatic or olefinic C-H compared to the BR-SECs.

Peaks between 1800 and 1600 cm^{-1} are associated with carbonyl $\text{C}=\text{O}$ stretching vibrations in the SECs spectra. The sharp peak in the ν_{CO} region of the spectrum of the BR-SEC sample at 1746 cm^{-1} , is most likely associated with saturated esters, and this broadens and strengthens to give peaks at 1804 (sh) , 1741 , $1712\text{ (sh)}\text{ cm}^{-1}$ in the spectrum of BL-SEC. These significant changes reflect different types of carbonyl (e.g. ketone, aldehyde, carboxylic acids) being formed resulting from oxidation of the phenols and alcohol groups, known to be present in sporopollenin.

The relatively strong broad peaks at 1655 cm^{-1} and 1570 cm^{-1} in the BR-SECs, which are characteristic of $\text{C}=\text{C}$ double bond unsaturation and aromatic/double bond C-H bending, are replaced by a weaker shoulder at 1642 cm^{-1} in the BL-SEC data which might reflect a loss of conjugation, which is consistent with the loss of the peak at 3006 cm^{-1} .

In the finger-print region between 1500 and 700 cm^{-1} there are also subtle differences between the IR spectra of the BR-SEC and BL-SEC samples. Features due to C-H bending in CH_2 and CH_3 aliphatic units at 1464 , 1457 and 1415 cm^{-1} are common to both the BR-SEC and BL-SEC but the peaks at 1438 and 1346 cm^{-1} are more prominent in the spectrum of the BL-SEC sample. A peak at 1380 cm^{-1} due to CH_3 symmetric deformations is common to both.

The complex set of bands at 1271, 1257 and 1240 cm^{-1} in the spectrum of the BR-SECs is replaced by one broad unstructured band at 1246 cm^{-1} for the BL-SECs. The 1271 cm^{-1} band is in the region expected for O-H bending in alcohols (O-H deformations in aromatic alcohols and phenols are at 1430 cm^{-1}), and it is weaker in the BL-SEC spectrum. The lower wavenumber bands are more associated with C-O stretching modes in unsaturated ethers. The broad absorption at 1150 cm^{-1} could be attributed to the presence of saturated ether groups, or tertiary alcohols.¹⁰⁸ In the broad feature the central peak at 1140 cm^{-1} grew in intensity in the BL-SEC spectrum, compared to the peaks at 1166 and 1117 cm^{-1} . This is summarised in Table 3.2.

Absorption frequency (cm^{-1})	Functional groups
~3450	-OH
3006	(C-H) stretching (aromatic/alkene)
~2960	(C-H) stretching (CH_3)
~2925	(C-H) _s stretching (CH_2)
~2855	(C-H) _{as} stretching (CH_2)
~1744	C=O stretching (esters)
~1650	C=C stretching
~1570	C-H bending (aromatic/double bond)
~1446	C-H bending
~1250	O-H bending
~1150	C-O stretching

Table 3.2 IR absorptions obtained from some SECs.^{108, 150}

To conclude, IR spectroscopy identifies differences between BR-SECs and BL-SECs. Identifying the exact differences is a challenge, but there does seem to be less conjugation in the BL-SECs than the BR-SECs, and there are some subtle differences in the carbonyl groups present.

3.4.2.2 Raman spectroscopy

The Raman spectra of single grain ragweed pollen recorded at 633 and 780 nm have been reported.¹¹¹ Although background fluorescence was an issue, the following spectra features were assigned to sporopollenin in the ragweed pollen: 2920-2855 cm^{-1} (CH_2 and CH_3 stretches); *ca.* 1600 cm^{-1} (ring stretching modes of phenyl groups); *ca.* 1440 cm^{-1} (CH_2 deformations); *ca.* 1080 cm^{-1} (C-C skeletal vibrations); *ca.* 860 cm^{-1} C-C stretches. Weaker bands at *ca.* 1000 (trigonal ring breathing) and *ca.* 600 cm^{-1} aromatic ring deformation were also believed to arise from sporopollenin. This work was then used to interpret the Raman and IR data of a number of other pollen samples but not *L. clavatum*.^{151, 152} Normal and surface enhanced Raman spectra (SERS) have also been obtained from rye and ragweed exines, where the exines were exposed to silver nanoparticles to facilitate SERS.¹⁵³ A recent report utilising gold nanoparticles for SERS studies of aqueous pollen extracts highlighted the problem of fluorescence from the spores¹⁵⁴ which has also been noticed by others.^{111, 155, 156} The normal Raman spectra of rye and ragweed exhibited fluorescence problems, but the SERS spectra were of much higher quality. Features at 1745 cm^{-1} were assigned to ester carbonyls, and at 1447 cm^{-1} to CH_2 scissoring in ragweed.¹¹¹

In this study, brown SECs and bleached SECs were studied using Raman spectroscopy (Figure 3.7 and Figure 3.8). The spectra are dominated by the different vibrational modes of sporopollenin. When comparing the Raman spectra of the brown (Figure 3.7) and bleached (Figure 3.8) SECs, one can observe that the colour of sporopollenin clearly affects Raman spectroscopy. The spectrum of the brown SECs (Figure 3.7) shows extensive background fluorescence which masks the vibrational Raman features. The fluorescence is caused by absorption of the 1064 nm excitation by the brown colouration (see UV-vis data) that results in the formation of an excited state in the SEC that then decays by fluorescence emission. The reduction in intensity at 0 cm^{-1} is due to the filter used to remove the Rayleigh scatter.¹⁵⁷ Very high fluorescence also overwhelmed the Raman signal when 514.5 nm excitation was employed, unless the sporopollenin was heated above 500 °C.^{151, 127}

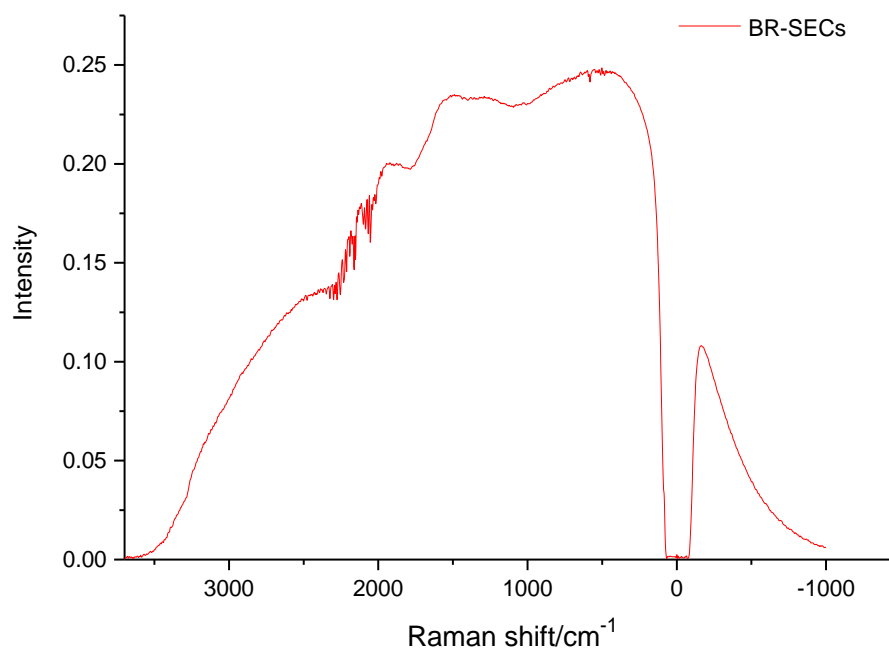


Figure 3.7 Raman spectrum from brown SECs (BR-SECs).

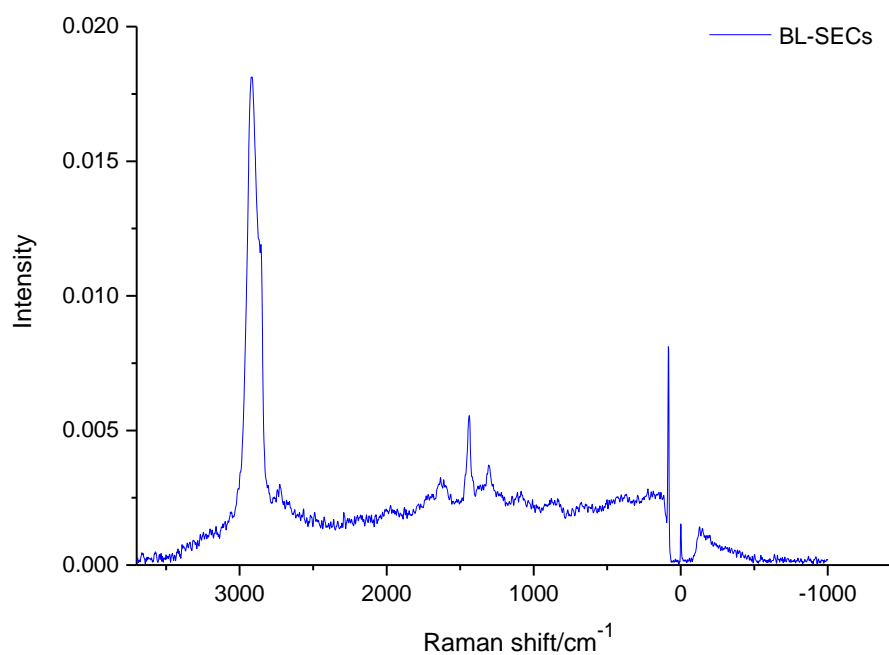


Figure 3.8 Raman spectrum from bleached SECs (BL-SECs).

The strong fluorescence in the spectrum of the brown SECs (Figure 3.7) is absent in the spectrum of the bleached SECs (Figure 3.8). The Raman spectrum of the bleached sporopollenin shows an intense band at 2918 cm^{-1} , with shoulders at 2870 and 2855 cm^{-1} . The C-H stretching modes in CH_2 units are usually found centred at 2926 and 2853 cm^{-1} ,

while those in CH₃ groups are at 2962 and 2872 cm⁻¹. Therefore, these can be assigned to CH₂ and CH₃ stretching modes. The medium intensity band at 1438 to 1304 cm⁻¹ may be assigned to 1438 cm⁻¹ band to CH₂ deformations. This reveals the existence of long aliphatic chains, which is in agreement with other works. The weaker bands at 1605, 1094 and 857 cm⁻¹ can be assigned to aromatic ring stretching modes, C-C skeletal vibrations and C-C stretches. Finally, the weak band at 1640 cm⁻¹ is most likely to be due to a carbonyl group which is C=O stretching vibrations.^{111, 112} These results are also in good agreement with the previously reported data.

The fluorescence level varies significantly with excitation wavelength, and sample colour. Therefore, whilst the Raman spectrum of the bleached sporopollenin is relatively free from background fluorescence, this may not be true for metal-sporopollenin complexes, which will be studied in subsequent chapters.

3.4.2.3 Nuclear magnetic resonance spectroscopy (NMR)

The ¹³C-NMR spectra of BR-SECs and BL-SECs are shown in Figure 3.9, the spectra for brown and bleached are nearly similar. Features in the spectra between 15 and 40 ppm indicate aliphatic carbon, and there are some slight changes in the peaks around 29 ppm. There are also some subtle changes in the 70 ppm region between the BR-SEC and BL-SEC, and these peaks belong to C-O units. The very weak features at ca. 120-140 ppm are indicative of olefinic carbons or aromatic.^{33, 51, 47} A broad signal at ca. 170 ppm shows the presence of ester or carboxylic acid groups.^{33, 51, 47} Although, there are limited differences between the NMR spectra of BR-SEC and BL-SEC, the NMR data is consistent with the IR data indicating the presence of an aliphatic backbone with esters and/or carboxylic acids, together with evidence for other C-O units. The weak olefinic/aromatic features are reduced in the BL-SECs compared to the BR-SECs.

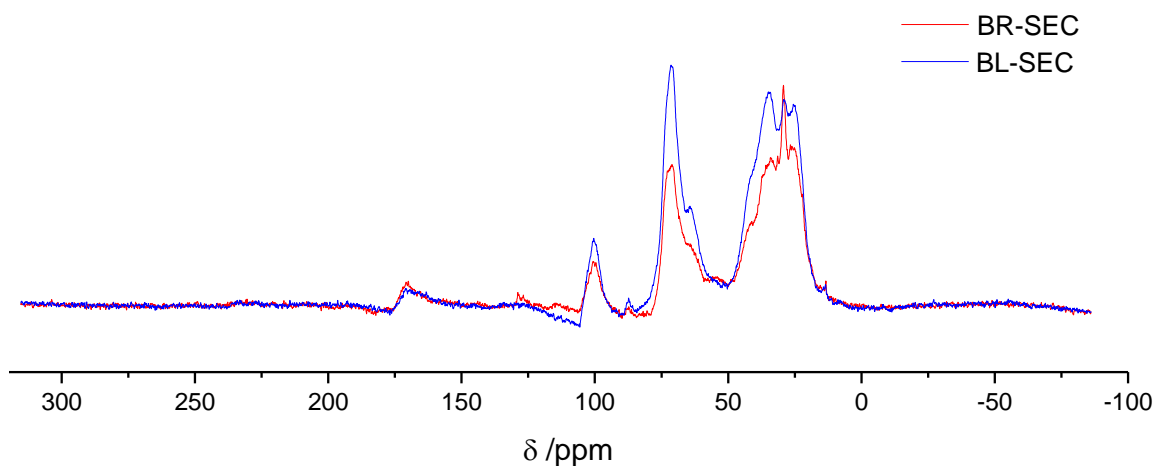


Figure 3.9 NMR spectra for brown and bleached SECs.

3.4.2.4 Electronic absorption spectroscopy (UV – visible - NIR)

UV-vis spectroscopy was used to demonstrate how the bleached SECs could be used for visible spectroscopy, especially when metals were attached.

The spectra for the BR-SECs shows masking of the spectral features in both the visible and UV regions above 10000 cm^{-1} (Figure 3.10). This masking effect meant that it was not possible to use UV-vis spectroscopy to analyse the BR-SECs. The BL-SECs however only absorbed in the UV region above 22000 cm^{-1} (Figure 3.10), and hence their visible spectra could be investigated. This allows for the investigation of both organic dyes and transition metals attached to SECs. The brown colour is due to the extensive conjugation which is reduced when it is bleached.

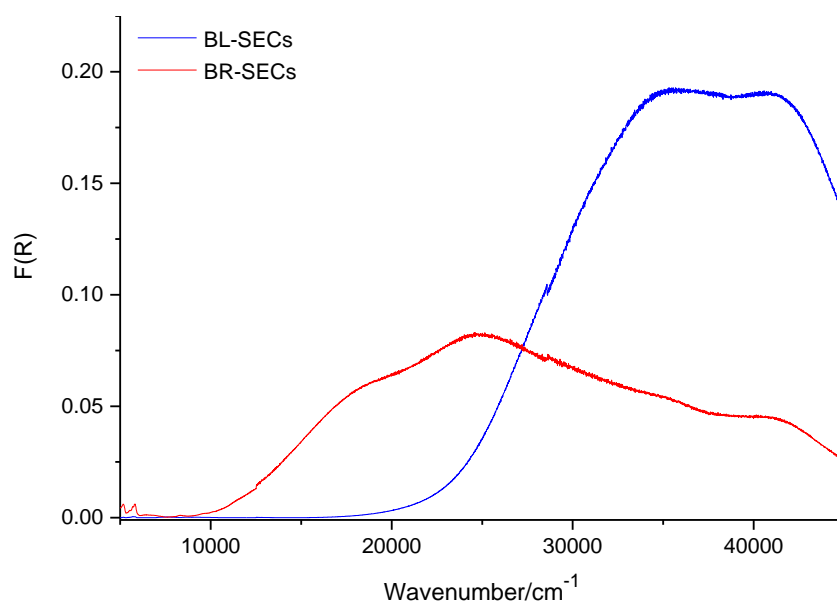


Figure 3.10 Diffuse reflectance (Kubelka-Munk) electronic absorption spectra from BL-SECs and BR-SECs.

Figure 3.11 shows the spectral features in the BL-SECs data for different stirring times, SEC was used alone without inorganic metals to act as a test material. This procedure also included 0.1g of bleached SECs with 25 mL of water stirring methods, which comprised overnight stirring, three days, week for two weeks. Table 3.3 shows the masses of bleached SEC in different stirring and the constant weights are nearly similar.

Sporopollenin stirring	Mass of BL-SEC (mg)
Overnight	63.7
3 days	60.9
1 week	63.1
2 weeks	68.7

Table 3.3 The masses of BL-SECs in different stirring.

The intensity within the UV region appears to increase gradually with increased stirring times, but with solid state UV-vis experiments it is hard to quantify. If genuine, this indicates an increase in UV absorption on prolonged contact with water, implying an increase in UV chromophores that may be as a result of more conjugation or quinone C=O

converting to aromatic. The band in the UV region is probably from $\pi \rightarrow \pi^*$ transitions in the aromatic or conjugated part of sporopollenin.

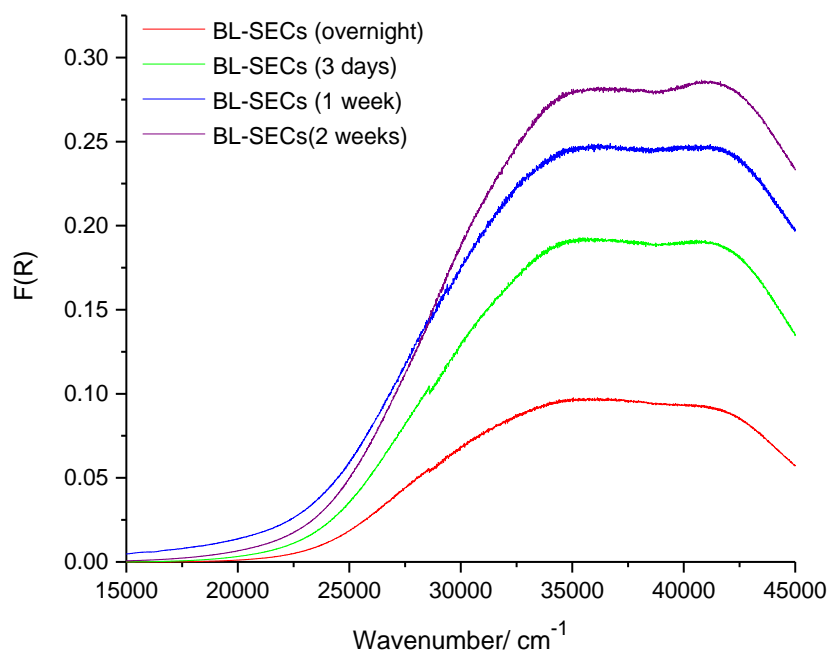


Figure 3.11 Diffuse reflectance (Kubelka-Munk) electronic absorption spectra for BL-SECs with different stirring times.

The intensity of the colour produced by the complex ion can be used to identify the concentration of metal within a sample via the Beer-Lambert law.¹³²

$$A = \epsilon cl$$

Equation 3.1 The Beer-Lambert law.

Because of the lack of the path length data in the solid state UV-vis reflectance spectra in this project, these were converted to a pseudo absorbance spectra (F(R)) using the Kubelka-Munk equation.¹³³

$$F(R) = (1-R)^2/2R = k/s = Ac/s$$

Equation 3.2 The Kubelka-Munk equation.

3.5 Conclusion

In this chapter brown SECs were successfully extracted from sporopollenin from *L. clavatum*. The brown SECs were successfully bleached using sodium hypochlorite to produce bleached SECs. SEM images showed the almost spherical shape of the sporopollenin particles, demonstrating that both the brown and bleached SECs were undamaged by the extraction procedure. Several spectroscopic and characterisation techniques were employed to further examine the structure and functional groups of the SECs. Elemental determination was carried out on the SECs by CHN analyses.

IR and Raman spectroscopy identified several functional groups in the SECs. Due to high background fluorescence, Raman spectroscopy could not be used to identify functional groups within the brown SECs. However, several functional groups were identified using the bleached SECs. These included unsaturated and aromatic functional groups such as phenolic groups. Using IR spectroscopy it was possible to identify functional groups in both the brown and bleached SECs. Both the Raman and IR spectra highlighted the significance of aliphatic chains in the macromolecule. The presence of hydroxyls, carbonyls, unsaturated hydrocarbons and ether groups was also revealed. Also, the NMR data is consistent with the IR data showing the presence of an aliphatic backbone with esters and/or carboxylic acids, together with evidence for other C-O units.

When examining the UV-vis spectra, the use of bleached SECs overcame issues of spectral masking caused by the brown colouration of the brown SECs. Increasing the sample stirring time from overnight to two weeks resulted in increased intensity of the characteristic features within the spectra.

Chapter 4

Copper attached to sporopollenin

4 Copper attached to sporopollenin

4.1 Introduction

Copper is a chemical element with symbol Cu (from Latin cuprum) and atomic number 29 and atomic mass 63.54. It is solid at room temperature and is in Group 11 of the Periodic Classification of the Elements. The electronic configuration of copper is: [Ar] 3d¹⁰ 4s¹. Researchers have paid considerable attention to use of sporopollenin exine capsules (SECs) for some applications such as for high protein adsorption capacity and as an economic and eco-friendly biosorption material.^{158, 159} The aim of this chapter is to investigate the impact of attaching copper complexes to SECs as shown schematically in Figure 4.1. These could then be used in a wide variety of applications including catalysis, imaging and biological delivery. Although some research groups have published work on the interaction of copper with chitosan/sporopollenin capsules for use in bioremediation^{90, 93, 95, 96, 100, 158-162}, there does not appear to be any published work on direct Cu-SECs interactions.^{158, 159} Therefore the aim of this study is to use a variety of spectroscopic techniques to investigate how copper is bound to the SECs.

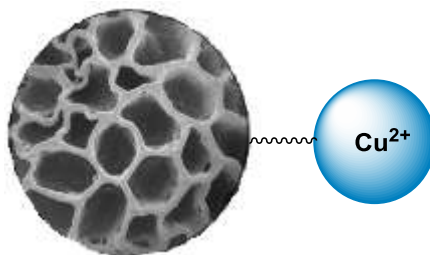


Figure 4.1 schematic representation of the attachment of copper complexes to SECs.

Bleached SECs allow for wider variety of spectroscopic techniques, especially UV-vis and Raman to investigate the nature of the interaction between copper and the SEC. As copper(II) has d-d transitions at relatively low energy, it is ideally suited to these studies. In addition, it is also possible to carry out electron paramagnetic resonance experiments. The aim of this chapter is to describe the preparation of copper complexes from loading experiments using copper acetate, copper nitrate or copper chloride solutions, with brown and bleached sporopollenin exine capsules (SECs). The microcapsules were characterised by elemental analysis (CHN and ICP-OES for Cu) and scanning electron microscopy (SEM), UV-visible spectroscopy, Infrared spectroscopy (IR), EPR spectroscopy and X-ray

absorption spectroscopy. This study provides insight into how copper salts attach and form complexes with SECs.

4.2 Synthetic methods

4.2.1 Preparation of sporopollenin samples for copper loading studies

Two different extractions of *L. clavatum* were used for studying copper loadings; bleached SECs (BL-SECs) and brown SECs (BR-SECs). The BL-SECs were prepared from the brown (BR-SECs) sporopollenin exine capsules, as described in Chapter 3. Reactions were carried out with solutions of the following copper salts: copper(II) chloride, copper(II) nitrate and copper(II) acetate.

100 mg of SECs were added to 25 mL solution of each copper salt. In order to determine the optimum conditions for metal loading of the SECs, the concentration of copper salt and length of stirring time was varied. The BL-SECs were stirred for the following lengths of time: overnight; three days; one week or two weeks. The BR-SECs were only stirred for three days as this was found to be the optimum during the work with the bleached SECs. The solutions were filtered, and washed with water followed by ethanol. The washings were air dried and then placed in a desiccator. This method was carried out with 1.0, 2.5 and 5.0 mmol of copper salt in 25 mL water for the BL-SECs and 2.5 mmol only for the BR-SECs. The colour of the copper salts with BL-SECs was pale green for copper chloride and nitrate, and a slightly deeper/darker green for acetate. The colour due to the copper was masked by the BR-SECs, so these all appeared brown in colour.

Copper salt	Mass of salt	mmol of copper salt	Mass of BL-SEC or BR-SEC
CuCl₂.2H₂O	170.6 mg	1.0	100 mg
CuCl₂.2H₂O	426.7 mg	2.5	100 mg
CuCl₂.2H₂O	853.4 mg	5.0	100 mg
Cu(NO₃)₂.3H₂O	241.4 mg	1.0	100 mg
Cu(NO₃)₂.3H₂O	603.6 mg	2.5	100 mg
Cu(NO₃)₂.3H₂O	1207.2 mg	5.0	100 mg
Cu(OAc)₂.H₂O	199.7 mg	1.0	100 mg
Cu(OAc)₂.H₂O	499.2 mg	2.5	100 mg
Cu(OAc)₂.H₂O	998.4 mg	5.0	100 mg

Table 4.1 Concentration of copper salts used in preparation of copper loaded SECs.

Additional experiments were carried out using 7.5 mmol of copper per 300 mg of SEC in 75 mL of water and a reaction time of three days in order to provide sufficient material for spectroscopic techniques.

4.3 Elemental analyses

The percentage of elements in sporopollenin were first measured by Zetzsche et al. in 1937.³² This and other previous elemental analyses showed that SECs contain C, H, and O, with only trace levels of nitrogen.¹⁶ The sporopollenin in the SECs is represented by an empirical formula based on a C₉₀ unit and the proportion of H and O varies from species to species.²⁰ ICP-OES and C, H, N combustion analyses were used to determine the elemental composition in the SECs and their metal complexes.

4.3.1 Inductively coupled plasma optical emission spectroscopy (ICP-OES)

The metal loadings in the SECs samples were analysed by ICP–OES using 10 mg portions of the samples. Table 4.2 displays the metal loadings for BL-SECs prepared with different stirring times and different initial quantities of metal complex.

Copper salt + BL-SECs	Time stirring	Copper loading on dry SECs (%w/w)
Copper(II)chloride solution (1 mmol:100 mg)	overnight	1.67±0.01
Copper(II)chloride solution (2.5 mmol:100 mg)	overnight	1.95±0.01
Copper(II)chloride solution (5 mmol:100 mg)	overnight	2.13±0.02
Copper(II)chloride solution (2.5 mmol:100 mg)	3 days	1.78±0.01
Copper(II)nitrate solution (1 mmol:100 mg)	overnight	1.83±0.02
Copper(II)nitrate solution (2.5 mmol:100 mg)	overnight	1.72±0.01
Copper(II)nitrate solution (5 mmol:100 mg)	overnight	2.03±0.01
Copper(II)nitrate solution (2.5 mmol:100 mg)	3 days	1.77±0.01
Copper(II)acetate solution (1 mmol:100 mg)	overnight	4.01±0.02
Copper(II)acetate solution (2.5 mmol:100 mg)	overnight	3.55±0.02
Copper(II)acetate solution (5 mmol:100 mg)	overnight	5.53±0.02
Copper(II)acetate solution (2.5 mmol:100 mg)	3 days	6.61±0.05
Copper(II)acetate solution (2.5 mmol:100 mg)	1 week	11.26±0.69
Copper(II)acetate solution (2.5 mmol:100 mg)	2 weeks	14.56±4.12

Table 4.2 The results of metal loading from ICP-OES.

It is evident from Table 4.2 that when comparing different metal loadings for the copper samples stirred overnight, copper acetate shows a higher copper loading than copper nitrate and copper chloride for all initial starting ratios of metal to SEC. For copper chloride and copper nitrate solutions no significant difference in copper loading was observed when longer stirring times were used. For example, at 2.5 mmol, the loading using a copper chloride solution is 1.95 % w/w after stirring overnight, and 1.78 % w/w after stirring for three days. For a copper nitrate solution the loading is 1.72 % w/w after stirring overnight and 1.77 % w/w after stirring for three days. In contrast, increasing the stirring times for copper acetate solutions resulted in a substantial increase in the amount of copper loaded, from 3.5 % w/w after stirring overnight to 14.5 % w/w after stirring for two weeks. Whilst all copper loadings are higher when 5 mmol of copper is used rather than 2.5 and 1 mmol, the difference is not that significant. The ICP-OES data showed an increase of approximately twice the amount of copper binding to surface functional groups for one or two weeks stirring compared to three days. The attachment level of copper to SECs was higher for acetate than that of chloride and nitrate for all cases investigated. In contrast, to copper acetate there was no significant difference in the amount of copper attached to the SEC when the stirring time was increased from overnight to three days for copper chloride and copper nitrate solutions and longer stirring times were not employed. However, when the experiments with copper acetate were repeated using 7.5 mmol copper and 300 mg of SECs in 75 mL of water the copper loading was largely independent of stirring time (see Table 4.6).

In order to check the sample to sample reproducibility of the ICP-OES analysis, the analyses of copper chloride and copper nitrate samples were repeated on three separate samples, in addition to the three determinations routinely carried out by the instrument for each sample.

It can be seen from Table 4.3 that for the copper chloride data the variation between the three samples in the second part is small but there is an offset between these and the first measurement. This offset could be due to variation in the dryness of the sample, but is most likely to be due to variation in the effectiveness of the digestion stage in the sample preparation. Therefore, these measurements indicate the copper loading is around 2 % w/w for the SECs treated with both copper chloride and copper nitrate. In the copper nitrate data in addition to this offset there also appears to be an outlier point. The first mean value in the table of copper nitrate solution is taken from two values lying close to each other,

and the second is from all three values. The outlying data point is most likely due to copper contamination during the digest stage. Therefore, samples with higher than expected metal loading were reanalysed.

Metal+ BL-SECs (2.5 mmol:100 mg) stirring 3 days	Copper loading (%w/w)	Mean metal loading (%w/w and error)
Copper(II) chloride solution	1.79±0.01	1.79±0.01
Copper(II) nitrate solution	1.78±0.01	1.78±0.01
* Copper(II) chloride solution	2.264	2.38±0.14
	2.328	
	2.549	
* Copper(II) nitrate solution	2.190	2.18±0.01
	2.175	
	4.199	

Table 4.3 ICP-OES results for BL-SECs following reaction with copper(II) acetate, chloride and nitrate solutions using Cu 327.393 nm emission line and * is carried out 3 times in ICP-OES analysis.

These results for the bleached SECs indicate that the optimum experimental conditions were a 2.5 mmol: 100 mg (metal: SEC) ratio stirred at room temperature for three days, and these were the conditions used in the remainder of experiments.

It can be seen from Table 4.4 that when comparing different copper samples with brown and bleached SECs, a higher copper loading is observed with brown SECs than bleached SECs for all of the copper salts. This may indicate that the bleaching process removes some of the functional groups that are involved in the copper coordination, as well as the effect of the ionisation state of the carboxylic acid and phenol groups discussed in section 3.3.2.

Sample with SEC (2.5 mmol: 100 mg)	Copper loading (% w/w)
Copper(II) acetate solution + BL-SECs	6.61±0.05
Copper(II) acetate solution + BR-SECs	9.02±0.08
Copper(II) chloride solution + BL-SECs	1.78±0.01
Copper(II) chloride solution + BR-SECs	6.93±0.01
Copper(II) nitrate solution + BL-SECs	1.77±0.01
Copper(II) nitrate solution + BR-SECs	6.58±0.06

Table 4.4 Comparison of the copper loading of SECs prepared from reaction with copper(II) acetate, chloride and nitrate solutions for stirring 3 days.

As seen previously, a higher copper loading is observed for the SECs reacted with copper acetate solutions than both copper chloride and copper nitrate solutions.

In order to carry out further spectroscopic experiments, a second batch of samples was prepared using 7.5 mmol of metal and 300 mg of SECs in 75 mL of water. These samples were stirred for three days. The ICP-OES data is collected in Table 4.5, together with that for the 100 mg: 2.5 mmol: 25 mL samples for comparison.

Sample	% w/w	
	300 mg : 7.5 mmol	100 mg : 2.5 mmol
Copper(II) acetate solution + BL-SECs	7.88±0.02	6.61±0.05
Copper(II) acetate solution + BR-SECs	8.96±0.07	9.02±0.08
Copper(II) chloride solution + BL-SECs	2.26±0.02	1.78±0.01
Copper(II) chloride solution + BR-SECs	7.42±0.05	6.93±0.01
Copper(II) nitrate solution + BL-SECs	2.11±0.02	1.77±0.01
Copper(II) nitrate solution + BR-SECs	6.03±0.07	6.58±0.06

Table 4.5 Comparison of ICP-OES results for Cu-SEC complexes prepared with different quantities of reagents (all stirred for three days).

It is evident from Table 4.5 that when comparing different metal loading using 7.5 mmol of metal and 300 mg of SECs, copper acetate shows higher copper loading than copper nitrate and copper chloride for all brown and bleached SECs, as seen for the 2.5 mmol and 100 mg experiments. For example, bleached SEC is 7.88 %w/w for copper acetate,

compared with 2.11 % w/w for copper nitrate and with 2.26 % w/w for copper chloride. Moreover, the difference between copper acetate and the other copper salts is greater with bleached SECs than brown SECs.

These results are compared with the original 2.5 mmol: 100 mg samples (Table 4.5). Whilst there is some variation, the trend of increased copper loading for the brown, rather than bleached SEC is still clearly evident.

The stirring duration had a greater effect on the final loading of copper when copper acetate was used compared to copper chloride or copper nitrate. The highest level of attachment of Cu to the SECs is found for acetate compared to chloride and nitrate.

Table 4.6 shows that when comparing copper acetate loading using 7.5 mmol of copper acetate and 300 mg of SECs, and 2.5 mmol of copper acetate and 100 mg of SECs in different stirring. The results show that when using 7.5 mmol of copper acetate and 300 mg of SECs are slightly similar, however when using 2.5 mmol of copper acetate and 100 mg of SECs, it can be show that the ICP-OES data showed an increase of approximately twice the amount of copper binding to surface functional groups for one or two weeks stirring compared to three days.

Sample	% w/w		Stirring time
	300 mg : 7.5 mmol	100 mg : 2.5 mmol	
Copper(II) acetate solution + BL-SECs	7.88±0.02	6.61±0.05	3 days
Copper(II) acetate solution + BL-SECs	9.10±0.005	11.26±0.69	1 week
Copper(II) acetate solution + BL-SECs	9.58±1.08	14.56±4.12	2 week
Copper(II) acetate solution + BR-SECs	8.96±0.07	9.02±0.08	3 days
Copper(II) acetate solution + BR-SECs	9.74±0.05	-	1 week
Copper(II) acetate solution + BR-SECs	10.05±0.08	-	2 week

Table 4.6 Comparison of ICP-OES results for Cu-SEC acetate prepared with different stirring.

The stirring time had the greatest impact on the loading of copper acetate-SEC complexes when it loading 100 mg of SECs however in the 300 mg of SECs all the results are nearly the same.

To conclude the ICP analyses from the results that whilst the amount of metal in the samples is dependent on the metal salt used, it is largely independent of stirring time for all metal salts. On the basis of these experiments it was decided to use a consistent set of conditions of ratios of 2.5 mmol of metal, with 100 mg of SECs in 25 mL of water and stirring for three days for all subsequent studies using copper and other metals. For the majority of reactions the actual amounts used were 7.5 mmol metal, 300 mg SEC and 75 mL water to provide enough sample for all of the analytical and spectroscopic measurements.

4.3.1.1 Solution UV-vis determination amount of copper extracted from solution

The ICP-OES data in Table 4.2 indicate the total copper remaining on the SECs after filtration, washing and drying. To identify the amount of copper initially adsorbed on to the SECs from the metal solution, the concentration of copper in the solution before addition of SECs and after initial filtering (but with no washing) was determined by solution UV-vis spectroscopy.

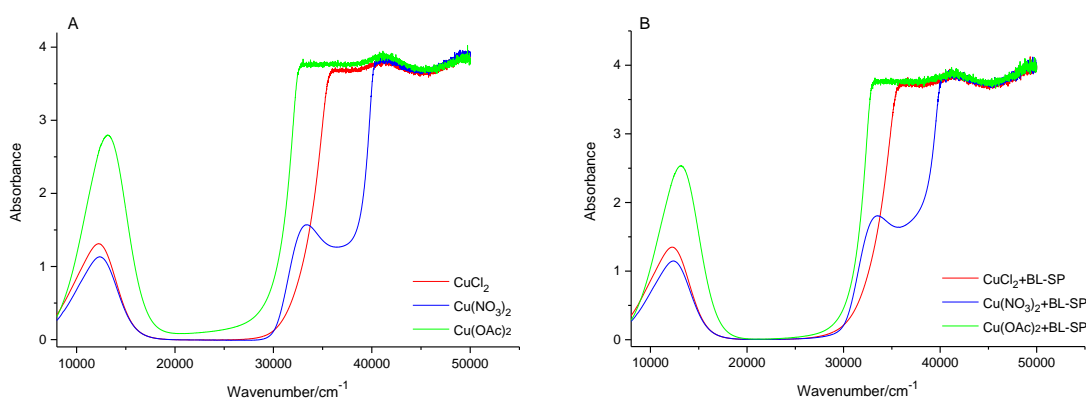


Figure 4.2 A) UV-vis-NIR spectra of copper solutions (0.1 M) before addition of BL-SECs. B) UV-vis-NIR spectra of copper solutions after addition of BL-SECs and stirred for 3 days.

The spectra of 0.1 M solutions before addition of the SECs are shown in Figure 4.2 A, and those of the filtrates are shown in Figure 4.2 B. The features at *ca.* 12500 cm⁻¹ are due to the d-d transitions in d⁹ Cu²⁺, and these have been used for the copper determination, the

other spectral features at higher wavenumber are totally absorbing. It is clear that the spectra for the copper(II) chloride and copper(II) nitrate solutions are very similar in the d-d region, but the spectrum of the copper acetate solution is different, indicating a different coordination environment. The features at higher energy are due to either charge transfer transitions or intra-ligand transitions. The speciation and structure of aqueous copper complexes is very complicated, due in part to the Jahn-Teller distortions, and is very dependent on the conditions. Even for the prototypical hydrated copper(II) blue solution that is usually described as being due to the $[\text{Cu}(\text{H}_2\text{O})_6]^{2+}$ ion, there is debate as to whether the solution contains static $[\text{Cu}(\text{H}_2\text{O})_6]^{2+}$, or if this is the time averaged structure rather than the instantaneous coordination of the complex believed to be present, namely $[\text{Cu}(\text{H}_2\text{O})_5]^{2+}$.¹⁶³⁻¹⁶⁶ Copper chloride solutions can appear the characteristic blue colour of the hydrated copper(II) ion in dilute solutions (e.g. 0.1 M), but in more concentrated solutions, and especially at higher Cl^- concentrations the solutions appear green and then yellow/red because of the formation of chlorocuprate complexes such as $[\text{CuCl}_4]^{2-}$.^{167, 168}

As the spectra of the copper chloride and nitrate solutions are similar, and it has been reported that the 0.1 M copper(II) chloride solution contains hydrated copper(II),¹⁶⁸ it is reasonable to assume that they are both due to the hydrated copper(II) ion. The peak position (12300 cm^{-1}) and the molar absorptivity (*ca.* $12 \text{ dm}^3 \text{ cm}^{-1} \text{ mol}^{-1}$) are in good agreement with the literature data.¹⁶⁸⁻¹⁷⁰ The spectrum of the copper acetate solution is different, both in terms of the position of the d-d peak (13100 cm^{-1} vs 12300 cm^{-1}), and the molar absorptivity of $28 \text{ dm}^3 \text{ cm}^{-1} \text{ mol}^{-1}$ that is over twice that in the copper(II) chloride and nitrate solutions. In the solid state, copper acetate is a dimer,¹⁷¹ but in solution it can either exist as a dimer or monomer. The dimer is favoured in organic solvents, but in water the dimer-monomer equilibrium lies essentially completely on the monomer side.¹⁷²⁻¹⁷⁷ Therefore, the electronic absorption spectrum is similar to that of other octahedral complexes,^{173, 178} rather than possessing features characteristic of the dimer at 27000 cm^{-1} .¹⁷⁹ The spectral features of various copper species in aqueous-acetic acid solutions are given in Table 4.7.¹⁸⁰

Species	λ_{\max} /nm	λ_{\max} / cm^{-1}	ϵ_{\max} / $\text{dm}^3 \text{ mol}^{-1} \text{ cm}^{-1}$
Cu²⁺	800	12500	11.3
CuOAc⁺	750	13330	24
CuOAc₂	740	13510	39
Cu₂OAc₄	670	14930	95

Table 4.7 Summary of spectral features of various copper species in aqueous-acetic acid solutions.¹⁸⁰

Therefore, on the basis of these data, the spectral feature at 13100 cm^{-1} is associated with copper with either one or two acetate ligands still attached. After addition of the SECs and their removal by filtration, the spectra were very similar Figure 4.2B, except that the intensity of the d-d peaks were lower.

Table 4.8 compares the amount of copper removed from the solution, with that found on the SECs. The amount of copper removed from the solution by the SECs was determined by UV-vis solution spectroscopy. Calibration curves were obtained for all copper solutions and gave the following molar absorptivity values, ϵ , copper acetate ($28.3 \text{ dm}^3 \text{ mol}^{-1} \text{ cm}^{-1}$), copper chloride ($13.5 \text{ dm}^3 \text{ mol}^{-1} \text{ cm}^{-1}$) and copper nitrate ($11.9 \text{ dm}^3 \text{ mol}^{-1} \text{ cm}^{-1}$). These are in good agreement with the literature values.¹⁶⁸⁻¹⁷⁰ The spectrum of the filtrate was measured and the difference in absorbance of the d-d bands in this and the initial spectrum was used to calculate how much copper had been removed. For example, in the case of copper(II) acetate the absorbance dropped from 2.83 to 2.53. A change of 0.30 absorbance units implies a concentration change of $(0.30/2.83) = 1.06 \times 10^{-2} \text{ M}$. As the volume of the solution was 25 mL, this means a change of 2.65×10^{-4} moles, which is 16.8 mg of copper.

Copper salt + BL-SECs	Copper loading on dry SECs (%w/w)	Mass of copper (mg) removed from solution from UV-vis data
Copper(II)chloride solution (1 mmol:100 mg) stirring overnight	1.67±0.01	14.3
Copper(II)chloride solution (2.5 mmol:100 mg) stirring overnight	1.95±0.01	17.4
Copper(II)chloride solution (5 mmol:100 mg) stirring overnight	2.13±0.02	21.9
Copper(II)chloride solution (2.5 mmol:100 mg) stirring 3 days	1.78±0.01	14.2
Copper(II)nitrate solution (1 mmol:100 mg) stirring overnight	1.83±0.02	18.9
Copper(II)nitrate solution (2.5 mmol:100 mg) stirring overnight	1.72±0.01	18.0
Copper(II)nitrate solution (5 mmol:100 mg) stirring overnight	2.03±0.01	30.1
Copper(II)nitrate solution (2.5 mmol:100 mg) stirring 3 days	1.77±0.01	15.7
Copper(II)acetate solution (1 mmol:100 mg) stirring overnight	4.01±0.02	11.3
Copper(II)acetate solution (2.5 mmol:100 mg) stirring overnight	3.55±0.02	13.1
Copper(II)acetate solution (5 mmol:100 mg) stirring overnight	5.53±0.02	Solution too absorbing
Copper(II)acetate solution (2.5 mmol:100 mg) stirring 3 days	6.61±0.05	16.8
Copper(II)acetate solution (2.5 mmol:100 mg) stirring 1 week	11.3±0.69	21.5
Copper(II)acetate solution (2.5 mmol:100 mg) stirring 2 weeks	14.6±4.12	Solution too absorbing

Table 4.8 Comparison of metal loading from ICP-OES and initial metal adsorption from UV-vis.

The mass of copper acetate removed increased with increased stirring times. For example, 13.1 mg of copper was removed from a 25 mL solution containing 2.5 mmol copper(II) acetate after stirring overnight compared to 16.8 mg after stirring for three days. Unexpectedly, increasing the stirring time decreased the amount of copper nitrate removed from a 25 mL solution of 2.5 mmol copper(II) nitrate from 18.0 mg overnight to 15.7 mg after three days. In the case of copper chloride solutions 17.4 mg of copper was removed

from a 25 mL solution of 2.5 mmol copper(II) chloride after stirring overnight, compared to 14.2 mg after stirring for three days.

In all cases the amount of copper that was removed from the solution during the stirring was greater than the amount of copper that remained on the SEC after filtration, washing and drying. This indicates that some of the copper is lost from the SEC during washing and that the SECs may be able to be reused several times for metal remediation.

4.3.1.2 Extraction studies under different conditions

To test how tightly the copper was bound to the SEC in the different complexes and under different conditions, a series of experiments at different pH values (pH 1.5, neutral pH and pH 12.5) were carried out. In order to correlate the values with the spectroscopic data (see later) these experiments used the samples prepared with 7.5 mmol of copper and 300 mg of SEC in 75 mL of water and a reaction time of three days. 20 mg of the Cu-SEC complex was added to 5 mL of water or the acidic or basic solution and stirred for three days. The solid was filtered, washed with water followed by ethanol, and dried in a desiccator. Both the initial filtrate prior to washing and the dried SECs were analysed for copper using ICP-OES, and the values compared to the copper loading in the initial Cu-SEC complex, also determined by ICP-OES.

1. Neutral pH

Table 4.9 shows the amount of copper in the dry Cu-SEC complexes before and after the extraction process at neutral pH. Table 4.10 compares this data with the amount of copper in the extraction solution.

Sample	% w/w Cu (ICP-OES) in solid before suspending in water	mg of copper in 20 mg of SEC before extraction in water	% w/w Cu (ICP-OES) in solid after suspending in water, filtering, washing and drying	mg of copper in SEC after suspension in water	Difference (mg)	% loss of Cu
Cu(OAc)₂ + BL-SECs	7.87	1.57	6.03	1.21	0.37	23.4
Cu(OAc)₂ + BR-SECs	8.96	1.79	6.10	1.22	0.57	31.9
CuCl₂ + BL-SECs	2.26	0.45	1.75	0.35	0.10	22.6
CuCl₂ + BR-SECs	7.42	1.48	6.70	1.34	0.14	9.70
Cu(NO₃)₂ + BL-SECs	2.11	0.42	1.61	0.32	0.10	23.7
Cu(NO₃)₂ + BR-SECs	6.03	1.21	5.23	1.05	0.16	13.3

Table 4.9 Copper loadings in dry Cu-SEC complexes before and after extraction in neutral pH solution.

Sample	ICP results for Cu filtrate solution / ppm	mg copper extracted into 5 mL solution	%loss of Cu into solution	mg lost from solid	Difference mg
Cu(OAc)₂ + BL-SECs	24.6	0.12	7.82	0.37	0.24
Cu(OAc)₂ + BR-SECs	13.9	0.07	3.90	0.57	0.50
CuCl₂ + BL-SECs	19.0	0.09	21.0	0.10	0.07
CuCl₂ + BR-SECs	24.7	0.12	8.30	0.14	0.02
Cu(NO₃)₂ + BL-SECs	29.1	0.15	34.4	0.10	-0.05
Cu(NO₃)₂ + BR-SECs	8.19	0.04	3.40	0.16	0.12

Table 4.10 complete the results for copper loading in dry Cu-SEC complexes and in solution.

Sample	mg of copper in 20 mg of SEC before extraction in water	mg of copper remaining in SEC after suspension in water	% loss of Cu from solid	mg copper extracted into 5 mL solution	%loss of Cu into solution	mg copper missing
Cu(OAc)₂ + BL-SECs	1.57	1.21	22.9	0.12	7.82	0.24
Cu(OAc)₂ + BR-SECs	1.79	1.22	31.9	0.07	3.9	0.50
CuCl₂ + BL-SECs	0.45	0.35	22.6	0.09	21.0	0.01
CuCl₂ + BR-SECs	1.48	1.34	9.7	0.12	8.3	0.02
Cu(NO₃)₂ + BL-SECs	0.42	0.32	23.7	0.15	34.4	-0.20
Cu(NO₃)₂ + BR-SECs	1.21	1.05	13.3	0.04	3.40	0.12

Table 4.11 Summary of results for copper loading in dry Cu-SEC complexes and in solution.

These results show that there is not much difference in copper loss between the dry brown and bleached copper acetate-SEC complexes. However, there is a higher proportion of the copper extracted into the filtrate of the bleached Cu-SEC complexes than the brown Cu-SEC complexes. The results of the extraction at neutral pH for the copper nitrate -SEC complex indicate that the copper is much more tightly bound to the brown Cu-SEC than the bleached Cu-SEC. The difference in concentration of copper extracted between the bleached and brown Cu-SEC complexes is greater for Cu-SEC complexes prepared from copper chloride and nitrate solutions than copper acetate solutions, it can be seen that there is a much larger discrepancy in where the copper has gone for the acetate samples compared to the others. There is a large reduction in the amount of copper in the solid, but this does not seem to appear in the filtrate. Presumably it was removed in the washing stage. There also appears to be a small gain in amount of copper in the brown copper nitrate-SEC complex because of the small quantities involved.

2. Acidic (pH 1.5) conditions

The results of the extraction in hydrochloric acid solution at pH 1.5 are shown in Table 4.12. This value was chosen because it is close to that in simulated gastric fluid.

Sample	mg of copper in initial 20 mg sample of SEC	mg of Cu lost from solid	ICP results for Cu filtrate solution / ppm	mg copper extracted into 5 mL solution	%Cu extracted into 5 mL solution	mg copper missing
Cu(OAc)₂ + BL-SECs	1.57	0.37	340.81	1.70	108	-1.34
Cu(OAc)₂ + BR-SECs	1.79	0.57	346.99	1.73	97	-1.16
CuCl₂ + BL-SECs	0.452	0.10	84.97	0.424	94	-0.32
CuCl₂ + BR-SECs	1.48	0.14	277.8	1.39	93.5	-1.24
Cu(NO₃)₂ + BL-SECs	0.422	0.10	83.34	0.416	98.7	-0.32
Cu(NO₃)₂ + BR-SECs	1.21	0.16	212.02	1.060	88.0	-0.90

Table 4.12 Summary of data for Cu-SEC complexes extracted in acid (pH 1.5).

The data in Table 4.12 show that essentially all of the copper is removed from all of the Cu-SEC complexes when extracted into solution at pH 1.5, except copper chloride and copper nitrate with bleached SEC which are very different from all of the others. The concentrations of copper in the filtrate for the brown and bleached copper acetate-SEC complexes are similar 346.99 ppm and 340.81 ppm, respectively. The filtrates of the brown copper nitrate and copper chloride SEC complexes contained higher concentrations of copper than the corresponding filtrates from bleached SEC complexes. For example, the concentration of copper in the filtrate for the brown and bleached copper chloride-SEC complexes is 277.8 ppm and 84.97 ppm respectively. Important observation is that at pH 1.5, ca. 90% of the copper is leached from the Cu-SEC complexes.

3. Basic (pH 12.5) conditions

20 mg of Cu-SEC complex was added to 5 ml of NaOH (0.0316 M, pH 12.5) and stirred for three days. The resulting solution was then filtered and analysed by ICP-OES, before washing with water then ethanol and drying in a desiccator. The amount of copper remaining in the solid SEC was measured by ICP-OES.

Sample	mg of metal before in 20 mg sample	mg lost from solid	ICP results for solution ppm	mg metal extracted into 5 mL solution	%Cu extract ed into 5 mL solution	mg copper missing
Cu(OAc)₂ + BL-SECs	1.57	0.37	8.38	0.042	2.7	0.33
Cu(OAc)₂ + BR-SECs	1.79	0.57	48.01	0.240	13.4	0.33
CuCl₂ + BL-SECs	0.452	0.10	1.06	0.005	1.17	0.09
CuCl₂ + BR-SECs	1.48	0.14	80.4	0.402	27.08	-0.26
Cu(NO₃)₂ + BL-SECs	0.422	0.10	1.37	0.006	1.62	0.09
Cu(NO₃)₂ + BR-SECs	1.21	0.16	36.7	0.183	15.20	-0.02

Table 4.13 Summary of data for Cu-SEC complexes extracted in basic condition (pH 12.5).

As with the acidic solution, there seems to be some discrepancy between the solid and solution data. The ICP data consistently show a higher concentration of copper in brown Cu-SEC complex solutions than the bleached Cu-SEC complex solutions after basic extraction at pH 12.5 (Table 4.13). For example, the concentrations of the brown and bleached copper acetate-SEC complexes are 48.01 ppm and 8.38 ppm respectively. The relatively low copper concentration in these measurements may be due to the fact that copper is insoluble in high pH solutions. The overall trend for the basic extraction is that there is the greatest loss of copper from the acetate samples, and that the loss is greater for the BR rather than the BL samples. This is in contrast to the acidic extraction where the loss is greater for the BL rather than the BR samples.

4.3.2 C, H, N analysis

C, H, N analysis of the Cu-SECs was carried out to complement the copper analysis using ICP-OES. As mentioned in Chapter 3 the sporopollenin in the SECs was represented by an empirical formula based on a C₉₀ unit which varied from species to species.²⁰ The C, H, N elemental analysis of a number of sporopollenin exine capsules are shown in Table 4.14, together with the copper analysis obtained from the ICP-OES data outlined above.

Sporopollenin sample	% Elemental analysis (C, H, N)			%O (assumed residual)	% Cu. (ICP-OES)	Empirical formula (assuming a C ₉₀ basis)
	C	H	N			
Cu(OAc)₂+BL-SEC	49.65	7.04	0.30	35.14	7.87	C ₉₀ H ₁₅₂ O ₄₇ Cu _{2.7}
Cu(OAc)₂+BR-SEC	50.70	6.68	0.57	33.03	9.02	C ₉₀ H ₁₄₁ O ₄₄ Cu _{3.0}
CuCl₂+BL-SEC	53.21	7.35	0.00	37.18	7.57	C ₉₀ H ₁₄₈ O ₄₇ Cu _{0.72}
CuCl₂+BR-SEC	52.70	6.79	0.55	34.05	5.91	C ₉₀ H ₁₃₈ O ₄₃ Cu _{1.9}
Cu(NO₃)₂+BL-SEC	54.43	7.70	0.34	35.42	2.11	C ₉₀ H ₁₅₂ O ₄₄ Cu _{0.66}
Cu(NO₃)₂+BR-SEC	53.80	7.27	0.45	32.92	5.56	C ₉₀ H ₁₄₅ O ₄₁ Cu _{1.8}

Table 4.14 Results of elemental analysis of SECs with copper salts.

The results showed that for SECs there were some differences in the carbon and hydrogen content, and as expected the largest drop in carbon content was observed for the acetate derived samples which have the highest copper loading. In all cases there was negligible nitrogen content, even for the samples prepared from copper nitrate solutions. As outlined in Chapter 3, the empirical formula for sporopollenin is usually given with a C₉₀ base, assuming that the missing mass is oxygen, and these values are also given in the table. In order to give an indication of the number of copper atoms, this methodology has been extended to include the number of copper atoms per C₉₀ formula unit. This varies from about 3 copper atoms per C₉₀ formula unit for the copper(II) acetate solution derived samples, to about 0.7 for the copper(II) chloride and nitrate solution derived samples for the bleached SECs. For the brown SECs, the number of copper atoms per C₉₀ formula unit varies from 3 for the copper(II) acetate solution derived samples, to about 1.9 for the copper(II) chloride and nitrate solution derived samples. However, given the uncertainty

in some of the ICP derived data, this should be taken as a guide rather than a definitive ratio. The amount of nitrogen attached in the Cu-SEC complexes varied between 0.00 to 0.57 %. The amount of nitrogen is similar in the SEC and the Cu-SECs. Therefore, this is most likely to be due to residual nitrogen not removed in the SECs preparation stage, rather than anything to do with adding copper. Moreover, it can be seen that from chapter 3 the bleached SECs contained a higher carbon content than the Cu-BL-SEC complexes. For example, the carbon content of the bleached SECs is 56.36 %, but in copper acetate with BL-SECs it is 49.65 %. There was little difference between the carbon content of the brown SECs and Cu-BR-SEC complexes. For example, the carbon content for brown SECs, copper acetate with brown SECs and copper nitrate with brown SECs was 52.17 %, 50.70 % and 53.80 %, respectively. In contrast, there was not much difference in the hydrogen and nitrogen content between the SECs and Cu-SEC complexes. The lack of additional nitrogen in copper nitrate with brown and bleached SECs (0.35 % and 0.45 % respectively) shows that the nitrate is not attached.

4.4 Scanning electron microscope images (SEM)

The samples prepared from 100 mg of BL-SECs or BR-SECs reacted with 25mL of 0.1 M copper(II) solution for 3 days were examined by scanning electron microscopy to investigate the copper on the structure of the SECs.

The images of BL-SECs reacted with 25 mL of copper acetate solution are shown in Figure 4.3. It can be seen from the first image in the right which is size 10 μm that the spores had tiny granules and scattered on their surface. Whilst some of the SECs remained intact, some had burst slightly or become distorted, resulting in small fragments being visible around the spores. When these images are compared to those of the BL-SECs with no metals attached (Figure 3.4) the original SECs are not damaged.

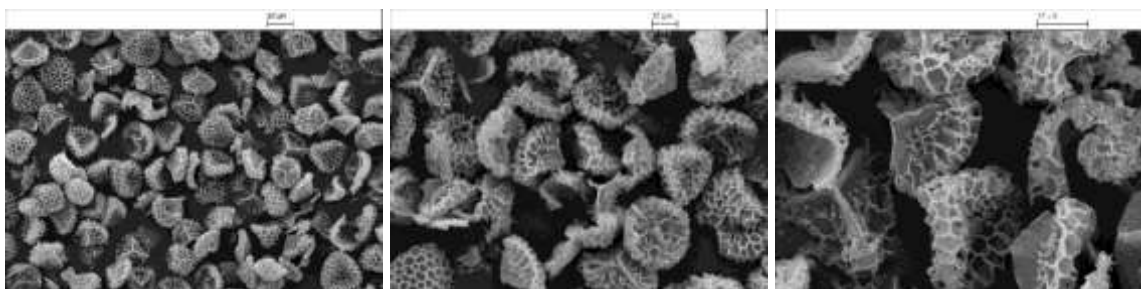


Figure 4.3 SEM images of BL-SECs following reaction with copper(II) acetate solution. (The left-hand scale bar is 20 μm , the central and right-hand ones are 10 μm).

The images of BR-SECs after reaction with copper acetate solutions are shown in Figure 4.4. Fewer of the BR-SECs remained intact than the BL-SECs when reacted with copper acetate solution. Some had burst slightly or had become distorted, and some of the spores had small fragments on their surface. Debris was also visible around the spores. The SEM images show that randomly arranged. When compared to the images of BL-SECs reacted with copper acetate it can be seen that the BR-SECs reacted with copper acetate are more damaged.

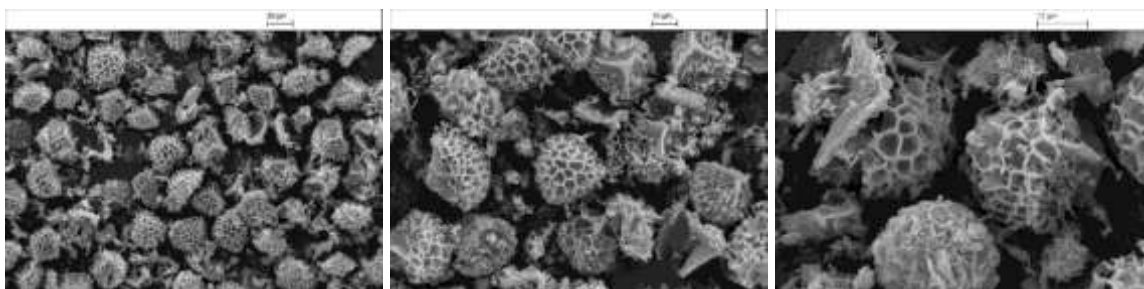


Figure 4.4 SEM images of BR-SECs following reaction with copper(II) acetate solution. (The left-hand scale bar is 20 μm , the central and right-hand ones are 10 μm).

The SEM images in Figure 4.5 clearly demonstrate the almost hemi-spherical with a trilete bottom shape of the SECs. Although most of the SECs remained intact, some are broken, with debris visible in the samples.

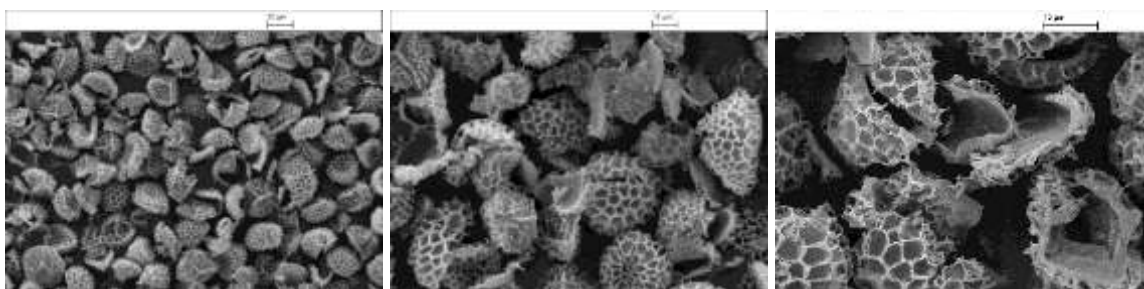


Figure 4.5 SEM images of BL-SECs following reaction with copper(II) chloride solutions. (The left-hand scale bar is 20 μm , the central and right-hand ones are 10 μm).

Figure 4.6 shows the images of BR-SECs after reaction with copper(II) chloride solution. The spores had tiny granules scattered on the surface with small fragments and debris visible around the SECs. There is a slight visible difference between the SEM images of the BR-SECs and the BL-SECs.



Figure 4.6 SEM images of BR-SECs following reaction with copper(II) chloride solution. (The left-hand scale bar is 20 μm , the central and right-hand ones are 10 μm).

The images of BL-SECs reacted with copper(II) nitrate solution are shown in Figure 4.7. The SEM images clearly demonstrate the almost spherical shape of the microcapsules. It can be showed like flat spores.



Figure 4.7 SEM images of BL-SECs following reaction with copper(II) nitrate solution. (The left-hand scale bar is 20 μm , the central and right-hand ones are 10 μm).

The SEM images in Figure 4.8 of BR-SECs reacted with copper(II) solution clearly show that a significant number of the BR-SECs are no longer intact and that debris is present around the BR-SECs. The images also show the images of copper nitrate on the outer surface morphology of the SECs. There is a slight difference between it the BR-SECs and BL-SECs. Most of the both brown and bleached SECs remained intact.

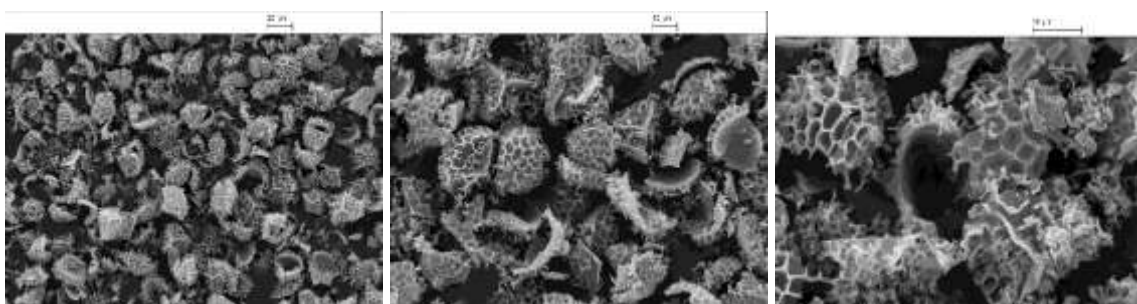


Figure 4.8 SEM images of BR-SECs reacted with copper(II) nitrate solution. (The left-hand scale bar is 20 μm , the central and right-hand ones are 10 μm).

To conclude, there are differences in the SEM images from the SECs images prior to metal loading, and between the BR-SECs and BL-SECs. Although there is little difference between the samples prepared from copper(II) acetate, chloride or nitrate, the extent of the damage to the SEC structure is significantly greater for the BR-SECs than BL-SECs for all three solutions. Therefore, it appears that the copper solutions result in the breakup of the SEC structure, and as this is greater for the BR-SEC than the BL-SEC implies that there are more available functional groups on the BR-SEC for the copper to coordinate to. Another important observation is that the SECs (and their fragments) are not full of a copper material, and this implies that the copper is on the external or internal surface or the channels between them.

4.5 Spectroscopic studies

Various spectroscopic techniques were used to study the Cu-SEC complexes: UV–vis spectroscopy was used to identify the presence of metals and their mode of coordination in the Cu-SEC complexes. Vibrational spectroscopy was used to examine the functional groups present and the structure of SECs. Finally, the structure of the obtained microcapsules was investigated by X- ray absorption and EPR spectroscopies.

4.5.1 Identification of metal coordination environment within sporopollenin using electronic absorption spectroscopy (UV – visible - NIR)

In this study, electronic absorption spectroscopy was used to analyse Cu-SEC complexes. UV–vis spectroscopy was carried out in the preceding sections to quantify the extent of copper removed from the solution. The spectral motifs observed can also be used to identify the coordination environment of the metal within the sporopollenin exine capsules. The metals are attached to the SEC by functional groups such as phenol and carboxylate. When the SEC is mixed with metal complexes, the d-electrons of these complexes may contribute to the production of different colours and depending on the number, shape and wavelength of the bands, it is possible to inquire about the metal complex geometry on the SECs.

The experiment consisted of recording the diffuse reflectance UV–vis spectra of solid metal-SEC complexes at loading ratios of 1 mmol: 100 mg; 2.5 mmol:100 mg and 5 mmol:100 mg. In these experiments, the complexes of copper with bleached SEC were

examined. The complementary samples prepared using brown SECs were not examined using solid-state UV-vis spectroscopy due to the masking of the spectral features of the copper by the SEC itself (for details see Chapter 3).

Figure 4.9 shows the spectra of 0.1 M solutions of the copper(II) acetate, copper(II) nitrate and copper(II) chloride which show the different spectra motifs for these compound in dilute aqueous solution.

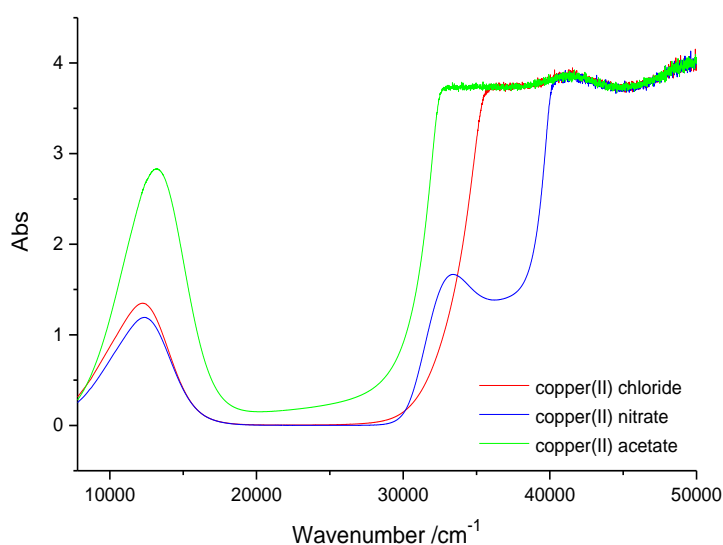


Figure 4.9 Superposition of the UV-vis spectra of 0.1 M solution of copper (II) acetate, copper(II) chloride and copper(II) nitrate.

Figure 4.10, illustrates the different diffuse reflectance UV-vis spectra of different copper-SEC complexes. The complexes were obtained after stirring solutions of different copper (II) salts (CuCl_2 , $\text{Cu}(\text{NO}_3)_2$ and $\text{Cu}(\text{OAc})_2$) with bleached SECs at 2.5 mmol:100 mg loading ratio for three days in 25 mL of water. All the spectra were similar and presented a set of bands with wavenumbers ranging from 5000 to 50000 cm^{-1} .

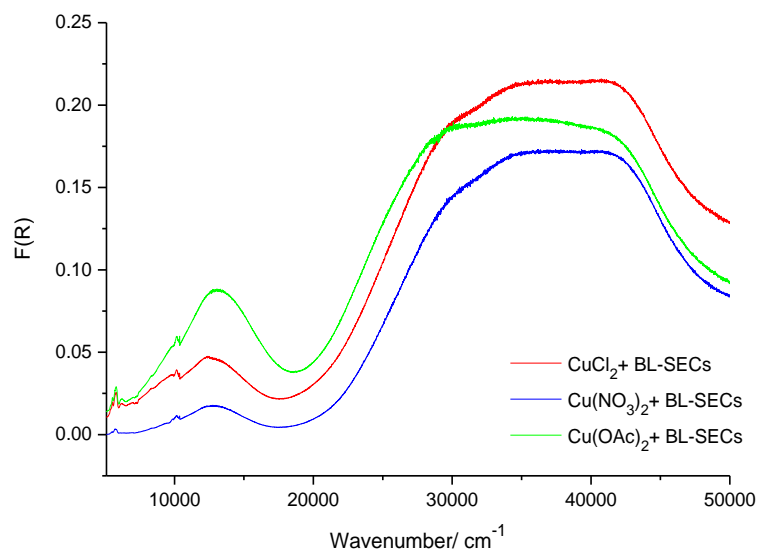


Figure 4.10 Superposition of the solid state diffuse reflectance UV-vis spectra of copper SEC complexes prepared using 2.5 mmol of metal, 100 mg of SEC and stirring for 3 days in 25 mL of water.

By analysing the results presented above, it is possible to divide the UV-vis absorption spectra into two parts: from 5000 to 25000 cm^{-1} , which comprises the bands characteristic of d-d transitions in the Cu(II) (d^9) metal ions, and from 25000 to 50000 cm^{-1} , which is the region where the absorptions $n-\pi^*$ and $\pi-\pi^*$ arising from the SECs functional groups appear. Interestingly, the $\text{Cu}(\text{OAc})_2$ -SECs complex, presents a higher intensity peak, when compared to the others. This could be due to the a higher proportion of copper, but it should be noted from Figure 4.9 that the copper(II) acetate solutions have a higher molar absorptivity.

Many copper complex salts produce quite similar absorption patterns, but different maximum absorbance wavelength. All synthesised complexes presented a distinctive d-d band centred at 13000 cm^{-1} (Figure 4.11), which absorbs in the red part of the visible region, giving them their characteristic blue-green colour. This is typical of octahedral copper (II) complexes with a Jahn-Teller tetragonal distortion, which are reported to have absorption in the 14200-12800 cm^{-1} range.¹⁸¹ The spectra of the copper SEC complexes derived from copper chloride and copper nitrate both show a d-d transition at 12780 cm^{-1} . Also the weak bands at ca. 5500 and 11000 cm^{-1} , that are most likely due to overtone and combination bands in the SECs. The spectrum of the copper SEC complex prepared with copper acetate solution however shows the d-d transition is at 13100 cm^{-1} . These values are similar to those observed for the solution species, indicating the structure of the copper

in the solution and SECs are likely to be very similar and the presence of a different coordination mode for the copper acetate derived complex in comparison with the copper chloride and nitrate derived samples, it also appears as though there is a difference between the acetate and the other two complexes at higher energy.

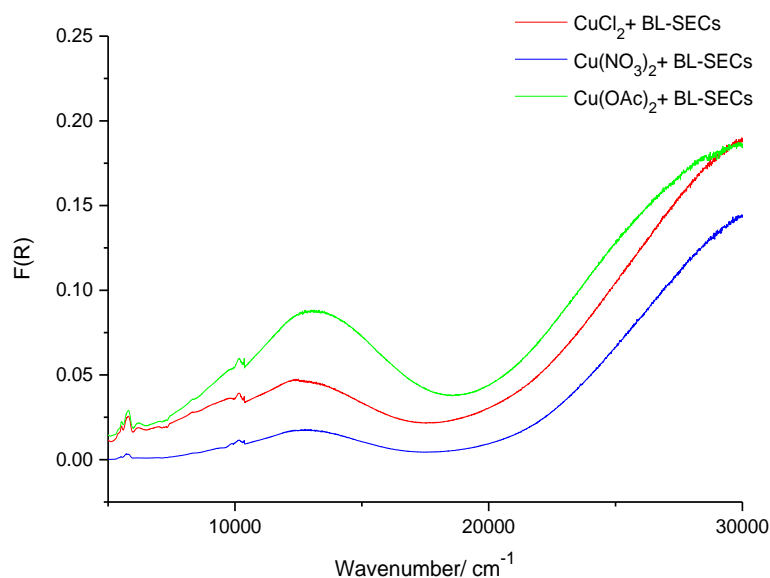


Figure 4.11 Expanded solid state diffuse reflectance UV-vis spectra for SECs loaded with different copper complexes from 5000 to 30000 cm^{-1} .

The metal-SEC ratio has different effects on the loading of the final copper-SEC complex. In general, higher ratios lead to higher loadings (Figure 4.12A-B and Figure 4.14A), the effect is dependent on the copper salt used and the spectral features are the same in all three cases. The variation in intensity with the amount of metal in the reaction for copper chloride and copper nitrate is much more likely to be due to the problems of acquiring solid state spectra where it is very challenging to control the effective path length, especially as the ICP-OES data in Table 4.2 indicates that the copper loadings are similar.

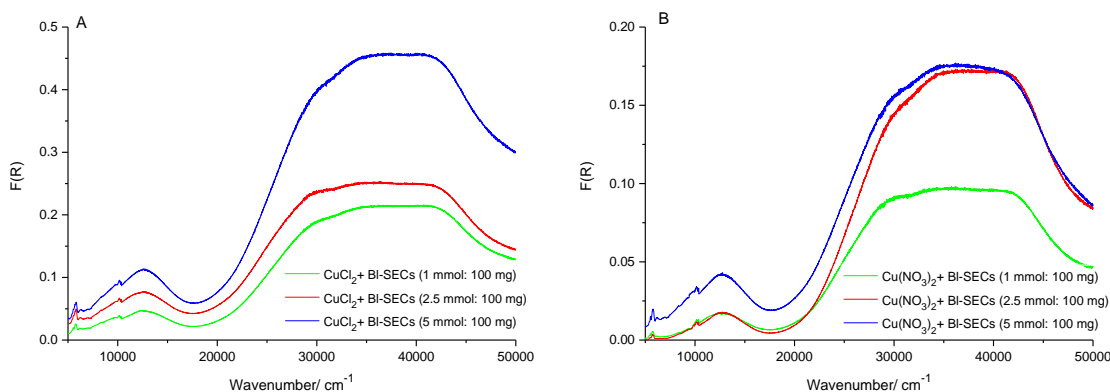


Figure 4.12 UV-vis spectra of different loading ratios of (A) copper chloride and (B) copper nitrate with BL-SECs stirring for 3 days.

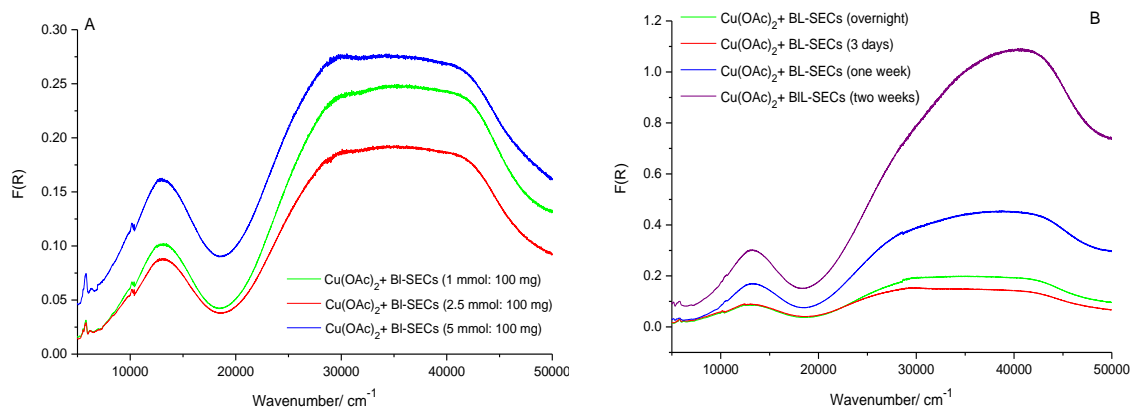


Figure 4.13 UV-vis spectra of (A) different loading ratios of copper acetate with BL-SECs and (B) copper acetate (2.5 mmol:100 mg) with BL-SECs in different stirring.

Figure 4.13 presents the UV-vis spectra of BL-SECs reacted with copper(II) acetate solutions (Figure 4.13A) contains spectra with different Cu:SEC ratios. And (Figure 4.13B) contains spectra at a loading ratio of 2.5 mmol:100 mg, mixed for different durations. After overnight and three days stirring (Figure 4.13B) the spectral features of the obtained complex were very similar to those of unreacted sporopollenin in the high energy region (see Figure 3.10, Chapter 3). The first changes in the spectra above 20000 cm^{-1} were observed after one week of exposure to the copper ions. After two weeks reaction time, drastic changes were observed in the spectral region associated with sporopollenin. This suggests that after stirring for a week, the structure of the sporopollenin has been modified by the copper acetate. The spectra were dependent on the concentration level and type of Cu salt used. Therefore, comparing the different loadings and stirrings,

one can see that the best results were obtained when 100 mg of bleached SECs and 2.5 mmol of the metal was used.

The reason for this finding might be related to structure and geometry. The complexes of the transition metals show similar colours. In addition, the highest copper loading was obtained when using the acetate salt in comparison to those obtained when using chloride or nitrate salts because the intensity of features and the position of the peak intensity for copper acetate is greater than copper nitrate or chloride. To conclude that the UV-vis results show that the copper environment in the copper chloride and nitrate samples are very similar, but that in the copper acetate sample is different. Using the solution spectra for comparison, the chloride and nitrate spectra are very similar to that of $[\text{Cu}(\text{H}_2\text{O})_6]^{2+}$, whereas the copper acetate is very similar to that for the 0.1 M copper (II)acetate solution where it is believed there are one or two acetate ligands still attached to the copper in a mononuclear complex.

4.5.2 Vibrational spectroscopic identification of functional groups in sporopollenin

4.5.2.1 Raman spectroscopy

Raman spectroscopy was used to study the structure of the Cu-SEC complexes with both BL and BR-SECs. The Raman spectra of sporopollenin have previously been described (Chapter 3). The spectrum is dominated by different vibrational modes of sporopollenin.

Raman spectra were obtained for the different Cu-SEC complexes. In comparison to the spectra of the bleached SECs in Chapter 3, the spectra of the Cu-SEC complexes were badly affected by fluorescence increasing towards 3000 cm^{-1} . An example (Cu(OAc)₂ - BL-SEC complex) is shown in Figure 4.14. This NIR or IR emission is due to heating of the sample when the Nd-YAG excitation source at 9398 cm^{-1} partially coincides with the absorption band at *ca.* 13000 cm^{-1} in the UV-vis spectra, and swamping any genuine Raman bands apart from the aliphatic C-H stretching modes at 2920 cm^{-1} . This was not an issue with the bleached SECs without copper, due to their pale colour. Raman spectroscopy cannot therefore be used to study the structure of Cu-SEC complexes.

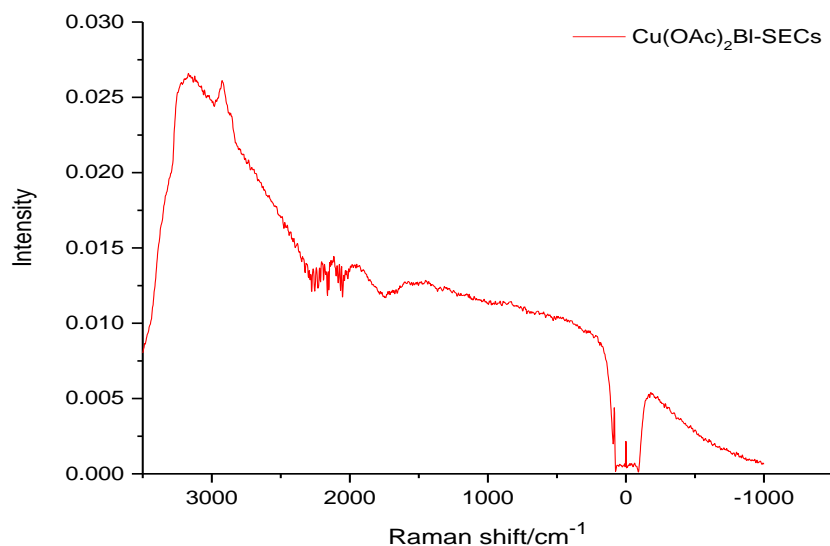


Figure 4.14 Raman spectrum from BL-SECs reacted with copper(II) acetate solution (2.5 mmol:100 mg).

4.5.2.2 Infrared spectroscopy (IR)

Because it was not possible to use Raman spectroscopy, IR spectroscopy was employed to detect the functional groups and gain insight into the structure of sporopollenin. IR is considered the most suitable technique for structural identification, because molecular vibrations depend on the interatomic distances, bond angles, and bond strengths, rather than on the bulk properties of the compound.

It was found that IR spectroscopy can be applied to identify the molecular constituents in the samples from their vibrational spectra in the mid-IR region (4000–400 cm⁻¹). Furthermore, it can be used to explore the structural framework of the Cu-SEC complexes without destroying their internal structure.

It can be seen from the Figure 4.15 when comparing the spectra for BL-SECs with no metals and the spectra for BL-SECs reacted with copper(II) acetate solution that there is not that much different between them. IR bands are in the SECs spectrum between 4000–400 cm⁻¹, and the largest differences are between 1700 and 500 cm⁻¹.

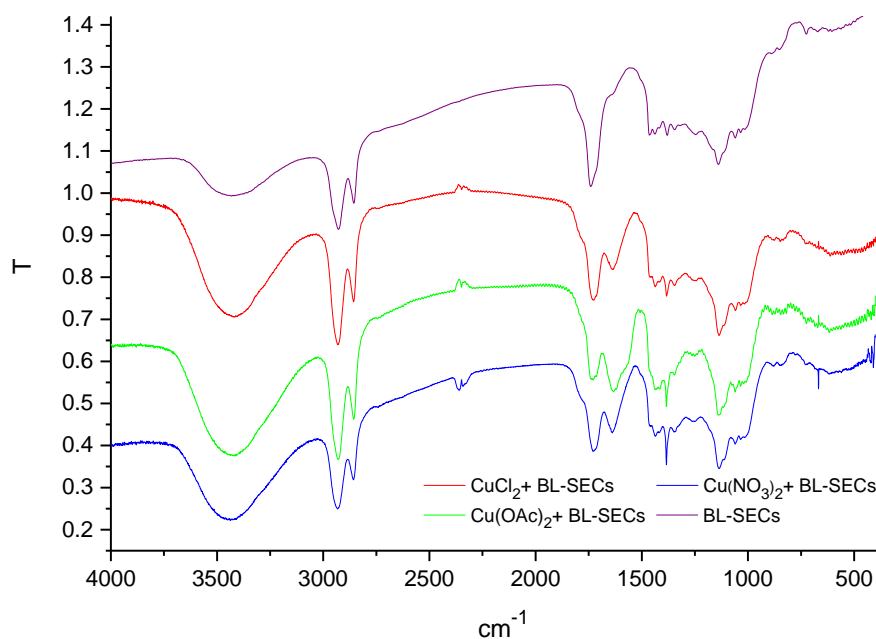


Figure 4.15 IR spectroscopy results from BL-SECs and copper complexes with BL-SECs (2.5 mmol: 100 mg).

IR spectra of the Cu-SEC complexes obtained from loading experiments using copper acetate, copper nitrate and copper chloride solutions and bleached sporopollenin SECs are illustrated in Figure 4.15. Characteristic bands can be observed in each of the three samples. In the $4000 - 1900 \text{ cm}^{-1}$ and $1300 - 400 \text{ cm}^{-1}$ regions the spectra of BL-SEC and the Cu-BL-SEC complexes are essentially identical. However, between 1900 and 1300 cm^{-1} there are some subtle and significant differences between BL-SEC and the Cu-BL-SEC complexes as well as within the Cu-BL-SEC complexes.

The IR spectra of bleached SECs with copper salts show typical broad bands at $3000 - 3750 \text{ cm}^{-1}$ due to the presence of hydroxyl groups (OH). The peaks at 2925 and 2855 cm^{-1} belong to C-H (aliphatic) stretching. There is only a very subtle change in this region on the addition of metal with a reduction in intensity of a shoulder at value. There is a much more marked change in the C=O stretching region, with a reduction in intensity of the 1744 cm^{-1} peak in the BL-SEC which was assigned to an ester mode in Chapter 3. In the metal loaded BL-SECs peaks at 1642 and 1385 cm^{-1} grew in intensity for all three copper salts. If these two values are the asymmetric and symmetric stretching modes of a copper carboxylate unit, then the difference between them of 257 cm^{-1} would indicate monodentate coordination according to the analysis of Deacon and Phillips.¹⁸² Alternatively, the 1385 cm^{-1} band could be due to phenolate C-O stretching mode. In the case of copper

acetate there was an additional peak at 1580 cm^{-1} , which may be due to presence of the acetate group attached to the copper on SECs surface. It should be noted that in copper(II) acetate monohydrate where the acetate bridges the two copper atoms the asymmetric C-O stretching mode is $1610 - 1600\text{ cm}^{-1}$.^{183, 184} Therefore, as in the case of the UV-vis-NIR data, the samples prepared from copper(II) chloride and nitrate solutions appear to be very similar, but with significant differences to the sample prepared from copper(II) acetate solutions. The fingerprint region below 1300 cm^{-1} is similar in all four spectra.

In conclusion the spectra of the three Cu- bleached SEC complexes were similar with features 1642 and 1385 cm^{-1} that are consistent with C-O stretching modes in carboxylate units that are probably mono-dentate. The spectra of the samples formed after reaction with copper chloride and copper nitrate solutions were essentially identical to each other, but there were significant differences in the spectrum of the sample derived from copper(II) acetate where a feature at 1580 cm^{-1} is most likely due to the presence of acetate group attached to the copper on SECs surface.

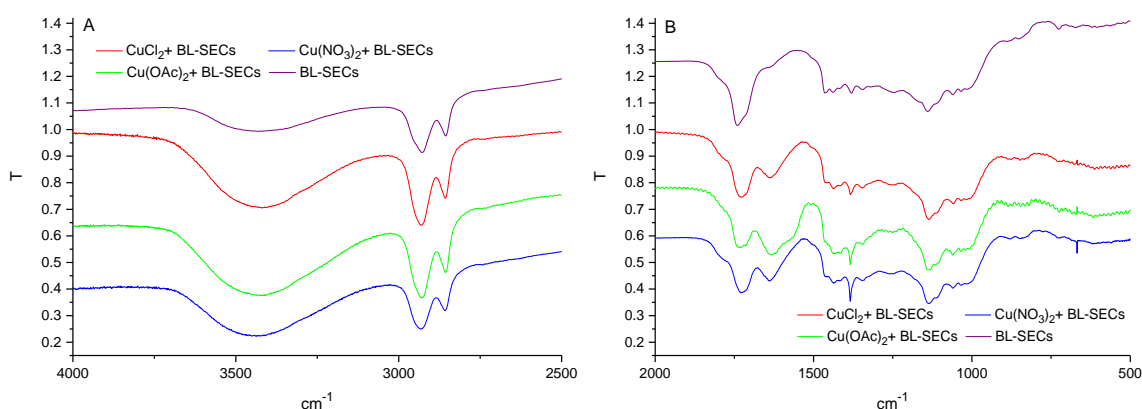


Figure 4. 16 IR spectroscopy results from BL-SECs and copper complexes with BL-SECs (2.5 mmol:100 mg) (A) The expanded from $4000\text{-}2500\text{ cm}^{-1}$, (B) The expanded from $2000\text{-}500\text{ cm}^{-1}$.

The IR absorption frequencies of different functional groups are summarised in Table 4.15.

Absorption frequency (cm^{-1})	Functional groups
~ 3450	-OH
~2925	(C H) stretching
~2855	(C H) stretching
~1744	C=O stretching (esters)
~1642	C=O stretching
~1446	C-H aliphatic carbons (CH_2)
~1150	C-O stretching ether group

Table 4.15 IR absorptions obtained from some SEC with metals.

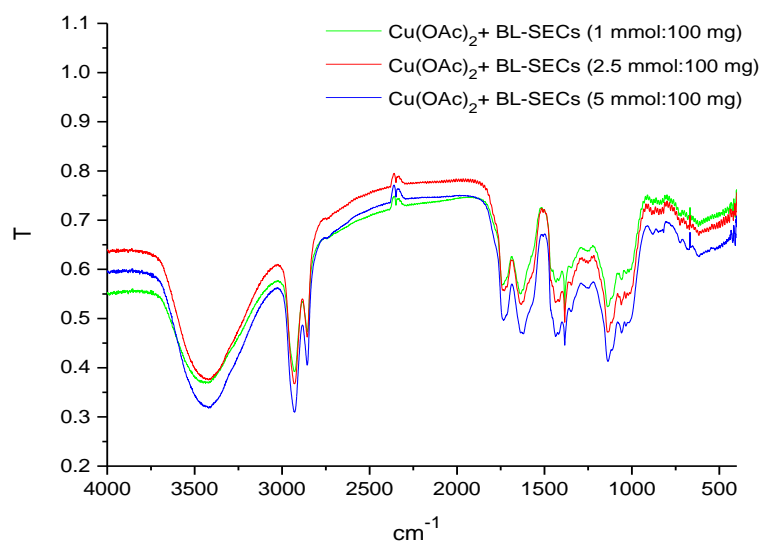


Figure 4. 17 IR spectroscopy results from copper acetate with BL-SECs different loading.

The loading ratio of copper acetate to bleached SECs (1 mmol:100 mg; 2.5 mmol:100 mg; 5 mmol:100mg) makes little difference to the IR spectra see above Figure 4.17.

The IR spectra for the Cu- brown SEC complexes were similar to the Cu-bleached SEC complexes see below Figure 4.18. Again, the spectrum of the copper acetate SECs complex shows slight differences from the copper nitrate and copper chloride spectra.

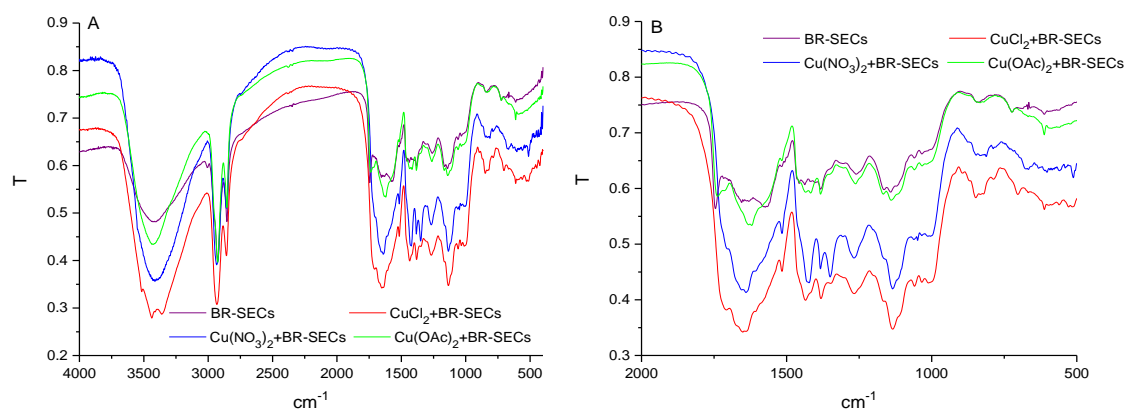


Figure 4.18 (A) IR spectroscopy results from copper complexes with BR-SECs (2.5 mmol: 100 mg), and (B) expanded from 2000-500 cm^{-1} IR spectroscopy results from copper complexes with BR-SECs.

In summary, the IR spectra of the copper- SECs complexes show correspondences in the occurrence of aromatics, aliphatic, and ether, carbonyl/carboxylic groups but also significant differences.¹⁷³ The most important spectral features are those at 1642 cm^{-1} and 1385 cm^{-1} in all of the complexes, and the shoulder at 1580 cm^{-1} in the acetate complexes. It should be noted that the difference in the diffuse reflectance UV-Vis data correlated very well with the differences in the IR spectra between the acetate solution derived complexes and those from copper chloride or nitrate solutions. Acetate derived complex correlates with the IR data as well, and both indicate that it is attached to copper.

4.5.3 X- Ray absorption spectroscopy

The aim of these X-ray absorption experiments is to identify the oxidation state of the copper and the mode of coordination of copper salts to the surfaces of the SECs so that the type and number of the surface binding groups can be identified. This information is vitally important in assessing these materials for drug delivery, metal remediation and other applications.

To provide enough sample for these experiments, the protocol was modified to use 7.5 mmol of the copper salt and 300 mg of BL-SECs and BR-SECs. In line with previous experiments,¹⁰¹ the samples were stirred three days, one week and two weeks and dried in a desiccator.

Bulk Cu K-edge XANES and EXAFS experiments on $\text{CuCl}_2 \cdot 2\text{H}_2\text{O}$ and $\text{Cu}(\text{NO}_3)_2 \cdot 3\text{H}_2\text{O}$ and the copper SEC-complexes were collected in transmission mode at the ESRF using the

BM26 XAFS beamline. Cu K-edge data for $\text{Cu}(\text{OAc})_2 \cdot \text{H}_2\text{O}$ and basic copper carbonate (malachite, $\text{Cu}_2(\text{CO}_3)(\text{OH})_2$) were collected in transmission mode at the Diamond Light Source using the B18 beamline. All spectra were acquired at *ca.* 80 K.

The XAS spectra were calibrated using the first maximum in the first derivative spectrum of a copper foil (8979.0 eV). The edge positions in the XANES spectra were defined as the energy corresponding to a normalised absorbance of 0.5. Figure 4.19 below shows the Cu K-edge XANES data for $\text{Cu}(\text{OAc})_2 \cdot \text{H}_2\text{O}$, $\text{Cu}(\text{NO}_3)_2 \cdot 3\text{H}_2\text{O}$, $\text{CuCl}_2 \cdot 2\text{H}_2\text{O}$ and $\text{Cu}_2(\text{CO}_3)(\text{OH})_2$. Although the weak 1s – 3d pre-edge features in $\text{Cu}(\text{OAc})_2 \cdot \text{H}_2\text{O}$, $\text{Cu}(\text{NO}_3)_2 \cdot 3\text{H}_2\text{O}$, $\text{CuCl}_2 \cdot 2\text{H}_2\text{O}$ and $\text{Cu}_2(\text{CO}_3)(\text{OH})_2$ are very similar, the edge structure is different, especially for $\text{Cu}(\text{OAc})_2 \cdot \text{H}_2\text{O}$ and $\text{CuCl}_2 \cdot 2\text{H}_2\text{O}$, and this is a reflection of the different copper environments in each of the compounds. For example, the structure of $\text{Cu}(\text{OAc})_2 \cdot \text{H}_2\text{O}$ involves a square plane of four Cu-O bonds at *ca.* 1.97 Å, one Cu-OH₂ at 2.16 Å and a Cu...Cu interaction at 2.62 Å.¹⁸⁵ In $\text{CuCl}_2 \cdot 2\text{H}_2\text{O}$, the structure has two oxygen atoms and two chlorine atoms *trans* to each other at relatively short distances in the equatorial plane, with two longer Cu-Cl interactions in the axial positions.^{186, 187} The structure of $\text{Cu}(\text{NO}_3)_2 \cdot 3\text{H}_2\text{O}$ is the same as that of $\text{Cu}(\text{NO}_3)_2 \cdot 2.5\text{H}_2\text{O}$, which involves an equatorial plane of four Cu-O at an average distance of 1.97 Å, with one Cu-O at 2.39 Å above the plane, and two Cu-O below the plane at 2.65 and 2.67 Å.¹⁸⁸ The copper environment in basic copper carbonate is similar to that in $\text{Cu}(\text{NO}_3)_2 \cdot 3\text{H}_2\text{O}$ with four Cu-O at *ca.* 1.98 Å, with two Cu-O at 2.36, and 2.55 Å.¹⁸⁹⁻¹⁹¹ Therefore, the presence of a step in the edge in $\text{Cu}(\text{OAc})_2 \cdot \text{H}_2\text{O}$ and $\text{CuCl}_2 \cdot 2\text{H}_2\text{O}$ is indicative of a copper environment containing more than just Cu-O in the first coordination shell.

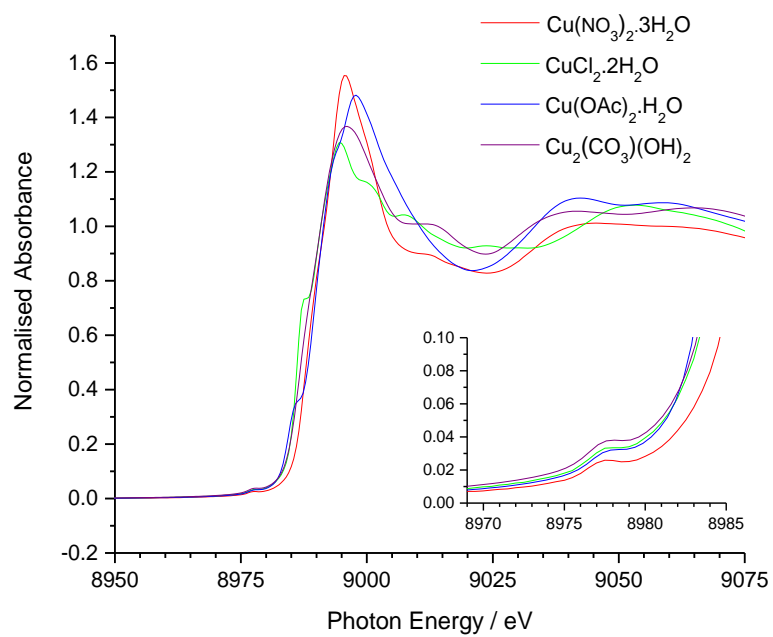


Figure 4.19 Cu K-edge XANES data for Cu(OAc)₂·H₂O, Cu(NO₃)₂·3H₂O, CuCl₂·2H₂O and Cu₂(CO₃)(OH)₂.

Figures 4.20 below show the Cu K-edge XANES data for BL-SECs and BR-SECS after reaction with copper(II) acetate, copper(II) nitrate and copper(II) chloride solutions.

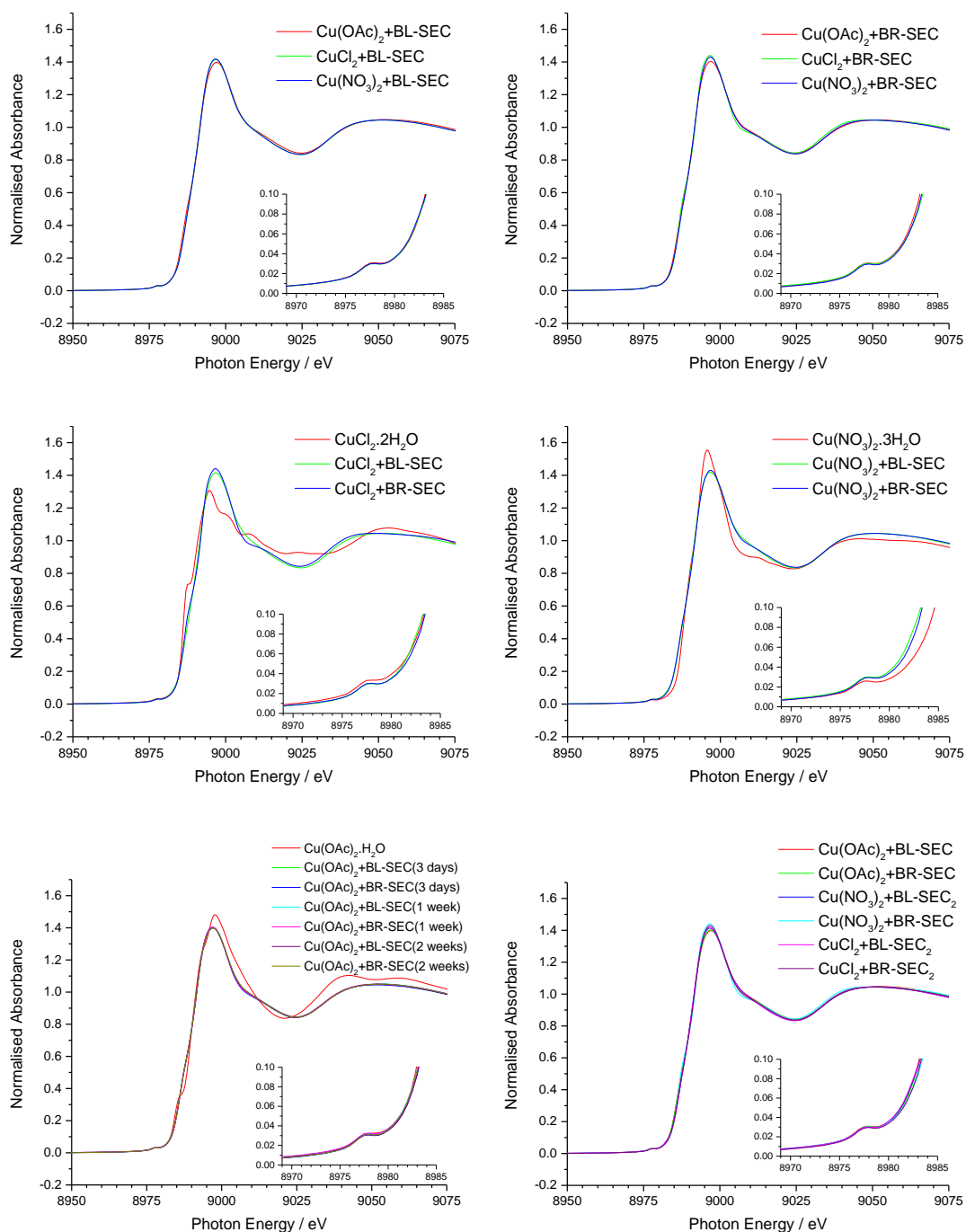


Figure 4.20 Cu K-edge XANES data for copper(II) acetate, copper(II) nitrate and copper(II) chloride solutions with BL and BR-SECs.

Cu K-edge XANES data provide information about the oxidation state and coordination environment of the copper salts. The similarity of position of the pre-edge features and the edge in the Cu-SEC complexes compared to the model compounds confirms the presence

of Cu(II). As all the peaks are nearly the same in both bleached and brown SEC copper complexes, this indicates that the structure is very similar in all cases, and the absence of a step in the edge implies that the local copper environment is more similar to that in $\text{Cu}(\text{NO}_3)_2 \cdot 3\text{H}_2\text{O}$ and $\text{Cu}_2(\text{CO}_3)(\text{OH})_2$ in a classic Jahn-Teller environment of a distorted Cu-O_6 octahedron, rather than in $\text{Cu}(\text{OAc})_2 \cdot \text{H}_2\text{O}$ or $\text{CuCl}_2 \cdot 2\text{H}_2\text{O}$, where there is the presence of Cu or Cl, respectively in the first coordination sphere.

The Cu K-edge EXAFS analyses of $\text{Cu}(\text{OAc})_2 \cdot \text{H}_2\text{O}$, $\text{Cu}(\text{NO}_3)_2 \cdot 3\text{H}_2\text{O}$, $\text{CuCl}_2 \cdot 2\text{H}_2\text{O}$ and $\text{Cu}_2(\text{CO}_3)(\text{OH})_2$ are shown in Figure 4.21 to Figure 4.24. The structure of $\text{Cu}(\text{OAc})_2 \cdot \text{H}_2\text{O}$ is a binuclear dimer ($[\text{Cu}(\text{OAc})_2 \cdot \text{H}_2\text{O}]_2$) with bridging acetate ligands, a relatively short Cu-Cu distance, with the final coordination position taken up by a water molecule. The EXAFS refinement of the first coordination used was modelled with four Cu-OAc distances of $1.96(2) \text{ \AA}$ and one Cu-OH₂ at $2.16(2) \text{ \AA}$. The Debye-Waller factors ($2\sigma^2$) for these two shells were refined together and gave a value of 0.009 \AA^2 . The Cu-Cu distance refined to a value of $2.60(3) \text{ \AA}$, with a Debye-Waller factors of 0.009 \AA^2 . In addition to this first coordination shell, it was also possible to fit the data to four Cu-C interactions at $2.87(3) \text{ \AA}$ Cu-C₄ and four more distant Cu-O at $3.13(3)$. These had Debye-Waller factors of 0.019 and 0.015 \AA^2 , respectively. The refined Cu K-edge EXAFS parameters are in very good agreement with those obtained by single crystal X-ray diffraction for copper acetate monohydrate which adopts a binuclear geometry $[\text{Cu}(\text{OAc})_2 \cdot \text{H}_2\text{O}]_2$. For example the average Cu-O distance for the equatorial plane of oxygens from the acetate ligands that bridge each copper is $1.96(2) \text{ \AA}$, the Cu-OH₂ distance was $2.15(2) \text{ \AA}$, and the Cu-Cu distance *trans* to the water was $2.61(3) \text{ \AA}$, with the Cu...C of the bridging acetates at $2.78(3) \text{ \AA}$ and a more distant Cu...O at $3.12(3) \text{ \AA}$.¹⁸⁵

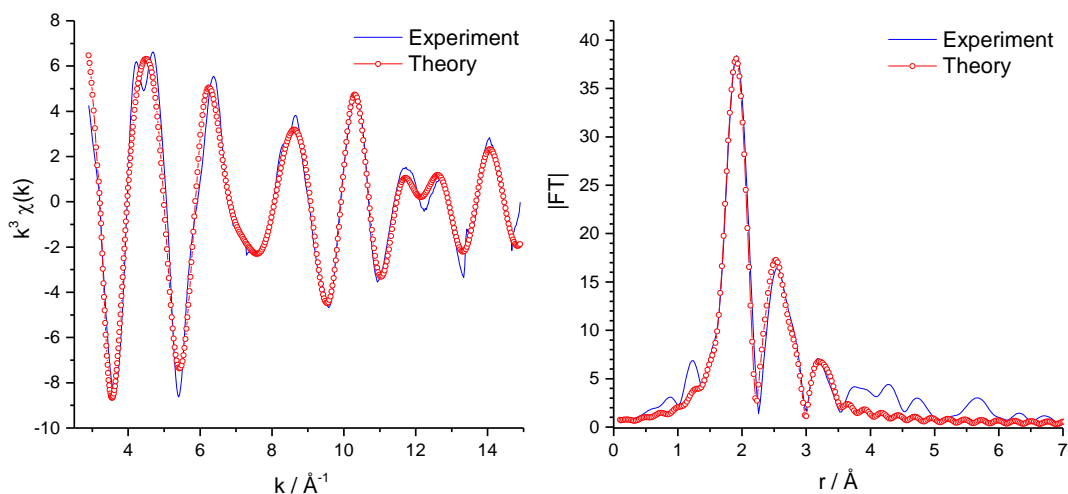


Figure 4.21 Cu K-edge EXAFS analysis of $\text{Cu}(\text{OAc})_2 \cdot \text{H}_2\text{O}$.

The structure of $\text{Cu}(\text{NO}_3)_2 \cdot 3\text{H}_2\text{O}$ consists of a Jahn-Teller distorted octahedron, with four equatorial oxygen atoms, two from nitrate and two from water molecules. In the axial positions there is one water on one side, and on the other side two longer oxygen atoms from the nitrate. In $\text{Cu}(\text{NO}_3)_2 \cdot 3\text{H}_2\text{O}$ the Cu K-edge EXAFS and FT data (Figure 4.22) was only fitted to the first shell which contained four Cu-O distances of $1.95(2) \text{ \AA}$ with Debye-Waller factors of 0.009 \AA^2 (see Table 4.16 for refinement details). This value compares very well with the single crystal X-ray data average value of Cu-O of 1.97 \AA .¹⁸⁸ Although the crystal structure also has axial Cu-O distances at 2.39, 2.653 and 2.675 \AA , these could not be satisfactorily fitted in the EXAFS data. The problem of characterising quantitatively the axial Cu-O bonds in Jahn-Teller distorted Cu(II) complexes by EXAFS has been noted previously.¹⁹²

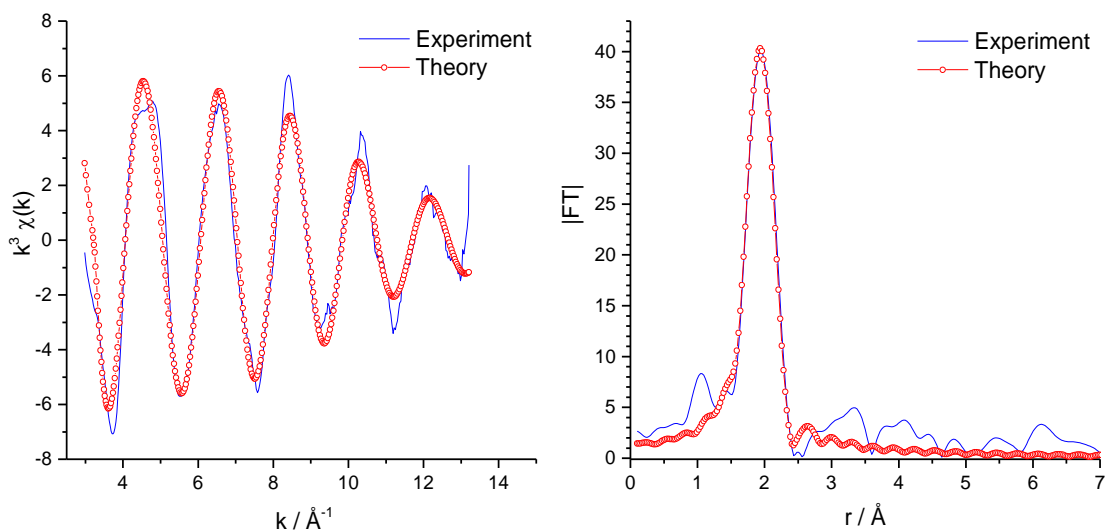


Figure 4.22 Cu K-edge EXAFS analyses of $\text{Cu}(\text{NO}_3)_2 \cdot 3\text{H}_2\text{O}$.

The structure of copper chloride dihydrate, $\text{CuCl}_2 \cdot 2\text{H}_2\text{O}$, consists of a square plane of *trans*- CuO_2Cl_2 with more distant axial Cu-Cl distances. For $\text{CuCl}_2 \cdot 2\text{H}_2\text{O}$ the Cu K-edge EXAFS data (Figure 4.23) the first coordination environment was fitted with six shells, which included two Cu-O bonds of 1.94(2) Å, with Debye-Waller factor of 0.009 Å², two Cu-Cl distances at 2.27(2) and two Cu-Cl at 2.84(3) Å, with Debye-Waller factors of 0.009 and 0.26 Å², respectively. The presence of Cu-Cl bonds is clearly evident in the FT. It was also possible to fit the data to include a two Cu-Cu distances of 3.73(4) Å, with Debye-Waller factor of 0.018 Å², eight Cu-O distances at 4.13(4) Å, with Debye-Waller factor of 0.065 Å², together with four Cu-Cl distances of 4.65(5) Å, with Debye-Waller factor of 0.015 Å². In the single crystal X-ray structure the average Cu-O₂ distance is 1.94(2) Å, the Cu-Cl₂ distance is 2.27(2) Å, and the longer Cu-Cl₂ distance is 2.92(3) Å, with the Cu-O₈ at 4.13(4) Å and a Cu-Cl₂ at 4.70(4) Å.¹⁸⁷ Therefore, the EXAFS analysis is in very good agreement with the X-ray diffraction data. $\text{CuCl}_2 \cdot 2\text{H}_2\text{O}$ has also been studied by Cu K-edge EXAFS in the solid and solution previously.

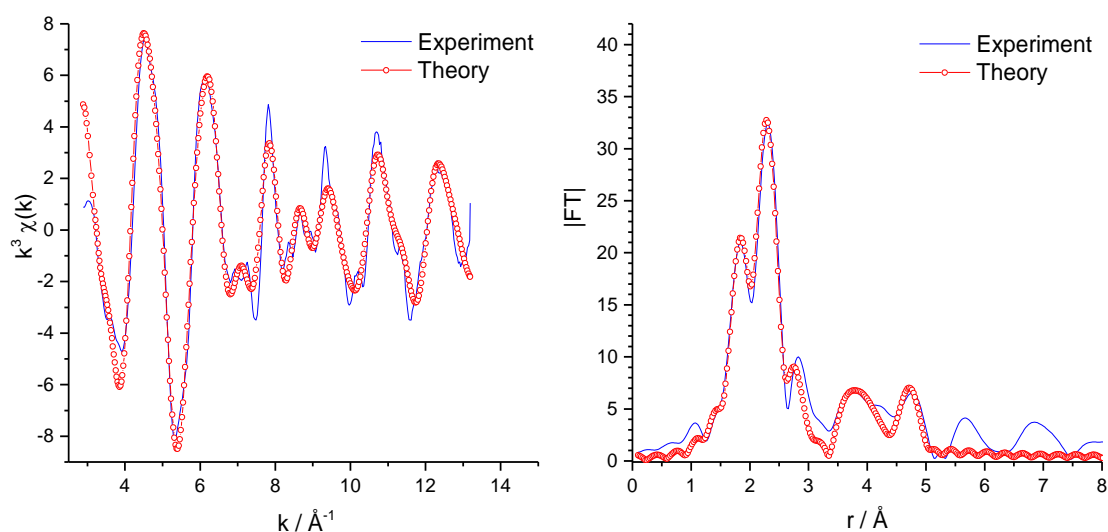


Figure 4.23 Cu K-edge EXAFS analyses of $\text{CuCl}_2 \cdot 2\text{H}_2\text{O}$.

The structure of basic copper carbonate, $\text{Cu}_2(\text{CO}_3)(\text{OH})_2$ (malachite), consists of edge sharing $\text{Cu}(\text{O},\text{OH})_6$ that form chains with a considerable number of Cu...Cu interactions. The Cu K-edge EXAFS data (Figure 4.24) for $\text{Cu}_2(\text{CO}_3)(\text{OH})_2$ could be fitted with six shells. These include which include four Cu-O distances of 1.94(2) and two Cu-O distance of 2.35(2) Å, with Debye-Waller factors of 0.019, 0.032 Å², respectively. The value of 0.032 Å² is quite large, especially compared to 0.019 Å², indicating that it is not well defined, as expected from the previous comments about the difficulty of locating the axial

oxygens with certainty. However, this confirms that the copper environment contains more than just one Cu-O distance in the first coordination shell. The peak in the FT at ca 3.5 Å was fitted to a number of Cu...Cu shells. These were fitted to one Cu...Cu at 3.04(3), two Cu...Cu at 3.18(3), two Cu...Cu at 3.31(3) and one at Cu...Cu at 3.75(4). This compares to the single crystal X-ray data for basic copper carbonate, $\text{Cu}_2(\text{CO}_3)(\text{OH})_2$, where the average Cu-O distance for the equatorial plane of oxygens that bridge each copper was 1.97(2) Å, the Cu-O₂ distance was 2.57(3) Å, and the Cu-Cu distance *trans* to the water was 3.06(3) Å, with a Cu-Cu₂ distance at 3.43(3) Å and a distant Cu-Cu₂ at 3.67(4) Å.¹⁹⁰

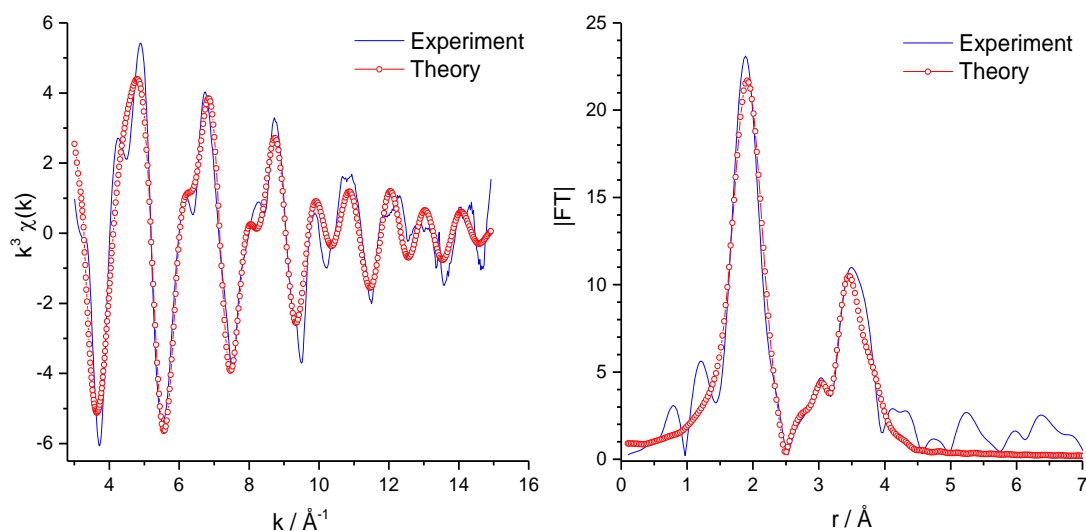


Figure 4.24 Cu K-edge EXAFS analyses of $\text{Cu}_2(\text{CO}_3)(\text{OH})_2$.

Sample	X-Ray data						
			r/Å	2σ ² /Å ²	E _f /V	FI	R
Cu(OAc)₂.H₂O	1.96 ¹⁸⁵	Cu-O ₄	1.963(3)	0.009(4)	-10.21(3)	0.18	21.6
	2.16 ¹⁸⁵	Cu-O ₁	2.163(12)	0.009(4)			
	2.62 ¹⁸⁵	Cu-Cu ₁	2.608(4)	0.009(7)			
	2.86 ¹⁸⁵	Cu-C ₄	2.871(16)	0.019(4)			
	3.12 ¹⁸⁵	Cu-O ₄	3.130(11)	0.015(2)			
Cu₂(CO₃)(OH)₂	1.97 ¹⁹⁰	Cu-O ₄	1.943(6)	0.019(1)	-8.46(7)	0.47	36.1
	2.57 ¹⁹⁰	Cu-O ₂	2.356(17)	0.032(6)			
	3.06 ¹⁹⁰	Cu-Cu ₁	3.037(21)	0.012(5)			
	3.24 ¹⁹⁰	Cu-Cu ₂	3.182(22)	0.016(9)			
	3.38 ¹⁹⁰	Cu-Cu ₂	3.314(14)	0.012(4)			
CuCl₂.2H₂O	3.67 ¹⁹⁰	Cu-Cu ₁	3.745(21)	0.017(4)			
	1.94 ¹⁸⁷	Cu-O ₂	1.940(6)	0.009(1)	-10.73(5)	0.34	25.9
	2.28 ¹⁸⁷	Cu-Cl ₂	2.279(4)	0.009(6)			
	2.93 ¹⁸⁷	Cu-Cl ₂	2.847(13)	0.026(3)			
	3.75 ¹⁸⁷	Cu-Cu ₂	3.730(11)	0.018(2)			
Cu(NO₃)₂.3H₂O	4.24 ¹⁸⁷	Cu-O ₈	4.131(5)	0.065(2)			
	4.70 ¹⁸⁷	Cu-Cl ₄	4.659(14)	0.015(3)			
Cu(NO₃)₂.3H₂O	1.97 ¹⁸⁸	Cu-O ₄	1.954(4)	0.009(7)	-8.25(6)	0.46	28.6

Table 4.16 Cu K-edge EXAFS data of Cu(OAc)₂.H₂O, Cu(NO₃)₂.3H₂O, CuCl₂.2H₂O and Cu₂(CO₃)(OH)₂.

From all Cu K-edge EXAFS data of the copper salts, it can be seen that copper nitrate is different to the other all copper salts (copper acetate, copper carbonate and copper chloride) as it only has one shell in the FT. For most of the salts it was difficult to characterise quantitatively the axial Cu-O bonds. In addition, the Cu K-edge EXAFS data from the copper model compounds shows that if there is a Cu-Cl interaction present in the SEC data this will be readily identifiable in the Cu K-edge EXAFS and FT. Likewise the copper acetate and basic copper carbonate data show that if there are Cu...Cu interactions present in the SECs, these will also be readily identified in both the EXAFS and the FTs.

Figures 4.25, 4.26 and 4.27 show the Cu K-edge EXAFS and FTs for BL-SECS and BR-SECS reacted with copper(II) acetate, copper(II) nitrate and copper(II) chloride solutions.

In each case the data are dominated by an intense feature at *ca.* 2 Å in the FT, with peaks at longer distances of varying intensity.

Figure 4.25 shows Cu K-edge EXAFS and FT data recorded on BM26 (ESRF) of the bleached and brown SECs were reacted with copper(II) acetate solution. For both the BL-SECs and the BR-SECs the EXAFS data are dominated by a single shell, which corresponds to the peak at *ca.* 2 Å in the FT. This first shell is very similar in both with Cu-O distances of 1.93(2) and 1.94(2) Å for the BL-SECs and BR-SECs, respectively. The occupation number was checked, and this clearly preferred to be four, which gave a Debye-Waller factor of 0.009 Å² in both cases. Axial Cu-O interactions of 2.32(2) and 2.33(2) were observed for the BL-SECs and BR-SECs, respectively. The relatively large Debye-Waller factors, even for one Cu-O distance, compared to the first shell means that they are relatively poorly defined. The weak features at *ca.* 3 Å in the FT could be fitted to more distant Cu...Cu interactions at 2.8(3) and 3.8(4) Å, but the very large Debye-Waller factors of *ca.* 0.05 Å² indicate that they are poorly defined, in contrast to those in the model compounds. Also the third shell has very similar Cu-Cu distances (2.84(3) and 2.86(3) Å) in both BL-SEC and BR-SEC samples, together with very similar Debye-Waller factors ($2\sigma^2$) of 0.050 and 0.053 Å², respectively.

These data indicate that the bleached and brown SECs reacted with copper(II) acetate solution have the same structure, which consists of a well defined Cu-O₄ unit at 1.94(2) Å. There is also evidence for a second Cu-O at 2.32(2) Å consistent with a Jahn-Teller distorted octahedron, and some fairly weak, longer distant Cu...Cu interactions. These weak features may be due to small traces of copper oxide (CuO) which has Cu...Cu distances of 2.901, 3.083, 3.173, 3.423, 3.749 Å,¹⁹³ rather than being part of the Cu-SEC structure.

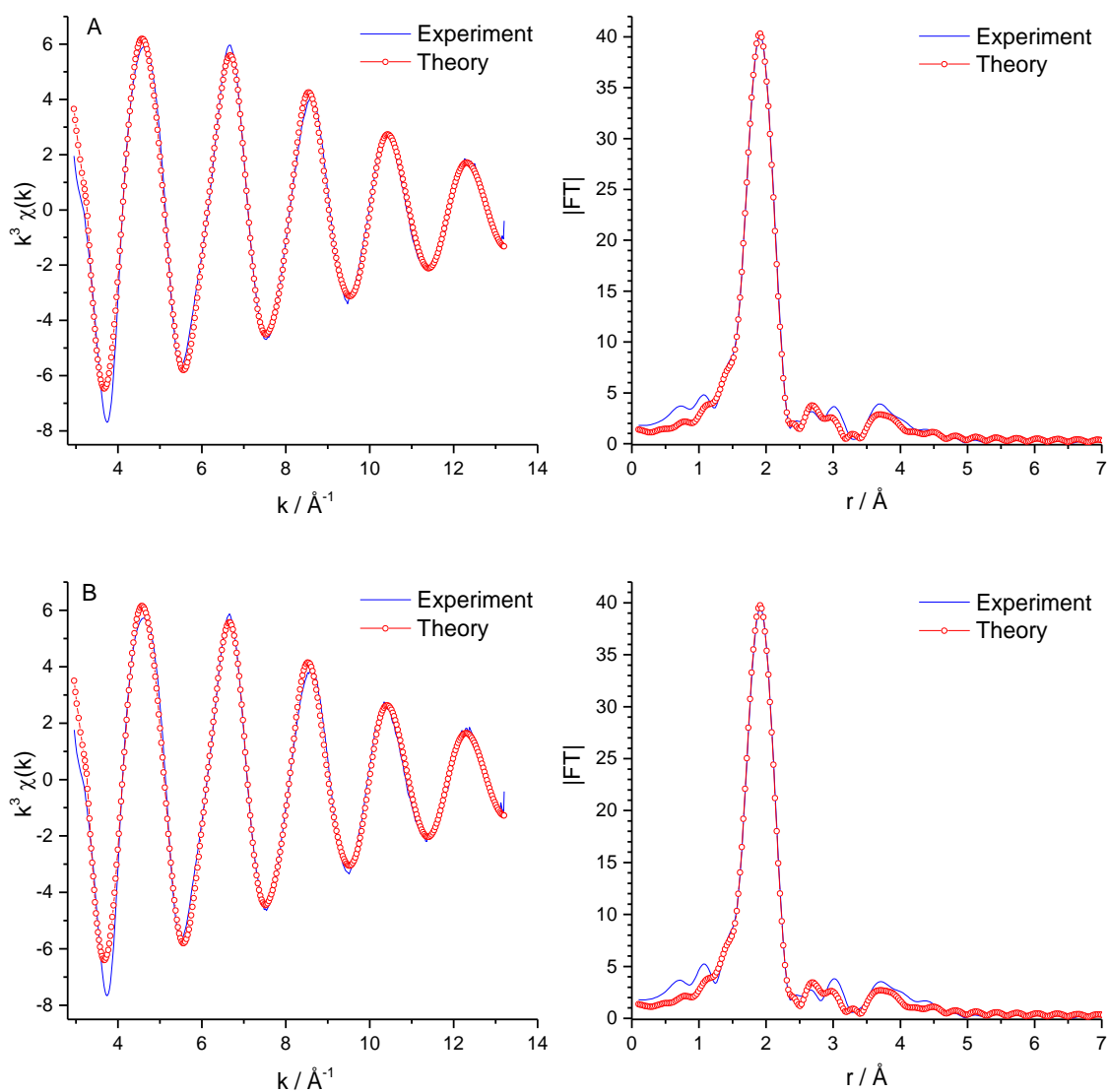


Figure 4.25 Cu K-edge EXAFS (left) and FTs (right) for (A) $\text{Cu}(\text{OAc})_2 \cdot \text{H}_2\text{O}$ with BL-SECs, (B) $\text{Cu}(\text{OAc})_2 \cdot \text{H}_2\text{O}$ with BR-SECs.

Sample		$r/\text{\AA}$	$2\sigma^2/\text{\AA}^2$	E_f/V	FI	R
$\text{Cu}(\text{OAc})_2 \cdot \text{H}_2\text{O} +$ BL-SECs	Cu-O ₄	1.938(2)	0.009(3)	-9.59(3)	0.08	11.12
	Cu-O ₁	2.317(19)	0.028(6)			
	Cu-Cu ₁	2.844(4)	0.050(1)			
	Cu-Cu ₂	3.807(18)	0.034(4)			
$\text{Cu}(\text{OAc})_2 \cdot \text{H}_2\text{O} +$ BR-SECs	Cu-O ₄	1.941(2)	0.009(3)	-9.46(4)	0.09	12.14
	Cu-O ₁	2.331(20)	0.028(6)			
	Cu-Cu ₁	2.861(4)	0.053(1)			
	Cu-Cu ₂	3.812(20)	0.035(5)			
	Cu-O ₁	2.331(20)	0.028(6)			

Table 4.17 Cu K-edge EXAFS data of $\text{Cu}(\text{OAc})_2 \cdot \text{H}_2\text{O}$ with BL-SECs and BR-SECs.

The Figure 4.26 shows Cu K-edge EXAFS and FT data recorded on BM26 of the brown and bleached SECs are reacted with copper(II) nitrate solutions. It can be seen that Cu K-edge EXAFS and FT of copper nitrate solutions reacted with brown SEC in Figure 4.26B are very similar to those of copper acetate(II) solution reacted with brown and bleached SEC in Figure 4.25. In both bleached and brown SECs the four Cu-O distances are very similar (1.93(2) and 1.94(2) Å), with very similar Debye-Waller factors of 0.009 and 0.010 Å². Also the second shell is very similar in both Cu-O distance are (2.28(2) and 2.30(2) Å), with the Debye-Waller factors of 0.028 and 0.020 Å² respectively. In the one Cu-Cu distance are (2.79(3) and 2.73(3) Å), with the Debye-Waller factors of 0.032 and 0.041 Å² respectively. The increased intensity of the Cu...Cu peak at 2.8 Å in the BL-SEC FT are correlated with a decrease in the Debye-Waller factor. As the coordination number was kept the same, this implies that either the Cu...Cu interaction is more ordered, or there are more of them. Cu-Cu distance in fourth shell are very similar in both bleached and brown SECs at 3.80(4) and 3.83(4) Å. And Debye-Waller factors of 0.031, 0.039 Å² respectively. The more distant Cu...Cu distances may be due to CuO as above, and it is interesting that they are slightly more pronounced in the BR-SEC data, and considerably so in the BL-SEC data. This indicates that the local environment of the copper in the BR-SECs reacted with copper(II) nitrate solution is the same as that in the BL-SECs and BR-SECs reacted with copper(II) acetate solution. For BL-SECs reacted with copper(II) nitrate solution the structure is very similar to these, especially the first coordination shell, but there appears to be an enhanced Cu...Cu interaction at *ca.* 2.8 Å.

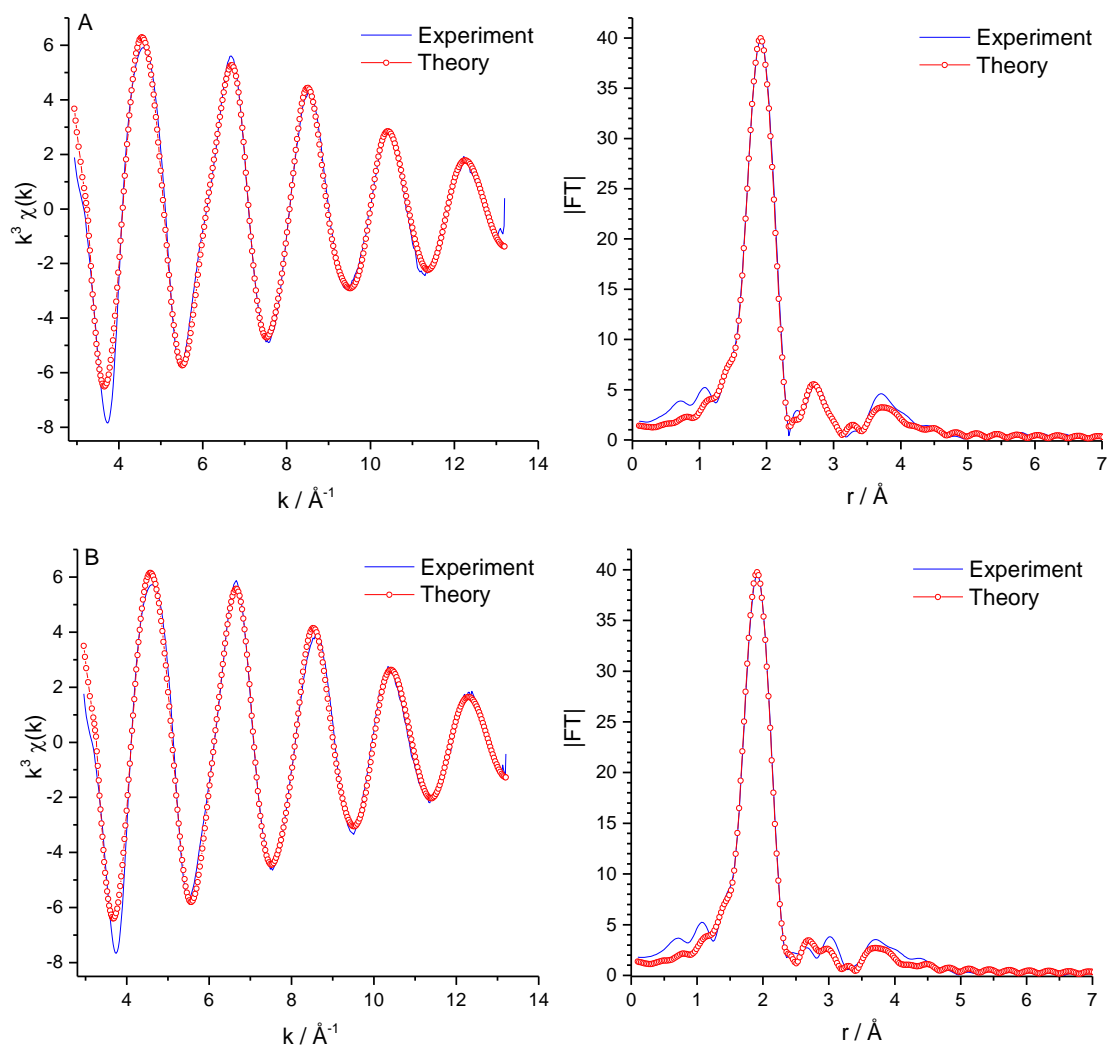


Figure 4.26 Cu K-edge EXAFS (left) and FTs (right) for (A) $\text{Cu}(\text{NO}_3)_2 \cdot 3\text{H}_2\text{O}$ with BL-SECs, (B) $\text{Cu}(\text{NO}_3)_2 \cdot 3\text{H}_2\text{O}$ with BR-SECs.

Sample		$r/\text{Å}$	$2\sigma^2/\text{Å}^2$	E_f/V	FI	R
$\text{Cu}(\text{NO}_3)_2 \cdot 3\text{H}_2\text{O} + \text{BL-SECs}$	Cu-O ₄	1.944(2)	0.009(3)	-9.78(3)	0.08	11.59
	Cu-O ₁	2.289(2)	0.028(6)			
	Cu-Cu ₁	2.798(2)	0.032(4)			
	Cu-Cu ₂	3.808(2)	0.031(4)			
$\text{Cu}(\text{NO}_3)_2 \cdot 3\text{H}_2\text{O} + \text{BR-SECs}$	Cu-O ₄	1.945(2)	0.010(4)	-9.70(4)	0.15	17.21
	Cu-O ₁	2.305(2)	0.020(5)			
	Cu-Cu ₁	2.732(3)	0.041(8)			
	Cu-Cu ₂	3.835 (3)	0.039(9)			

Table 4.18 Cu K-edge EXAFS data of $\text{Cu}(\text{NO}_3)_2 \cdot 3\text{H}_2\text{O}$ with BL-SECs and BR-SECs.

Figure 4.27 shows Cu K-edge EXAFS and FT data recorded on BM26 (ESRF) of the BR-SECs and BL-SECs reacting with copper(II) chloride solutions. It can be seen from Figure 4.27 that copper chloride with bleached SECs are very similar with copper acetate and copper nitrate with brown and bleached SECs, but that the data for BR-SEC reacted with copper(II) chloride solution is more different. In both bleached and brown SECs the four Cu-O distance are (1.94(2) and 1.94(2) Å), with the Debye-Waller factors of 0.009 and 0.010 Å². In second shell for the bleached SEC the Cu-O distance is 2.29(2) Å, with the Debye-Waller factors ($2\sigma^2$) of 0.028 Å². Also in both Cu-Cu distance are (2.79(3) and 3.07(4) Å), with the Debye-Waller factors of 0.032 and 0.021 Å² respectively. In Cu-Cu distance are very similar in both bleached and brown SECs at 3.80(4) and 3.81(4) Å. And Debye-Waller factors of 0.031, 0.033 Å² respectively.

The Cu...Cu shells are more intense in both the BL-SEC and BR-SEC data for the copper(II) chloride solution reactions, with the BR-SEC being even more different. This indicates that the copper chloride with bleached SECs has the same structure as copper acetate for bleached and brown SECs and with copper nitrate with brown SECs apart of copper nitrate with bleached SEC is slightly different and all of them used the same parameter and the number of shells. However the copper chloride with brown SECs is different. All copper salts with bleached and brown SECs the EXAFS data showed that the local environment around the copper contains a range of Cu-O distances and Cu-Cu distances. The first shell of four Cu-O bonds is very similar in terms of both distance and Debye-Waller factor. This means that the local copper environment is very similar in all cases. The second shell of Cu-O at slightly longer distances is also very similar for all but the BR-SEC reacted with copper(II) chloride solution. Therefore the Cu K-edge EXAFS data indicates that the local copper environment consists of a four short Cu-O distances, with some longer Cu-O in a classic Jahn-Teller distorted octahedron. The fact that the longer Cu...Cu shells are most likely to arise from small quantities of CuO, and that these are weakest in the samples prepared from copper acetate solutions indicates that the acetate provides some protection of the copper in the SECs.

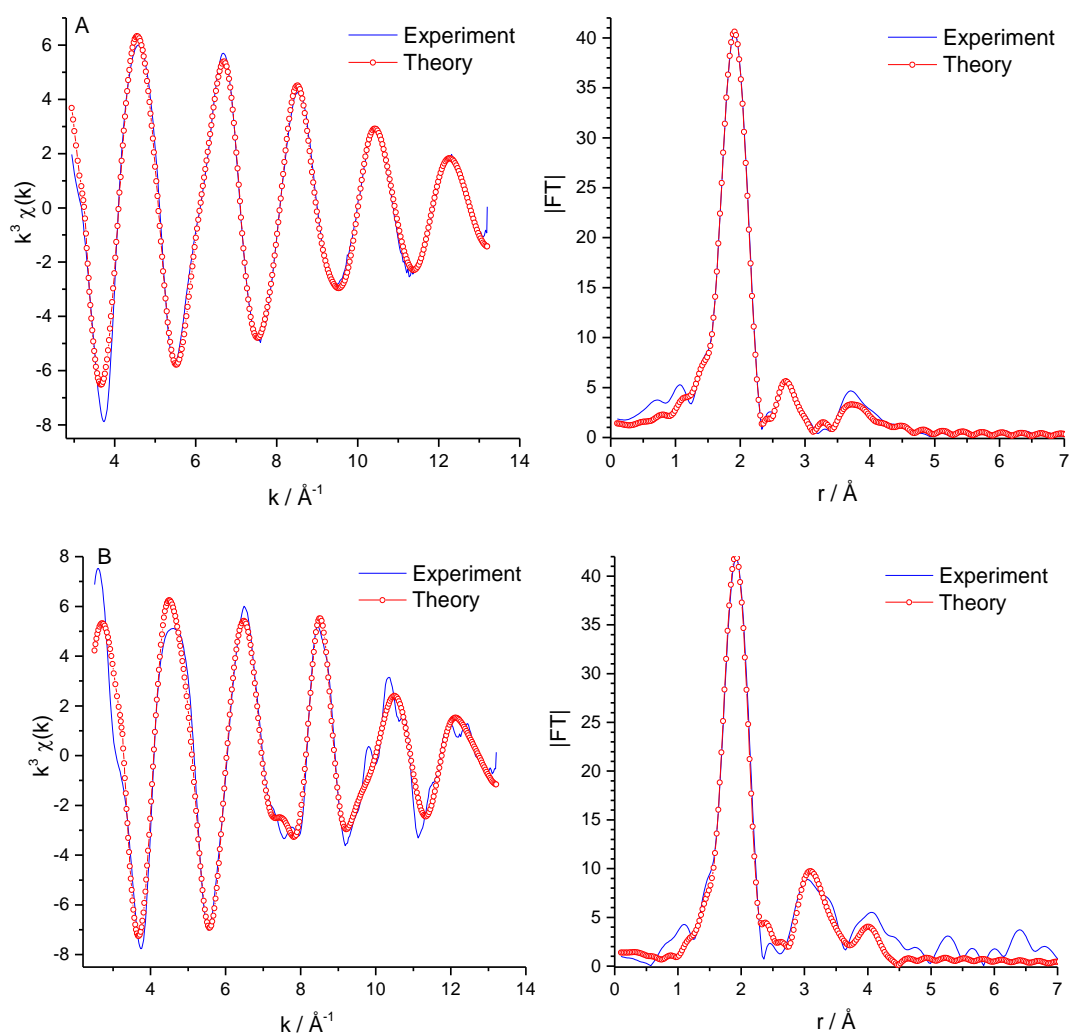


Figure 4.27 Cu K-edge EXAFS (left) and FTs (right) for (A) $\text{CuCl}_2 \cdot 2\text{H}_2\text{O}$ with BL-SECs, (B) $\text{CuCl}_2 \cdot 2\text{H}_2\text{O}$ with BR-SECs.

Sample		$r/\text{\AA}$	$2\sigma^2/\text{\AA}^2$	E_f/V	FI	R
$\text{CuCl}_2 \cdot 2\text{H}_2\text{O}$ + BL-SECs	Cu-O ₄	1.944(2)	0.009(3)	-9.73(3)	0.08	10.96
	Cu-O ₁	2.293(2)	0.028(6)			
	Cu-Cu ₁	2.798(2)	0.032(4)			
$\text{CuCl}_2 \cdot 2\text{H}_2\text{O}$ + BR-SECs	Cu-Cu ₂	3.806(2)	0.031(4)			
	Cu-O ₄	1.949(3)	0.010(5)	-8.83(4)	0.22	20.82
	Cu-Cu ₂	3.074(8)	0.021(2)			
	Cu-Cu ₃	3.817(2)	0.033(5)			

Table 4.19 Cu K-edge EXAFS data of $\text{CuCl}_2 \cdot 2\text{H}_2\text{O}$ with BL-SECs and BR-SECs.

4.5.4 XRF images

XRF images were used to help identify whether the interaction between copper and the SECs was specific or more general in nature, and whether the SECs were filled with copper.

Figure 4.28 shows the Cu K_{α} XRF image of the BL-SECs and BR-SECs prepared from a copper acetate solution. The physical structure of the SECs can be clearly seen in these images indicating that the copper is closely associated with the BL- SEC or BR-SEC structure in the samples prepared using both 2.5 mmol and 7.5 mmol of copper and stirred for three days.

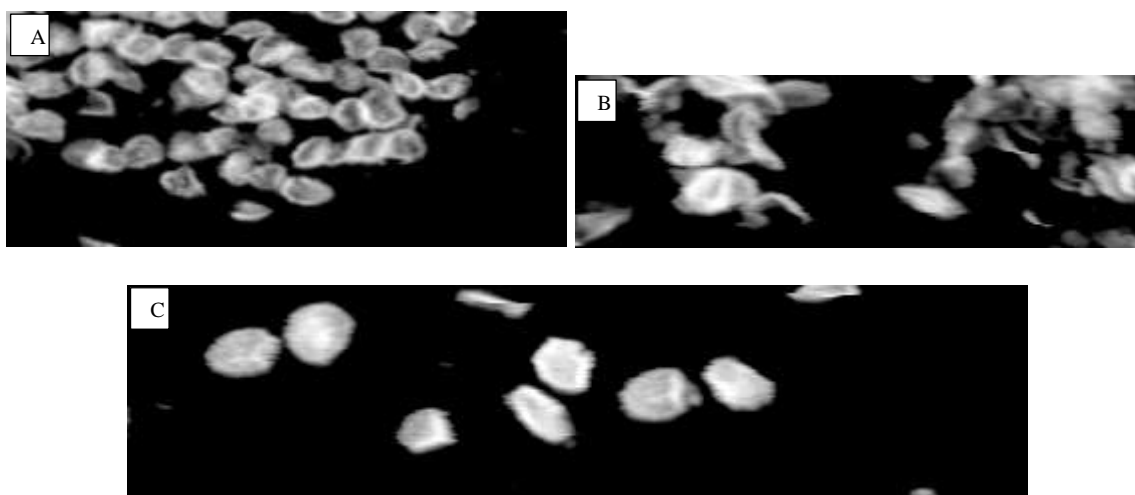


Figure 4.28 Cu K_{α} XRF images stirred three days. (A) BR-SECs with 7.5 mmol of copper(II) acetate solution. (B) BL-SECs with 7.5 mmol of copper(II) acetate solution. (C) BL-SECs with 2.5 mmol of copper(II) acetate solution.

Figure 4.29 shows the Cu K_{α} XRF image of the BL-SECs and BR-SECs prepared from a copper nitrate solution. It can be seen that the copper being associated with the BL- SEC or BR- SEC structure at both in 2.5 mmol and 7.5 mmol with stirring three days. Data sufficiently sensitive that can see both whole and broken SECs.

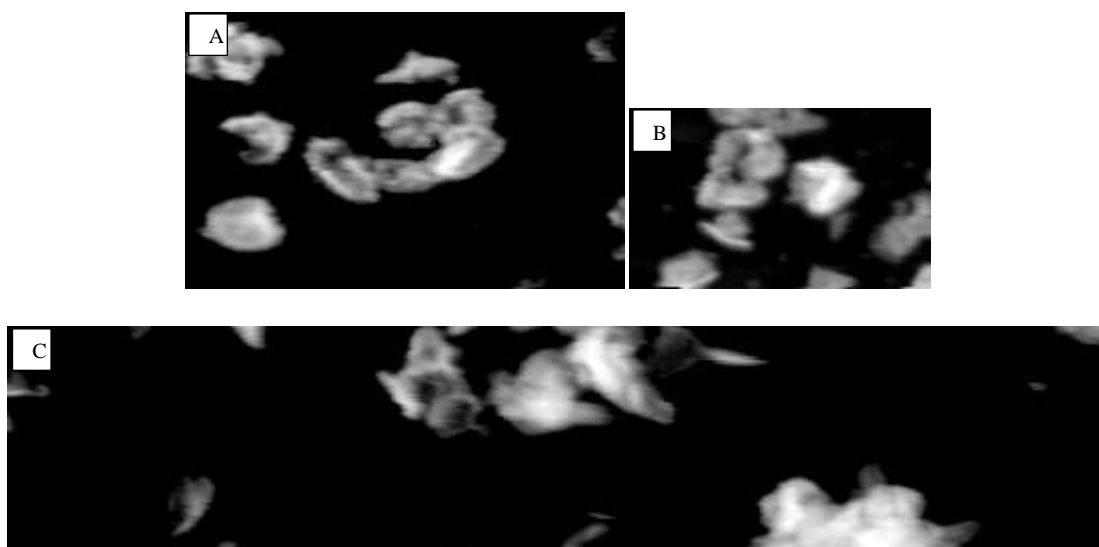


Figure 4.29 Cu K_{α} XRF images stirred three days. (A) BR-SECs with 7.5 mmol of copper(II) nitrate solution. (B) BL-SECs with 2.5 mmol of copper(II) nitrate solution. (C) BL-SECs with 7.5 mmol of copper(II) nitrate solution.

Figure 4.30 shows the Cu K_{α} XRF image of the broken BR-SECs prepared from a copper chloride solution in both in 2.5 mmol and 7.5 mmol with stirring three days, the images indicated that the copper being associated with BR-SEC structure.

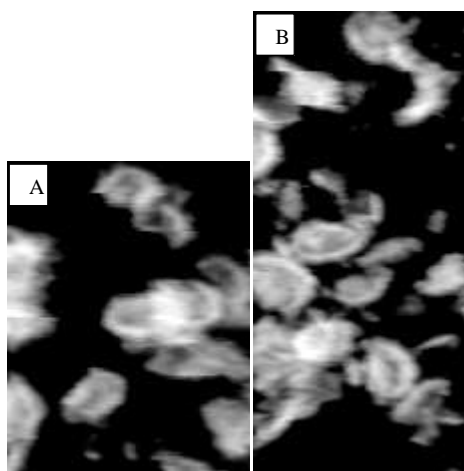


Figure 4.30 Cu K_{α} XRF images stirred three days. (A) BR-SECs with 7.5 mmol of copper(II) chloride solution. (B) BR-SECs with 2.5 mmol of copper(II) chloride solution.

The Cu K_{α} XRF images show that the interaction between copper and the SECs is similar for all copper(II) acetate, copper(II) nitrate and copper(II) chloride, with a high correlation between SECs structure and copper(II) location. Also, the fact that the structure of the SECs is clearly visible in these images indicates that the copper is closely associated with the BL-SECs or BR-SECs structure. In addition, there is no evidence for the copper to be collecting

either within the SECs or as a thick layer on the surface. Therefore, all the evidence points towards a specific interaction between the copper and the SEC surface.

4.5.5 Electron paramagnetic resonance spectroscopy (EPR)

The X-band (9.87 GHz) EPR spectra shown in Figure 4.31 and Figure 4.32. Electron paramagnetic resonance (EPR) is used to study samples with unpaired electrons. Spectra are readily obtained from samples containing one unpaired electron, and other odd numbers of unpaired electrons, although the latter can be very complex to interpret. Spectra from samples with odd numbers of unpaired electrons are much more challenging to obtain as the energy gaps between the ground and excited states are often too large to access with conventional magnet/microwave frequency combinations. However, spin triplets are sometimes accessible.

EPR spectra are usually presented in the form of first derivatives because of the way the data is acquired. The important parameters derived from EPR spectra are the g value, and the hyperfine coupling constant A . The g -value for a free electron is 2.0023. g -values are obtained from the experimental spectrum using the following equation.

$$g = 714.46 \times (\nu(\text{GHz})/H(\text{G}))$$

Equation 4.1 The equation for determining the g -value in EPR spectroscopy.

For these experiments the operating frequency was *ca.* 9.87 GHz, and the magnetic field was swept from 200 to 6000 Gauss.

g values very close to 2.00 are observed for radicals where the only contribution to the electron's magnetic properties comes from the angular momentum of the electron spin. This is usually the case for main group radicals, but for transition metal compounds that contain unpaired electrons, the g -value can be different from 2.00 because of spin-orbit coupling due to the effect of the angular momentum associated with the orbital motion of the electron. If the d orbitals are less than half-filled, then g will be smaller than that for the free electron (but appear at higher magnetic field), and if the d orbitals are more than half-filled, then g will be greater than the free electron value (but occur at lower magnetic field). The hyperfine coupling constant, A , is a measure of the interaction of the unpaired electron with magnetic nuclei ($I \geq 1/2$) in the radical, and the number of observed lines is

given by $2nI + 1$. Both g and A can be resolved into their x , y and z components, to give g_x , g_y , g_z , A_x , A_y and A_z . In high symmetry, cubic, compounds, or for rapidly tumbling radicals in solution, where x , y and z are equivalent, these are averaged into isotropic g_{iso} and A_{iso} values. A special case is in compounds with axial symmetry where $x = y \neq z$, so that g_{\perp} ($g_{x,y}$) and g_{\parallel} (g_z), and A_{\perp} ($A_{x,y}$) and A_{\parallel} (A_z) are observed. This is the case for Cu(II), d^9 , compounds subject to a Jahn-Teller distortion, and for a tetragonal elongation g_{\perp} ($g_{x,y}$) < g_{\parallel} (g_z). For the Cu-SEC complexes there are not expected to be any superhyperfine interactions, as there are no oxygen isotopes with $I > 0$ with high abundance, and it is known there is no significant amount of nitrogen in the SECs.

For spin doublets ($S = 1/2$) with one unpaired electron, the spectrum will contain one feature, that may be split into its g_x , g_y , g_z , A_x , A_y and A_z components. However, a special case is for spin triplets ($S = 1$) in dimeric metal complexes where two unpaired electrons can couple ferromagnetically to give $S = 1$, or antiferromagnetically to $S = 0$. For most copper dimeric systems the antiferromagnetic $S = 0$ state is the ground state with an excited ferromagnetically coupled triplet state. However, as the energy separation is small (*ca.* 300 cm^{-1}) there is substantial population of the excited triplet state at room temperature, and this will be temperature dependent so that the triplet state features reduce in intensity as the temperature is reduced. The EPR spectra of dimeric copper complexes are more complicated and in general more transitions are allowed than for spin triplets than spin doublets. Spin singlets are EPR silent. For example the X-band spectrum of dimeric $[\text{Cu}(\text{OAc})_2 \cdot \text{H}_2\text{O}]_2$ has peaks at very low magnetic field (close to 0 G), as well as around 4500 G and 6000 G,¹⁹⁴ whereas monomeric species just have g_{\perp} ($g_{x,y}$) and g_{\parallel} (g_z) at 3000 – 3500 G. In particular “half-field” transitions at the equivalent of $g = 4$ (*ca.* 1650 G for X-band experiments) due to the forbidden $\Delta m_s = 2$ transition within the triplet states are very characteristic of the presence of dimeric (or higher) copper structures.^{195, 196, 197} Therefore, EPR spectra of the Cu-SEC complexes will provide information on the copper local environment.

The X-band spectra (*ca.* 9.87 GHz) with a wide magnetic field range in Figure 4.31 and Figure 4.32 only contain features characteristic of monomeric copper(II) centres with a tetragonal elongated Jahn-Teller distortion, and there is no evidence of features at higher or lower magnetic field characteristic of dimeric copper(II). The different signal:noise ratios are caused by a variation in the amount of sample used for each experiment. From

these wide-scan spectra it is clear that the the spectral motifs are essentially the same for all of the BL-SEC samples, and all of the BR-SEC samples, but that there is a slight, but consistent increase in the resolution of the features in the spectra of the BL-SEC complexes. This is displayed more clearly in the expansion of the central features shown in Figure 4.32. Each of these spectra contain one intense feature at g 2.08- 2.09, and four weaker features centred at higher g (2.35) (lower magnetic field) which are not resolved in all cases. The four peaks on the $g = 2.35$ feature are due to hyperfine coupling of the unpaired electron to ^{63}Cu and ^{65}Cu . As these both have $I = 3/2$, four lines of equal intensity are expected for each of them, but the two sets of four lines are overlapped as the magnetogyric ratios are very similar. As $g_{\perp} (g_{x,y})$ are more intense than those due to $g_{\parallel} (g_z)$, the features at $g = 2.08 - 2.09$ are assigned to $g_{\perp} (g_{x,y})$ and those at $g = 2.35$ to $g_{\parallel} (g_z)$. The $g_{\perp} (g_{x,y}) < g_{\parallel} (g_z)$ values confirm that the Cu(II) is in a tetragonally elongated environment due to the Jahn-Teller, as a tetragonally compressed distortion would result in $g_{\perp} (g_{x,y}) > g_{\parallel} (g_z)$. The resolved hyperfine coupling on the $g_{\parallel} (g_z)$ transitions, A_{\parallel} is of the order of 135 – 140 G for all spectra. These values of g and A consistent with literature values for Cu(II) in a Jahn-Teller distorted tetragonally elongated environment.¹⁹⁴ The lack of resolved A_{\perp} hyperfine coupling is not uncommon as A_{\perp} is usually significantly smaller than A_{\parallel} .

Therefore, these EPR spectra confirm that the copper in the SECs is in the form of molecular, monomeric species as there is no evidence for the triplet states expected if the copper atoms are coupled together. In addition the g values show that the copper is in a tetragonally elongated environment due to the Jahn-Teller distortion. The copper environment is essentially the same in all of the BL-SEC samples, and is slightly more ordered than in the BR-SEC samples.

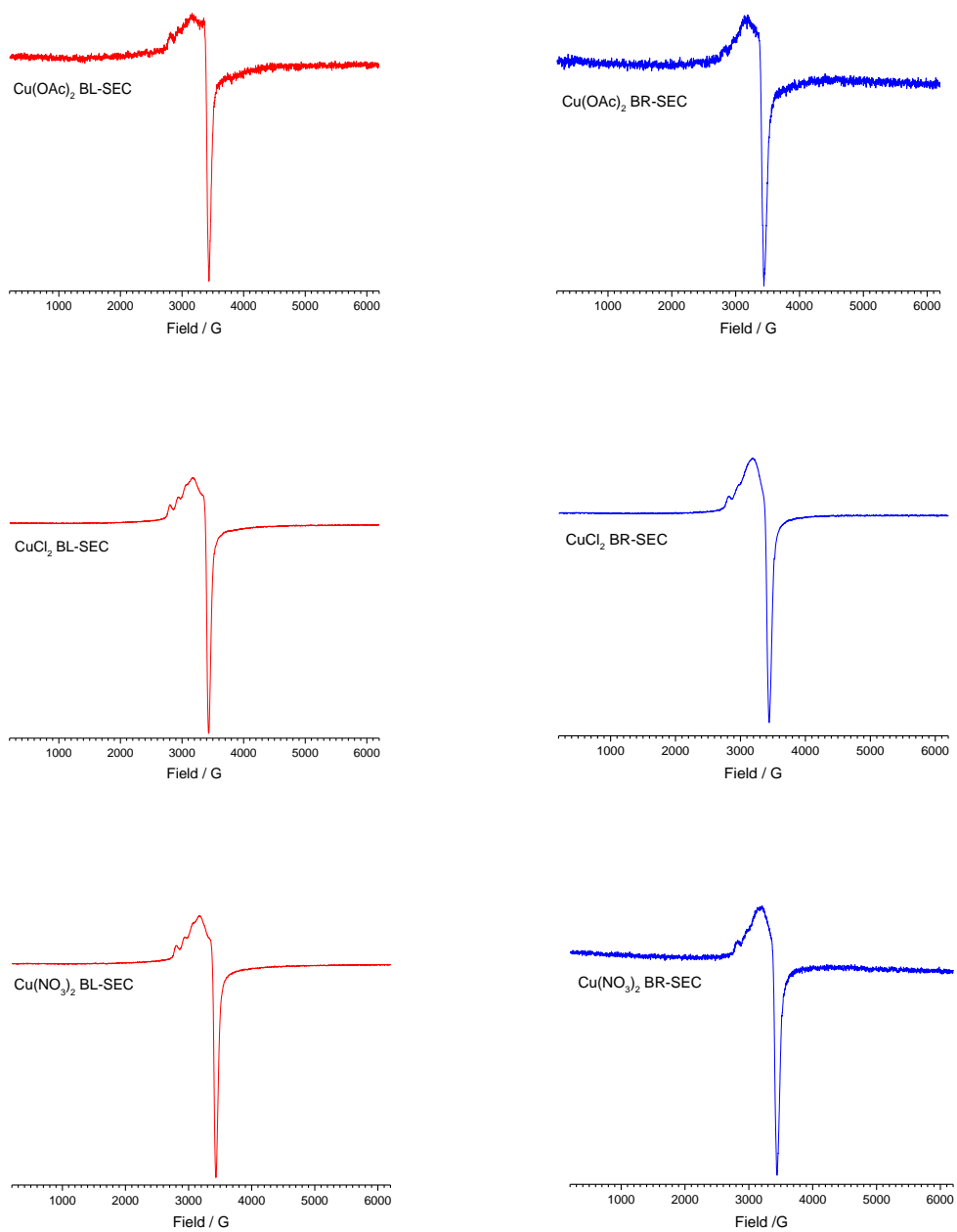


Figure 4.31 X-band (9.87 GHz) EPR spectra of copper SEC complexes at room temperature.

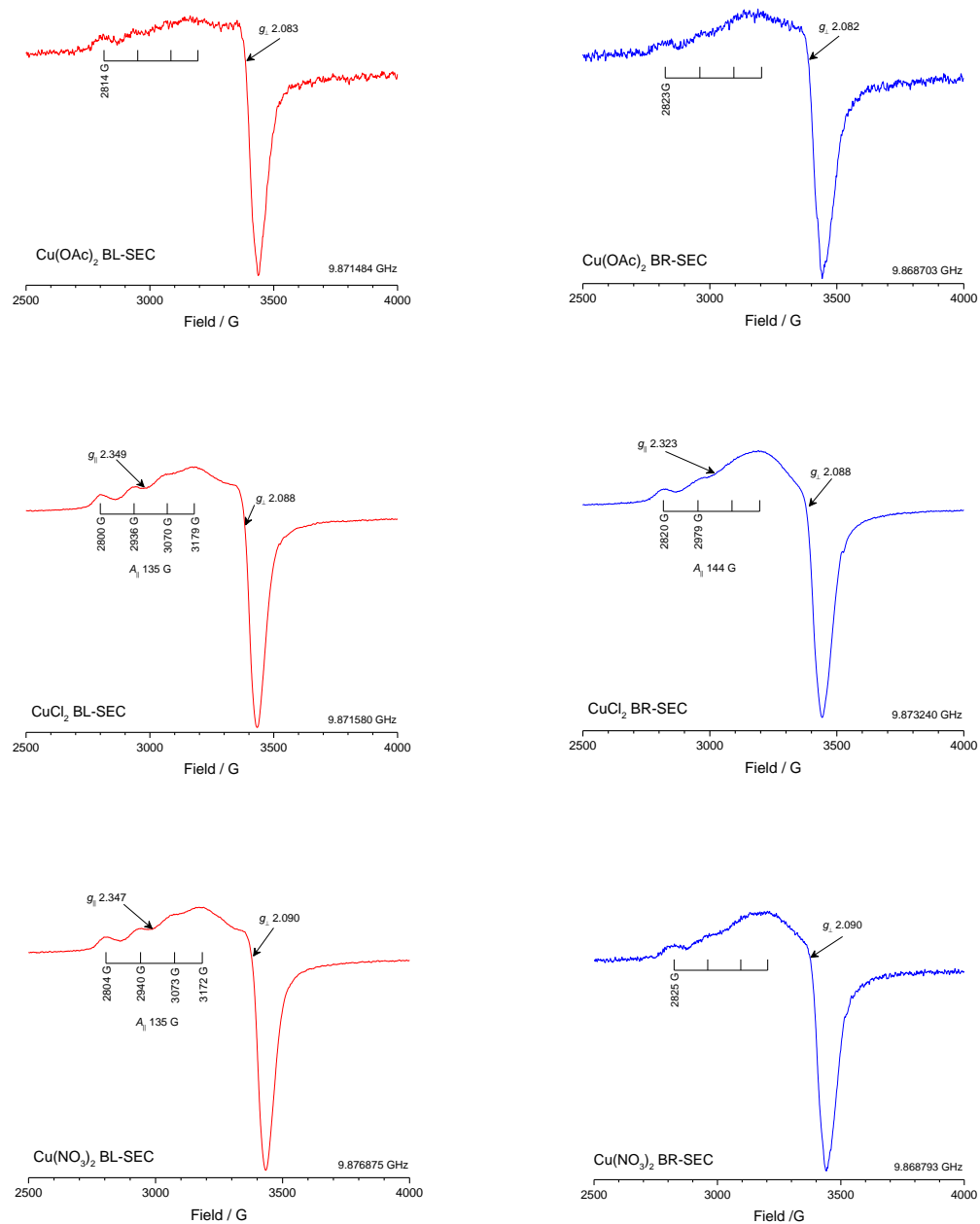


Figure 4.32 X-band (9.87 GHz) EPR spectra of copper SEC complexes at room temperature.

4.6 Conclusion

This work provides evidence of direct copper attachment to SECs derived from *L. clavatum*. Several spectroscopic and characterisation techniques were employed. The amount of metal in the samples is dependent on the SECs and metal salt used. As expected the copper loading is greater for brown SECs than bleached SECs due to the effect of the ionisation state of the carboxylic acid and phenol groups discussed in section 3.3.2.

It is largely independent of stirring time for all metal salts. The copper-SECs complexes exhibited more intense d-d transitions. Elemental determination was carried out on the SEC complexes by ICP-OES and CHN analysis. Increasing the stirring duration resulted in greater loading for copper acetate-SEC complexes, with a four-fold %w/w increase observed from overnight to two weeks. Copper acetate showed higher attachment ratios to the SECs compared to copper chloride and copper nitrate. The optimum conditions were found to be a ratio of 2.5 mmol: 100 mg (copper: SECs) and stirring for three days.

The use of the bleached SECs enabled UV-vis spectra to be obtained from copper-SEC complexes. The UV-vis spectra displayed the characteristic features of copper(II). In addition, the spectra appeared to be dependent on both the concentration and the copper salt used.

Functional groups in the spore complexes were observed using IR spectroscopy. Due to the fluorescence of the copper with bleached SECs from *L. clavatum*, Raman spectroscopy cannot be used to analyse Cu-SECs complexes. IR can be used to observe the functional groups of SECs with the copper complexes. The overall features of the SECs infrared spectra highlighted the significance of aliphatic chains in the macromolecule. Interpretation relied upon the quality of the spectra, but the prime bands consistently revealed hydroxyls, aliphatic carbons, carbonyls, unsaturated hydrocarbons and ether groups. An important observation is that the IR spectrum of the copper acetate sample is different from that of the copper chloride and copper nitrate samples as well as the parent SECs. This probably indicates the presence of acetate in the copper coordination environment, which may explain why higher loadings are observed for the acetate samples.

Cu K-edge XANES spectra for copper samples with SECs indicates that copper environment contains only Cu-O in the first coordination shell. The EXAFS data

confirmed that the first coordination shell consists of a Jahn-Teller distorted octahedron with a well defined Cu-O₄ square plane, and longer Cu-O distances that were not always easy to identify with certainty. In addition that the local environment around the copper contains a range of Cu-O distances and Cu-Cu distances.

The Cu K_α XRF images observed that the structure of the SECs is visible in these images indicating that the copper is closely associated with the BL- SEC or BR-SEC structure.

EPR spectroscopy observed that the copper environment is the same in all of the BL-SEC samples, and is slightly more ordered than in the BR-SEC samples.

Taken together these results show that the copper adopts a monomeric Jahn-Teller tetragonally elongated octahedral coordination environment as shown in Figure 4.33. The higher loadings observed for acetate results compared to nitrate and chloride as well as the presence of characteristic IR spectra indicate that the acetate groups are part of the coordination environment, as well as the surface carboxylate and phenolic surface groups. Figure 4.33 shows schematic illustrations of possible surface structures of copper interacting with the SEC surface. Figure 4.33(A) and (C) include acetate, whereas Figure 4.33(B) is representative of the samples derived from chloride and nitrate.

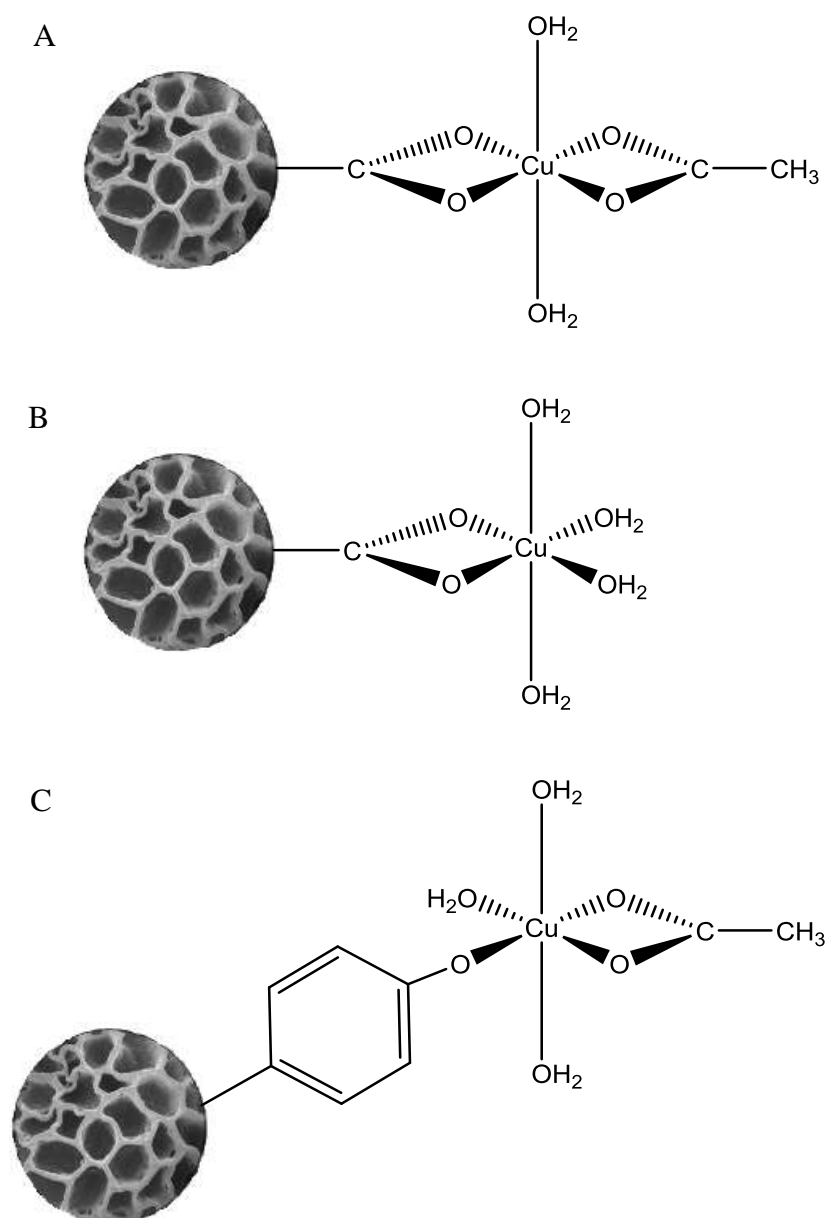


Figure 4.33 Schematic illustrations of possible interaction of copper with SEC surface. (A) copper acetate with carboxylate on SEC surface, (B) copper chloride or nitrate with carboxylate on SEC surface and (C) copper acetate with phenolate on SEC surface.

Chapter 5

Iron attached to sporopollenin

5 Iron attached to sporopollenin

5.1 Introduction

Iron (Fe) is a chemical element with an atomic number of 26 and atomic mass of 55.84. It is in Group 8 of the periodic table, and its electronic configuration is: [Ar] 3d⁶ 4s². Iron is an abundant and chemically active element that commonly forms compounds in two oxidation states in the natural environment; iron (II) (ferrous compounds) and iron (III) (ferric compounds).¹⁹⁸ It is present in soils and natural waters in molecular complexes or colloids and is found at the centre of haemoglobin in the form of Fe(II).¹⁹⁸

Fe-sporopollenin exine capsule (SEC) complexes have a wide variety of applications including catalysis, imaging and biological delivery. SECs have been well studied for some applications such as their high DNA adsorption capacity¹⁹⁹ and there is some existing research into how iron interact with SECs for drug delivery.^{26, 27, 30, 73, 78, 81, 85, 101}

Bleached SECs enable the use of a wider variety of spectroscopic techniques to investigate the interaction between iron and SECs, in particular UV-vis and Raman. As iron(II) has d-d transitions at relatively low energy, it is ideally suited to these studies. Additionally, Mössbauer can be used to study iron(II) and X-ray is to identify the oxidation state of the iron.

The aim of this chapter is to use a variety of spectroscopic techniques to investigate how iron is bound to SECs (Figure 5.1).

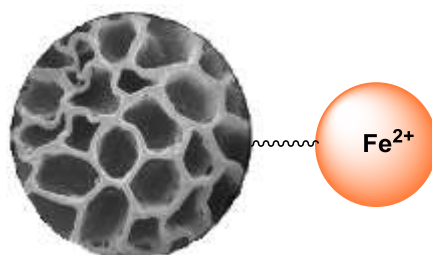


Figure 5.1 Schematic representation of the attachment of iron complexes to SECs.

This chapter describes the preparation of Fe-SEC complexes from a loading experiment using iron(II) acetate, iron(II) chloride, iron(III) chloride, ammonium iron(III) sulfate or iron(II) ammonium sulfate solutions with brown and bleached SECs. The synthesised

microcapsules were characterised by elemental analysis (ICP-OES), scanning electron microscopy (SEM), infrared spectroscopy (IR), UV-visible spectroscopy, X-ray absorption spectroscopy and Mössbauer spectroscopy. This study provides insight into how iron salts attach and form complexes with SECs.

5.2 Synthetic methods

5.2.1 Preparation of sporopollenin samples for iron loading

Two different extractions of *L. clavatum* were used for studying iron loadings; bleached SECs (BL-SECs) and brown SECs (BR-SECs). BL-SECs were prepared from brown SECs, as described in chapter 2. Reactions were carried out with aqueous solutions of the following iron salts: iron(II) chloride, iron(III) chloride, iron(II) acetate, ammonium iron(II) sulfate and ammonium iron(III) sulfate. The colour of the complexes with BR-SECs were brown, and those for the BL-SECs were all pale brown (but darker than the starting BL-SECs).

300 mg of SECs were added to a 7.5 mmol solution of each iron salt using Schlenk techniques. The resulting solutions were stirred for three days, filtered, washed with ethanol, dried under vacuum, and stored under argon.

Iron salt	Mass of salt	mmol of iron salt	Mass (BL-SEC or BR-SEC)
FeCl₂	950.62 mg	7.5	300 mg
FeCl₃	1216.57 mg	7.5	300 mg
Fe(OAc)₂	1304.55 mg	7.5	300 mg
(NH₄)₂Fe(SO₄)₂+6H₂O	2941.05 mg	7.5	300 mg
NH₄Fe(SO₄)₂+12H₂O	3616.35 mg	7.5	300 mg

Table 5.1 Concentration of iron salts used in preparation of iron loaded SECs.

5.3 Elemental analyses by ICP-OES

Inductively coupled plasma optical emission spectroscopy ICP-OES was used to determine the elemental composition of the Fe-SEC complexes. The iron loadings in the SEC samples were analysed by ICP-OES using 10 mg samples. Table 5.2 displays the iron loadings for

brown and bleached SECs prepared with a 7.5 mmol: 300 mg (iron: SEC) ratio stirred at RT for three days.

Iron salt + (BL-SECs & BR-SECs)	Iron loading on dry SECs (%w/w)
Iron(II) chloride solution + BR-SECs	4.79±0.01
Iron(II) chloride solution + BL-SECs	0.97±0.02
Iron(III) chloride solution + BR-SECs	2.03±0.02
Iron(III) chloride solution + BL-SECs	0.82±0.03
Iron(II) acetate solution + BR-SECs	2.99±0.01
Iron(II) acetate solution + BL-SECs	2.34±0.003
Ammonium iron(II) sulfate solution + BR-SECs	4.35±0.08
Ammonium iron(II) sulfate solution + BL-SECs	1.03±0.01
Ammonium iron(III) sulfate solution + BR-SECs	1.45±0.007
Ammonium iron(III) sulfate solution + BL-SECs	0.27±0.003

Table 5.2 ICP-OES results for Fe-SEC complexes.

It is evident from Table 5.2 that a higher iron loading is observed with brown SECs than bleached SECs for all of the iron salts. Previous work¹⁰¹ using BR-SECs found higher loading for Fe(II) than Fe(III) when FeCl₂ and FeCl₃ solutions and extensive air drying were used, and this was explained as due to a specific interaction of the iron with Fe(II) solutions, rather than a generic coating with Fe(III). When Schlenk techniques were used with FeCl₂ solutions the loading value dropped.¹⁰¹ For example, the iron(II)chloride and ammonium iron(II) sulfate BR-SEC complexes have an iron loading of over four times that of their respective BL-SEC complexes (4.79 % w/w, 4.35 % w/w, 0.97 % w/w and 1.03 % w/w, respectively). The largest difference was between the brown and bleached SEC complexes and ammonium iron (III) sulfate (1.45 % w/w and 0.27 % w/w respectively). For iron(III) chloride, approximately twice the amount of iron was attached to surface functional groups of the BR-SECs (2.03 % w/w) compared with the BL-SECs (0.82 % w/w). The smallest difference was between the brown and bleached SECs with iron(II) acetate (2.99 % w/w and 2.34 % w/w respectively). These differences may indicate that the bleaching process removes some of the functional groups that are involved in the iron coordination.

5.3.1 Extraction studies in neutral pH

In order to correlate the values with the spectroscopic data (see later) these experiments used the samples prepared with 7.5 mmol of copper and 300 mg of SEC and a reaction time of three days. 20 mg of Fe-SEC (both BR-SEC and BL-SEC) was added to 5 mL of water and stirred for three days. The solid was filtered, washed with water followed by ethanol, and dried in a desiccator. And then the solution and solid were analysed for Fe using ICP-OES.

Table 5.4 and 5.5 show the results of suspending the iron loaded SECs in neutral water. Table 5.5 presents the data obtained from the solids before after suspension in neutral water for three days, while Table 5.4 shows the change in iron concentration in the solution. There is some change in the amount of iron on the SECs before and after being suspending in neutral solution, but there is no evidence for an increase in the amount of iron in the solution. These differences in the solid data are all of the order of 0.2 mg and in some cases there appears to be more iron after suspension in water than before, therefore we take this to be the limit of detection in these experiments and conclude that there is no leaching of the iron in neutral solution. This is confirmed by the lack of increase in the amount of iron in the solution. The only exception is possibly that of ammonium iron(II) sulfate solutions with BR-SECs, where there is a larger loss of iron from the solid, but as there is no significant change in the concentration of iron in the solution, we do not believe this is significant.

Therefore, these experiments show that once the iron is attached to the SECs it is not leached in neutral solutions.

Sample	% w/w Fe (ICP-OES) in solid before suspending in water	mg of Fe in 20 mg of SEC before extraction in water	% w/w Fe (ICP-OES) in solid after suspending in water filtering, washing and drying	mg of iron in SEC after suspension in water	Difference (mg)	% loss of Fe
Iron(II) chloride solution + BR-SECs	4.79	0.958	4.63	0.926	0.032	3.34
Iron(II) chloride solution + BL-SECs	0.97	0.194	0.83	0.166	0.028	14.4
Iron(III) chloride solution + BR-SECs	2.02	0.404	2.23	0.446	-0.042	-10.4
Iron(III) chloride solution + BL-SECs	0.82	0.164	1.01	0.202	-0.038	-23.2
Iron(II) acetate solution + BR-SECs	2.98	0.596	2.92	0.584	0.012	2.013
Iron(II) acetate solution + BL-SECs	2.34	0.468	2.67	0.534	-0.066	-14.1
Ammonium iron (II) sulfate solution + BR-SECs	4.35	0.87	3.3	0.66	0.21	24.1
Ammonium iron (II) sulfate solution + BL-SECs	1.03	0.206	0.85	0.17	0.036	17.5
Ammonium iron (III) sulfate solution + BR-SECs	1.44	0.288	1.38	0.276	0.012	4.16
Ammonium iron (III) sulfate solution + BL-SECs	0.26	0.052	0.35	0.07	-0.018	-34.6

Table 5.3 Iron loadings in dry SECs before and after extraction in neutral pH.

Sample	ICP-OES results for Fe filtrate solution / ppm	mg Fe extracted into 5 mL solution	%loss of Fe into solution	mg lost from solid	mg iron missing
Iron(II) chloride solution + BR-SECs	9.88	0.049	5.157	0.032	-0.017
Iron(II) chloride solution + BL-SECs	2.14	0.011	5.515	0.028	0.017
Iron(III) chloride solution + BR-SECs	0.01	0.0001	0.012	-0.042	-0.042
Iron(III) chloride solution + BL-SECs	0.89	0.005	2.713	-0.038	-0.042
Iron(II) acetate solution + BR-SECs	0.01	0.0001	0.009	0.012	0.012
Iron(II) acetate solution + BL-SECs	0.35	0.002	0.374	-0.066	-0.067
Ammonium iron (II) sulfate solution+ BR-SECs	0.01	0.0001	0.006	0.21	0.21
Ammonium iron (II) sulfate solution + BL-SECs	1.92	0.009	4.66	0.036	0.026
Ammonium iron (III) sulfate solution + BR-SECs	1.35	0.007	2.344	0.012	0.005
Ammonium iron (III) sulfate solution + BL-SECs	0.39	0.002	3.75	-0.018	-0.019

Table 5.4 Complete results of all data calculations of both dry Fe-SEC complexes and in solution.

Sample	mg of iron in 20 mg of SEC before extraction in water	mg of iron remaining in SEC after suspension in water	% loss of Fe from solid	mg iron extracted into 5 mL solution	%loss of Fe into solution	mg iron missing
Iron(II) chloride solution + BR-SECs	0.96	0.93	3.34	0.05	5.16	-0.02
Iron(II) chloride solution + BL-SECs	0.19	0.17	14.4	0.01	5.52	0.02

Iron(III) chloride solution + BR-SECs	0.40	0.45	-10.4	0.0001	0.01	-0.04
Iron(III) chloride solution + BL-SECs	0.164	0.20	-23.2	0.004	2.71	-0.04
Iron(II) acetate solution + BR-SECs	0.59	0.58	2.01	0.0001	0.01	0.01
Iron(II) acetate solution + BL-SECs	0.47	0.53	-14.1	0.002	0.38	-0.07
Ammonium iron (II) sulfate solution+ BR-SECs	0.87	0.66	24.1	0.0001	0.006	0.21
Ammonium iron (II) sulfate solution + BL-SECs	0.21	0.17	17.5	0.01	4.66	0.03
Ammonium iron (III) sulfate solution + BR-SECs	0.29	0.28	4.16	0.01	2.34	0.01
Ammonium iron (III) sulfate solution + BL-SECs	0.05	0.07	-34.6	0.002	3.75	-0.02

Table 5.5 The results of all data calculations of both dry Fe-SEC complexes and in solution.

5.4 Scanning electron microscope images (SEM)

The samples prepared from 300 mg of BL-SECs or BR-SECs reacted with 75mL of 7.5 mmol iron(II) and iron(III) solution for 3 days were examined by scanning electron microscopy to investigate the effect of the iron on the structure of the SECs.

Figure 5.2 shows a clear difference between the SEM images of the attachment of iron(II) chloride to the surface of BR-SECs compared to BL-SECs. Small fragments and debris are visible around the SEC spores in the SEM image of iron(II) chloride with BR-SECs (Figure 5.2A). Whilst some of the SECs remain intact, some have burst slightly or become distorted. The SEM image of iron(II) chloride with BL-SECs (Figure 5.2B) however clearly shows the almost spherical shape of the microcapsules, verifying that the sporopollenin particles were not damaged during the binding process with iron(II) chloride.

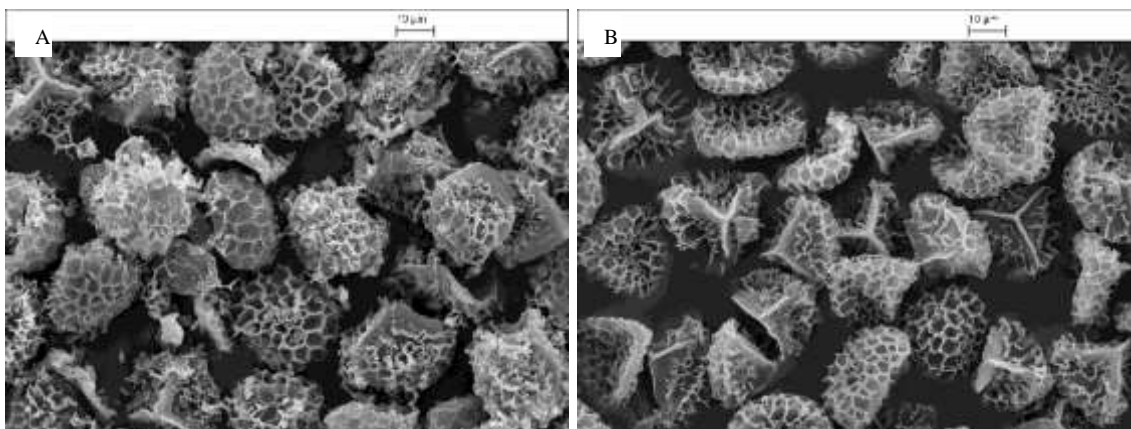


Figure 5.2 (A) SEM images of iron(II) chloride with BR-SECs, (B) SEM images of iron(II) chloride with BL-SECs.

Figure 5.3 again shows a difference between the SEM images of iron(III) chloride with the BR-SECs compared with BL-SECs. The image of iron(III) chloride with BR-SECs (Figure 5.3A) shows spores which are broken and flat and some that have burst slightly or become distorted. In contrast, whilst some small fragments can be seen in the image of iron(III) chloride with BL-SECs (Figure 5.3B), many of the SECs have remained intact.

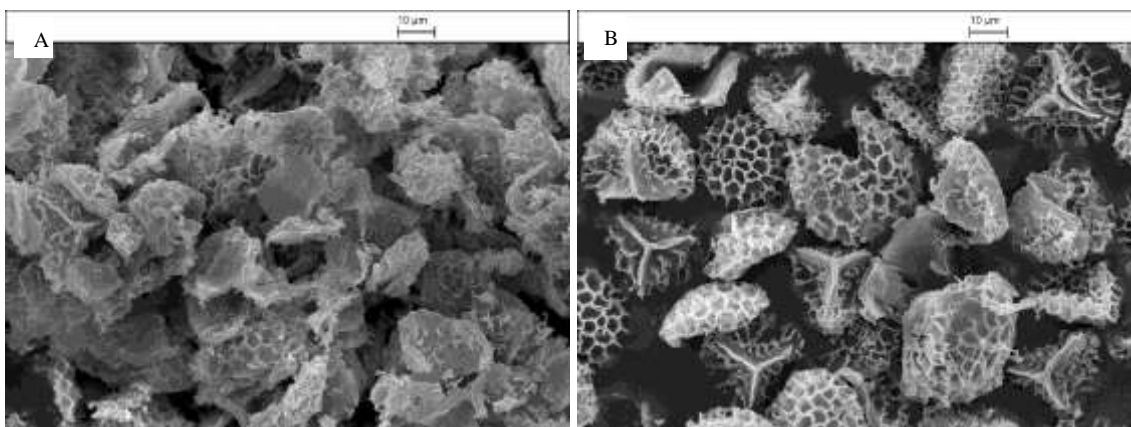


Figure 5.3 (A) SEM images of iron(III) chloride with BR-SECs, (B) SEM images of iron(III) chloride with BL-SECs.

Figure 5.4 shows a clear difference between the SEM images of the attachment of iron(II) acetate to the surface of BR-SECs compared to BL-SECs. Debris is visible around the SEC spores in the SEM image of iron(II) acetate with BR-SECs (Figure 5.4A). Whilst some of the SECs remain intact, some have burst slightly or become distorted. The SEM image of iron(II) acetate with BL-SECs (Figure 5.4B) however clearly shows the almost spherical shape of the microcapsules, verifying that the sporopollenin particles were not damaged during the binding process with iron(II) acetate.

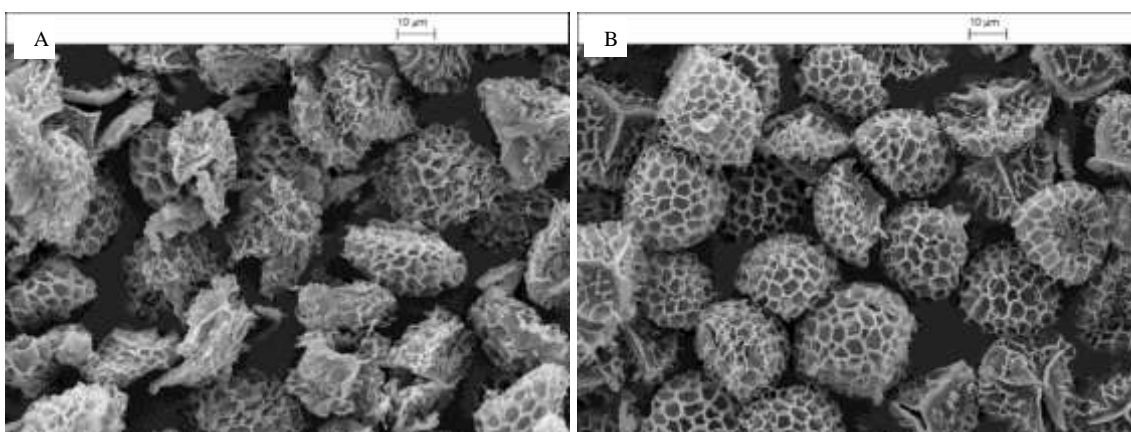


Figure 5.4 (A) SEM images of iron(II) acetate with BR-SECs, (B) SEM images of iron(II) acetate with BL-SECs.

The SEM images of ammonium iron(II) sulfate attached to BR-SECs and BL-SECs again show a visible difference between the two SECs (Figure 5.5). Tiny granules can be seen scattered on the surface of the BR-SECs (Figure 5.5A), with high fragmentation and bursting visible around the SECs. The SEM image of ammonium iron(II) sulfate with BL-SECs (Figure 5.5B) show that many of the SECs have remained intact, with only small fragments visible around the spores.

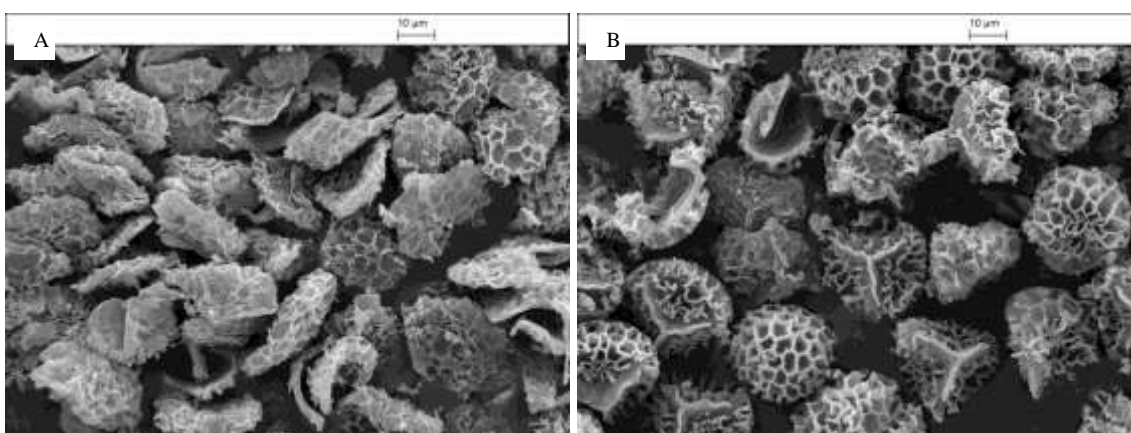


Figure 5.5 (A) SEM images of ammonium iron(II) sulfate with BR-SECs, (B) SEM images of ammonium iron(II) sulfate with BL-SECs.

There is a clear difference between the SEM images of the attachment of ammonium iron(III) sulfate to the surface of BR-SECs compared to BL-SECs (Figure 5.6). Figure 5.6A shows substantial bursting and damage in the SEM image of ammonium iron(III) sulfate with BR-SECs. In contrast, the SEM image of ammonium iron(III) sulfate with BL-SECs (Figure 5.6B) illustrates the almost spherical shape of the microcapsules whilst some have been flattened, some of the spores remain intact.

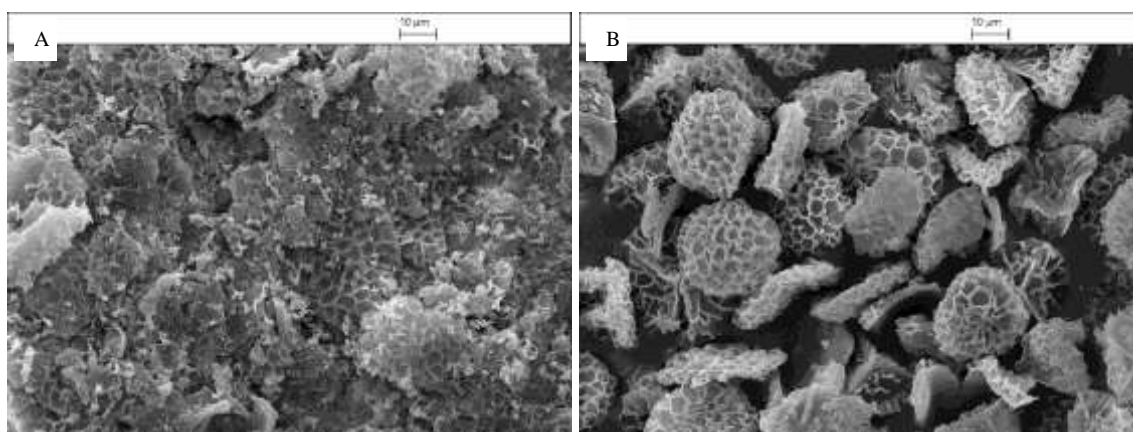


Figure 5.6 (A) SEM images of iron(III) sulfate with BR-SECs, (B) SEM images of iron(III) sulfate with BL-SECs.

In conclusion, with all of the different iron-SEC complexes, there was much greater damage when BR-SECs were used than BL-SECs.

5.5 Spectroscopic studies

Various spectroscopies were used to study the Fe-SEC complexes: UV–vis spectroscopy was used to identify the presence of metals and their mode of coordination into Fe-SEC complexes; vibrational spectroscopy was used to examine the functional groups present and the structure of the SECs; X- ray absorption and Mössbauer spectroscopies were used to investigate the structure of the microcapsules.

5.5.1 Identification of metal coordination environment within sporopollenin using electronic absorption spectroscopy (UV – visible - NIR)

The complexes of transition metals, particularly in different oxidation states, exhibit distinctive colours. When the oxidation state changes, the metal complexes can alter their colour, as is the case with green iron(II) compounds, which become brown in the corresponding iron(III) compound. This change is related to the change in the d-electrons of the metal centre of the complex, which change when the oxidation state changes. The energy in the ultraviolet and visible light spectra excites the electrons in complex ions and molecules. An absorption spectrum is normally obtained when the full range of wavelengths of UV–vis radiation is passed through a sample. The absorption levels of the metals are shown as a display of different colours according to the different types of metals. The graph figures in the experiment show the spectra for the different metal samples as

they absorb visible light. This gives the horizontal axis in a UV–vis spectrum wavelength in cm^{-1} and the vertical axis of a UV–vis spectrum, showing the extent of the absorption.

When SECs are mixed with iron salts, the d-electrons of these complexes contribute to the production of different colours. Hence UV-visible spectroscopy may be used to identify the coordination environment of iron within SECs. Iron salts may be attached to SECs by functional groups such as phenol and carboxylate. For this study, UV-visible spectra of iron salts with bleached SECs were determined on samples prepared with 7.5 mmol:300 mg iron: SEC. The complementary samples prepared using brown sporopollenin were not examined using UV-vis.

Figure 5.7 shows the different results of the UV–vis spectroscopy for different iron salt-SEC complexes from 5000 to 50000 cm^{-1} . By analysing the results presented above, it is possible to divide the UV-vis absorption spectra into two parts: from 5000 to 25000 cm^{-1} , which comprises the bands characteristic of d-d transitions in the Fe(II) (d^6) metal ions, and from 25000 to 50000 cm^{-1} , which is the region where the absorptions $n-\pi^*$ and $\pi-\pi^*$ arising from the SEC functional groups appear. The ammonium iron(II) sulfate-SEC complex has the highest intensity peak in the SEC functional group region and the iron(III) chloride has the lowest.

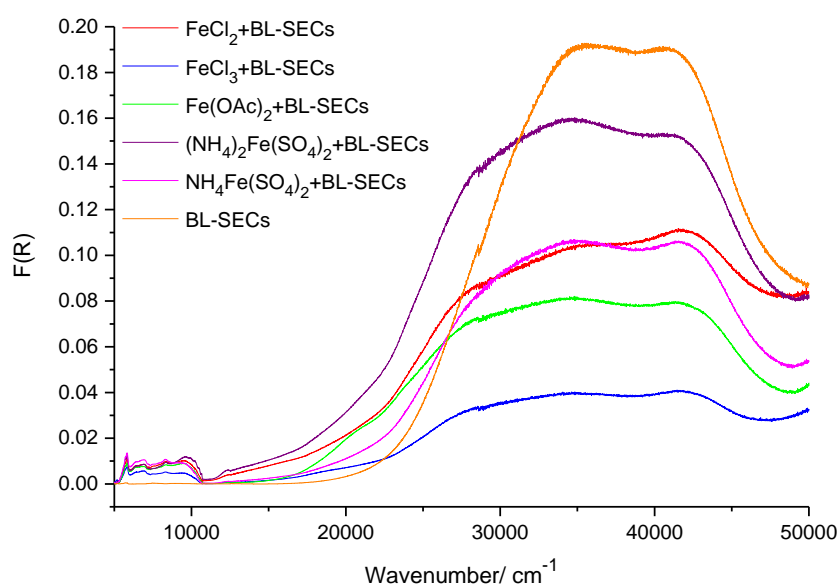


Figure 5.7 UV–vis spectra for iron salts with bleached SECs.

Many iron complex salts produce quite similar absorption patterns, and slightly different maximum absorbance wavelengths. All iron-SEC complexes presented a distinctive d-d band centred at 12780 cm^{-1} (Figure 5.8), which absorbs in the red part of the visible region, giving them their characteristic blue-green colour. This is typical of octahedral iron(II) complexes with an oxidation state of +2, with a co-ordination number of 6, which are reported to have absorption in the $14200\text{--}12800\text{ cm}^{-1}$ range.¹⁸¹ It can be seen that peak in the Fe(III) mean their oxidation state has been changed by adsorption to the SECs. The weak bands at ca. 5500 and 11000 cm^{-1} are most likely due to overtone and a combination bands in the SEC. Iron samples with SECs are shifted to low energy.

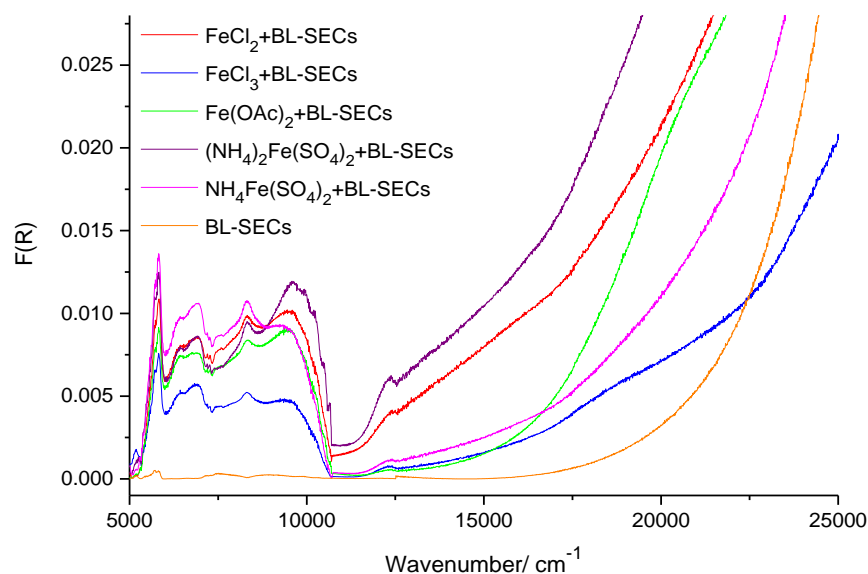


Figure 5.8 Expanded from 5000 to 25000 cm^{-1} of the UV-vis experiment for iron salts with bleached SECs.

The complementary samples prepared using brown sporopollenin were not examined using UV-vis.

5.5.2 Vibrational spectroscopic identification of functional groups in sporopollenin

5.5.2.1 Infrared spectroscopy (IR)

IR spectroscopy was used to identify the functional groups involved in the binding of iron-salts to sporopollenin. For this study, IR spectra of iron salts with bleached and brown SECs were determined on samples with a loading of 7.5 mmol:300 mg iron: SEC.

All the iron salt-SEC complexes for both brown and bleached SECs have similar IR spectra Figure 5.9 and Figure 5.10. The peak characteristic of carbonyl stretching is at 1712 cm^{-1} for the BR-SEC complexes and at 1720 cm^{-1} for the BL-SEC complexes. This is consistent with the conversion of C=O, carboxylic acids. The broad peak around 3300 cm^{-1} in the both BR-SEC complexes and the BL-SEC complexes can be assigned to the O–H group. The peak around 2800 cm^{-1} to 2950 cm^{-1} is from the aliphatic CH and the peak around 1137 cm^{-1} could be attributed to the presence of ether groups. In conclusion, IR spectroscopic data supports the hypothesis that the iron salts are attached to both brown and bleached SECs.

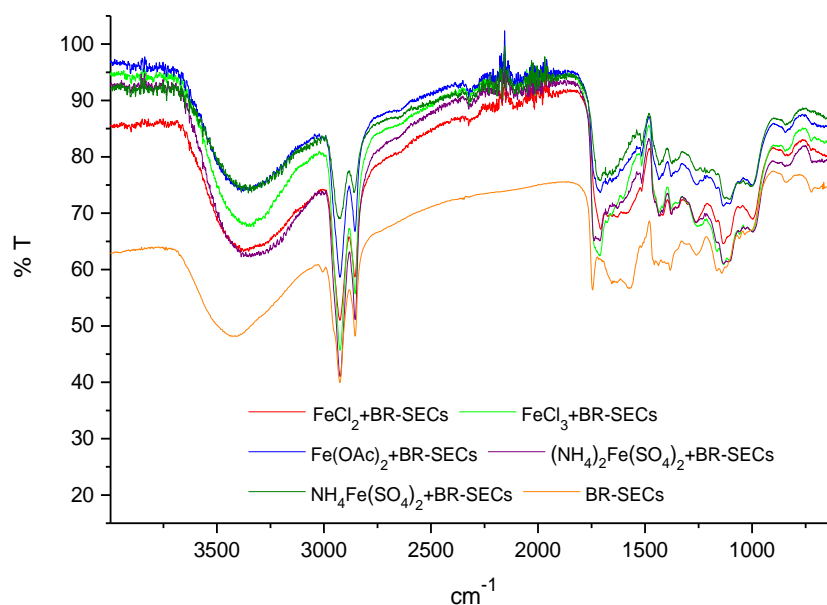


Figure 5.9 IR spectroscopy results for iron salts with BR-SECs.

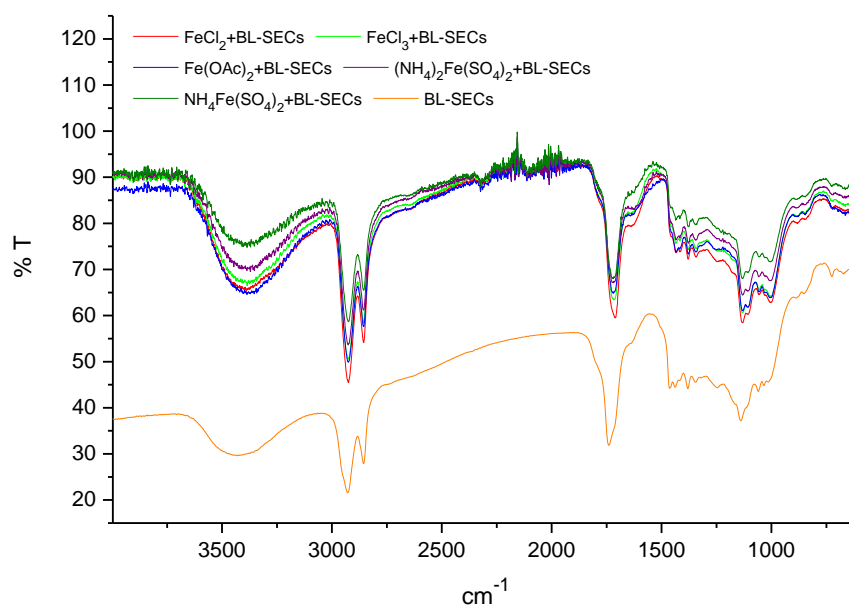


Figure 5.10 IR spectroscopy results for iron salts with BL-SECs.

5.5.3 X- Ray absorption spectroscopy

The aim of these X-ray absorption experiments was to identify the oxidation state of the iron and the mode of coordination of the iron to the surfaces of the SECs so that the type and number of the surface binding groups could be identified. Whilst the expectation is that octahedral coordination to O-donor ligands will be favoured for the 3d transition elements, these XANES and EXAFS experiments will confirm the oxidation state and structural motif. This information is vitally important in assessing these materials for drug delivery, metal remediation and other applications.

To provide enough sample for these experiments, the protocol was modified to use 7.5 mmol of the iron salt and 300 mg of BL-SECs and BR-SECs. In line with previous experiments,¹⁰¹ the samples were stirred for three days, and filtered, both under argon using Schlenk techniques.

Bulk Fe K-edge XANES and EXAFS experiments were collected in transmission mode at the Diamond Light Source using the B18 beamline.

The XAS spectra were calibrated using the first maximum in the first derivative spectrum of an iron foil (7112.0 eV). The edge positions in the XANES spectra were defined as the

energy corresponding to a normalised absorbance of 0.5. The Figure 5.11 below shows the Fe K-edge XANES data for $(\text{NH}_4)_2\text{Fe(II)}(\text{SO}_4)_2 \cdot 6\text{H}_2\text{O}$ and $(\text{NH}_4)\text{Fe(III)}(\text{SO}_4)_2 \cdot 12\text{H}_2\text{O}$, which are really best thought of as $[\text{Fe}(\text{H}_2\text{O})_6](\text{NH}_4)_2(\text{SO}_4)_2$ and $[\text{Fe}(\text{H}_2\text{O})_6](\text{NH}_4)(\text{SO}_4)_2 \cdot 6\text{H}_2\text{O}$, respectively. Both of these compounds contain octahedral iron, surrounded by six water ligands.^{200, 201}

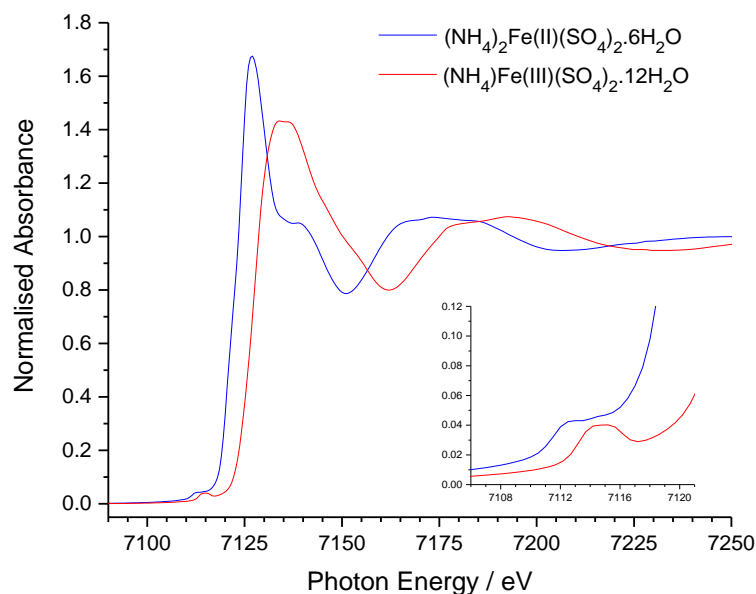


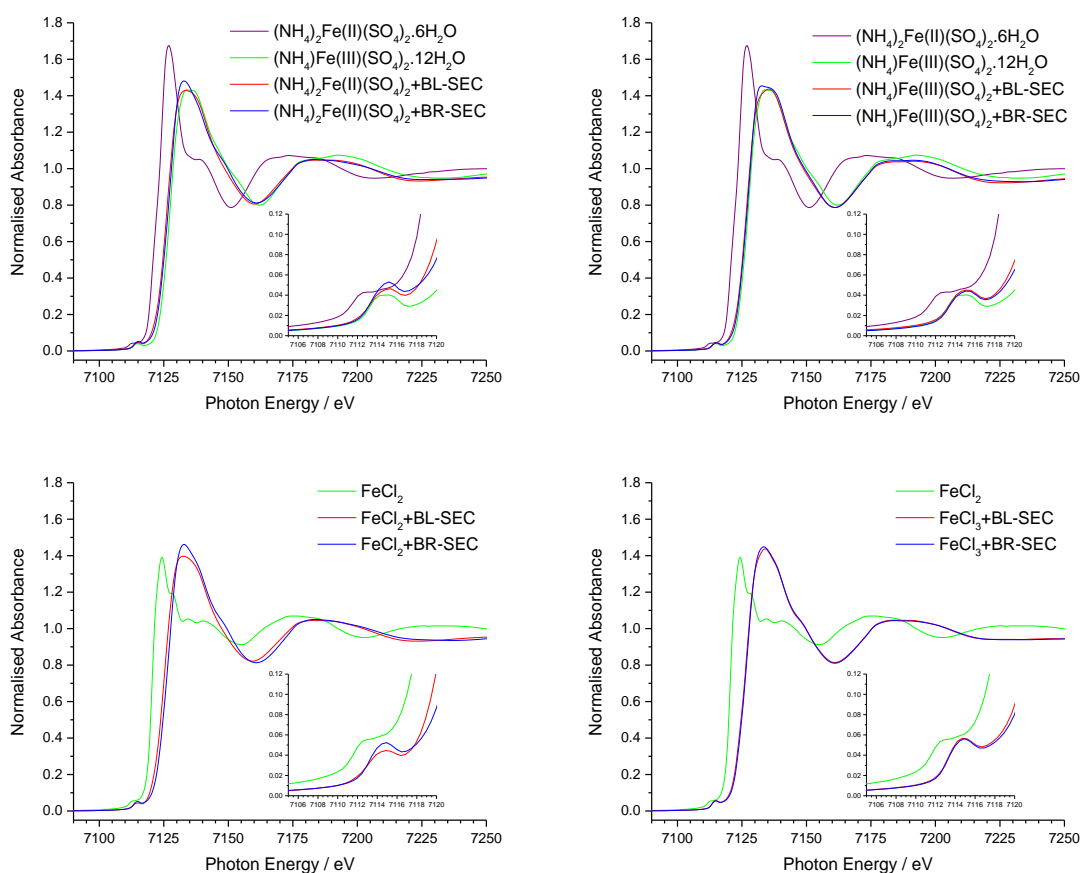
Figure 5.11 Fe K-edge XANES data for ammonium iron(II) sulfate and ammonium iron(III) sulfate.

The spectra indicate the differences in the Fe K-edge XANES spectra of Fe(II) and Fe(III) compounds. As expected the 7120.8 eV edge position in $(\text{NH}_4)_2\text{Fe(II)}(\text{SO}_4)_2 \cdot 6\text{H}_2\text{O}$ moves to higher energy, 7125.8 eV, in $(\text{NH}_4)\text{Fe(III)}(\text{SO}_4)_2 \cdot 12\text{H}_2\text{O}$. The position of the 1s – 3d pre-edge features at 7112.7 and 7114.6 eV for $(\text{NH}_4)_2\text{Fe}(\text{SO}_4)_2 \cdot 6\text{H}_2\text{O}$ are in good agreement with the previous study.²⁰² For $(\text{NH}_4)\text{Fe}(\text{SO}_4)_2 \cdot 12\text{H}_2\text{O}$ the peak at 7114.8 eV in Figure 5.11 was resolved into two features at 7113.9 and 7115.4 eV in the previous detailed study of Fe K-edge XANES spectra in a wide variety of compounds.²⁰²

There is some previous work by Archibald et al.¹⁰¹ on the interaction of iron with SECs using X-ray absorption study. Fe K-edge XANES data provide some information about the oxidation state and coordination environment of the iron coordinated to the SEC surface. The edge position is very sensitive to oxidation state and is at higher energies for higher oxidation states. The pre-edge peaks are often labelled 1s - 3d, and are also sensitive to oxidation state. These can be used diagnostically to identify different coordination geometries because of the selection rules. The 1s - 3d transitions are orbitally forbidden,

but the pre-edge peaks have some intensity due to quadrupole transitions, as well as relaxation of the Laporte and orbital selection rules.²⁰²

Figure 5.12 below shows the Fe K-edge XANES data for ammonium iron(II) sulfate, ammonium iron(III) sulfate, iron(II) chloride, iron(III) chloride and iron(II) acetate adsorbed onto both bleached and brown SECs. The Figures show the spectra from iron salts in the brown and bleached SECs to identify the oxidation states and coordination geometry. The iron is in an octahedral environment in all the Fe(II) and Fe(III) samples. The Fe K-edge XANES spectra of the ammonium sulfate alums in Figure 5.12 displayed a shift of ca. 5 eV in the edge position between the two oxidation states (7120.8 eV (Fe(II)) and 7125.8 eV (Fe(III))). Moreover, it can be identified from the remaining spectra in Figure 5.12 that all of the SEC samples contain iron(III), whether or not the initial salt contained iron (II) or iron(III). A similar situation was also found in the earlier work by Archibald et al.,¹⁰¹ even when very stringent precautions were taken to exclude air. The Fe- K-edge XANES spectra of the samples prepared from BR-SEC and BL-SEC with iron acetate are identical, as are those prepared from FeCl₃. However, there are subtle variations in the XANES spectra samples prepared from FeCl₂, and the two alums.



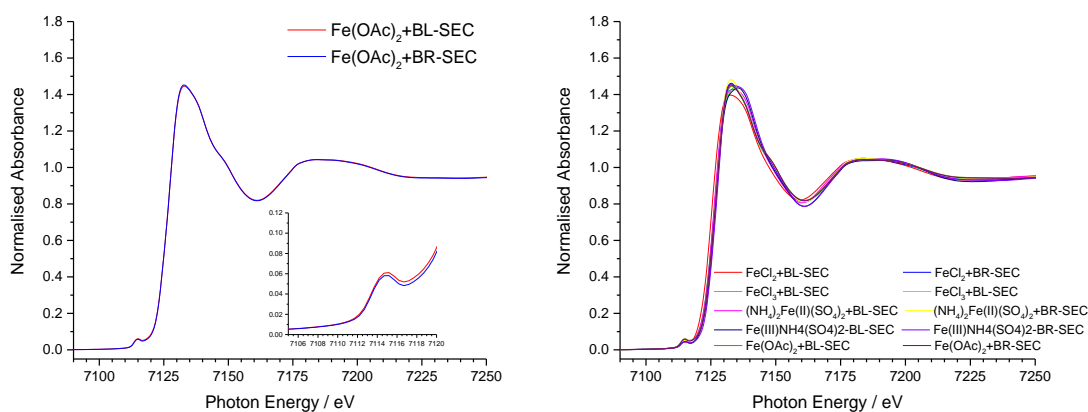


Figure 5.12 Fe K-edge XANES data for BL-SECs and BR-SECs reacted with ammonium iron(II) sulfate, ammonium iron(III) sulfate, iron(II) chloride, iron(III) chloride and iron(II) acetate solutions.

The Fe K-edge EXAFS analyses of ferrous and ferric ammonium sulfates are shown in Figure 5.13. As there are no significant features in the FTs beyond the first shell, a single shell fit was used and the refined parameters are given in Table 5.6. The single crystal X-ray diffraction data shows that in both $(\text{NH}_4)_2\text{Fe}(\text{SO}_4)_2 \cdot 6\text{H}_2\text{O}$ and $(\text{NH}_4)\text{Fe}(\text{SO}_4)_2 \cdot 12\text{H}_2\text{O}$, the iron is in an octahedral environment with average Fe-O bond lengths of 2.125 \AA ,²⁰¹ and 1.939 \AA ,²⁰⁰, respectively. The spread of distances is from 2.087 to 2.155 \AA for $[\text{Fe}(\text{H}_2\text{O})_6](\text{NH}_4)_2(\text{SO}_4)_2$ and 1.917 to 1.959 \AA for $[\text{Fe}(\text{H}_2\text{O})_6](\text{NH}_4)(\text{SO}_4)_2 \cdot 6\text{H}_2\text{O}$. The refined iron oxygen bond length in $[\text{Fe}(\text{H}_2\text{O})_6](\text{NH}_4)_2(\text{SO}_4)_2$ is 2.121 \AA and for Fe(III) ammonium sulfate $[\text{Fe}(\text{H}_2\text{O})_6](\text{NH}_4)(\text{SO}_4)_2 \cdot 6\text{H}_2\text{O}$ it is 1.994 \AA , with Debye-Waller factors ($2\sigma^2$) of $0.0188(10)$ and $0.0126(7) \text{ \AA}^2$, respectively. The EXAFS derived bond length for $[\text{Fe}(\text{H}_2\text{O})_6](\text{NH}_4)_2(\text{SO}_4)_2$ is in very good agreement with the single crystal X-ray data, although there is a discrepancy with the $[\text{Fe}(\text{H}_2\text{O})_6](\text{NH}_4)(\text{SO}_4)_2 \cdot 6\text{H}_2\text{O}$ value, it is still within reasonable agreement. In the previous work¹⁰¹ using ferrous acetate and basic ferric acetate, Fe-O distances of 2.016 and 2.133 \AA were found for Fe(II) and Fe(III), respectively. Both the alum and the acetate values provide markers for the Fe-O bond lengths expected for Fe(II) and Fe(III) in the SEC complexes. The static disorder in these complexes is fairly small, 2.087 to 2.155 \AA for $[\text{Fe}(\text{H}_2\text{O})_6](\text{NH}_4)_2(\text{SO}_4)_2$ ²⁰¹ and 1.917 to 1.959 \AA for $[\text{Fe}(\text{H}_2\text{O})_6](\text{NH}_4)(\text{SO}_4)_2 \cdot 6\text{H}_2\text{O}$,²⁰⁰ indicating a fairly regular octahedral environment, and this is reflected in the relatively small Debye-Waller factors of 0.0188 and 0.0126 \AA^2 , respectively.

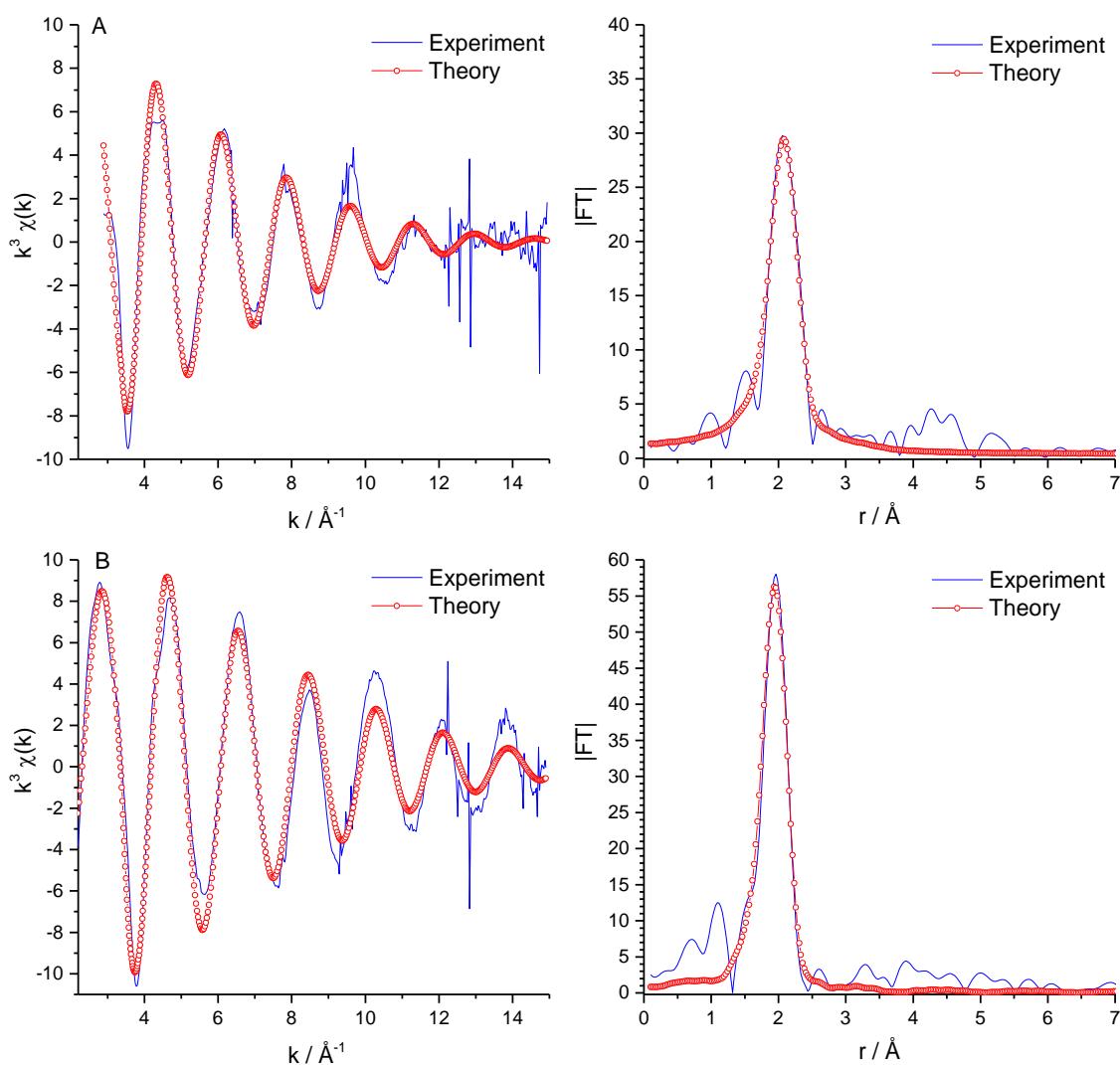


Figure 5.13 Fe K-edge EXAFS (left) and FTs (right) for (A) ammonium iron(II) sulfate, (B) ammonium iron(III) sulfate.

Sample	Fe-O ₆		E _f /V	FI	R
	r/Å	2σ ² /Å ²			
(NH ₄) ₂ Fe(II)(SO ₄) ₂ ·6H ₂ O	2.121(5)	0.0188(10)	-10.24(4)	0.45	32.83
(NH ₄)Fe(III)(SO ₄) ₂ ·12H ₂ O	1.994(4)	0.0126(7)	-13.9(3)	0.23	28.9

Table 5.6 Fe K-edge EXAFS data of ammonium iron(II) sulfate, ammonium iron(III) sulfate.

The EXAFS analysis of the alum model compounds used a single shell of six oxygen atoms in the first coordination shell. As it is important to know the Fe-O coordination number in the SEC samples the relationship between the R factor (measure of goodness of fit) and the coordination number (CN) was determined for coordination numbers from 1 to 8 for all of the samples, and these are shown in Figure 5.14 below.

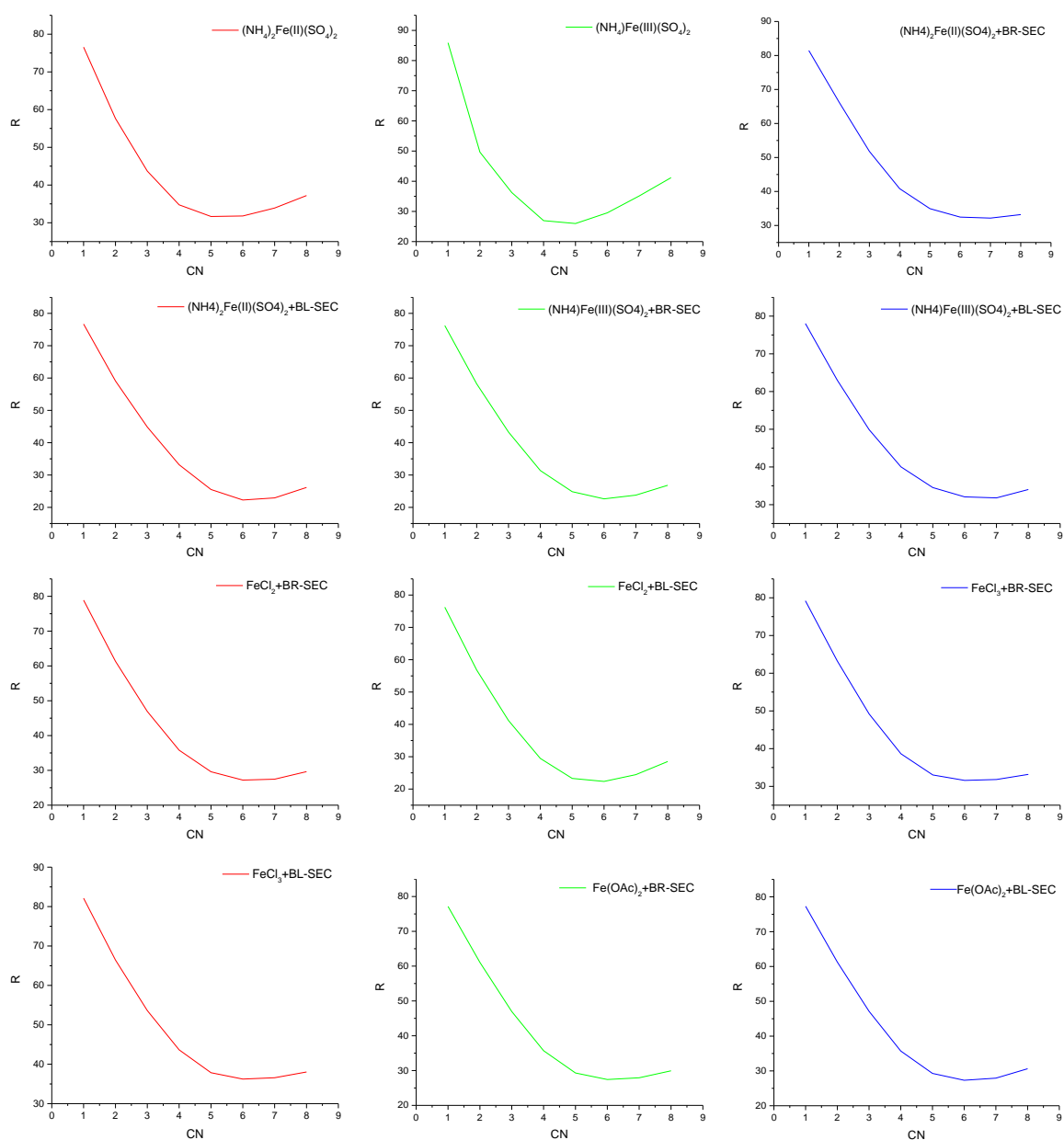


Figure 5.14 Plots of R (goodness of fit) vs. CN (coordination number) for all iron samples.

The minimum for the alum samples is between a coordination number of five and six, whilst the minimum for the SEC samples appears to be slightly higher, it is clear that the coordination number is very similar in all of these. On this basis the EXAFS analysis used a first shell coordination environment to six oxygen atoms.

The previous Fe K-edge XAFS study of SECs prepared using aqueous ferric and ferrous chloride solutions and which were extensively air-dried showed that the local iron environment was similar to ferrihydrite (FeOOH).¹⁰¹ When ferrous chloride solutions were used under inert conditions, there was still extensive oxidation to Fe(III), but the longer range interactions were much reduced, indicating smaller particle sizes, or more disorder

in the local iron environment. As the Fe K-edge spectra of the samples prepared in this work Figure 5.15 were very similar to those obtained previously, the model developed for the smaller, more disordered particles involving a first coordination shell of six oxygen atoms, together with two more distant Fe...Fe₃ interactions at *ca.* 3.0 and 3.4 Å, was used as a starting point for all the samples. The Debye-Waller factors (and the uncertainty in them) were used as a guide to the coordination number, rather than refining the coordination number.

EXAFS data were obtained for all iron salts samples with bleached and brown SECs. The structure of iron contains a range of Fe-O distances and Fe...Fe distances. Figure 5.15 and Figure 5.16 show Fe K-edge EXAFS and FT data recorded on B18 of iron salts adsorbed onto both bleached and brown SECs.

All of the Debye-Waller factors associated with the first Fe-O shell are very similar, apart from those of (NH₄)Fe(III)(SO₄)₂, which are lower (0.0180(9) and 0.0172(6)), and the same for both the BR-SEC and BL-SEC. This is reflected in the FTs, where the first peak has an intensity of *ca.* 35 for all of the samples apart from the (NH₄)Fe(III)(SO₄)₂ for both BR-SEC and BL-SEC where the intensity is *ca.* 40. The Fe-O distance of *ca.* 2.00 Å is very similar in all cases indicating a similar coordination environment, and is consistent with the presence of Fe(III) rather than Fe(II). This is also consistent with the Fe K-edge XANES and ⁵⁷Fe Mössbauer spectra (see below). Although the similar Fe-O distances indicate a similar coordination environment, there are subtle differences in the Debye-Waller factors for the first shell. The majority are *ca.* 0.022 Å², apart from those for the SEC samples derived from [Fe(H₂O)₆](NH₄)(SO₄)₂.6H₂O which are significantly lower, indicating a more ordered Fe-O environment in these materials.

For the BR-SEC the FTs are very similar for all of the salts indicating a very similar structure, apart from the (NH₄)Fe(III)(SO₄)₂ sample, where the intensity of the Fe...Fe interactions are much weaker.

For the BL-SECs, the FTs of the FeCl₂, and both of the ammonium sulfate samples are very similar. That of the FeCl₃ SECs resembles the BR-SEC, and has the largest Fe...Fe peaks. The Fe(OAc)₂ SECs data is intermediate and more closely resembles that of the BR-SEC.

The features due to the Fe...Fe interactions around 3 Å were refined using the same model as used by Archibald et al.¹⁰¹, with the Debye-Waller factor being used as an indicator of coordination number. Large values indicate lower coordination numbers and/or higher levels of disorder than smaller values. The features present in the FTs at 3 Å, together with the features in the EXAFS at 8 – 10 Å⁻¹ fall into three categories. Those for the BL-SEC and BR-SEC samples prepared from FeCl₃ solutions show a clear dip in the EXAFS at 8.5 Å⁻¹ and have the most intense Fe...Fe interactions, with the smallest Debye-Waller factors. They are also the most similar to those for FeCl₃ data reported previously which were extensively air-dried.¹⁰¹ The data for the BR-SEC sample prepared with [Fe(H₂O)₆](NH₄)₂(SO₄)₂ also belongs to this group. In the EXAFS spectra of the BL-SEC and BR-SEC samples prepared with iron acetate, and the BR-SEC sample prepared with FeCl₂ the dip at 8.5 Å is replaced by an inflection, and the peaks in the FT are weaker, and similar to those prepared using FeCl₂ under inert atmospheres.¹⁰¹ The third set of data comprises the BR-SEC and BL-SEC samples prepared using [Fe(H₂O)₆](NH₄)(SO₄)₂.6H₂O, and the BL-SEC samples prepared with FeCl₂, and [Fe(H₂O)₆](NH₄)₂(SO₄)₂ where the EXAFS is almost a single damped sine wave, and the 3 Å features are very weak, and are associated with large Debye-Waller factors, indicating a low Fe...Fe coordination number or very high disorder.

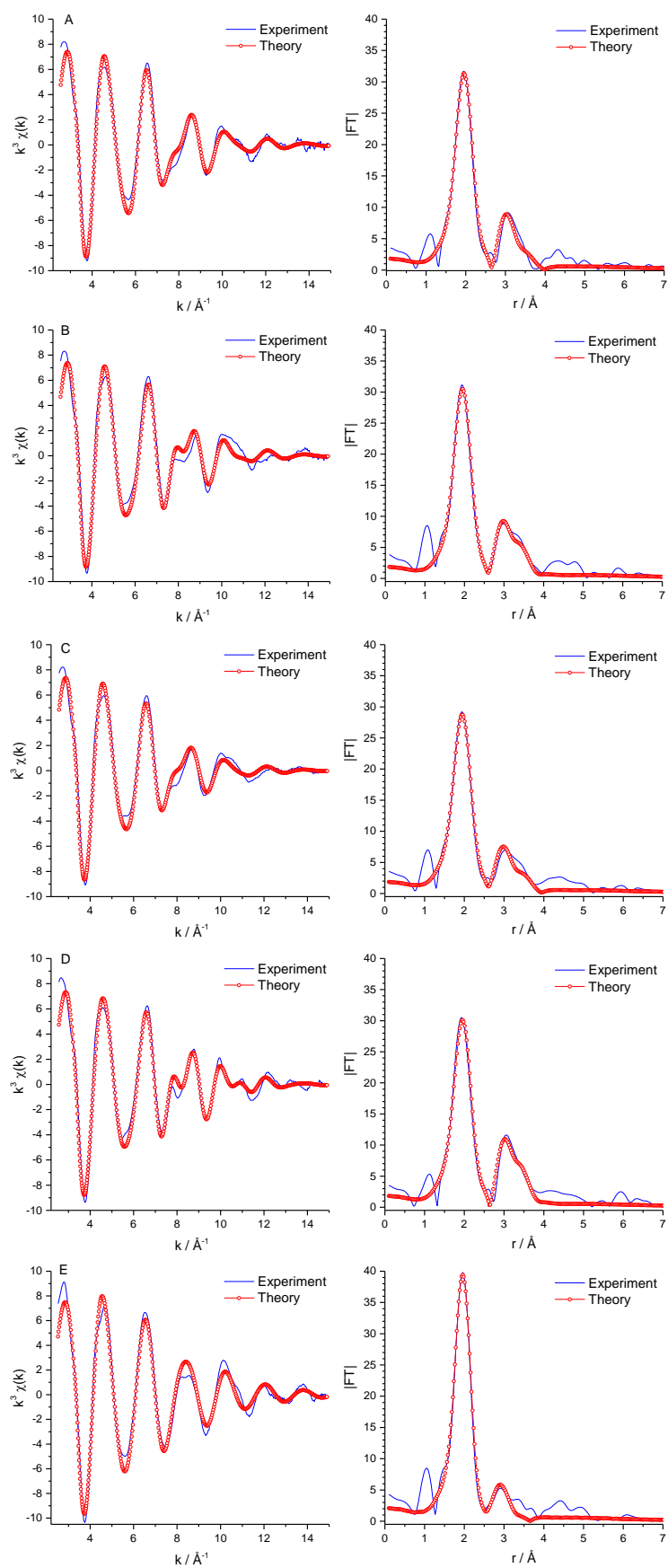


Figure 5.15 Fe K-edge EXAFS (left) and FTs (right) for BR-SEC with (A) iron(II) chloride, (B) iron(III) chloride, (C) iron(II) acetate, (D) ammonium iron(II) sulfate, (E) ammonium iron(III) sulfate.

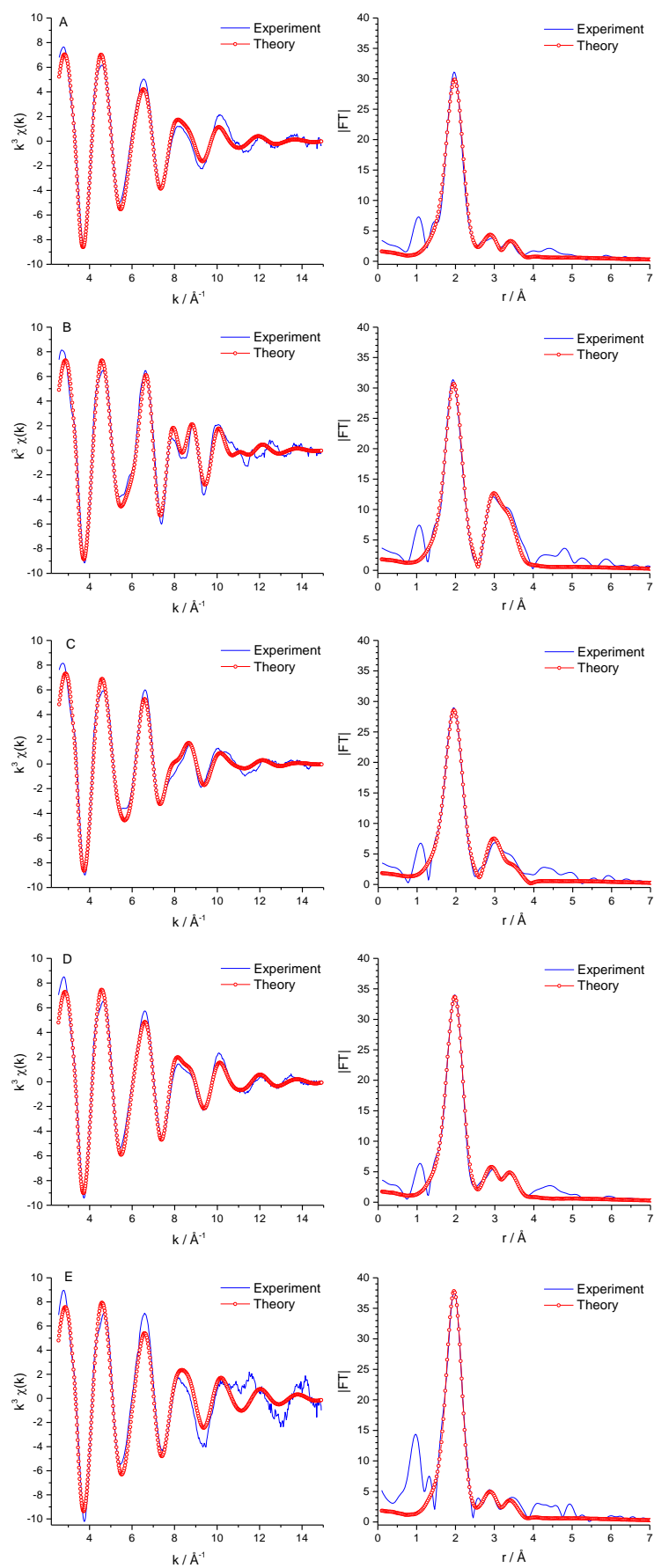


Figure 5.16 Fe K-edge EXAFS (left) and FTs (right) for BL-SEC with (A) iron(II) chloride, (B) iron(III) chloride, (C) iron(II) acetate, (D) ammonium iron(II) sulfate, (E) ammonium iron(III) sulfate.

Sample	Fe-O ₆		Fe-Fe ₃		Fe-Fe ₃		E _f /V	FI	R
	r/Å	2σ ² /Å ²	r/Å	2σ ² /Å ²	r/Å	2σ ² /Å ²			
(NH ₄) ₂ Fe(II)(SO ₄) ₂ ·6H ₂ O+ BL-SEC	2.01 4(3)	0.0203(6)	3.002(15)	0.043 (43)	3.319(13)	0.035(34)	- 13.9 (2)	0.1 1	17. 8
(NH ₄) ₂ Fe(II)(SO ₄) ₂ ·6H ₂ O+ BR-SEC	2.00 3(4)	0.0234(8)	3.036(8)	0.028 (22)	3.354(11)	0.030(32)	- 13.7 (3)	0.1 7	20. 7
FeCl ₂ BL-SEC	2.02 4(3)	0.0229(6)	3.020(21)	0.050 (59)	3.332(19)	0.041(50)	- 13.3 (3)	0. 13	20. 3
FeCl ₂ BR-SEC	2.00 5(3)	0.0223(7)	3.047(10)	0.032 (23)	3.397(39)	0.061(3)	- 13.6 (3)	0.1 4	19. 7
Fe(OAc) ₂ BL-SEC	2.00 0(4)	0.0248(8)	3.015(12)	0.036 (31)	3.366(29)	0.052(98)	- 13.6 (3)	0.1 7	21. 8
Fe(OAc) ₂ BR-SEC	1.99 9(4)	0.0246(8)	3.022(12)	0.036 (32)	3.379(30)	0.053(11)	- 13.6 (3)	0.1 7	21. 9
(NH ₄)Fe(II)I(SO ₄) ₂ ·12H ₂ O+ BR-SEC	2.00 6(5)	0.0180(9)	3.001(35)	0.047 (102)	3.322(35)	0.049 (3)	- 14.1 (4)	0.2 9	31. 1
(NH ₄)Fe(II)I(SO ₄) ₂ ·12H ₂ O+ BR-SEC	2.00 4(3)	0.0172(6)	2.987(18)	0.040 (49)	3.252(51)	0.061(16)	- 14.3 (3)	0.1 4	20. 7
FeCl ₃ BLSEC	2.00 4(4)	0.0228(8)	2.990(8)	0.027 (21)	3.338(10)	0.029(31)	- 13.7 (3)	0.1 9	24. 0
FeCl ₃ BR-SEC	2.00 0(4)	0.0231 (8)	3.011(11)	0.032 (29)	3.349(16)	0.036(47)	- 13.6 (3)	0.1 9	24. 3

Table 5.7 Fe K-edge EXAFS data of all iron solutions with BL and BR-SECs.

From all iron salts with bleached and brown SECs the Fe K-edge XANES show that iron is present as Fe(III) in an octahedral environment. The Fe K-edge EXAFS data confirmed that the local environment around the iron is octahedral and the Fe-O distances are consistent with Fe(III). The Fe...Fe distances with low coordination numbers indicating small clusters.

5.5.4 Mössbauer spectroscopy

Mössbauer spectroscopy probes tiny changes in the energy levels of an atomic nucleus in response to its environment.²⁰³ It has been used to predict the oxidation and spin states of iron(III) and iron(II) compounds, including porphyrin derivatives.²⁰³ Data were collected over 512 channels, which were then folded to produce 256 unique channels. The isomer shift (δ) and quadrupole splitting (ΔE_Q) values were obtained by fitting these data to a set of two Lorentzian pairs. In the following figures, the experimental data is represented by + signs and the solid lines were simulated computationally by varying ΔE_Q and δ .

Mössbauer spectra of four model iron compounds were analysed at temperatures ranging acquired at 80 K, and these are shown in Figure 5.17. These compounds represented different spin and oxidation states of iron: $K_3[Fe(CN)_6]$, low-spin Fe(III); $Fe_2(SO_4)_3 \cdot nH_2O$, high-spin Fe(III); $K_4[Fe(CN)_6] \cdot 3H_2O$, low-spin Fe(II); and $(NH_4)_2Fe(SO_4)_2 \cdot 6H_2O$, high-spin Fe(II). Only the spectra taken at 80 K are shown in Figure 5.17 as the values of ΔE_Q and δ changed little with temperature. The small temperature variation is indicative of the lack of low-lying excited states.

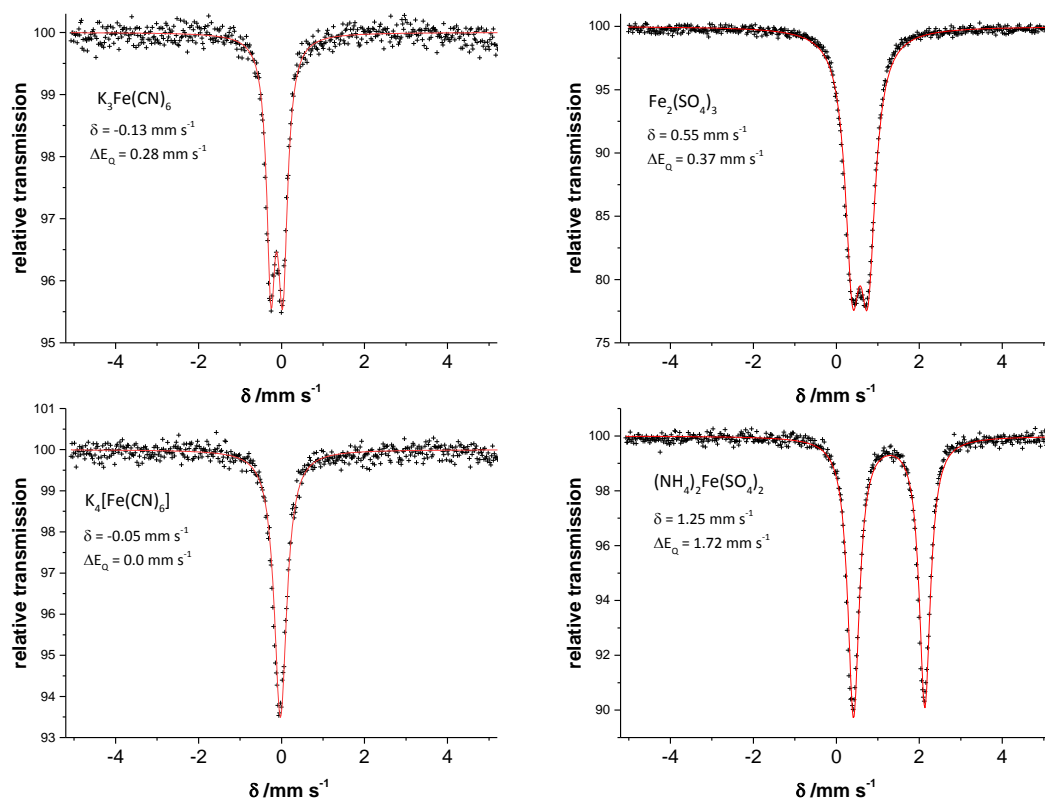


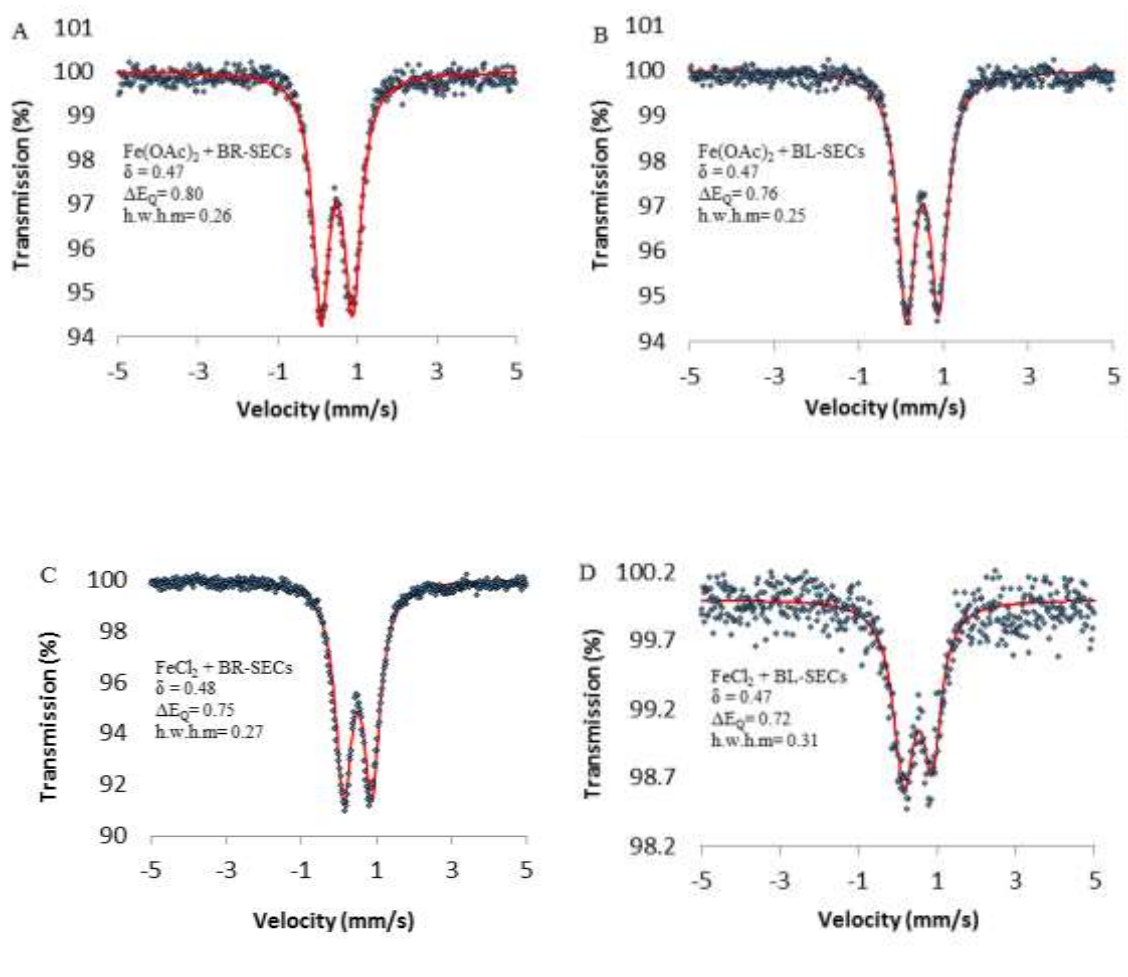
Figure 5.17 Illustrative ^{57}Fe Mössbauer spectra of high- and low- spin iron (II) and iron(III) complexes at 80 K.

For ^{57}Fe , increasing electron density at the nucleus results in a decrease in the isomer shift due to the negative $\Delta R/R$. Hence an increase in oxidation state (e.g.: Fe(II) to Fe(III)) and an increase in ligand donation will both give rise to a decrease in the isomer shift (lower, more negative values). The extent of covalency is greater in low-spin complexes compared to high-spin complexes, hence low-spin complexes will have a smaller isomer shift than high-spin complexes. The low-spin cyanide complexes have lower isomer shifts than the high-spin sulfate complexes. As predicted, high-spin Fe(II) has the largest isomer shift (1.25 mm s^{-1}) of the four complexes. However, there was little difference between the isomer shifts of the cyanide complexes.

The quadrupole splitting, ΔE_Q , can also be used to differentiate the spin and oxidation states. Assuming that the complexes are octahedral there will be only a small geometric contribution to the Electric Field Gradient (EFG). A valence electron induced EFG is associated with an E or T ground state term. Assuming an octahedral environment the ground terms are as follows: low spin Fe(III), $^2T_{2g}$; high spin Fe(III), $^6A_{1g}$; low spin Fe(II), $^1A_{1g}$; high spin Fe(II), $^5T_{2g}$. Therefore, for low spin iron(II), there are minimal geometric

and electronic effects to the EFG, hence ΔE_Q is zero. For low-spin iron(III) however there is an electronic contribution to the EFG, hence a larger ΔE_Q is observed. High-spin iron(II) has a large ΔE_Q as predicted. However, the high spin iron(III) has a small ΔE_Q despite the fact that no valence electron EFG is expected, and this may be due to geometric rather than electronic effects.

Figure 5.18 shows the Mössbauer spectra of the five iron salt-SEC complexes iron(II) acetate, iron(II) chloride, iron(III) chloride, ammonium iron(II) sulfate and ammonium iron(III) sulfate for both brown (left side) and bleached (right side) SECs. Unfortunately it was not possible to obtain a spectrum for the $(\text{NH}_4)_2\text{Fe}(\text{SO}_4)_2$ -BL-SEC complex due to low iron loading.



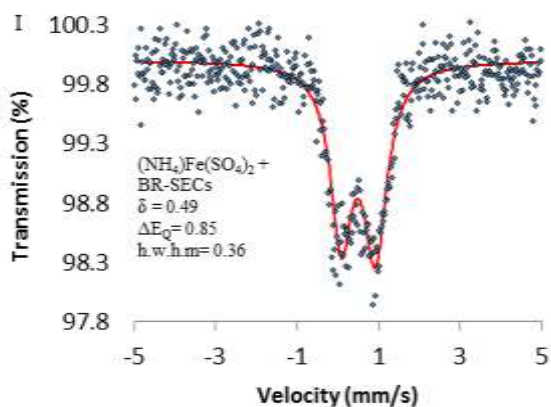
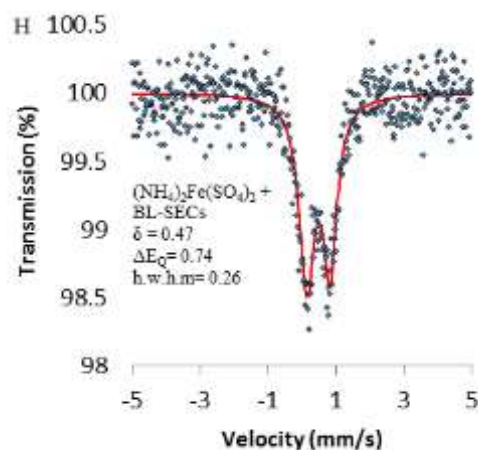
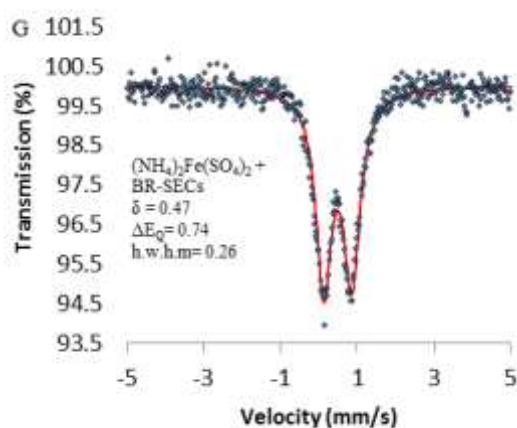
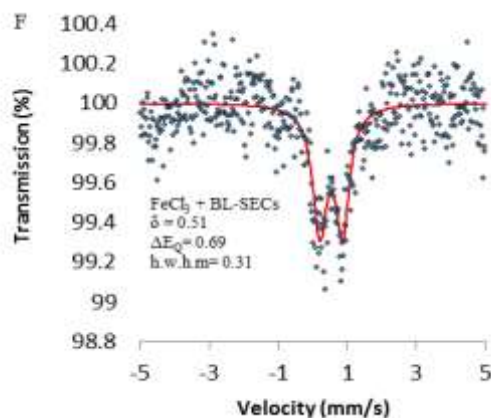
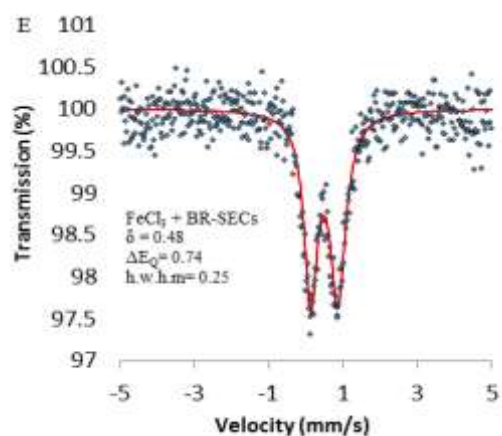


Figure 5.18 The figures on the left show ⁵⁷Fe Mössbauer spectra of iron salts with BR-SEC at 80 K; the figures on the right show ⁵⁷Fe Mössbauer spectra of iron salts with BL-SEC in 80 K .

All the iron-SEC complexes share similar ΔE_Q and δ values for both brown and bleached SECs, which are consistent with the presence of Fe(III) rather than Fe(II). However, lower iron loading of the bleached SECs resulted in noisier spectra compared to the brown SECs.

To conclude the ^{57}Fe Mössbauer spectra show that both the isomer shift and quadrupole splitting indicate the presence of Fe(III) in all of the iron-SEC samples. If the iron(III) was present as a bulk phase of iron oxide or oxyhydroxide a six line pattern would be expected due to magnetic effects. As only quadrupole split doublets are observed, the ^{57}Fe Mössbauer spectra confirm that the iron centres are dilute or any oxide/oxyhydroxide mineral phases are very small.

5.6 Conclusion

A higher iron loading is observed with brown SECs than bleached SECs for all of the iron salts. This may indicate that the bleaching process removes some of the functional groups that are involved in the iron coordination. The SEM images show substantially damage to the surface of the SECs in the brown iron-SEC complexes compared with the BL-SEC complexes.

It is possible to divide the UV-vis absorption spectra into two parts: from 5000 to 25000 cm^{-1} , which comprises the bands characteristic of d-d transitions in the Fe(II) (d^6) metal ions, and from 25000 to 50000 cm^{-1} , which is the region where the absorptions $n-\pi^*$ and $\pi-\pi^*$ arising from the SEC functional groups appear. There were slight differences between all the spectra of the iron-BL-SEC complexes, with the $\text{NH}_4\text{Fe}(\text{SO}_4)_2$ -SEC complex presenting the highest intensity peak.

Furthermore, by applying IR, one can observe the functional groups in the iron-SEC complexes. It was found that the overall features of the SEC IR spectra highlighted the significance of aliphatic chains in the macromolecule. Interpretations are more or less precise depending upon the quality of the spectra, but the prime bands consistently revealed hydroxyls, aliphatic carbons, carbonyls, unsaturated hydrocarbons and ether groups. The spectra for all the samples are similar.

The Fe K-edge XANES spectra of the iron-SEC complexes showed that the iron is present as Fe(III) in all of them. Fe K-edge EXAFS and FT data recorded of iron salts adsorbed onto both bleached and brown SECs show the Fe-O distance is essentially the same in all

of the samples, irrespective of salt or SEC. All of the Debye-Waller factors are very similar, apart from those of $(\text{NH}_4)\text{Fe}(\text{III})(\text{SO}_4)_2$ which are lower (0.018(9) and 0.017(6), and the same for both the BR-SEC and BL-SEC.

Similar ΔE_Q and δ values were obtained from the Mössbauer spectra for both brown and bleached iron-SEC complexes, but the data for bleached iron-SEC complexes was noisier due to lower iron loading. The XANES and Mössbauer data indicate that the iron is present as Fe(III) rather than Fe(II).

The overall conclusion from all of the spectroscopic data is that the iron is present as Fe(III) in all of the samples. This is in contradiction to the reported anti-oxidant properties of SECs.²⁰⁴ One explanation for this is that the iron is finally dispersed on the SEC surface, and therefore the ease of oxidation by aerial oxygen is more facile. However, this does not explain the fact that even when the sample is prepared and handled under rigorous anaerobic conditions, there is still some oxidation of iron(II) to iron (III).¹⁰¹ The presence of phenolic groups in sporopollenin would normally be regarded as anti-oxidant as they can be oxidised to quinones. Previous work has shown that the electrochemical oxidation properties of the SECs are due to the mixture of conjugated phenolic functionalities resulting in either two-electron two- proton, or a two-electron-one-proton processes.¹⁶ Therefore, there is no simple explanation for this behaviour, but it could be a result of radical reactions involving quinone/quinol reactions, or the conjugated polyenes. What is clear is that the iron is very easily oxidised.

The immediate iron environment is essentially the same in all samples, but with some variation in the longer Fe...Fe distances indicating a range of particle sizes. This probably indicates that the iron is not present in the form of isolated octahedral coordination complexes, but as small iron oxide or oxyhydroxide clusters attached to the SEC surface, as observed previously.¹⁰¹

Chapter 6

Other metals (nickel and zinc) attached to sporopollenin

6. Metals attached to sporopollenin

6.1 Introduction

This chapter discusses the interaction of metals such as zinc and nickel with SECs. Zn has an atomic number of 30, relative atomic mass of 65.38 and electronic configuration $[\text{Ar}] 3d^{10} 4s^2$. Ni has an atomic number of 28, relative atomic mass of 58.69 and electronic configuration of $[\text{Ar}] 4s^2 3d^8$. They are solid at room temperature. Researchers have paid considerable attention to use of sporopollenin exine capsules (SECs) for some applications such as for adsorptive removal of metal ions from aqueous media using sporopollenin as novel biosorbent.¹⁵⁹ The aim of this chapter is to investigate the attachment of the metals complexes to SECs as shown in Figure 6.1. These could then be used in a wide variety of applications including catalysis, imaging and biological delivery. Although some studies have used functionalised sporopollenin, there do not appear to be any with the metal directly bound to the SEC.⁹¹ The aim of this study is to use a variety of spectroscopic techniques to investigate how metals are bound to the SECs.

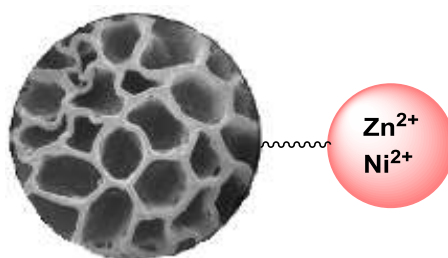


Figure 6.1 The attachment of metal complexes to SECs.

BL-SECs allow for wider variety of spectroscopic techniques, especially UV-vis to investigate the nature of the interaction between metals and the SEC. Zn is diamagnetic and has no d-d transitions. Octahedral Ni(II) has two unpaired electrons and three d-d transitions at relatively low energy, and is ideally suited to these studies. The aim of this chapter is to describe the preparation of metal complexes from a loading experiment using nickel acetate, nickel nitrate or nickel chloride solutions and zinc acetate, zinc nitrate or zinc chloride solutions, with brown and bleached sporopollenin exine capsules (SECs). The synthesised microcapsules were characterised by elemental analysis, ICP-OES and scanning electron microscopy (SEM), Infrared spectroscopy (IR), Raman spectroscopy, UV-visible spectroscopy, X-ray absorption spectroscopy and NMR spectroscopy. This

study provides insight into how the metal salts attach and form complexes with the BR-SECs and BL-SECs.

6.2 Synthetic methods

6.2.1 Preparation of sporopollenin samples for nickel and zinc loading studies

As in the earlier chapters, two different SECs of *L. clavatum* were used for studying metal loading; bleached SECs (BL-SECs) and brown SECs (BR-SECs). The BL-SECs were prepared from the BR-SECs, as described in Chapter 2. Reactions were carried out with aqueous solutions of the following metal salts: nickel (II) chloride, nickel (II) nitrate and nickel (II) acetate; zinc (II) chloride, zinc (II) nitrate and zinc (II) acetate.

In the first instance, 100 mg of BL-SECs were added to 25 mL 0.1 M solutions containing 2.5 mmol of the metal of each of the nickel and zinc salts and stirred overnight, for three days, 1 week or two weeks), before the solutions were then filtered, and washed with water followed by ethanol. The washings were air dried and then placed in a desiccator.

In order to have sufficient material for the spectroscopic measurements, a second set of experiments were carried out using 300 mg of SECs using 75 mL 0.1 M solutions (prepared with 7.5 mmol of metal) of each nickel and zinc salt. Having determined the optimum conditions for metal loading of the SECs, these reactions were just stirred for three days, filtered, washed and dried as for smaller batch. The colour of the nickel and zinc BR-SEC and BL-SEC complexes were not significantly different from the BR-SECs and BL-SECs.

Metal salt	Mass of salt	mmol of metal salt	Mass (BL-SEC or BR-SEC)
NiCl₂.6H₂O	1782.8 mg	7.5	300 mg
Ni(NO₃)₂.6H₂O	2181.07 mg	7.5	300 mg
Ni(OAc)₂.4H₂O	1866.4 mg	7.5	300 mg
ZnCl₂	1022.1 mg	7.5	300 mg
Zn(NO₃)₂.6H₂O	2231.1 mg	7.5	300 mg
Zn(OAc)₂	1376.1 mg	7.5	300 mg

Table 6.1 Concentration of metals salts used in preparation of nickel and zinc loaded SECs.

6.3 Elemental analyses by ICP-OES

The metal loadings in the sporopollenin samples were analysed by ICP-OES to determine the quantity of metal present on the SECs. The ICP-OES results in Table 6.2 were obtained using 10 mg portions of the samples from the BL-SECs reacted for different stirring times and all with 2.5 mmol of metal and 100 mg of SECs. These results show that the length of stirring time does not have a very significant effect on the metal loading for all of the nickel and zinc samples reacted with the BL-SECs. For example for nickel chloride solutions the loading after being stirred overnight is 0.86 % w/w, for three days is 0.98 % w/w, one week is 0.92 % w/w and for two weeks is 0.95 % w/w. There is a similar case for all the zinc samples. For example for zinc acetate solutions the loading after being stirred for overnight is 3.52 % w/w, for three days is 3.47 % w/w, one week is 3.46 % w/w and for two weeks is 4.08 % w/w. Whilst the stirring time had little effect on the metal loading, Table 6.2 shows that the amount of metal on the SEC is very dependent on the solution used. It can be seen for both nickel and zinc that samples prepared from the acetate solutions had higher loadings than those prepared from nitrate or chloride solutions. The nickel loading from the acetate solutions is 3.5 – 4 %, compared to *ca.* 1 % for chloride and nitrate solutions. For zinc acetate solutions the loadings are also 3.5 – 4 %, for zinc chloride solutions *ca.* 2.01 % and for zinc nitrate solutions *ca.* 1 %.

Metal salts+ BL-SECs	Time stirring	Metal loading on dry SECs (%w/w)
Nickel(II) chloride solution	overnight	0.86+-0.03
Nickel(II) chloride solution	3days	0.98+-0.05
Nickel(II) chloride solution	week	0.92+-0.04
Nickel(II) chloride solution	2weeks	0.95+-0.15
Nickel(II) nitrate solution	overnight	0.90+-0.1
Nickel(II) nitrate solution	3days	1.13+-0.3
Nickel(II) nitrate solution	week	0.92+-0.08
Nickel(II) nitrate solution	2weeks	0.79+-0.16
Nickel(II) acetate solution	overnight	3.92+-0.81
Nickel(II) acetate solution	3days	3.82+-0.61
Nickel(II) acetate solution	week	3.22+-0.51
Nickel(II) acetate solution	2weeks	3.42+-0.47
Zinc(II) chloride solution	overnight	1.87+-0.09
Zinc(II) chloride solution	3days	2.01+-0.03
Zinc(II) chloride solution	week	1.81+-0.17
Zinc(II) chloride solution	2weeks	2.40+-0.11
Zinc(II) nitrate solution	overnight	0.63+-0.07
Zinc(II) nitrate solution	3days	0.92+-0.03
Zinc(II) nitrate solution	week	0.81+-0.03
Zinc(II) nitrate solution	2weeks	0.80+-0.11
Zinc(II) acetate solution	overnight	3.52+-0.1
Zinc(II) acetate solution	3days	3.47+-0.33
Zinc(II) acetate solution	week	3.46+-0.37
Zinc(II) acetate solution	2weeks	4.08+-0.90

Table 6.2 ICP-OES results for Ni-SEC and Zn-SEC complexes for the 100 mg, 25 mL, 0.1 M solutions.

The results in Table 6.2 indicate that the most appropriate experimental conditions for were stirring for three days, and this was used in subsequent experiments.

6.3.1 ICP-OES analyses for nickel-SECs

Having shown that the length of stirring has no appreciable effect on the uptake of the metal, three days stirring was used for larger batches of material of both BL-SECs and BR-SECs. Table 6.3 displays the nickel loadings for BL-SECs and BR-SECs prepared with three days stirring times and 7.5 mmol of metal with 300 mg of SECs in 75 mL of water. It is evident from Table 6.3 that when comparing different metal loadings for the nickel samples stirred for three days, the results for the BL-SECs for are very similar for samples prepared using both 25 mL and 75 mL 0.1 M solutions, and that nickel acetate again showed a significantly higher nickel loading than nickel nitrate and nickel chloride. The consistent increase in metal loading for the acetate solutions may indicate that acetate is involved with the binding of the nickel to the SEC surface. For BR-SECs, the nickel loading is greater than for the BL-SECs, and that they are now all more similar: nickel acetate, 4.84 % w/w; nickel chloride, 4.50 % w/w; and nickel nitrate, 3.71 % w/w. The higher nickel loading in the BR-SECs may indicate that the bleaching process removes some of the functional groups that are involved in the nickel coordination.

Nickel salt + (BL-SECs & BR-SECs)	Nickel loading on dry SECs (%w/w)
Nickel(II) chloride solution + BL-SECs	0.83±0.01
Nickel(II) chloride solution + BR-SECs	4.50±0.07
Nickel(II) nitrate solution + BL-SECs	0.95±0.01
Nickel(II) nitrate solution + BR-SECs	3.71±0.02
Nickel(II) acetate solution + BL-SECs	3.84±0.04
Nickel(II) acetate solution + BR-SECs	4.84±0.07

Table 6.3 ICP-OES results for Ni-SEC complexes for 300 mg SEC, 75 mL and 0.1 M solution samples.

6.3.2 Extraction studies for nickel-SECs in neutral pH

Table 6.4 shows the amount of nickel in the dry Ni-SEC complexes before and after the extraction process at neutral pH (see Section 2.5 for experimental details). Table 6.5 compares this data with the amount of metal in the extraction solution. These results show that there is not much difference between the dry brown and bleached nickel acetate-SEC complexes. However, a higher proportion of the nickel is extracted into the filtrate of the BL-SECs than the BR-SECs for all of the nickel salts (Table 6.5). The results of the extraction at neutral pH for the nickel nitrate -SEC and nickel chloride -SEC (Table

indicate that the nickel is more tightly bound to the brown Ni-SEC than the bleached Ni-SEC. There is a loss of 10- 20% of nickel from all of the samples when stirred for three days in neutral solutions.

Sample	% w/w Ni (ICP-OES) in solid before suspending in water	mg of Ni in 20 mg of SEC before extraction in water	% w/w Ni (ICP-OES) in solid after suspending in water, filtering, washing and drying	mg of nickel in SEC after suspension in water	Difference (mg)	% loss of Ni
Nickel(II) chloride solution + BL-SECs	0.83	0.17	0.75	0.15	0.02	12
Nickel(II) chloride solution + BR-SECs	4.50	0.900	3.93	0.79	0.11	12.2
Nickel(II) nitrate solution + BL-SECs	0.95	0.19	0.75	0.15	0.04	21
Nickel(II) nitrate solution + BR-SECs	3.71	0.742	3.07	0.61	0.132	17.7
Nickel(II) acetate solution + BL-SECs	3.84	0.768	2.87	0.57	0.198	25.7
Nickel(II) acetate solution + BR-SECs	4.84	0.967	3.95	0.79	0.177	18.3

Table 6.4 Nickel loadings in dry SECs before and after extraction at neutral pH.

Sample	ICP results for Ni filtrate solution / ppm	mg nickel extracted into 5 mL solution	%loss of Ni into solution	mg lost from solid	mg nickel missing
Nickel(II) chloride solution + BL-SECs	10.4	0.051	31.3	0.016	-0.036
Nickel(II) chloride solution + BR-SECs	13.4	0.067	7.45	0.114	0.047
Nickel(II) nitrate solution + BL-SECs	11.4	0.056	29.9	0.04	-0.017
Nickel(II) nitrate solution + BR-SECs	35.9	0.179	24.2	0.128	-0.051
Nickel(II) acetate solution + BL-SECs	26.7	0.134	17.4	0.194	0.060
Nickel(II) acetate solution + BR-SECs	22.2	0.111	11.5	0.178	0.067

Table 6.5 Complete results of data calculations of both dry Ni-SEC complexes and in solution.

Sample	mg of nickel in 20 mg of SEC before extraction in water	mg of nickel remaining in SEC after suspension in water	% loss of Ni from solid	mg nickel extracted into 5 mL solution	%loss of Ni into solution	mg nickel missing
Nickel(II) chloride solution + BL-SECs	0.17	0.15	12	0.051	31.3	-0.036
Nickel(II) chloride solution + BR-SECs	0.900	0.79	12.2	0.067	7.45	0.047
Nickel(II) nitrate solution + BL-SECs	0.19	0.15	21	0.056	29.9	-0.017
Nickel(II) nitrate solution + BR-SECs	0.742	0.61	17.7	0.179	24.2	-0.051
Nickel(II) acetate solution + BL-SECs	0.768	0.57	25.7	0.134	17.4	0.060
Nickel(II) acetate solution + BR-SECs	0.967	0.79	18.3	0.111	11.5	0.067

Table 6.6 The results of all data calculations of both dry Ni-SEC complexes and in solution.

6.3.3 ICP-OES analyses for zinc-SECs

Table 6.7 shows the ICP-OES results for the zinc solutions with the bleached and brown SECs (7.5 mmol: 300 mg (metal: SEC) ratio) stirred at room temperature for three days. It can be seen from Table 6.7 that when comparing different metal loadings for the zinc samples stirred for three days, with different zinc solutions with brown and bleached SECs, a higher zinc loading is observed with brown SECs than bleached SECs for all of the zinc salts. For example, the reaction of zinc acetate solution with BR-SECs results in a zinc loading of 6.55 % w/w, but with BL-SECs it is 4.15 % w/w. For zinc nitrate solutions and BR-SECs the loading is 4.33 % w/w but with BL-SECs it is 1.15 % w/w, and for zinc chloride solutions and BR-SECs it is 6.1 % w/w but with BR-SECs it is 2.20 % w/w. This may indicate that the bleaching process removes some of the functional groups that are involved in the zinc coordination as mentioned in previous Chapter 3.

When comparing the reactions with different zinc solutions, zinc acetate shows a higher zinc loading than zinc nitrate and slightly higher with zinc chloride. For example, with BR-SECs it can be seen that the loading with zinc acetate is 6.55 % w/w, for zinc chloride it is 6.10 % w/w but for zinc nitrate is 4.33 % w/w. Also, for BL-SECs it can be seen that the loading using zinc acetate solutions shows a higher zinc loading of 4.15 % w/w than zinc nitrate (1.15 %) and zinc chloride (2.2%).

Zinc salt + SECs	Zinc loading on dry SECs (%w/w)
Zinc(II) chloride solution + BL-SECs	2.20±0.02
Zinc(II) chloride solution + BR-SECs	6.10±0.08
Zinc(II) nitrate solution + BL-SECs	1.15±0.01
Zinc(II) nitrate solution + BR-SECs	4.33±0.03
Zinc(II) acetate solution + BL-SECs	4.15±0.02
Zinc(II) acetate solution + BR-SECs	6.55±0.03

Table 6.7 ICP-OES results for Zn-SEC complexes for 300 mg SEC, 75 mL and 0.1 M solution samples.

6.3.4 Extraction studies for zinc-SECs in neutral pH

Table 6.8 shows the amount of zinc in the dry Zn-SEC complexes before and after the extraction process at neutral pH (see Section 2.5 for experimental details). Table 6.9

compares this data with the amount of metal in the extraction solution. These results show that there is not much difference between the dry brown and bleached zinc acetate-SEC complexes. Also, there is a higher proportion of the zinc extracted into the filtrate of the brown SECs with zinc chloride and zinc nitrate than the bleached zinc chloride and zinc nitrate. The results of the extraction at neutral pH for the zinc nitrate -SEC and zinc chloride -SEC indicate that the zinc is much more tightly bound to the brown Zn-SEC than the bleached Zn-SEC. The difference in concentration of zinc extracted between the bleached and brown Zn-SEC complexes is greater for zinc nitrate than zinc chloride.

Sample	% w/w Zn (ICP-OES) in solid before suspending in water	mg of zinc in 20 mg of SEC before extraction in water	% w/w Zn (ICP-OES) in solid after suspending in water, filtering, washing and drying	mg of zinc in SEC after suspension in water	Difference (mg)	% loss of Zn
Zinc(II) chloride solution + BL-SECs	2.20	0.44	2.19	0.438	0.002	0.45
Zinc(II) chloride solution + BR-SECs	6.06	1.21	5.93	1.18	0.026	2.15
Zinc(II) nitrate solution + BL-SECs	1.15	0.23	1.04	0.208	0.022	9.57
Zinc(II) nitrate solution + BR-SECs	4.33	0.866	3.74	0.748	0.118	13.6
Zinc(II) acetate solution + BL-SECs	4.15	0.83	3.5	0.7	0.13	15.7
Zinc(II) acetate solution + BR-SECs	6.55	1.31	5.39	1.078	0.232	17.7

Table 6.8 Zinc loadings in dry SECs before and after extraction in neutral pH.

Sample	ICP results for Zn filtrate solution / ppm	mg zinc extract ed into 5 mL solution	%loss of Zn into solution	mg lost from solid	mg zinc missing
Zinc(II) chloride solution + BL-SECs	7.84	0.039	8.91	0.002	-0.037
Zinc(II) chloride solution + BR-SECs	41.8	0.209	17.3	0.026	-0.183
Zinc(II) nitrate solution + BL-SECs	6.13	0.030	13.3	0.022	-0.009
Zinc(II) nitrate solution + BR-SECs	24.3	0.121	14.06	0.118	-0.004
Zinc(II) acetate solution + BL-SECs	no sample	-	-	0.13	-
Zinc(II) acetate solution + BR-SECs	10.03	0.050	3.82	0.232	0.182

Table 6.9 Complete results of all data calculations of both dry Zn-SEC complexes and in solution.

Sample	mg of zinc in 20 mg of SEC before extraction in water	mg of zinc remaining in SEC after suspension in water	% loss of Zn from solid	mg zinc extract ed into 5 mL solution	%loss of Zn into solution	mg zinc missing
Zinc(II) chloride solution + BL-SECs	0.44	0.438	0.454	0.039	8.91	-0.037
Zinc(II) chloride solution + BR-SECs	1.21	1.18	2.15	0.209	17.3	-0.183
Zinc(II) nitrate solution + BL-SECs	0.23	0.208	9.57	0.030	13.3	-0.009
Zinc(II) nitrate solution + BR-SECs	0.866	0.748	13.6	0.121	14.06	-0.004
Zinc(II) acetate solution + BL-SECs	0.83	0.7	15.7	-	-	-
Zinc(II) acetate solution + BR-SECs	1.31	1.078	17.7	0.050	3.82	0.182

Table 6.10 The results of all data calculations of both dry Zn-SEC complexes and in solution.

To conclude, the ICP-OES results show that the best conditions were 2.5 mmol:100 mg:25 mL (metal: SECs: water) and stirring for three days. The highest level of attachment of Ni and Zn to the SECs is found for acetate compared to chloride and nitrate. For all different metals samples with brown and bleached SECs, a higher metal loading is usually observed with brown SECs than bleached SECs for all of the metal salts nickel or zinc.

6.4 Scanning electron microscope images (SEM)

The images of BL-SECs reacted with nickel(II) solutions are shown in Figure 6.2. The first image on the left, is from BL-SECs reacted with nickel(II) chloride solution, the second image after reaction of BL-SECs with nickel(II) nitrate solution, and the image on the right is of BL-SECs reacted with nickel(II) acetate solution. There is not much difference between them, with the majority of the spores still intact, but some of the spores are broken, and there is debris visible around the spores.



Figure 6.2 SEM images of BL-SECs after reaction with (A) NiCl_2 solution, (B) $\text{Ni}(\text{NO}_3)_2$ solution and (C) $\text{Ni}(\text{OAc})_2$ solution.

The images of BR-SECs after reaction with the nickel(II) solutions are shown in Figure 6.3. In the first image on the left, the reaction of nickel(II) chloride solution with BR-SECs results in almost all of the spores being damaged and broken. In the image in the middle, it can be seen that the reaction of nickel(II) nitrate solution with BR-SECs does not result in such significant damage and that many more of spores are unbroken and the SECs remained intact. However, in the image on the right, the reaction with nickel(II) acetate solution results in the same sort of damage as from the nickel chloride solutions. When comparing between all nickel samples with BR-SECs and BL-SECs, the SEM images of BL-SECs show less damage, in contrast to nickel with BR-SECs where some of the spores are flat and broken.

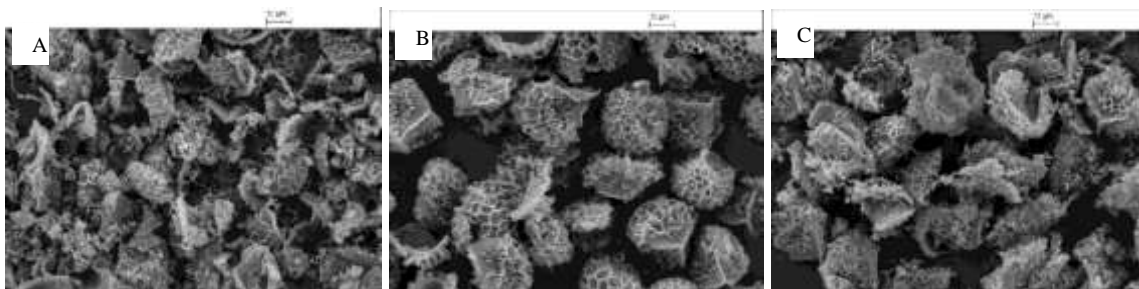


Figure 6.3 SEM images of BR-SECS reacted with (A) NiCl_2 solution, (B) $\text{Ni}(\text{NO}_3)_2$ solution and (C) $\text{Ni}(\text{OAc})_2$ solution.

The images of BL-SECS after reaction with zinc(II) solutions are shown in Figure 6.4. The first image on the left, the reaction of zinc(II) chloride solution with BL-SECS has images of spores which are broken, and some had burst slightly or become distorted. The middle image for zinc(II) nitrate is similar to the image for reaction with zinc chloride solutions with significant disruption of the SECS. In the image on the right, it can be seen that when BL-SECS are reacted with zinc(II) acetate solution, a large proportion of the SECS remain intact.

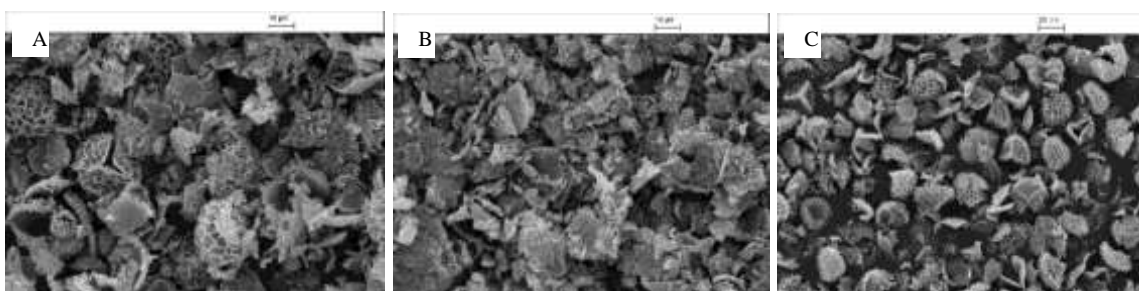


Figure 6.4 SEM images of BL-SECS after reaction with (A) ZnCl_2 solution, (B) $\text{Zn}(\text{NO}_3)_2$ solution and (C) $\text{Zn}(\text{OAc})_2$ solution.

The images of BR-SECS after reaction with zinc(II) solutions are shown in Figure 6.5. The first image on the left, after reaction of the BR-SECS with zinc(II) chloride solution shows the almost spherical shape of the microcapsules, verifying that the sporopollenin particles were not damaged when reacted with zinc(II) chloride solution. Whilst in the image in the middle, it can be seen the zinc(II) nitrate with BR-SECS is different to zinc chloride, where fewer of the SECS remained intact, some had broken slightly or become distorted. In the image on the right, the zinc(II) acetate SECS are damaged and broken. When comparing between all zinc samples with BR-SECS and BL-SECS, SEM images showed that the BR-SECS are only slightly damaged image in contrast to the BL-SECS where some of the spores burst, are flat or broken.

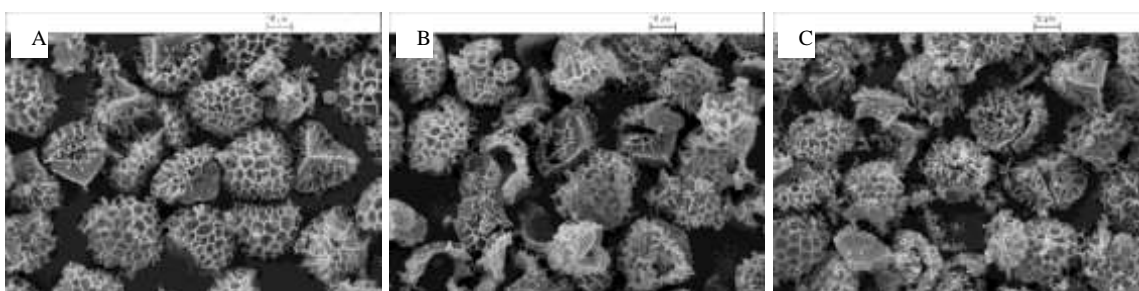


Figure 6.5 SEM images of BR-SECs after reaction with (A) ZnCl_2 solution, (B) $\text{Zn}(\text{NO}_3)_2$ solution and (C) $\text{Zn}(\text{OAc})_2$ solution.

In conclusion, with all of the different metals-SECs complexes, there was much greater damage when BR-SECs were used than BL-SECs. For zinc-SECs the images of BR-SECs are slightly damaged image in contrast the zinc with BL-SECs. In contrast, for nickel-SECs the images of BL-SECs are better and slightly damaged image that the nickel with BR-SECs. That there is no evidence for the inside of the spores filling up with metal salts for any of the metals.

6.5 Spectroscopic studies

Various spectroscopies were used to study the metal-SEC complexes: UV-vis spectroscopy was used to identify the presence of metals and their mode of coordination into metal-SEC complexes. Vibrational spectroscopy was used to examine the functional groups present and the structure of SECs and NMR spectroscopy was used for the zinc-SEC complexes. Finally, the structure of the obtained microcapsules was investigated by X-ray absorption.

6.5.1 Identification of metal coordination environment within sporopollenin using electronic absorption spectroscopy (UV – visible - NIR)

Electronic absorption spectroscopy was used to analyse metal-SEC complexes. UV-vis spectroscopy can be used to identify the coordination environment of the metal within the sporopollenin exine capsules. The metals are believed to be attached to the SEC by functional groups such as phenol and carboxylate. When the SEC is mixed with metal complexes, the d-electrons of these complexes contribute to the production of different colours and depending on the number, shape and wavelength of the bands, it is possible to inquire about the metal complex geometry on the SECs.

UV-vis spectra were obtained from metal containing bleached SEC samples prepared from 2.5 mmol: 100 mg metal: SEC. The spectra show characteristic features for nickel(II) and zinc(II), UV-vis at different stirring ratios (overnight, 3 days, one week and two weeks). The complementary samples prepared using brown SECs were not examined using solid-state UV-vis-NIR spectroscopy due to the masking of the spectral features of the metal by the SEC itself (for details see Chapter 3).

In Figure 6.6, the spectrum of the BL-SEC reacted with nickel acetate solution shows bands at about 8-9000 cm^{-1} and a broad feature at 15000 cm^{-1} are possibly nickel d-d bands. Three d-d transitions are expected for octahedral Ni(II). As it is anticipated that the coordination environment is NiO_6 , the three d-d transitions in $[\text{Ni}(\text{H}_2\text{O})_6]^{2+}$ which are at 8500, 13800 and 25300 cm^{-1} can be used as a guide, and similar values are observed for other complexes with NiO_6 coordination environments.²⁰⁵ As the 25300 cm^{-1} band will be obscured by the SECs absorption, it is expected to see two d-d bands, which are the broader features in Ni(II) spectra. The sharper features are either due to C-H, O-H overtone and combination bands or spin-forbidden band in Ni^{2+} . If they are common between the metals then they are much more likely to be the former. It is strange that they are not present without the metal. There was a slight difference among the stirring times of overnight, three days, one week, and two weeks (see Table 6-2).

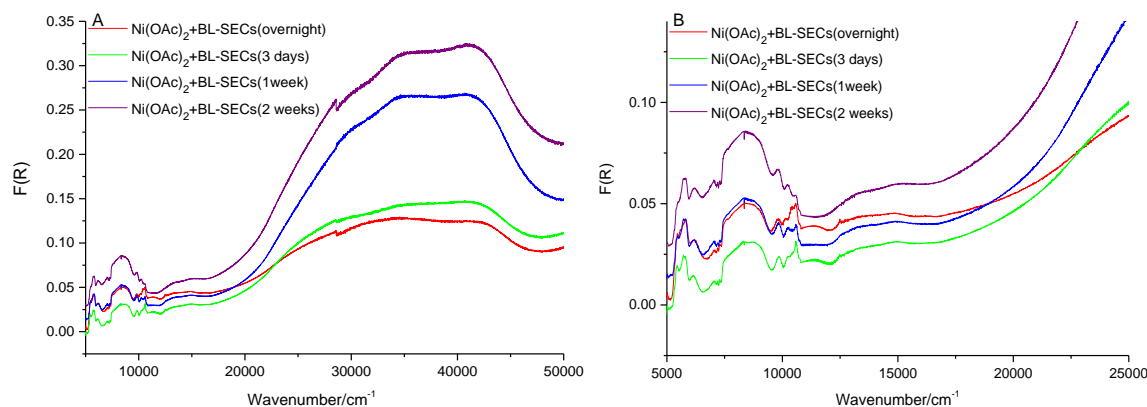


Figure 6.6 (A) UV-vis spectra for BL-SECs stirred with nickel acetate solution for varying times, (B) Expanded UV-vis spectra.

Figure 6.7 shows that the results of nickel nitrate with BL-SECs are similar for all the stirring times. In the one week spectrum the low energy features are present, but their overall intensity is low, probably due to varying amounts of sample present in the sampling

volume. The broader features are probably d-d transitions, with sharp features due to the SECs.

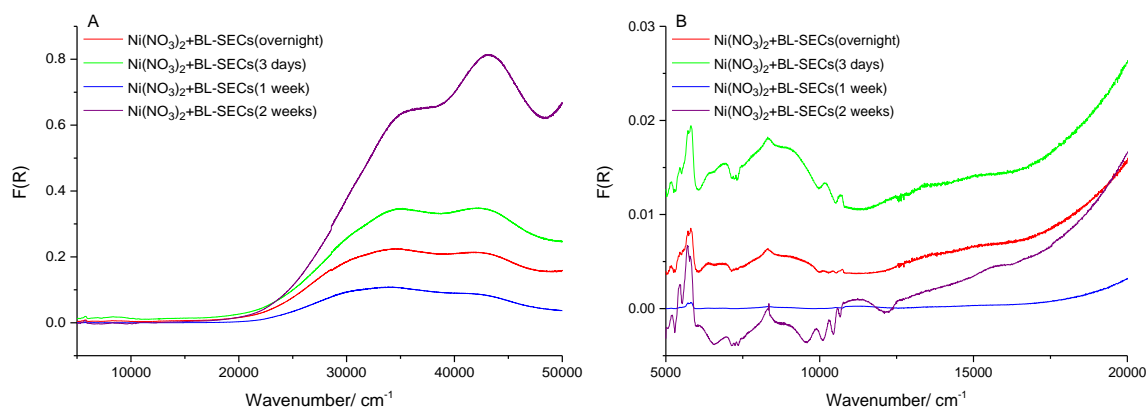


Figure 6.7 Data of the UV-vis experiment for nickel nitrate, (B) Expanded UV -vis spectra for nickel nitrate.

Figure 6.8 shows that the results of nickel chloride are similar to the nickel nitrate, and there is a gradual change in the spectra with loss of the broader features with increased stirring times.

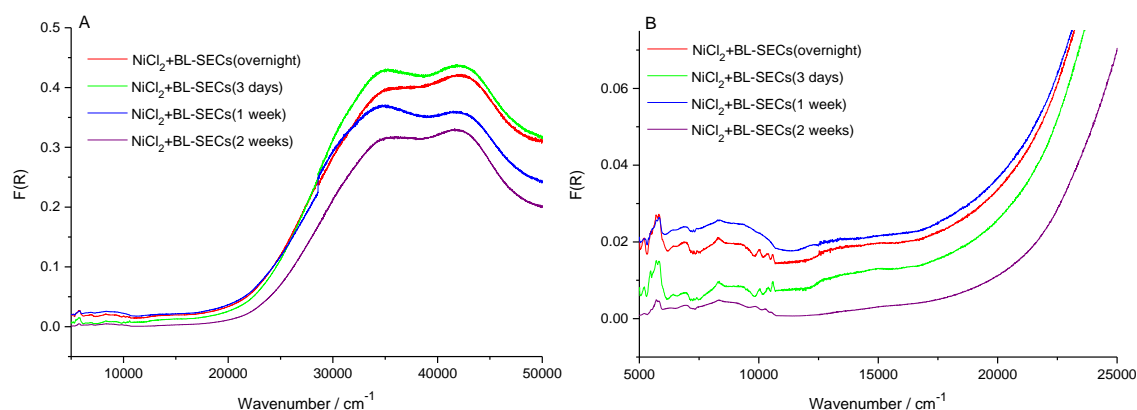


Figure 6.8 (A) Data of the UV-vis experiment for nickel chloride, (B) Expanded UV -vis spectra for nickel chloride.

By analysing the results presented above, it is possible to divide the UV-vis-NIR absorption spectra into two parts: from 5000 to 25000 cm⁻¹, which comprises the bands characteristic of d-d transitions in the Ni(II) (d⁸) metal ions, and from 25000 to 50000 cm⁻¹, which is the region where the absorptions n-π* and π-π* arising from the SEC functional groups appear, as well as higher energy d-d bands and charge transfer transitions associated with the nickel.

Many nickel complex salts produce quite similar absorption patterns, but different maximum absorbance wavelength. It is clear from spectra that the BL-SECs after reaction with nickel chloride and nitrate are very similar, but are different to those after reaction with nickel acetate solution. In Figure 6.9 shows that the nickel nitrate and nickel chloride are similar with peaks that are most probably d-d transitions at 15800 and 11000 cm^{-1} , but in the nickel acetate sample the higher energy peak shifts to 15400 cm^{-1} and the 11000 cm^{-1} peak is absent. The features below 10000 cm^{-1} are principally from the SEC itself.

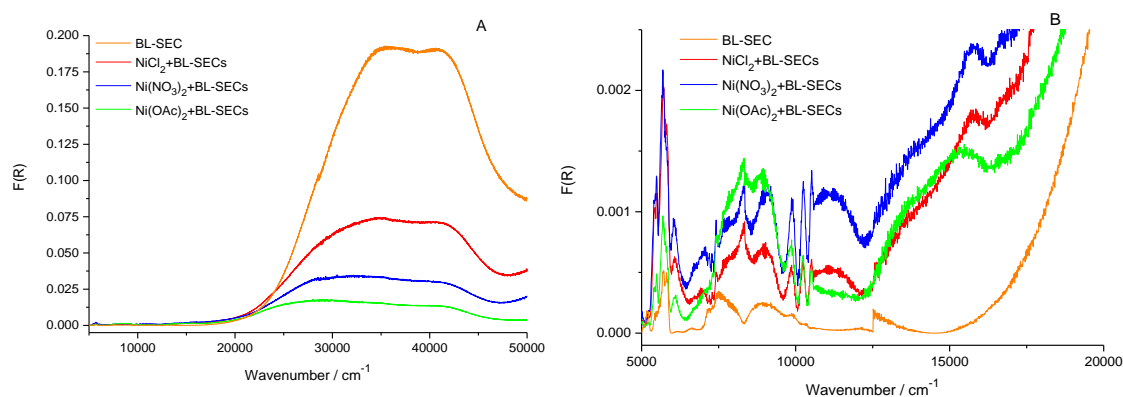


Figure 6.9 (A) Data of the UV-vis experiment for nickel salts with BL-SECs, (B) Expanded UV -vis spectra for nickel salts with BL-SECs at loading 7.5mmol and three days stirring.

In Figure 6.10, show the spectra of BL-SECs reacted with zinc acetate solutions. The higher intensity peak observed when BL-SECs were stirred with $\text{Zn}(\text{OAc})_2$ solution for three days is most likely due to differing quantities of sample in the BaSO_4 and taking this into account there is not much difference among the stirring times of overnight, one week, and two weeks.

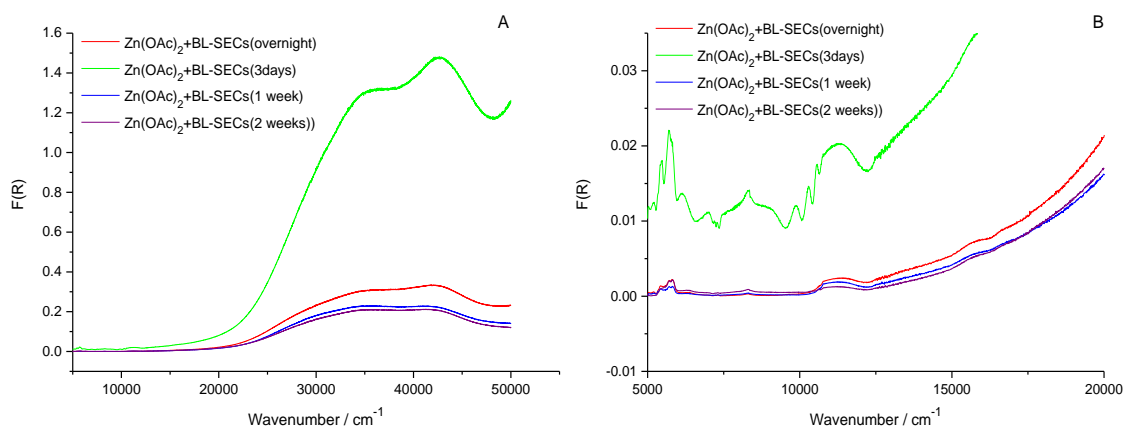


Figure 6.10 Data of the UV-vis experiment for zinc acetate (2.5mmol:100mg) at in different stirring, (B) Expanded UV -vis spectra for zinc acetate.

Figure 6.11 and Figure 6.12 show that the results of zinc nitrate and zinc chloride are similar, and as there will be no d-d transitions in Zn(II), these features must be characteristic of the SEC itself.

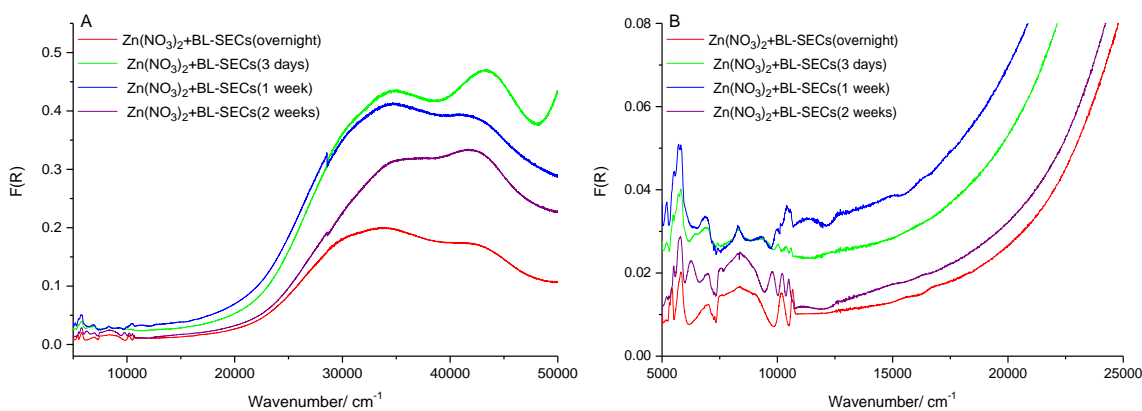


Figure 6.11 (A) Data of the UV-vis experiment for zinc nitrate, (B) Expanded UV -vis spectra for zinc nitrate.

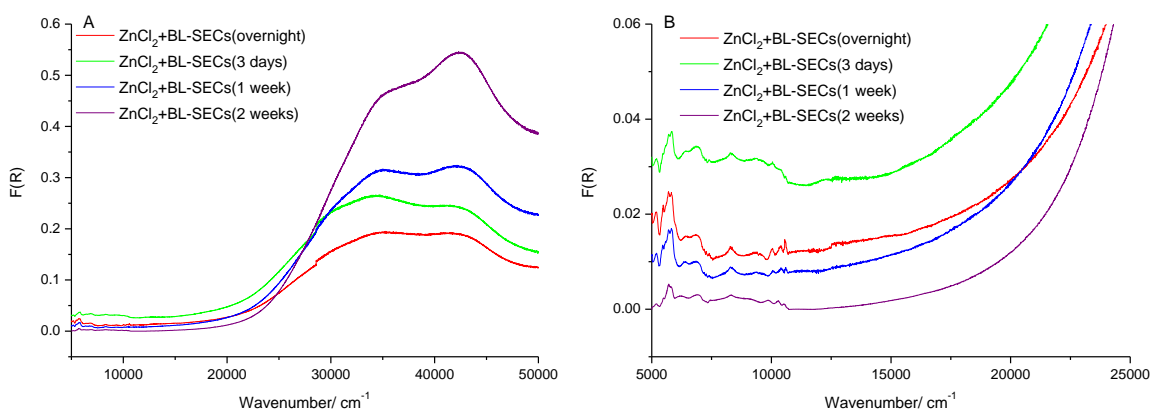


Figure 6.12 Data of the UV-vis experiment for zinc chloride, (B) Expanded UV -vis spectra for zinc chloride.

By analysing the results in Figure 6.13 it is possible to divide the UV-vis-NIR absorption spectra into two parts: from 5000 to 25000 cm^{-1} , which comprises the bands characteristic of d-d transitions in the other metals ions, however there are no d-d transitions in Zn(II), and from 25000 to 50000 cm^{-1} , which is the region where the absorptions $n-\pi^*$ and $\pi-\pi^*$ arising from the SEC functional groups appear.

Figure 6.13 shows the different results of the UV-vis spectroscopy for zinc and different ions from 5000 to 50000 cm^{-1} when loading 2.5 mmol:100 mg metal:bleached SEC and stirring three days. Various zinc complex salts produced quite similar absorption patterns,

but different maximum wavelength of absorbance. There is a different coordination mode for the zinc acetate derived complex, than the zinc chloride and zinc nitrate.

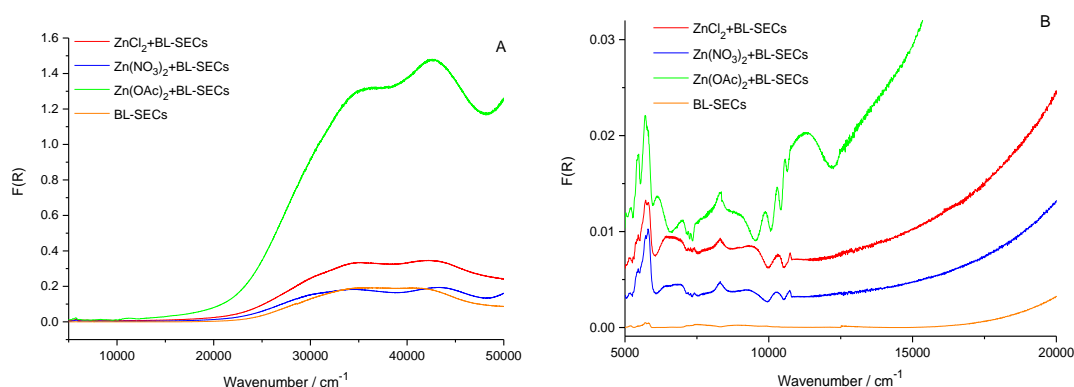


Figure 6.13 Data of the UV–vis experiment for different zinc salts (2.5mmol:100mg) at in three days stirring.

In conclusion, the spectra of the nickel and zinc samples in the figures present results of the experiment for spore metal complexes from 5000 cm^{-1} to 50000 cm^{-1} . The figures show a low level of absorption between 5000 and 20000 cm^{-1} , which then increased significantly from 20000 cm^{-1} . The high energy part of the spectrum is associated with the π - π^* transitions in the SEC. The lower energy transitions arise from both the metal and the SEC parts of the sample. In the case of zinc, there no d-d transitions, so they must all arise from the SEC, but in the case of nickel there are also d-d transitions. Although the intensity of the colour produced by the complexation could be used to determine the concentration of the metal present in a sample, this is not as straight forward for solid-state samples as those in solution. The most important aspect of these results is that the UV-vis spectra clearly indicate that there is different coordination environments present in the metal SEC complexes prepared from acetate solutions, compared to chloride and nitrate solutions.

6.5.2 Vibrational spectroscopic identification of functional groups in sporopollenin

6.5.2.1 Infrared spectroscopy (IR)

IR spectroscopy can be applied to identify the molecular constituents in the samples from their vibrational spectra in the mid-IR region (4000 – 400 cm^{-1}). Furthermore, it can explore the structural framework of the spore metal complex without destroying its internal structure.

In figures below show the IR spectra of metals salts with BL-SECs and BR-SECs when loading (2.5mmol: 100 mg) and different stirring time (overnight, three days, one week or two weeks).

In Figure 6.14 it can be seen that there is no significant difference between all the BL-SECs prepared from nickel acetate solution with same loading and different stirring time. Figure 6.15 also confirms that the same spectra are obtained for different stirring times for nickel nitrate and chloride solutions.

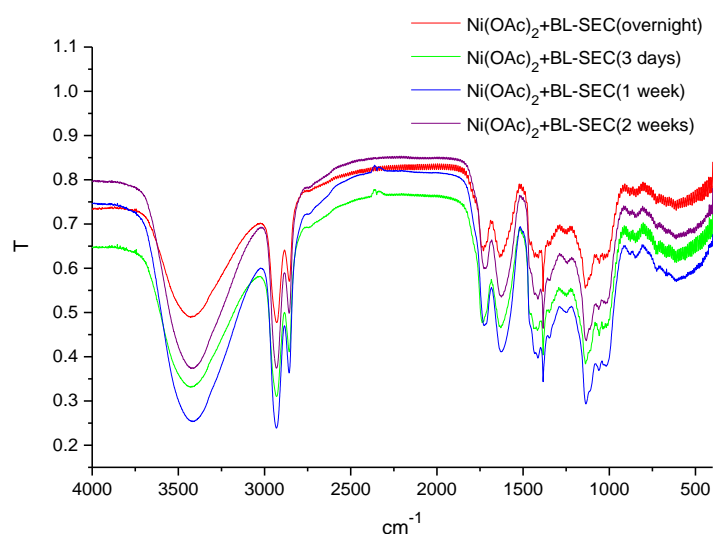


Figure 6.14 IR spectroscopy results for Ni(OAc)₂ with BL-SEC with different stirring times.

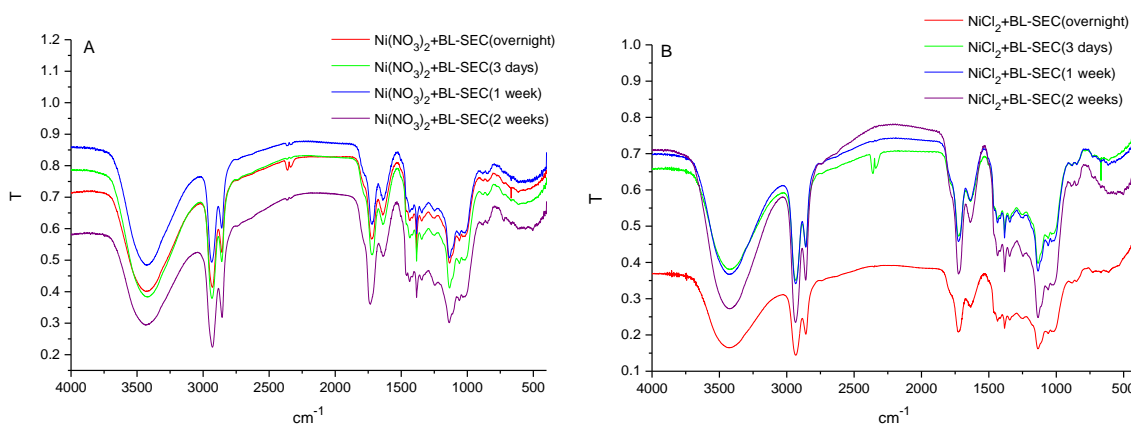


Figure 6.15 IR spectroscopy results with different stirring times (A) Ni(NO₃)₂ with BL-SEC, (B) NiCl₂ with BL-SEC.

When loading (2.5mmol: 100mg) of nickel salts with BL-SECs, it can be seen from Figure 6.16 that there is a slight difference spectra in nickel acetate compared to the nickel nitrate and nickel chloride. It can be seen that the spectrum of the nickel acetate sample is different

to those from the nickel chloride and nitrate samples, and all are different from the spectrum of the unreacted BL-SEC. In the unreacted BL-SEC there is a peak at 1740 cm^{-1} assigned to $\nu_{\text{C=O}}$. In nickel nitrate and chloride this shifts to 1720 cm^{-1} and there is a new peak at 1634 cm^{-1} . In the nickel acetate spectrum, the initial peak is split into components at 1734 and 1713 cm^{-1} , the new peak is broader and more intense, with the main feature at 1630 cm^{-1} and a shoulder at 1585 cm^{-1} . The 1634 cm^{-1} peak is associated with the SEC-Ni interaction, with the peak at 1585 cm^{-1} arising from the Ni-acetate interaction.

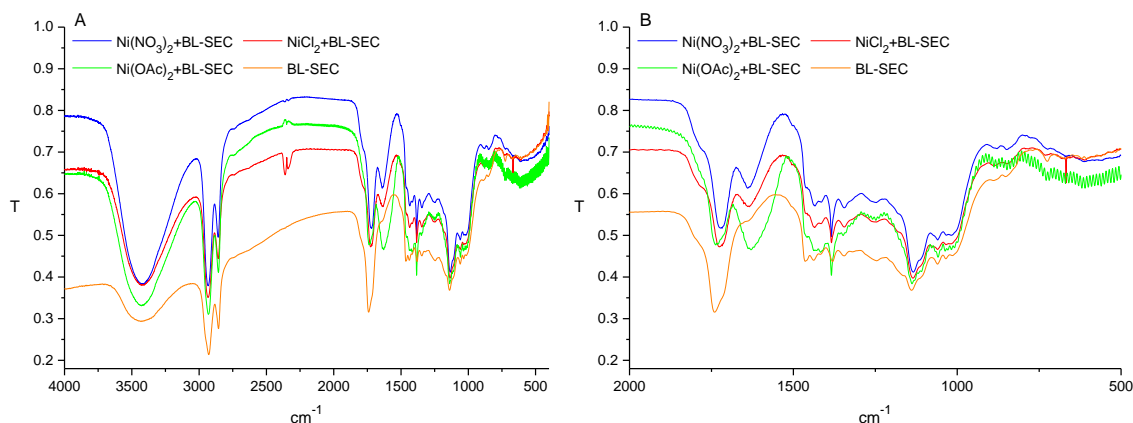


Figure 6.16 (A) IR spectroscopy results for nickel salts with BL-SEC, (B) Expanded IR spectroscopy for nickel salts with BL-SEC.

When comparing between different nickel salts with BL-SECs and BR-SECs at the same stirring time and the same loading, it can be seen that Figure 6.17 the spectra of the BR-SECs are different to those of the nickel salts with BL-SECs. In particular, the 1745 cm^{-1} peak (assigned to Chapter 3) in the parent BR-SEC is replaced in all of the SEC spectra after reaction with the nickel solutions by a broad peak at 1713 cm^{-1} . In this case there is no significant difference between the three nickel BR-SEC spectra.

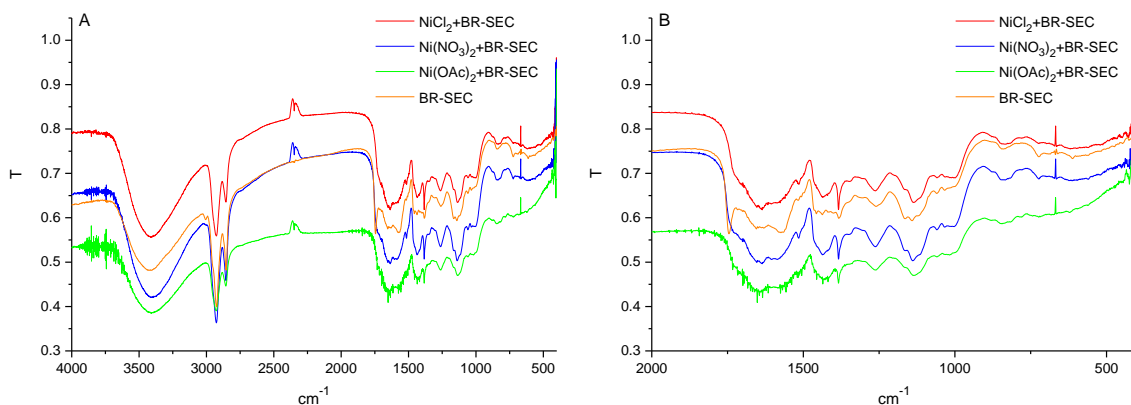


Figure 6.17 IR spectroscopy results for nickel salts with BR-SEC, (B) Expanded IR spectroscopy for nickel salts with BR-SEC.

In Figure 6.18 the spectra from the zinc acetate with BL-SEC there is no difference between the spectra with same loading but different stirring times. In the case of reactions with the zinc nitrate and zinc chloride solutions (Figure 6.19) there is also no dependence on the stirring times.

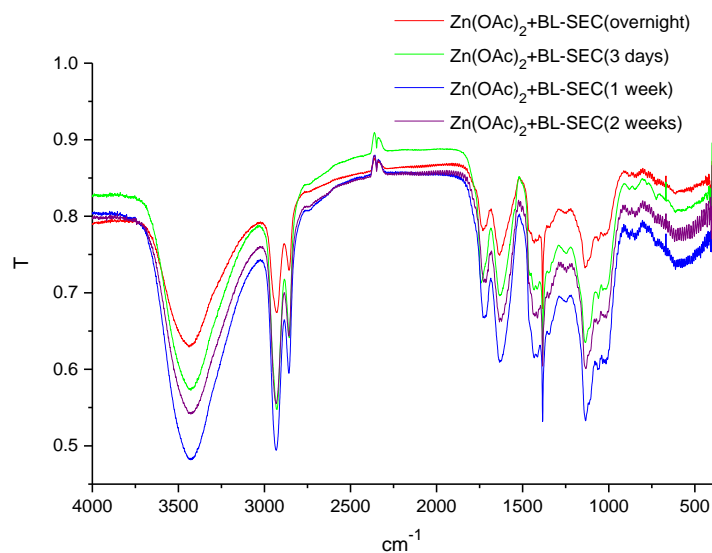


Figure 6.18 IR spectroscopy results for Zn(OAc)₂ with BL-SEC with different stirring times.

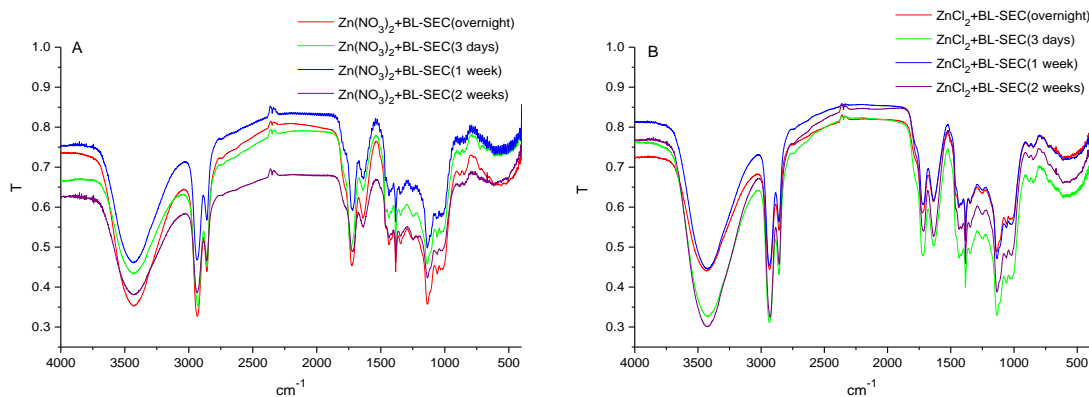


Figure 6.19 IR spectroscopy results with different stirring times (A) Zn(NO₃)₂ with BL-SEC, (B) ZnCl₂ with BL-SEC.

It can be seen from Figure 6.20 that there is a difference between the spectra of the zinc salts with BL-SEC. In the spectra of BL-SEC and zinc acetate and zinc nitrate there is a peak at 1740 cm⁻¹ but in the spectra for zinc chloride it moved to 1720 cm⁻¹. In the spectra for zinc nitrate and zinc chloride there is a peak at 1637 cm⁻¹ but for zinc acetate this shifts slightly 1632 cm⁻¹.

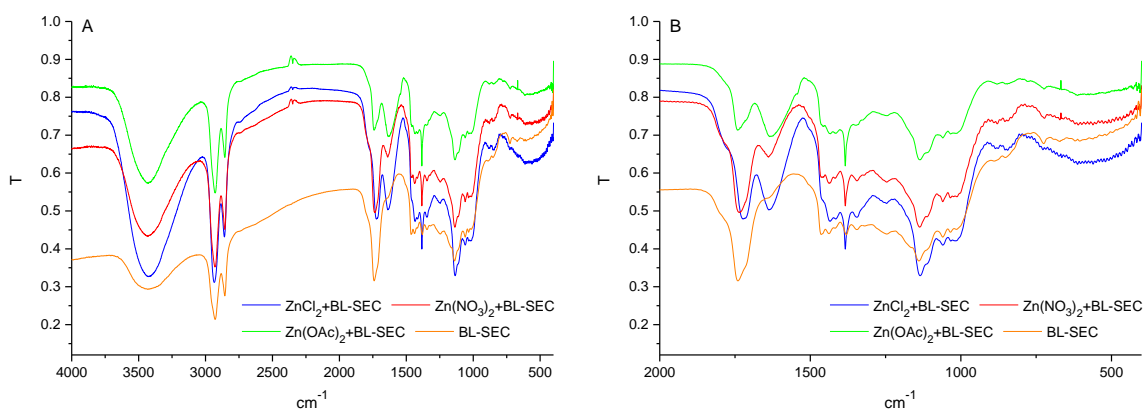


Figure 6.20 (A) IR spectroscopy results for zinc salts with BL-SEC, (B) expanded IR spectroscopy results for zinc salts with BL-SEC.

When comparing between different zinc salts with BL-SECs and BR-SECs at the same stirring time and the same loading, it can be seen that in Figure 6.21 the BR-SECs is different compared to zinc salts with BL-SECs. Also, it showed from Figure 6.21 that the zinc chloride with BR-SECs is slightly different compared to zinc nitrate and zinc acetate. 1745 cm^{-1} peak is still present in the zinc chloride spectrum, but is absent from the zinc nitrate and zinc acetate spectra, but there is a new shoulder at 1725 cm^{-1} . A peak at 1649 cm^{-1} is present in all of the spectra, but peak at 1752 cm^{-1} has reduced intensity in the chloride and nitrate spectra, but in the acetate spectrum it is split into peaks at 1588 and 1556 cm^{-1} .

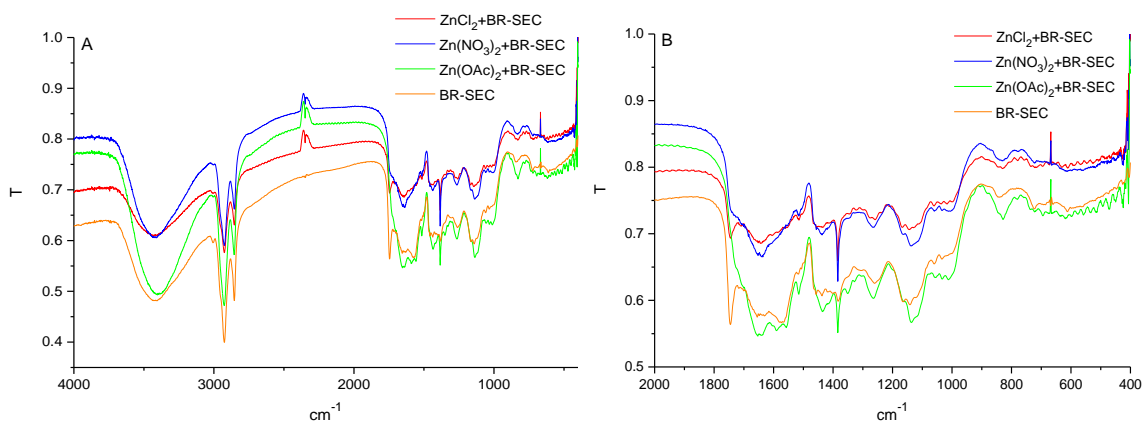


Figure 6.21 (A) IR spectroscopy results for zinc salts with BR-SEC, (B) expanded IR spectroscopy results for zinc salts with BR-SEC.

To conclude there is no dependence of the spectra on the stirring time for each of the nickel and zinc solutions for both the BR-SECs and BL-SECs. However, there are distinct differences between the spectra of the BL-SECs and BR-SECs, depending on the metal solution. For nickel, the spectral motifs were different for acetate compared to chloride and

nitrate as well as for zinc. These differences indicate different binding modes for the various samples.

6.5.2.2 Raman spectroscopy

Raman spectroscopy was also used to study the structure of the metal-SEC complexes. The Raman spectra of sporopollenin have previously been described (Chapter 3). The spectrum is dominated by the different vibrational modes of sporopollenin.

Raman spectra were obtained for the different Ni-SEC complexes. In comparison to the spectra of the bleached SECs in Chapter 3, the spectra of the Ni-SEC complexes were badly affected by fluorescence increasing towards 3000 cm^{-1} . An example (Ni(OAc)₂-SEC complex) is shown in Figure 6.22. The fluorescence background increases with longer stirring time in Ni(OAc)₂-SEC complex. Also, it looks as though the band at 1605 cm^{-1} which can be assigned to aromatic ring stretching modes, grows in intensity compared to the 1440 cm^{-1} band due to CH₂ deformations, with increased stirring, but the spectra are noisy.^{111, 112}

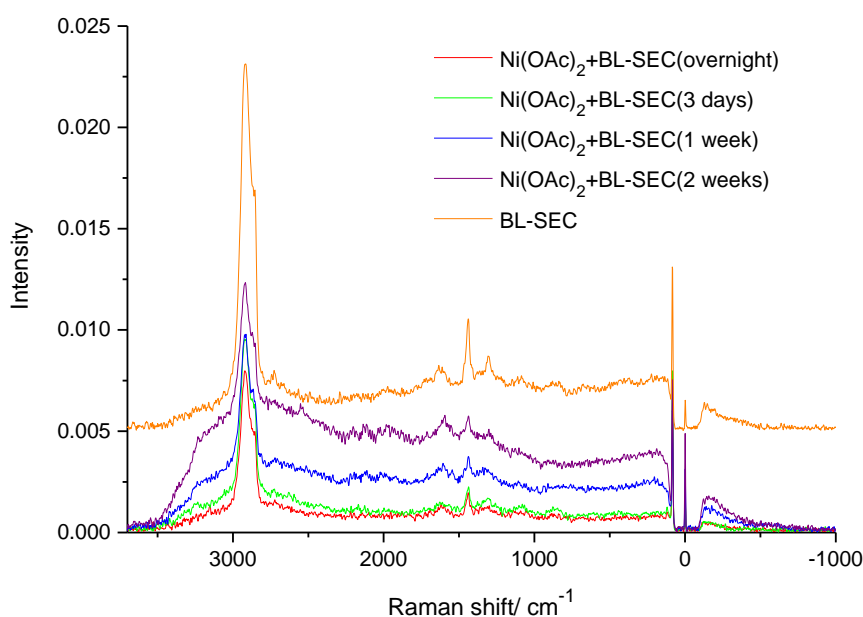


Figure 6.22 (A) Raman spectra from Ni(OAc)₂ with BL-SEC (2.5 mmol:100 mg), (B) Expanded Raman spectra from Ni(OAc)₂ with BL-SEC.

It can be seen from Figure 6.23 that the fluorescence background increases with longer stirring time from overnight to two weeks for the reaction of BL-SEC with both nickel chloride and nickel nitrate solutions with a loading of 2.5 mmol of nickel salts with 100

mg of BL-SEC. In this case there is no meaningful change in the relative intensity of the other bands in the spectrum with different stirring times.

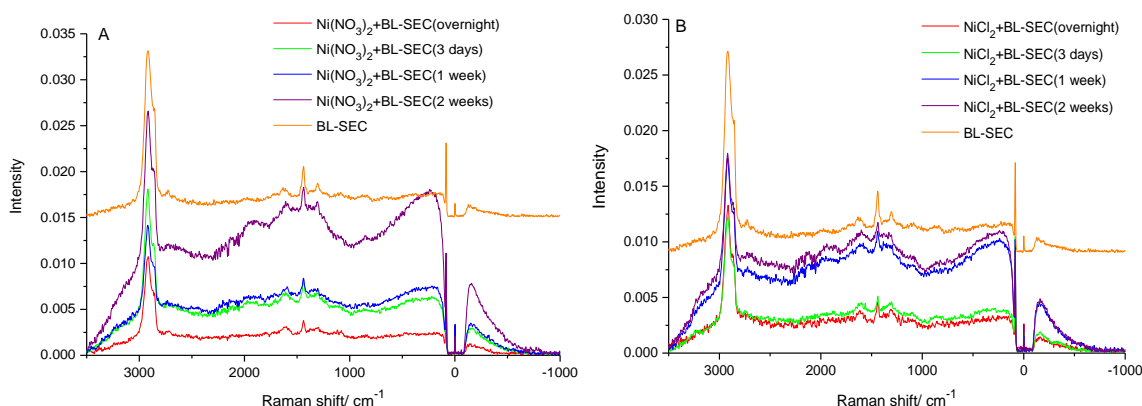


Figure 6.23 Raman spectra from $\text{Ni}(\text{NO}_3)_2$ with bleached SEC (2.5 mmol:100 mg), (B) Raman spectra from NiCl_2 with bleached SEC (2.5 mmol:100 mg).

On the other hand, the zinc with bleached SEC yielded slightly different results. There is evidence of fluorescence for the zinc samples, but the underlying sporopollenin spectral features can still be observed. The fluorescence increases with stirring time as for the nickel samples.

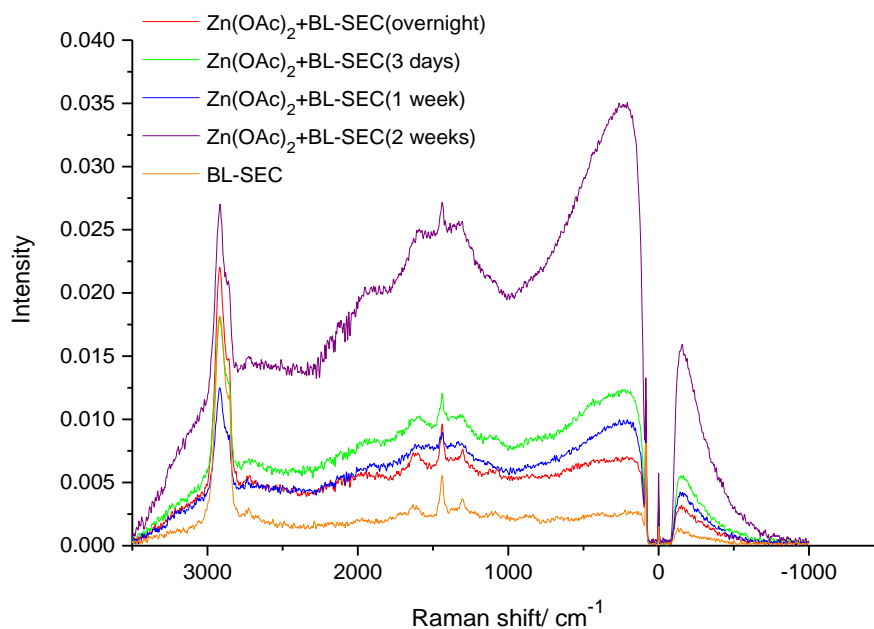


Figure 6.24 (A) Raman spectra from $\text{Zn}(\text{OAc})_2$ with BL-SECs (2.5 mmol:100 mg) (B) Expanded Raman spectra from $\text{Zn}(\text{OAc})_2$ with BL-SECs.

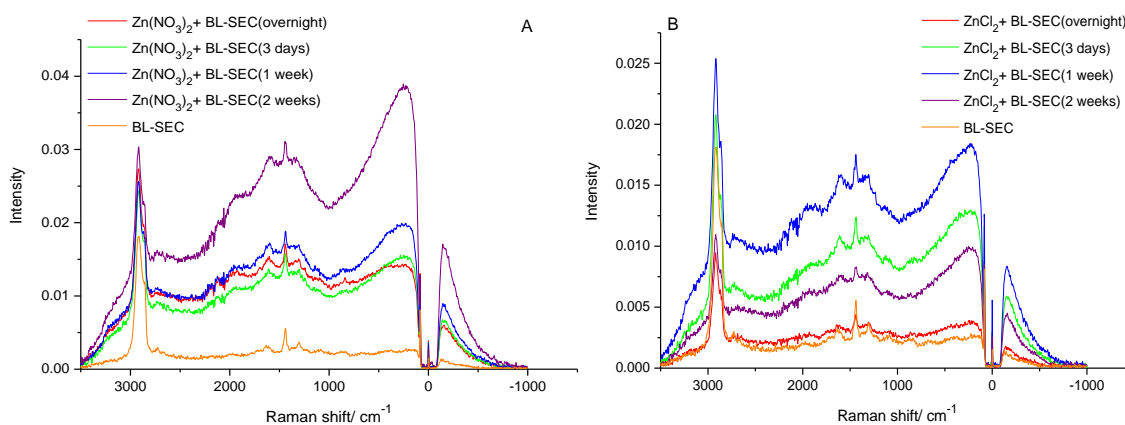


Figure 6.25 Raman spectra from $\text{Zn}(\text{NO}_3)_2$ with BL-SECs (2.5 mmol:100 mg), (B) Raman spectra from ZnCl_2 with BL-SECs (2.5 mmol:100 mg).

6.5.3 Nuclear Magnetic Resonance Spectroscopy (NMR)

^{13}C Solid State NMR has been used to identify the structure of a number of SECs with Zn salts as zinc chloride, zinc nitrate and zinc acetate. All of SECs all spectra have similar structural characteristics, but there are show some significant differences between them, some functional groups have been found by solid-state ^{13}C NMR,^{33, 34, 106} as aliphatic carbons including methyls, oxygenated functions, olefinic and aromatic unsaturations, carboxylic acids and esters. Other studies^{39, 52} showed the features of sporopollenin as unsaturations, phenols, carboxylic acids, ethers and hydroxyls.

Shaw and Yeadon⁴⁹ showed that this analyses was capable for identifying variation in a wide range of compounds involved under the general term sporopollenin. This led to their viewpoint that sporopollenin was a polymerised fatty acid, based on the high proportion of aliphatics shown by their analysis.

The ^{13}C NMR spectra from zinc acetate, zinc chloride and zinc nitrate with BL-SECs and BR-SECs are shown in Figure 6.26, the spectra indicated some of the functional groups. Features in the spectra between 15 and 40 ppm indicate aliphatic carbon,³³ a peak at about 69 ppm is indicative of C-O units. The peak at around 170-175 ppm indicate to presence of ester or carboxylic acid groups.^{33, 52} All spectra show peaks at 90-95 ppm that are likely to be from aromatics and peaks at 120- 140 ppm, show the presence of aromatic or olefinic carbons. For the zinc acetate with BL-SECs the spectrum is different than that of zinc nitrate and zinc chloride with BL-SEC. However, the spectra are similar for all zinc salts with BR-SECs.

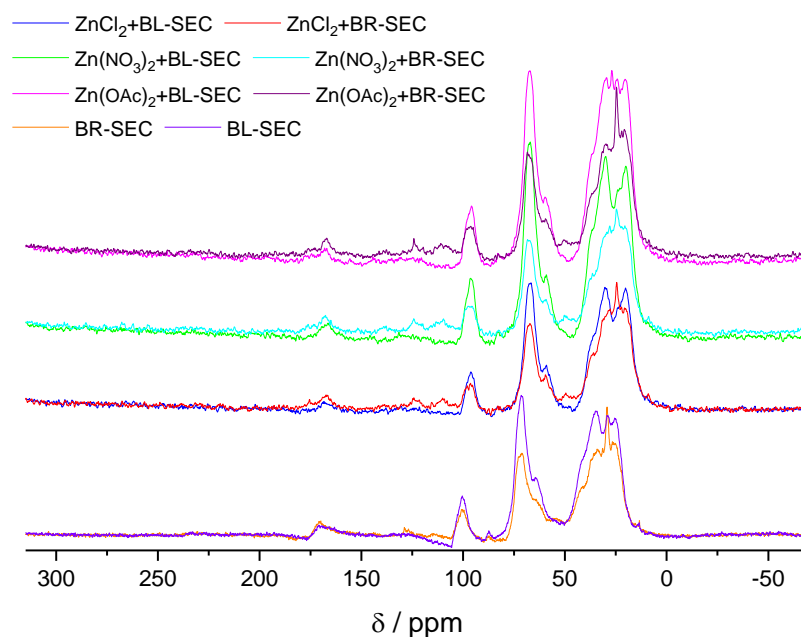


Figure 6.26 NMR data for Zinc salts with BL-SEC and BR-SEC.

6.5.4 X-Ray absorption spectroscopy

The aim of these X-ray absorption experiments is to identify the mode of coordination of metals to the surfaces of the SECs so that the type and number of the surface binding groups can be identified. Whilst the expectation is that octahedral coordination to O-donor ligands will be favoured for the 3d transition elements, there is no experimental data available, so these XANES and EXAFS experiments will provide the first structural data. The XANES spectra are distinctive for different oxidation states and geometries,^{206, 207, 208} and the EXAFS gives local structural information.

To provide enough sample for these experiments, the protocol was modified to use 7.5 mmol of the zinc and nickel salt and 300 mg of BL-SECs and BR-SECs. In line with previous experiments,¹⁰¹ the samples were stirred three days, and dried in a desiccator.

6.5.4.1 X-Ray analyses for nickel salts

The XAS spectra were calibrated using the first maximum in the first derivative spectrum of a nickel foil (8333.0 eV). The edge positions in the XANES spectra were defined as the energy corresponding to a normalised absorbance of 0.5. Figure 6.27 shows the Ni K-edge

XANES data for Ni(OAc)₂, Ni(NO₃)₂ and NiCl₂ as well as nickel salts with brown and bleached SECs. The weak pre-edge features are due to 1s-3d transitions, and in all cases they are consistent with an octahedral environment,²⁰⁷ which is consistent with the known structures²⁰⁹⁻²¹⁴ for these Ni salts. Ni(OAc)₂·4H₂O²¹² and Ni(NO₃)₂·4H₂O^{210, 211} are octahedral, and NiCl₂·6H₂O is six coordinate with two *trans* chlorine atoms.^{213, 214} All the Ni K-edge XANES spectra of the SEC samples are very similar, but there are subtle differences between the salt and the SEC sample for chloride and acetate, but the spectra of the nitrate salt and SEC samples are much more similar, indicating that the SEC structure is probably most similar to that in the nitrate salt.

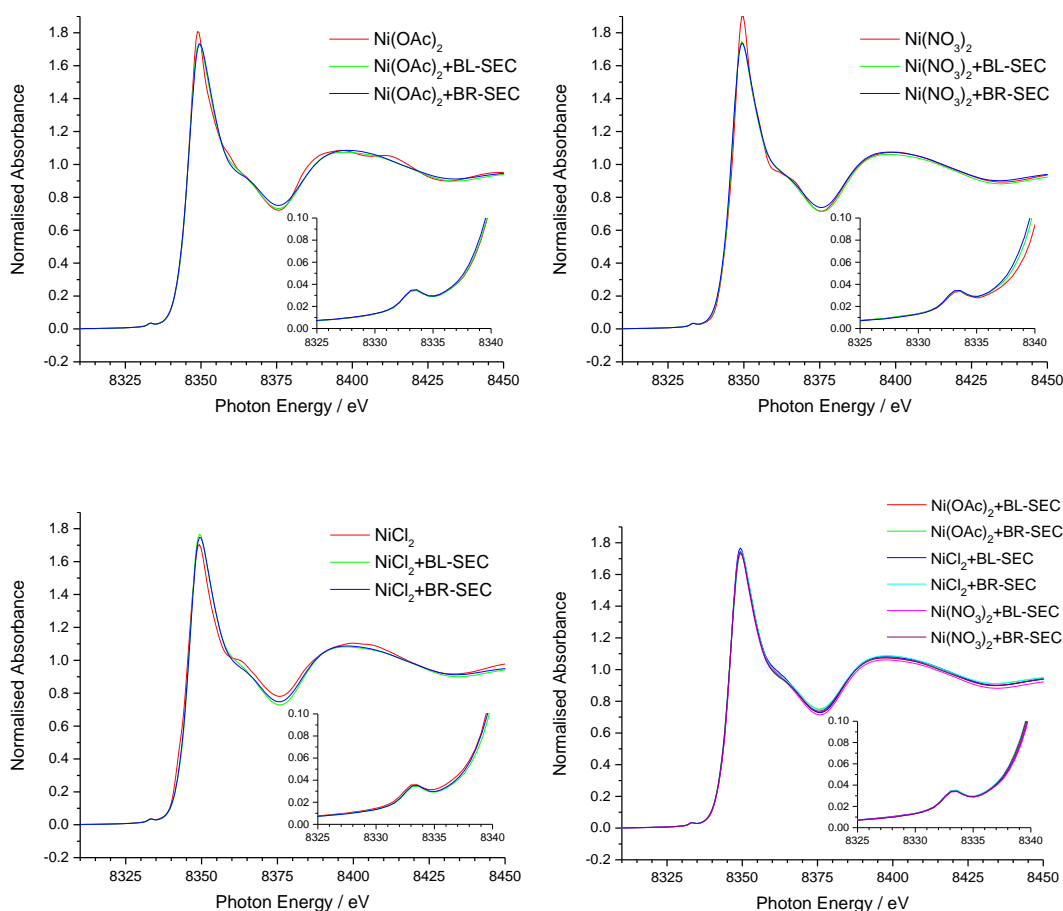


Figure 6.27 Ni K-edge XANES data for nickel(II) acetate, nickel(II) nitrate, nickel(II) chloride solutions with BL and BR-SECs, and nickel(II) salts solution with BL and BR-SECs.

Ni K-edge EXAFS analysis of nickel acetate, nickel nitrate and nickel chloride salts are shown in Figure 6.28, refinement of the data yielded a nickel oxygen bond length in Ni(II) acetate of 2.06(2)Å, in Ni(II) nitrate of 2.05(2)Å and in Ni(II) chloride of 2.05(2)Å, with Debye-Waller factors ($2\sigma^2$) of 0.01, 0.01 and 0.008Å², respectively.

These compare favourably with the diffraction which indicates an octahedral environment for $\text{Ni}(\text{OAc})_2 \cdot 4\text{H}_2\text{O}$,²¹² and $\text{NiCl}_2 \cdot 6\text{H}_2\text{O}$.^{213, 214}

The Ni K-edge EXAFS analysis of $\text{Ni}(\text{NO}_3)_2 \cdot 4\text{H}_2\text{O}$ gave a Ni-O bond length of 2.05(2) Å. The X-ray structure determination shows an octahedral environment with four oxygen atoms from water molecules at an average of 2.06 Å, and two oxygen atoms from the nitrate ions at 2.06 Å in the first coordination sphere.^{210, 211} Ni K-edge EXAFS analysis of $\text{Ni}(\text{OAc})_2 \cdot 4\text{H}_2\text{O}$, gave a Ni-O bond length of 2.06(4) Å. The X-ray structure shows there are four oxygen atoms from water molecules at an average of 2.08 Å and two oxygen atoms from monodentate acetates at 2.12 Å making up the octahedral coordination sphere.²¹² For $\text{NiCl}_2 \cdot 6\text{H}_2\text{O}$, the Ni K-edge EXAFS analysis gave a Ni-O bond length of 2.05(2) Å and Ni-Cl bond length of 2.36 Å, and this gave a substantially better fit (27.5%) than with six oxygens (41.6%). The X-ray structure determination shows that there are four oxygen atoms at 2.05 Å and two chlorine atoms *trans* to each other at 2.36 Å.^{213, 214} In nickel nitrate the average Ni-O bond length in local environment is Ni-O₆ with where the structure of nickel chloride axial Ni-Cl distances For $\text{NiCl}_2 \cdot 6\text{H}_2\text{O}$ is the two chlorine atoms at 2.36 Å, the Ni K-edge EXAFS data (Figure 6.) the first coordination environment was fitted with one shell, which is Ni-O bond of 2.07(2) Å, with Debye-Waller factor of 0.015 Å², Therefore, the structure of the nickel acetate, nitrate or chloride as coordination number 6.

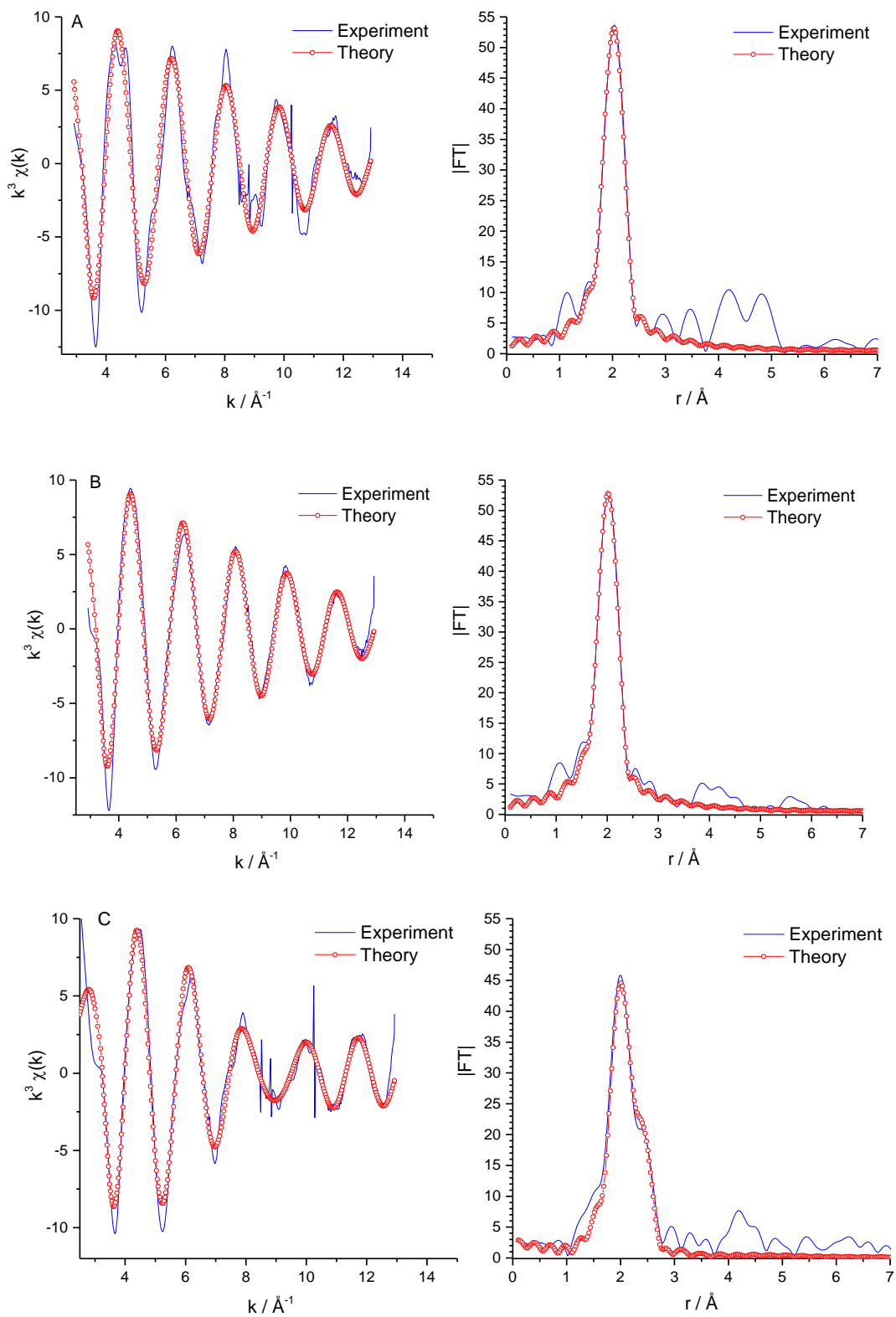


Figure 6.28 Ni K-edge EXAFS (left) and FTs (right) for (A) Ni(OAc)₂·4H₂O, (B) Ni(NO₃)₂·6H₂O, (C) NiCl₂·6H₂O.

Sample	$r/\text{\AA}$	$2\sigma^2/\text{\AA}^2$	E_f/V	FI	R
Ni-O₆					
Ni(OAc)₂·4H₂O	2.060(4)	0.010(7)	-12.1(5)	0.459	32.0
Ni(NO₃)₂·6H₂O	2.052(2)	0.010(5)	-11.9(3)	0.227	19.0
NiCl₂·6H₂O	2.051(6)	0.008(1)	-12.1(6)	0.532	27.25
Ni-Cl₂					
	2.378(11)	0.016(2)			

Table 6.11 Ni K-edge EXAFS data of Ni(OAc)₂·4H₂O, Ni(NO₃)₂·6H₂O and NiCl₂·6H₂O .

Figure 6.29 shows the plots of R (goodness of fit) vs CN, which is the coordination number, for the nickel salts as well as all the nickel samples on brown and bleached SECs. The minimum for the pure nickel samples is between a coordination number of five and six, whilst the minimum for the SEC samples appears to be slightly higher, it is clear that the coordination number is very similar in all of these, and as a result, the EXAFS analysis used a first shell coordination environment of six oxygen atoms.

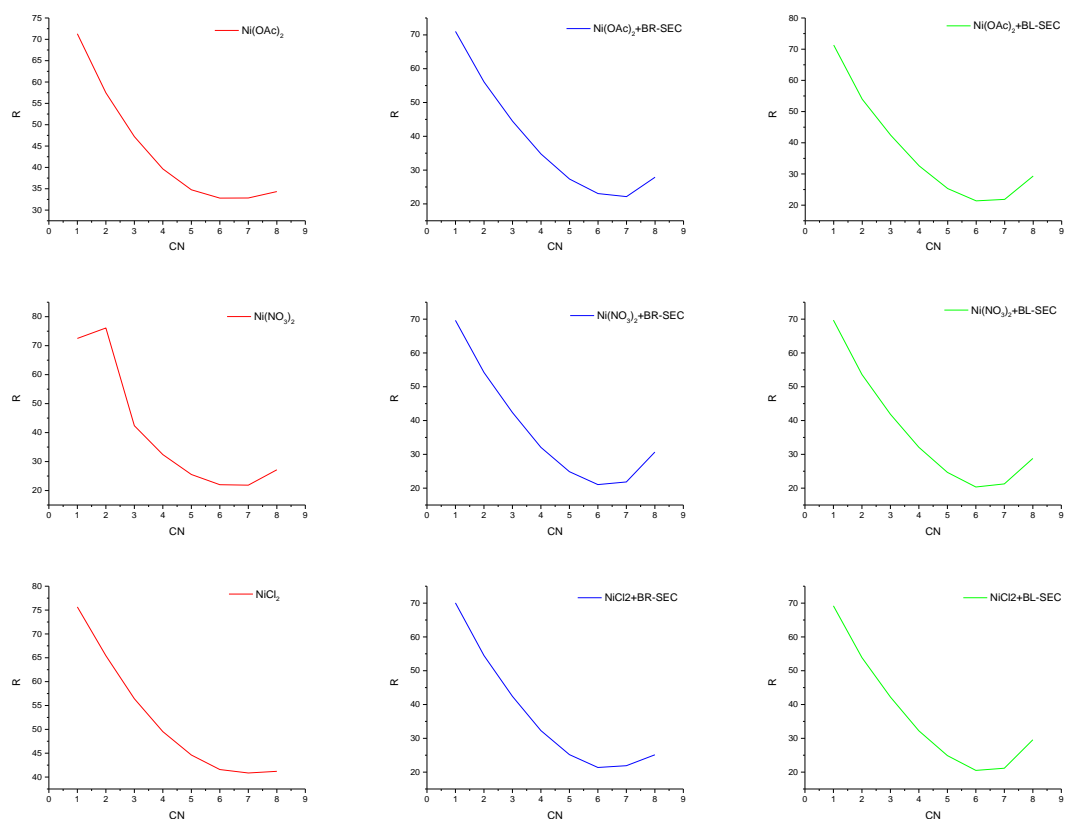


Figure 6.29 The plots of R vs CN for all nickel samples.

EXAFS data were obtained for all nickel salts samples with bleached and brown SECs. The structure of nickel contains a range of Ni-O. The figure shows Ni K-edge EXAFS and FT data recorded on BM26 of nickel salts (acetate, nitrate and chloride) adsorbed onto both brown and pale SECs. Whilst the first shell is very similar in all cases around (Ni-O 2.04 Å) (see Table 6.12). The presence of peaks in the FT implies a highly ordered environment. The Ni-O distance is essentially the same in all of the samples, irrespective of salt or SEC. There is no evidence for Cl in the materials prepared using nickel chloride solutions.

All of the D-W factors are very similar around (0.01) Å², and the same for both the BR-SEC and BL-SEC, as well as the parent salt. For the both BL-SECs and BR-SECs the FTs are similar for all of the salts indicating a slightly similar structure.

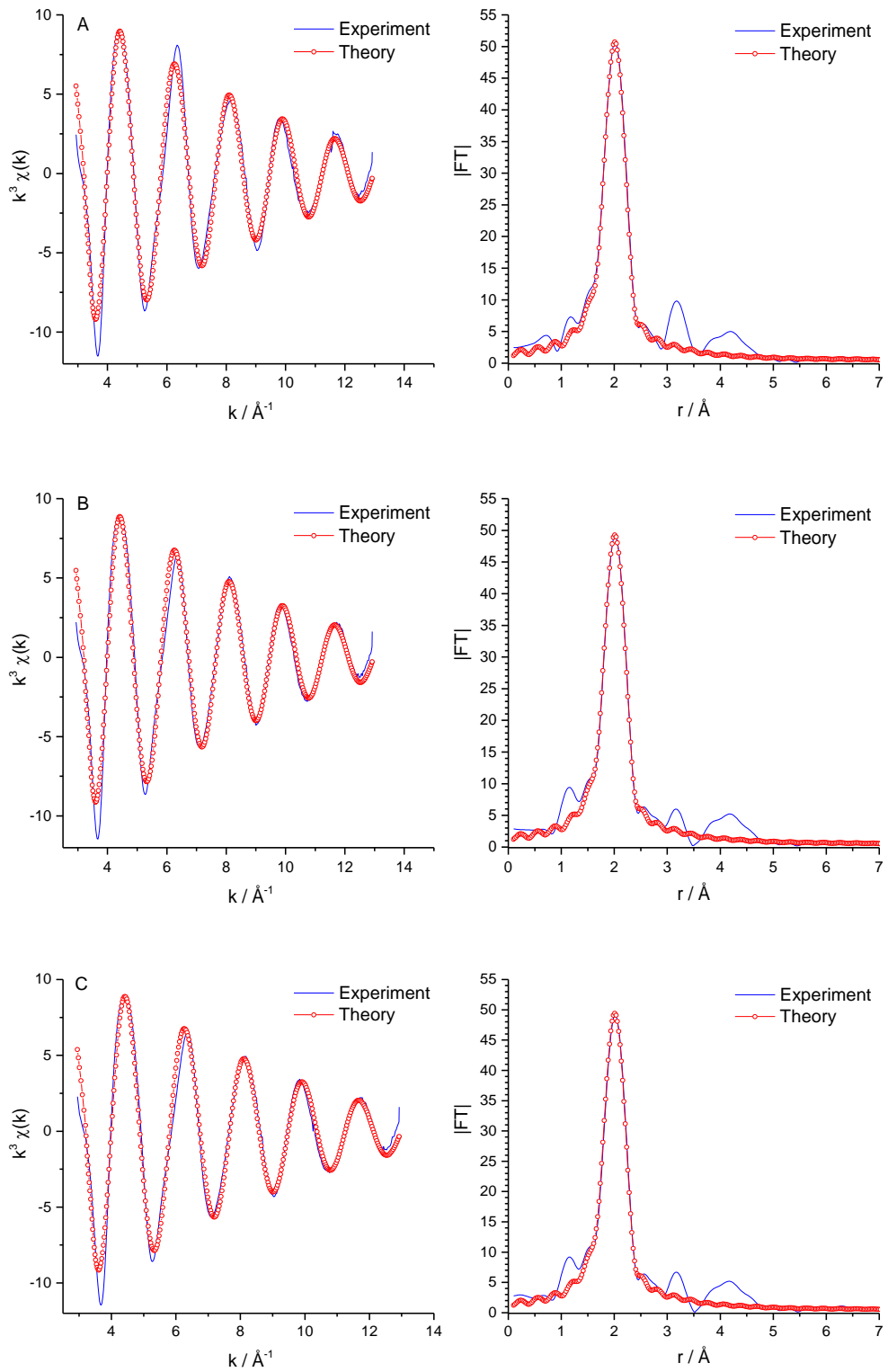


Figure 6.30 Ni K-edge EXAFS (left) and FTs (right) for (A) Ni(OAc)₂ with BR-SEC, (B) Ni(NO₃)₂ with BR-SEC, (C) NiCl₂ with BR-SEC.

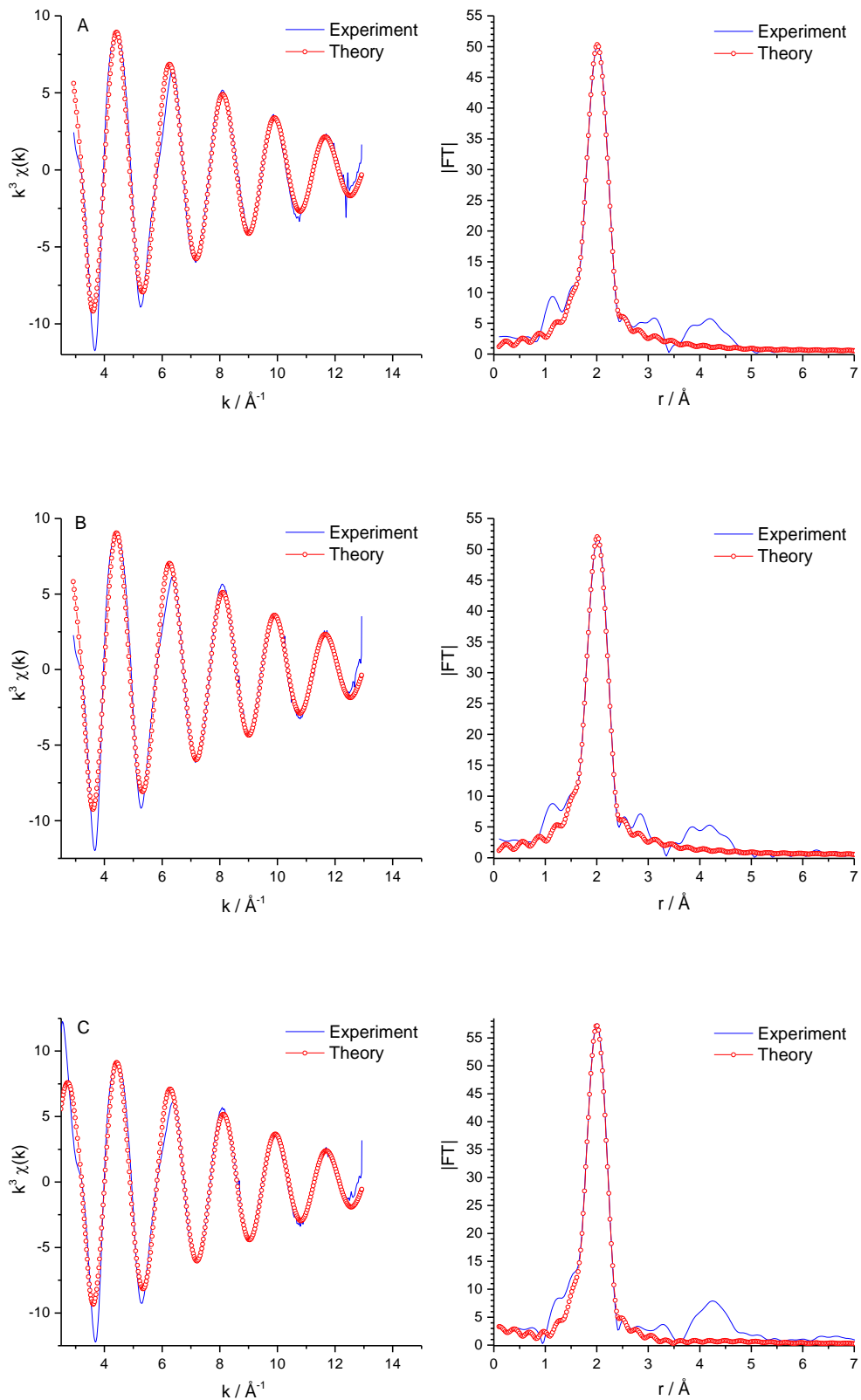


Figure 6.31 Ni K-edge EXAFS (left) and FTs (right) for (A) Ni(OAc)₂ with BL-SEC, (B) Ni(NO₃)₂ with BL-SEC, (C) NiCl₂ with BL-SEC.

Sample	Ni-O ₆	E _t /V	FI	R	
	r/Å	2σ ² /Å ²			
Ni(OAc) ₂ + BL-SEC	2.047(3)	0.0111(5)	-11.6(3)	0.215	19.1
Ni(OAc) ₂ + BR-SEC	2.048(3)	0.0110(5)	-11.6(3)	0.215	20.8
Ni(NO ₃) ₂ + BL-SEC	2.047(3)	0.0105(5)	-11.9(3)	0.212	17.6
Ni(NO ₃) ₂ + BR-SEC	2.048(3)	0.0115(5)	-11.5(3)	0.120	18.9
NiCl ₂ + BL-SEC	2.042(3)	0.0102(6)	-11.2(4)	0.306	20.8
NiCl ₂ + BR-SEC	2.046(3)	0.0115(5)	-11.3(3)	0.202	19.1

Table 6.12 Ni K-edge EXAFS data of all nickel solutions with BL and BR-SECs.

6.5.4.2 X-Ray analyses for zinc salts

The XAS spectra were calibrated using the first maximum in the first derivative spectrum of a zinc foil (9659.0eV). The edge positions in the XANES spectra were defined as the energy corresponding to a normalised absorbance of 0.5. Figure 6.32 below shows the Zn K-edge XANES data for zinc acetate and zinc nitrate as well as zinc salts reacted with brown and bleached SECs.

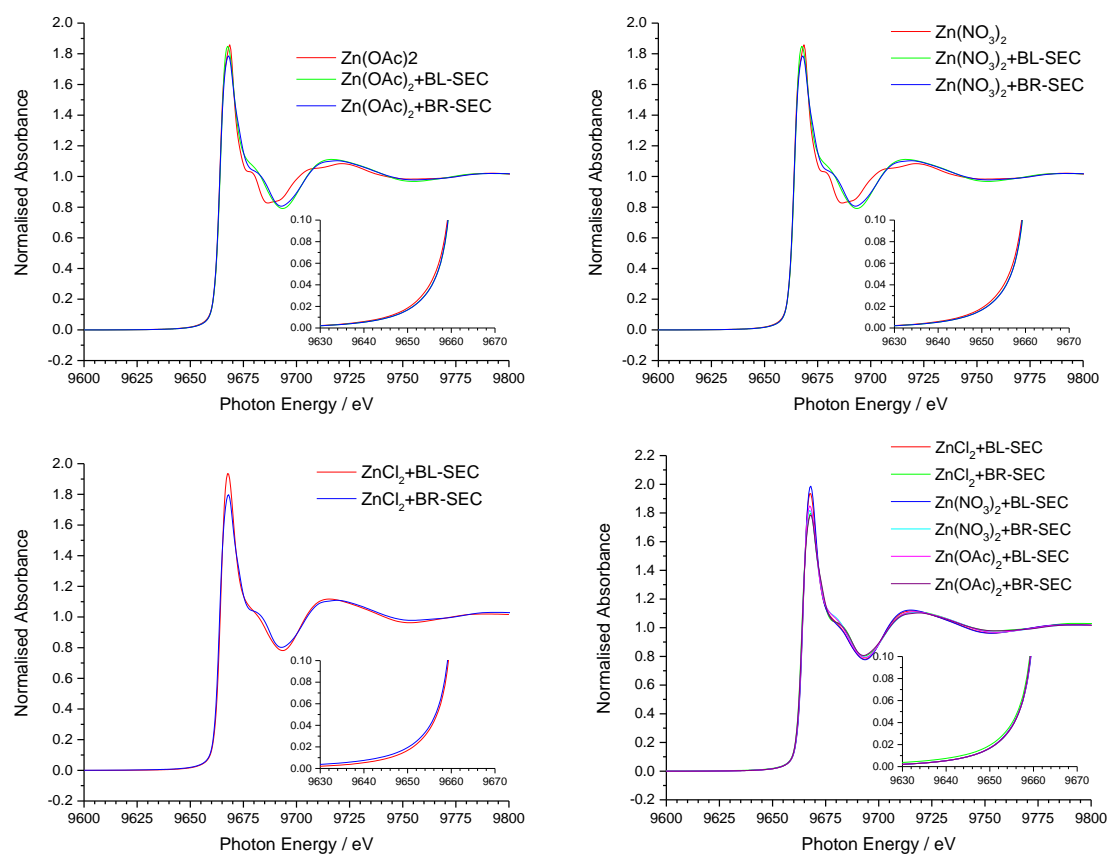


Figure 6.32 Zn K-edge XANES data for zinc(II) acetate, zinc(II) nitrate, zinc(II) chloride solutions with BL and BR-SECs, and zinc(II) salts solutions with BL and BR-SECs.

Figure 6.32 shows Zn K-edge XANES data for both bleached and brown SECs reacted with solutions of $\text{Zn}(\text{OAc})_2$, $\text{Zn}(\text{NO}_3)_2$ and ZnCl_2 . The zinc acetate and nitrate figures contain the same data. There are no $1s - 3d$ transitions in these spectra as $\text{Zn}(\text{II})$ is d^{10} and hence there are no vacancies for the $1s$ electron. The intense “white line” is due primarily to dipole allowed $1s - 4p$ transitions. Its relative intensity is dependent on the coordination environment, (more intense for octahedral light atoms).

EXAFS analysis of zinc acetate and zinc nitrate are shown in Figure 6.33, the average zinc oxygen bond length in $\text{Zn}(\text{II})$ acetate is 2.000\AA and for zinc nitrate is 2.083\AA , with Debye-Waller factors ($2\sigma^2$) of $0.0176(8)$ and $0.0193(7)\text{\AA}^2$, respectively. The structure of the anhydrous zinc acetate has a Zn-O coordination number 4,²¹⁵⁻²¹⁷ but in zinc nitrate the Zn-O coordination number is 6.²¹⁸

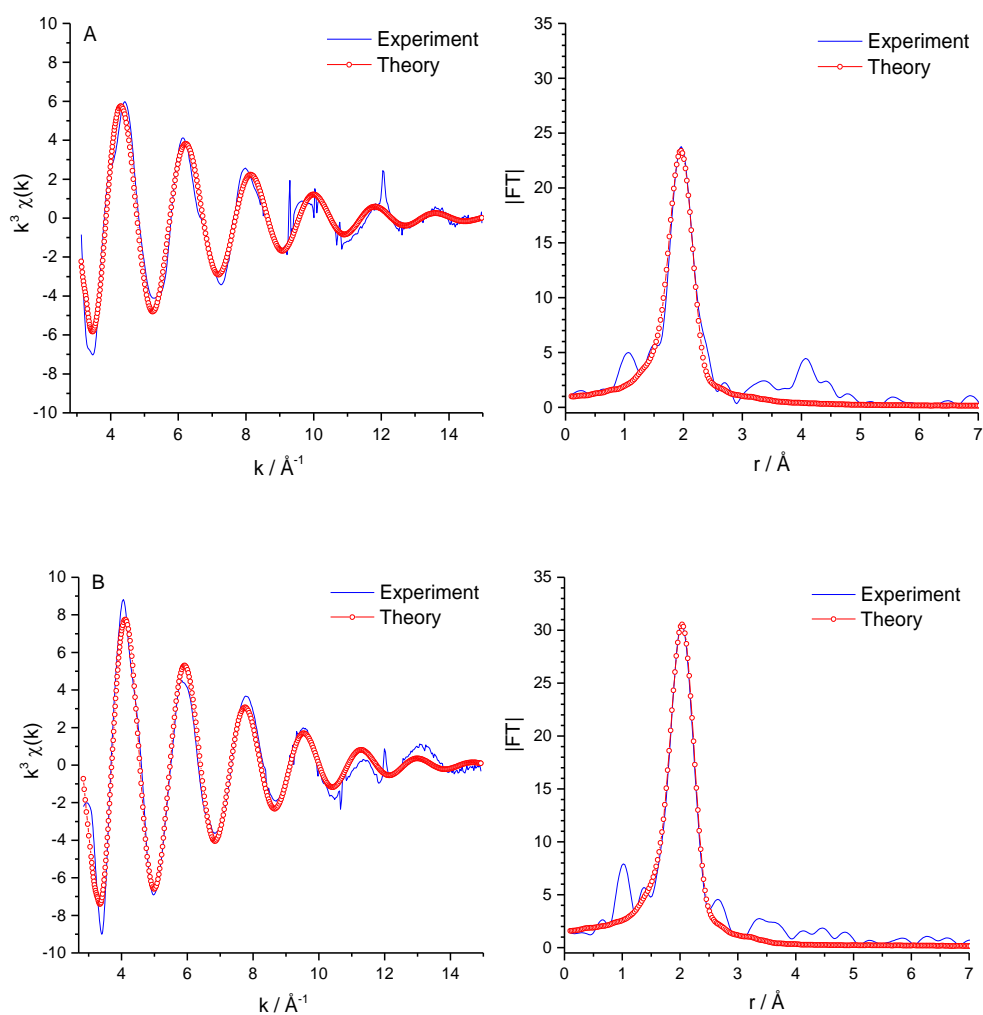


Figure 6.33 Zn K-edge EXAFS (left) and FTs (right) for (A) $\text{Zn}(\text{OAc})_2$, (B) $\text{Zn}(\text{NO}_3)_2 \cdot 6\text{H}_2\text{O}$.

Sample	Zn-O		E_f/V	FI	R
	$r/\text{\AA}$	$2\sigma^2/\text{\AA}^2$			
Zn(OAc)₂	2.001(5)	0.0176(9)	-2.9(6)	0.350	29.4
Zn(NO₃)₂·6H₂O	2.083(7)	0.0193(7)	-7.8(3)	0.231	24.9

Table 6.13 Zn K-edge EXAFS data of all zinc solutions.

Figure 6.34 shows the plots of R vs CN, which is mean the coordination number for all the zinc samples onto brown and bleached SECs the same as well as the zinc acetate and zinc nitrate. The validity of this approach is demonstrated in the data for Zn(OAc)₂ where a coordination number of four is confirmed in agreement with the X-ray crystal data.²¹⁵ In contrast the coordination number for Zn(NO₃)₂·6H₂O is six.²¹⁸ For the SEC samples the coordination number from these data is predicted to be between five and six, and six was adopted for all examples.

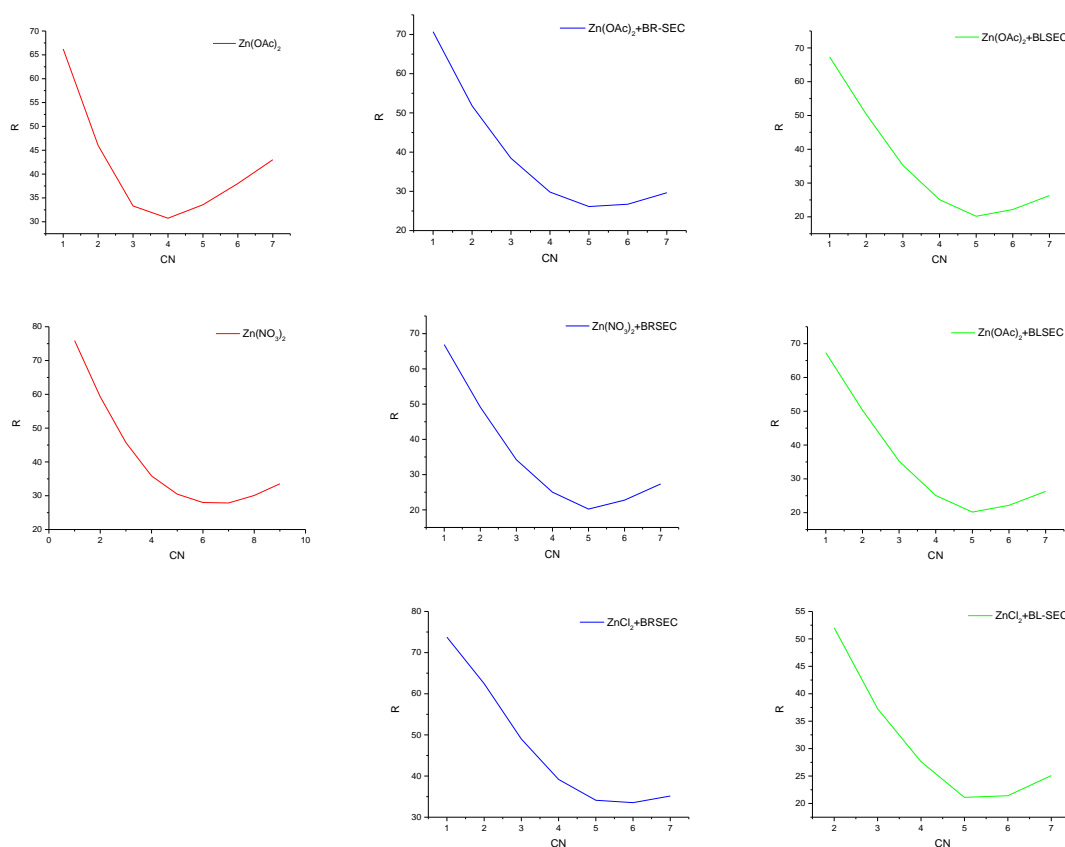


Figure 6.34 The plots of R vs CN for all zinc samples.

The Figure 6.35 and Figure 6.36 shows Zn K-edge EXAFS and FT data recorded on B18 of zinc salts (acetate, nitrate and chloride) adsorbed onto both brown and pale SECs. The first shell is very similar in both cases around with Zn-O bond lengths of ca. 2.00 Å. When zinc nitrate was used, the first Zn-O shell lengthened slightly to 2.03 Å in the bleached SEC data, but remained at 2.00 Å in the brown SEC data. A similar difference was also observed in the more remote shells observed between the bleached and brown SEC samples. The Zn-O distance is essentially the same in all of the samples, irrespective of salt or SEC. The bleached ones are very similar, but that there are some variations in the brown data, especially for the zinc chloride sample.

All of the D-W factors are very similar around (0.02) Å², and the same for both the BR-SEC and BL-SEC. For the BR-SEC the FTs are slightly similar for all of the salts indicating a slightly similar structure. For the BL-SECs, the FTs are very similar.

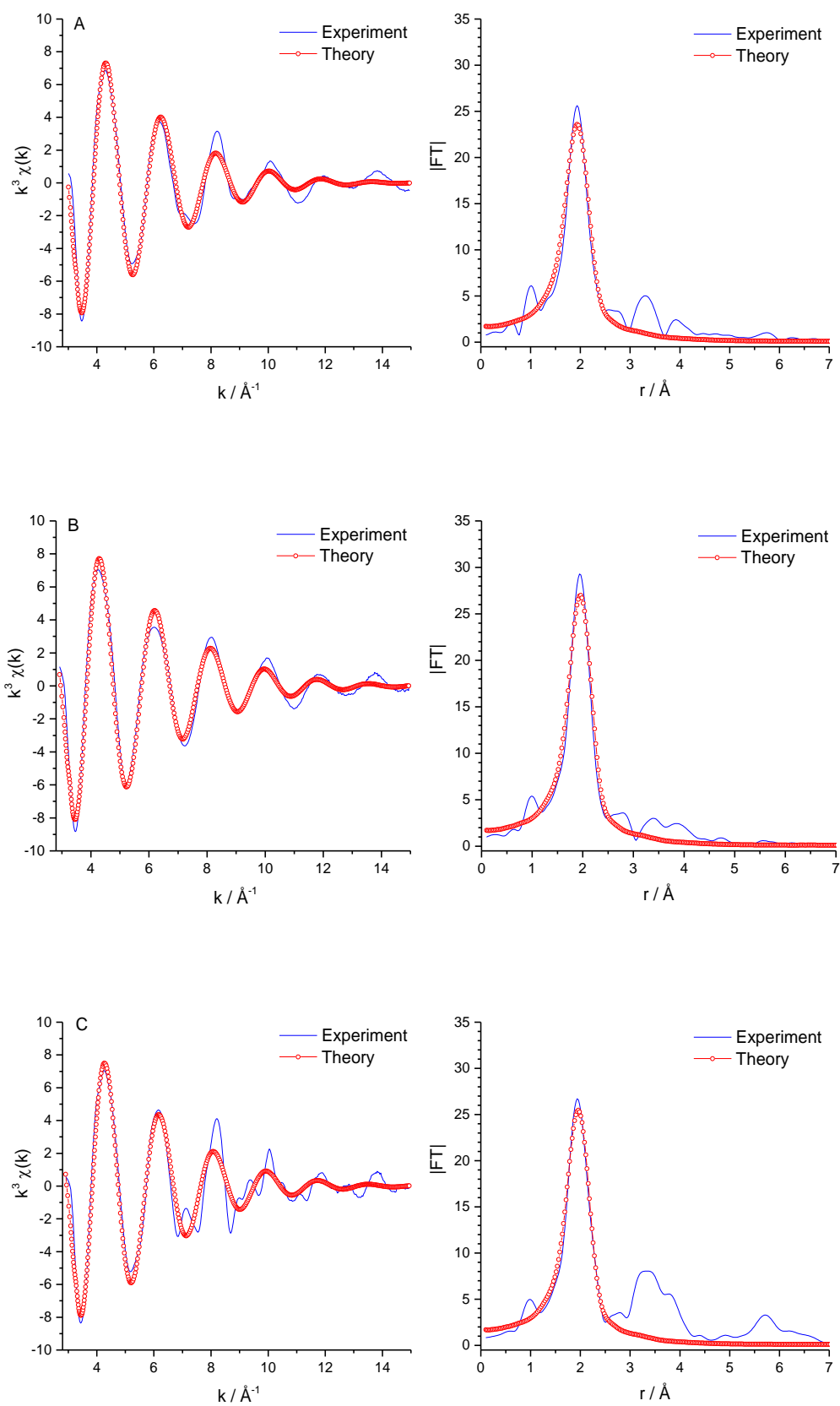


Figure 6.35 Zn K-edge EXAFS (left) and FTs (right) for (A) Zn(OAc)₂ with BR-SEC, (B) Zn(NO₃)₂ with BR-SEC, (C) ZnCl₂ with BR-SEC.

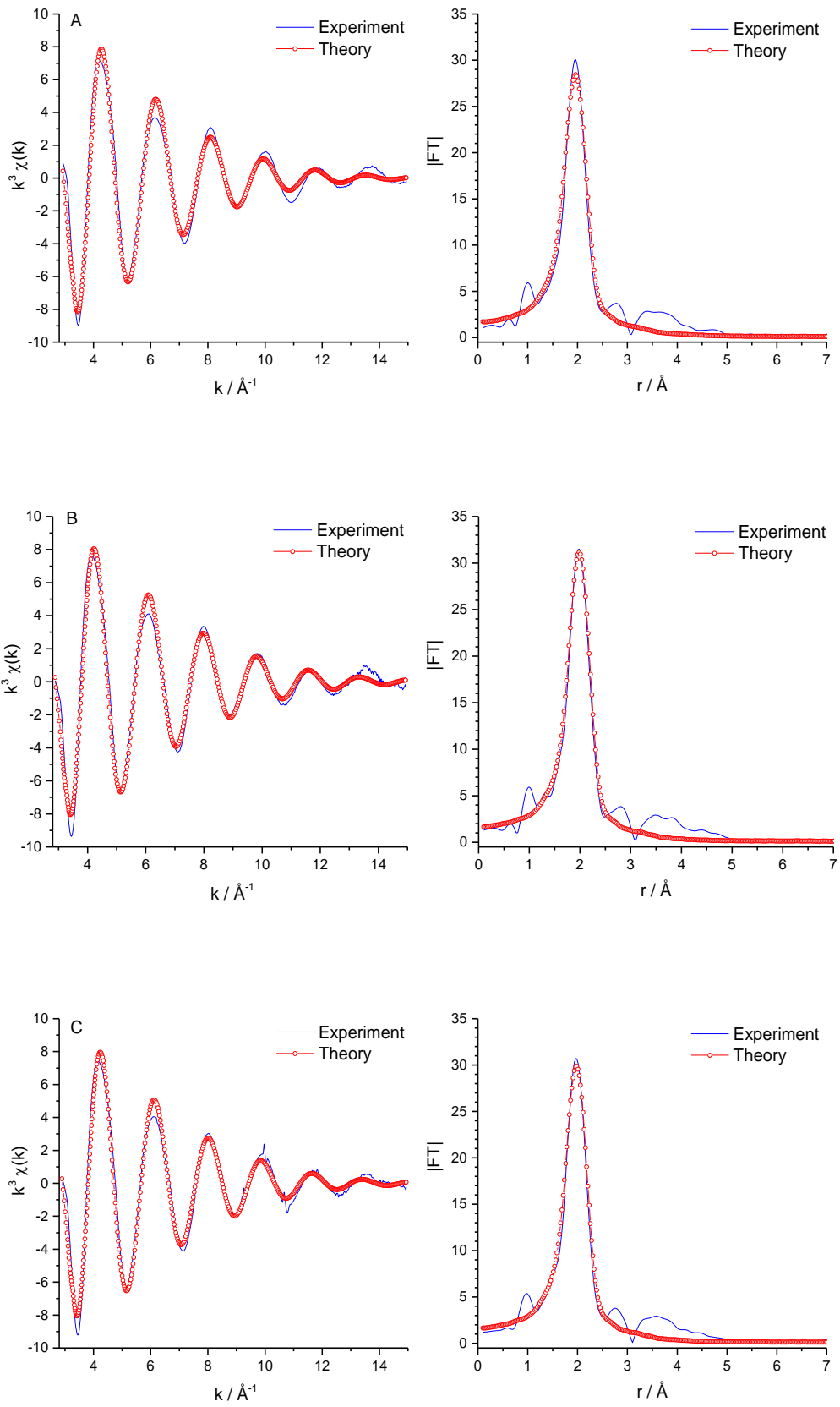


Figure 6.36 Zn K-edge EXAFS (left) and FTs (right) for (A) Zn(OAc)₂ with BL-SEC, (B) Zn(NO₃)₂ with BL-SEC, (C) ZnCl₂ with BL-SEC.

Sample	Zn-O	E _f /V	FI	R	
	r/Å	2σ ² /Å ²			
Zn(OAc)₂+ BL-SEC	2.013(4)	0.022(7)	-6.4 (3)	0.17	21.0
Zn(OAc)₂+ BR-SEC	1.999(5)	0.027(9)	-5.4(4)	0.25	25.1
Zn(NO₃)₂+ BL-SEC	2.035(3)	0.020(6)	-7.1(3)	0.17	19.6
Zn(NO₃)₂+ BR-SEC	2.007(3)	0.023(7)	-6.4(3)	0.18	21.6
ZnCl₂+ BL-SEC	2.028(3)	0.021(6)	-6.8(3)	0.16	19.7
ZnCl₂+ BR-SEC	2.015(5)	0.025(10)	-6.7(4)	0.39	31.5

Table 6.14 Zn K-edge EXAFS data of all zinc solutions with BL and BR-SECs.

For all nickel salts with bleached and brown SECs the EXAFS data showed that the coordination number for all the nickel samples onto brown and bleached SECs is the same number which is 6, the local environment around the nickel contains Ni-O distances of *ca.* 2.05 Å. The Zn K-edge EXAFS data shows that the local environment around the zinc is probably octahedral with a range of Zn-O distances from 2.00 to 2.04 Å.

6.5.5 XRF images

XRF images were used to help identify whether the interaction between nickel, zinc and the SECs was specific or more general in nature, and whether the SECs were filled with nickel and zinc.

Figure 6.37 shows the Ni K_α XRF image of the BL-SECs and BR-SECs prepared from a nickel acetate solution stirred for three days. The physical structure of the SECs can be clearly seen in these images indicating that the nickel is closely associated with the BL- SEC or BR-SEC structure.

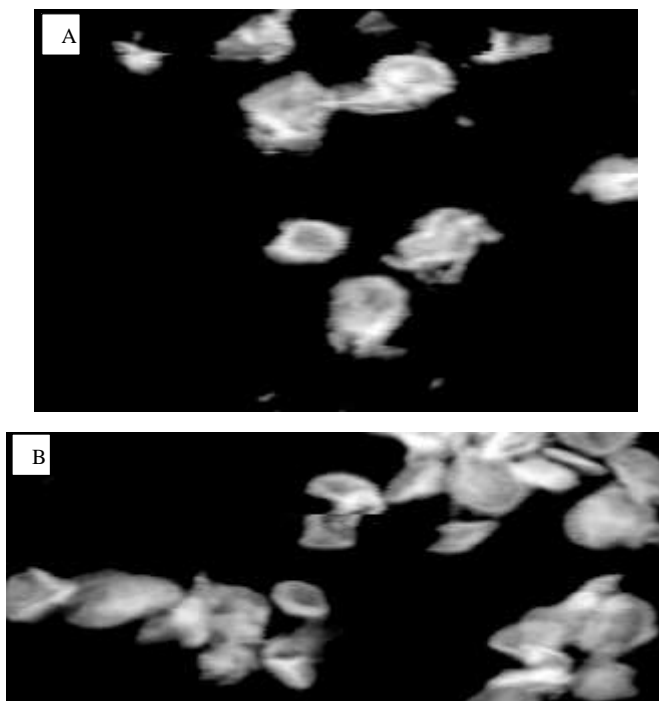


Figure 6.37 Ni K_{α} XRF images stirred three days. (A) BR-SECs with 7.5 mmol: 300 mg, of nickel(II) acetate solution. (B) BL-SECs with 7.5 mmol: 300 mg of nickel(II) acetate solution.

Figure 6.38 shows the Ni K_{α} XRF image of the BL-SECs and BR-SECs prepared from a nickel chloride solution at 7.5 mmol with stirring for three days. It can be seen that the nickel is associated with the BL- SEC or BR-SEC structure. The data is sufficiently sensitive that can see both whole and broken SECs.

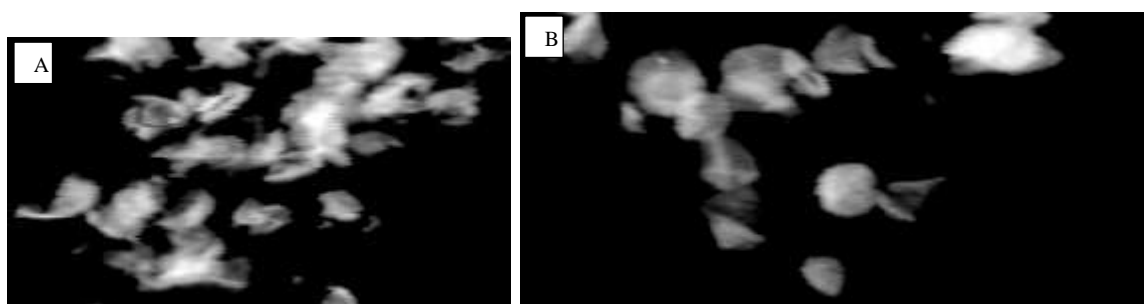


Figure 6.38 Ni K_{α} XRF images stirred three days. (A) BR-SECs with 7.5 mmol: 300 mg of nickel(II) chloride solution. (B) BL-SECs with 7.5 mmol: 300 mg of nickel(II) chloride solution.

Figure 6.39 shows the Ni K_{α} XRF image of the BR-SECs and BL-SECs prepared from a nickel nitrate solution in 7.5 mmol with stirring three days, the images indicate that the nickel is associated with BR-SEC and BL-SECs structure.

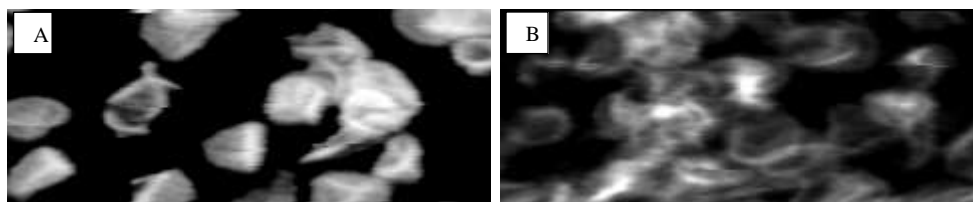


Figure 6.39 Ni K_{α} XRF images stirred three days. (A) BR-SECs with 7.5 mmol: 300 mg of nickel(II) nitrate solution. (B) BL-SECs with 7.5 mmol: 300 mg of nickel(II) nitrate solution.

Figure 6.40 shows the Zn K_{α} XRF image of the BL-SECs and BR-SECs reacted with a zinc acetate solution at 7.5 mmol with stirring three days. It can be seen that the zinc is associated with the BL- SEC or BR-SEC structure. The data are sufficiently sensitive that both whole and broken SECs can be observed.

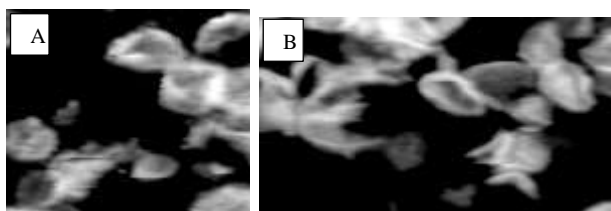


Figure 6.40 Zn K_{α} XRF images stirred three days. (A) BR-SECs with 7.5 mmol: 300 mg of zinc(II) acetate solution. (B) BL-SECs with 7.5 mmol: 300 mg of zinc(II) acetate solution.

Figure 6.41 shows the Zn K_{α} XRF image of the BL-SECs and BR-SECs reacted with a 0.1 M zinc chloride solution stirred for three days. The physical structure of the SECs can be clearly seen in these images indicating that the zinc is closely associated with the BL- SEC or BR-SEC structure.

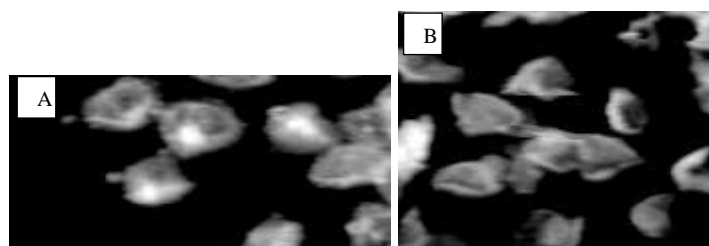


Figure 6.41 Zn K_{α} XRF images stirred three days. (A) BR-SECs with 7.5 mmol: 300 mg of zinc(II) chloride solution. (B) BL-SECs with 7.5 mmol: 300 mg of zinc(II) chloride solution.

Figure 6.42 shows the Zn K_{α} XRF image of the both broken BR-SECs and BL-SECs prepared from a zinc nitrate solution in 7.5 mmol with stirring three days, the images indicated that the zinc is associated with BR-SEC and BL-SECs structure.

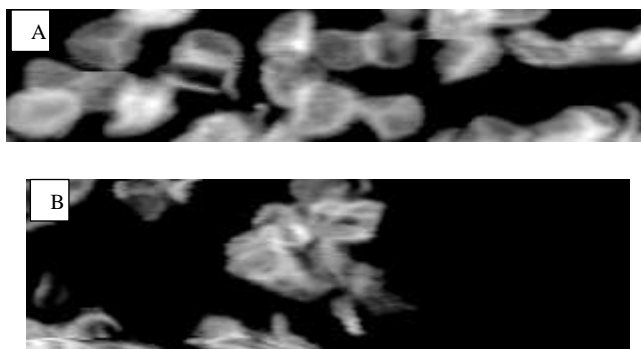


Figure 6.42 Zn K_{α} XRF images stirred three days. (A) BR-SECs with 7.5 mmol: 300 mg of zinc(II) nitrate solution. (B) BL-SECs with 7.5 mmol: 300 mg of zinc(II) nitrate solution.

In conclusion, the Ni K_{α} XRF and Zn K_{α} XRF images show that the interaction between nickel, zinc and the SECs is similar for all nickel(II) salts and zinc(II) salts with a high correlation between SECs structure and nickel(II) or zinc(II) location. Also, the fact that the structure of the SECs is clearly visible in these images indicates that the nickel and zinc are closely associated with the BL- SEC or BR-SEC structure. There is no evidence for a build up of nickel and zinc with the SEC structures, which was also observed in the SEM images.

6.4 Conclusion

The amount of metal (nickel and zinc) in the samples is approximately the same for all stirring times and loadings, but is dependent on the metal salt used. This is unexpected, because extended stirring should increase the amounts of the metals attached to the SECs. The best attachment rate to the SECs is for acetate compared to chloride and nitrate. The optimal experimental conditions were found to be stirring for three days 0.1 M metal solutions with either 100 mg of SECs in 25 mL of water or 300 mg of SECs in 75 mL of water.

Furthermore, by applying IR and Raman spectroscopy, one can observe the functional groups in the spore metal complexes. Due to the diminished fluorescence of the bleached SEC from *L. clavatum*, Raman spectra could be obtained, but unfortunately there does not appear to be any significant difference in the Raman spectra of the metal loaded SEC compared to the bleached SEC itself. In addition, the IR technique can be used to observe the functional groups of SEC with the metal complexes. It was found that the overall features of the SEC infrared spectra highlighted the significance of aliphatic chains in the macromolecule. Interpretations are more or less precise relying on the quality of the spectra, but the prime bands consistently revealed hydroxyls, aliphatic carbons, carbonyls,

unsaturated hydrocarbons and ether groups. Probably the most important observation is that the IR spectrum of the acetate samples are different from that of the parent SEC. For nickel this also appears to be the case, but for zinc it is less clear.

The ^{13}C NMR spectra for the zinc acetate with BL-SECs is different than that of zinc nitrate and zinc chloride with BL-SEC. However, the spectra are similar for all zinc salts with BR-SECs.

From all nickel salts with bleached and brown SECs the EXAFS data showed that the coordination number for all the nickel samples onto brown and bleached SECs the same number which is 6, the local environment around the nickel contains a range of Ni-O distances. The local environment around the zinc contains a range of Zn-O distances. (2.00 – 2.04 Å) with a coordination number of six.

The Ni K_{α} XRF and Zn K_{α} XRF images showed that the interaction between nickel, zinc and the SECs is similar for all nickel(II) salts and zinc(II) salts with a high correlation between SECs structure and nickel(II) or zinc(II) location. Moreover, the fact that the structure of the SECs is clearly visible in these images indicates that the nickel and zinc are closely associated with the SEC structure.

Taken together, these results show that the nickel and zinc adopt a monomeric octahedral coordination environment when attached to the SEC surface. The higher loadings observed for acetate compared to nitrate and chloride as well as the presence of characteristic IR spectra indicate that the acetate groups are part of the coordination environment, as well as the surface carboxylate and phenolic surface groups. Figure 6.43 shows schematic illustrations of possible surface structures of nickel or zinc interacting with the SEC surface. Figure 6.43(A) and (C) include acetate, whereas Figure 6.43(B) is representative of the samples derived from chloride and nitrate.

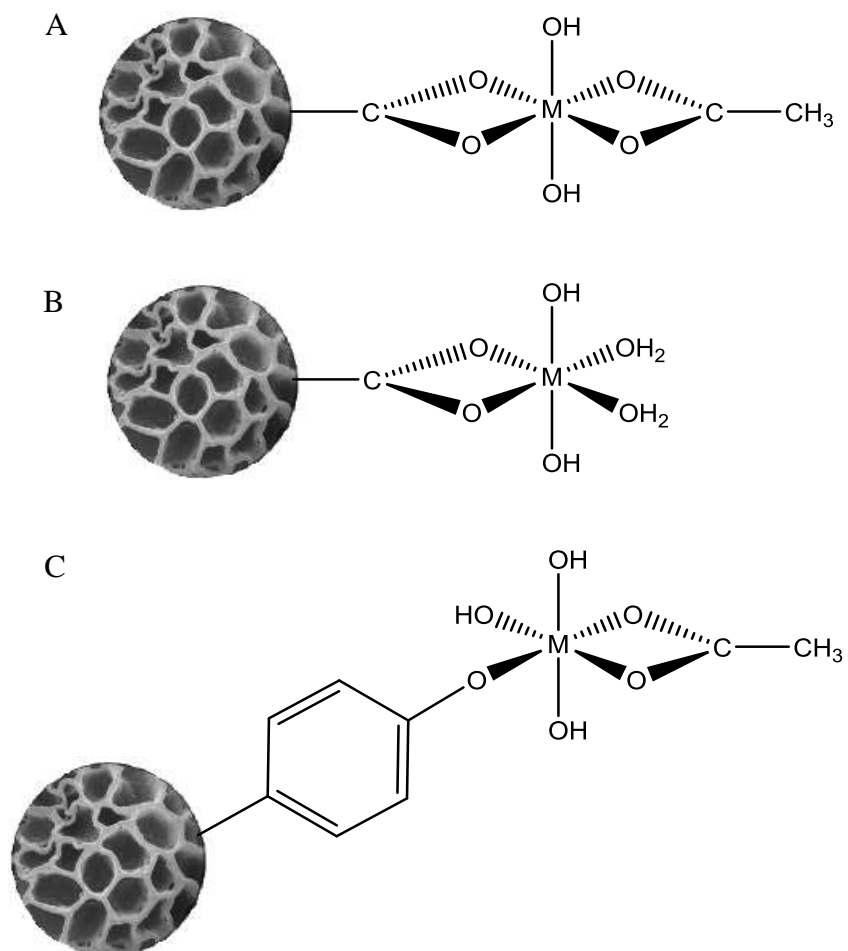


Figure 6.43 Schematic illustrations of interaction of metals (M = Ni, Zn) with SEC surface. (A) metal acetate with carboxylate on SEC surface, (B) metal chloride or nitrate with carboxylate on SEC surface and (C) metal acetate with phenolate on SEC surface.

Chapter 7

***In vitro* assessment of encapsulation and release of proteins using sporopollenin**

7 Encapsulation and release studies

7.1 Introduction

7.1.1 Encapsulation of proteins for drug delivery

The encapsulation of protein drugs for oral administration and sustained drug release is a highly attractive procedure but there are still important challenges in the biotechnology of this process that need to improve.²¹⁹⁻²²¹ Antibodies and hormones are examples of the development of recombinant protein drugs which have high molecular weights and are highly sensitive to environmental conditions.²²² One of the main drawbacks of protein drugs is the degradation that occurs on attempting oral administration that is related to the acidic environment in the stomach and the gastrointestinal tract. Moreover, poor absorption into the blood stream is observed for these substances when administered orally due to their high molecular weight.^{222, 223} Protein drugs can be prepared for controlled release drug delivery by the use of polymers and they can also be formulated into pH-sensitive released and into nanoparticles.²²⁴ A wide variety of hydrogels made from natural and synthetic polymers may be used as pH-sensitive hydrogels for the controlled delivery.²²⁵ A hydrogel is a three-dimensional network that shows the ability to swell in water and retains a significant fraction of water within its structure. Their ability to absorb water is due to the presence of hydrophilic groups such as –OH, –CONH–, –CONH₂, –COOH, and –SO₃H.²²⁴

Silica materials, nanoparticles and peptide based nanostructures have been used to stably encapsulate proteins and provide useful release profiles for the drug in model some systems with some progressing to clinical trials.²²⁶⁻²²⁸

7.1.2 Potential of microencapsulation

Encapsulating, transporting and selectively releasing active components, for example drugs within the bloodstream, can be achieved by the use of the polymeric material in the form of a microcapsule. The key properties for an oral delivery microcapsule are; an empty spherical nature, inertness, consistent size, and the ability to be ingested orally with no ill effects (non-toxic) and, ideally, to pass into the blood stream *via* the digestive system.^{73, 79} The capsule should be resistant to rapid biological breakdown, but it should be

susceptibility to more controlled degradation within the bloodstream to allow for the targeted release of the encapsulated components in the bloodstream.⁷³

Protection of the contents from degradation by UV light as well as chemical resistance would make an ideal material for encapsulating active components. This could potentially extend the shelf life of actives encapsulated into the sample.⁸⁰

The use of a polymer to support or carry a drug or bioactive agent will give a controlled drug delivery systems.⁸⁴ Once inside the body, the release of the drug from the polymer should occur a pre-determined rate. For applications in drug delivery, both synthetic and natural polymers have been widely investigated.⁸³ The need to be both physically and mechanically stable support the use of polymeric materials. They should have both a sufficient high drug loading capacity and reasonable rate of biodegradation to be effective, with both the support and degradation products being non-toxic. Finally, they should be cheap and easy to prepare.

Sporopollenin exines fit these criteria and there has been work carried out to load sporopollenin with active components. Many of the currently used methods have limitations and so more effective and versatile approaches of loading are the focus of development at present, with sporopollenin as an interesting new encapsulation agent.⁸¹ The delivery of highly potent macromolecules, such as nucleic acids, proteins or peptides, to the body using sporopollenin has received attention recently.^{81, 82} The use of sporopollenin in drug delivery could potentially replace the use of injections with oral formulations. This would allow protected oral administration of the sensitive biomacromolecular drug and potentially controlled release. High concentrations immediately after administration can create toxic side effects which could be solved by a controlled drug delivery system, allowing a drug to remain at a constant concentration in the blood for an extended period of time.⁸³

7.2 Flow cytometry

Methods are required to monitor and count cells to determine their properties. These methods can also be used to track the interactions of fluorescent dyes or biomolecules tagged with fluorescent dyes with the cells. To determine if an antibody binds to a target,

a fluorescently tagged antibody can be directly detected in the cells by the intensity of the fluorescence signal.

Flow cytometry is a method for counting and analysing cells that are suspended in a stream of liquid.²²⁹ Incubation with a fluorophore into the cells would take a place before analysis; the intensity of fluorescence, depending on the assay type, will lead to different conclusions. There are three parts that make up a standard flow cytometer: 1) sensing system and laser light source, 2) the control of the movement of the cells by a hydraulic system and 3) collating the data and presenting it in an understandable format by a computer system. A technique called sheath flow is used, where the cells are taken up into the sensing system and drawn into a stream. This ensures that the individual analysis of the cells occurs as they pass through the point of detection. The fluorescence of the fluorophore in the cells is initiated as the cells pass through the light source, which is most commonly a laser. Recording and conversion of the fluorescence signals into readings of electrical pulses occurs, which are subsequently changed into a numerical readout. Presentation of the results is normally produced in the form of histograms.²³⁰

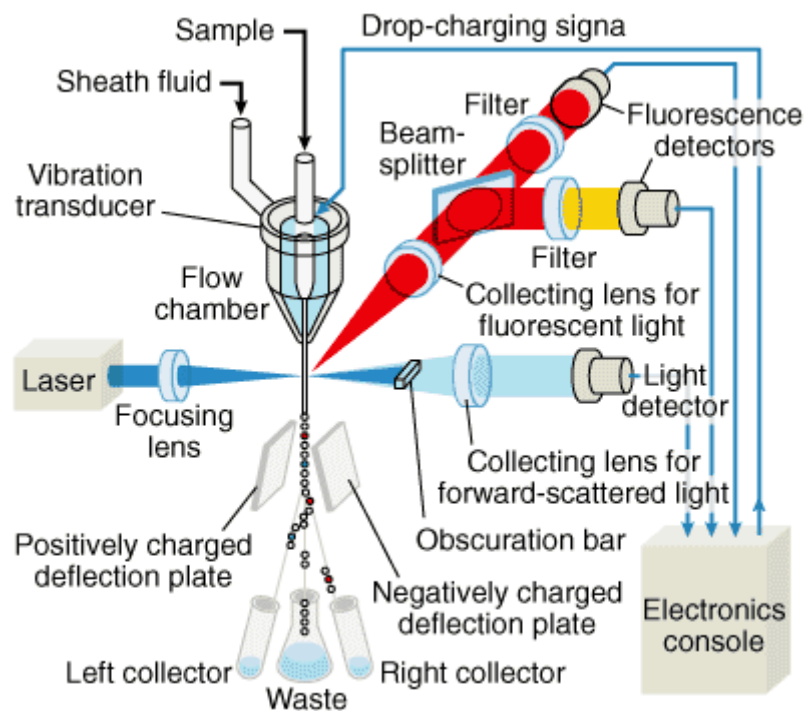


Figure 7.1 A schematic diagram of the components of a flow cytometer.²³¹

Flow cytometry has many applications in medicine and biology but there are some limitations as the analysed cells are usually discarded after use.²²⁹ This restriction means that the same cells cannot be reanalyzed with another probe in a second study. Other limitations are that individual cells cannot be examined with time-resolved events and that the cells need to be isolated (e.g. in the case of analysis of solid tissue) which causes information about the tissue structure to be lost. Nonetheless, flow cytometry analysis of suspended tumor cells, such as malignant ascites is particularly good.^{230, 232} Another key application is the binding of compounds which can be evaluated when fluorescently labelled molecules are combined with flow cytometry.²³³ In comparison with methods using radiolabeled ligands, one of the main advantages of flow cytometry is that binding to individual cells can be observed in real time and unbound ligands do not need to be separated from bound ligands.^{230, 234, 235}

The flow cytometry assay used in this work utilises a fluorescently tagged antibody specific to the CXCR4 receptor to allow detection of when this antibody interacts with the cells. A higher intensity fluorescence signal corresponds to more antibody bound to the receptors (either on the surface of the cell or internalized). The measurement of the efficiency of binding can be calculated through the use of a positive and negative control. The positive control represents the highest possible amount of fluorescence and corresponds to the receptors saturated with mAb. The sample for the positive control consists of the fluorescently tagged CXCR4 specific mAb added at a saturating concentration. The negative control consists of cells, a non-CXCR4 specific mAb and phosphate buffer solution (PBS) and should show no fluorescence signal.

7.3 Aims of the biological study

The aim of this chapter is to encapsulate an active protein component, in this case a monoclonal antibody, and to confirm that it remains intact. In order to have any applications in protein drug delivery it must first be demonstrated that encapsulation and release can be achieved without denaturing the protein. The plan in this work was to encapsulate then release the monoclonal antibody from the SECs (shown in Figure 7.2) and then to conduct flow cytometry binding experiments to confirm binding to the chemokine receptor CXCR4 in cellular systems. Hence showing that the protein was intact and active on release.

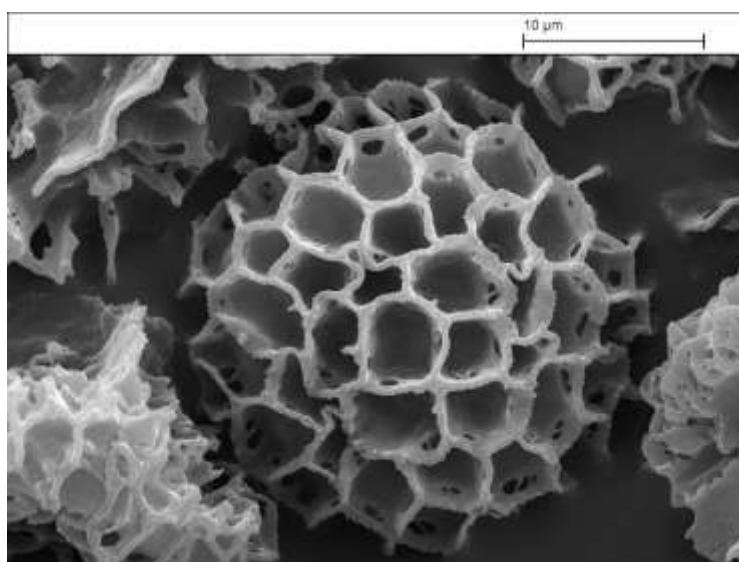


Figure 7.2 SEM image of BL-SECs.

7.4. *In vitro* biological assessment of mAb released from the sporopollenin

The CXCR4 chemokine receptor is one of the most prominent members of the chemokine receptor family and a central component of the signaling pathways in the body.^{236, 237} CXCR4 is involved in three fundamental stages of various cancer types (e.g., in lung, breast, prostate, ovarian, colon, melanoma, brain cancers): primary tumor growth; migration of cancer cells; and establishment of metastases. CXCR4 has been shown to be overexpressed in more than 70% of cancers, generating the need for personalised medicine through a combination of diagnosis and treatment.²³⁶⁻²³⁸ A schematic of the CXCR4 receptor is shown in Figure 7.3.

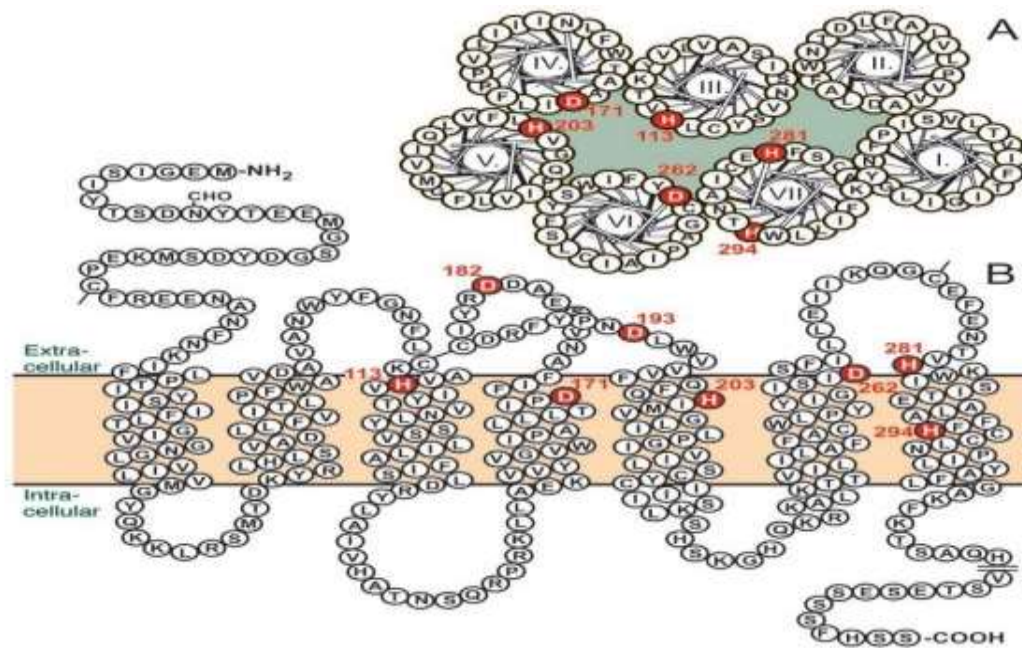


Figure 7.3 Helical wheel (A) and serpentine (B) diagrams of the CXCR4 receptor.²³⁹

Antibody encapsulation into sporopollenin and antibody release from sporopollenin were evaluated followed by binding towards CXCR4. This assay was carried out using Jurkat cells which overexpress the CXCR4 receptor (normal cells which express the receptor often show about 10,000 copies whereas Jurkat cells express *ca.* 140,000 copies). The ability of the SEC microcapsules to encapsulate and release antibodies in a controlled manner, was investigated using Mouse IgG2A PE-conjugated Isotype Control and Human CXCR4 PE conjugated antibody 12G5. Phycoerythrin (PE) is a fluorescent protein that can be used to tag larger proteins, such as antibodies, to allow them to be directly detected. The control antibody should not show any binding to the cells.

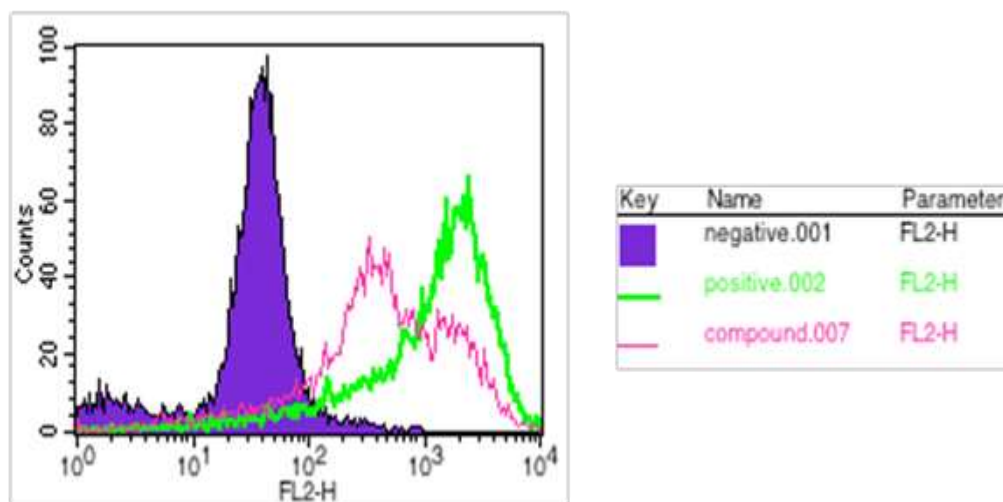


Figure 7.4 Example flow cytometry plot showing negative control (purple), positive control (green) and an intermediate binding profile (pink).

To summarise the CXCR4 binding evaluation process section, the procedure can be broken down into four steps.

1. Encapsulation of the antibody in saline solution into the SECs under vacuum (freeze drying). The sample can then be stored for several days.
2. Vortex the loaded SECs in water to allow release of the protein.
3. Freeze dry the released solution and reconstitute in phosphate buffer solution (PBS).
4. Perform the cell binding assay (see results in Figure 7.5)

The results from this set of experiments are shown in Figure 7.5. The negative control (purple) represents the experiment where none of the which should not show any mAb binding (no antibody is present) and the positive control (pink) represents mAb binding where an excess of the mAb has been used without encapsulation. The green trace is recorded after exposure to the isotype antibody which will not bind to the receptor, hence no signal is observed. Binding is observed for the encapsulated and released 12G5 monoclonal antibody. The intensity is lower that for the control 12G5 (pink) although this is to be expected as the amount of antibody released is likely to be lower on the 10 min release profile. These results show that the antibody can be stably encapsulated and, at least partially, released with a short incubation in an aqueous solution. It is likely that much of the antibody remains encapsulated and would be subject to a slower release profile. This

would be appropriate for sustained release as too rapid a release profile would not be compatible with the timescale for absorption into the blood pool after oral administration.

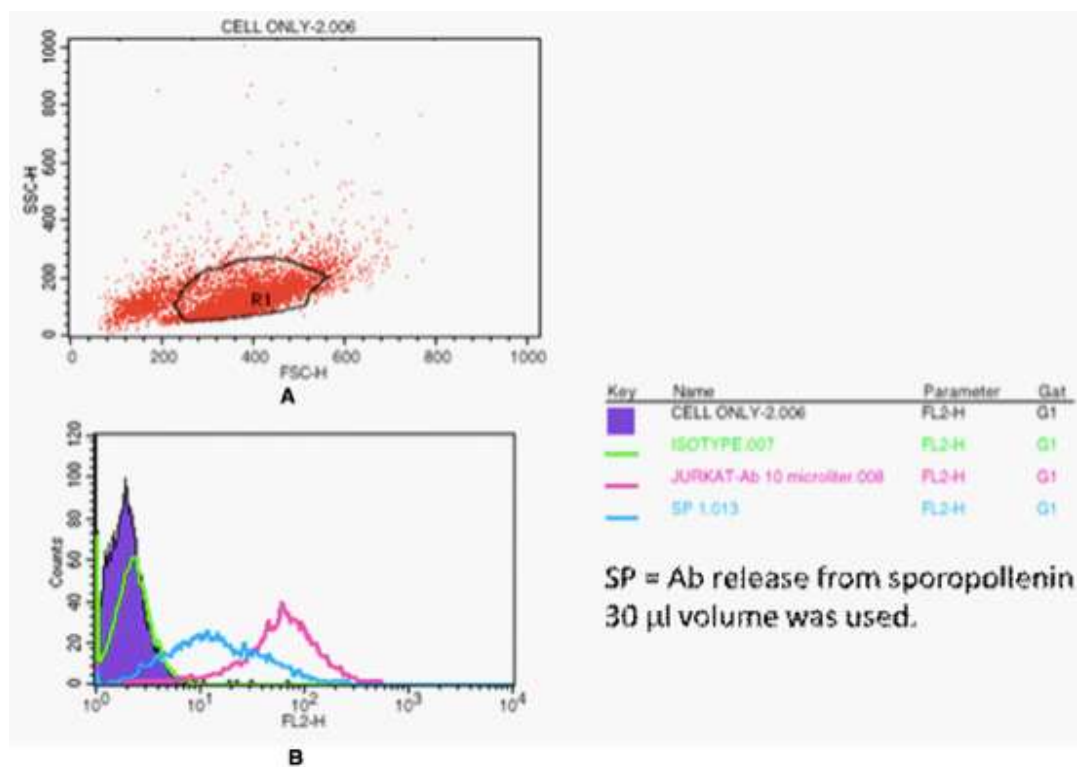


Figure 7.5 (A) dot plot, Forward-scattered light (FSC) is proportional to cell-surface area or size and Side-scattered light (SSC) is proportional to cell granularity or internal complexity, (B) Histogram, Purple is the negative control (cells only), green is isotype mAb (no binding should be observed), blue is cells incubated with released 12G-5 mAb and pink is cells incubated with non-encapsulated 12G-5 mAb.

7.5 Conclusions and Further Work

This work shows that an antibody can be encapsulated and released using sporopollenin exines. The binding properties of the monoclonal antibody (in this case binding to the important therapeutic target CXCR4) were retained. This clearly shows that the protein is not denatured. This is an advance in the use of sporopollenin materials as this has not previously been demonstrated.

The next step in this study would be to look at the longer term release profile of the mAb and to determine a time course for release. It would also be useful to demonstrate that the SEC protects the protein from an acidic environment, such as that encountered in the stomach and gastrointestinal tract. The final part of a future study would be to show a therapeutic response on oral administration of the SEC containing the mAb drug.

Chapter 8

Conclusion and Future Work

8. Conclusion and Future Work

8.1 Conclusion

Regarding the entire work that was conducted during the project, one can observe many positive aspects with respect to the interaction of inorganic metal complexes with sporopollenin from *L. clavatum*. SEC samples from different extractions were used, but the main emphasis was on the white/pale coloured SEC particles obtained by bleaching with sodium hypochlorite and then comparing between the bleached and brown coloured SECs. SEM images showed the almost spherical shape of the sporopollenin particles, indicating that both the brown and bleached SECs were undamaged by the extraction procedure. Several spectroscopic and characterisation techniques were used to further examine the structure and functional groups of the SECs. Elemental determination was provided on the SECs by CHN analyses.

IR and Raman spectroscopy identified several functional groups in the bleached or brown SECs. Due to high background fluorescence, Raman spectroscopy could not be used to identify functional groups within the brown SECs. However, many functional groups were identified using the bleached SECs. These contained unsaturated and aromatic functional groups as phenolic groups. Using IR spectroscopy it was possible to identify functional groups in both the brown and bleached SECs. The presence of hydroxyls, carbonyls, unsaturated hydrocarbons and ether groups was also revealed. Moreover, the NMR data is consistent with the IR data showing the presence of an aliphatic backbone with esters and/or carboxylic acids, together with evidence for other C-O units.

With UV-Vis spectra, the use of bleached SECs overcame the issues of spectral masking caused by the brown colouration of the brown SECs. Increasing the sample stirring time from overnight to two weeks resulted in increased intensity of the characteristic features within the spectra. Whilst it can be hard to quantify intensity changes from solid state UV-vis experiments, these data indicate a probable increase in loading on stirring.

The major emphasis was on metals with bleached SECs because this opens up the possibility of using UV-vis spectroscopy to complement the other spectroscopic techniques, such as infrared, Raman, NMR, EPR, X-ray absorption and Mössbauer

spectroscopy, as well as ICP-OES and elemental analysis, which were employed for both brown and bleached SECs.

The first SEC-metal experiments involved copper attached to both brown and white SECs derived from *L. clavatum*. The amount of copper in the samples is dependent on the copper salt used, but there is inconsistent behaviour with increased stirring time. The copper-SECs complexes exhibited more intense d-d transitions than for the other metal-SECs. Elemental determination was carried out on the SEC complexes by ICP-OES and CHN analysis. Copper acetate solutions resulted in higher attachment ratios to the SECs compared to copper chloride and copper nitrate solutions. The best conditions were found to be a ratio of 2.5 mmol: 100 mg (copper: SECs) and stirring for three days.

The use of the bleached SECs enabled UV-vis spectra to be obtained from copper-SEC complexes. The UV-vis spectra displayed the characteristic features of copper(II) with the spectra of the complexes prepared from chloride and nitrate solutions being essentially identical, but different to that from the acetate solution.

IR was used to detect the functional groups of SECs with the copper complexes. Due to the fluorescence of the copper with bleached SECs from *L. clavatum*, Raman spectroscopy could not be used to analyse the Cu-SECs complexes. The overall features of the SECs' infrared spectra highlighted the significance of aliphatic chains in the macromolecule. Interpretation relied upon the quality of the spectra, but the prime bands consistently revealed hydroxyls, aliphatic carbons, carbonyls, unsaturated hydrocarbons and ether groups, as in the uncomplexed SECs. An important observation is that the IR spectrum of the copper acetate sample is different from that of the copper chloride and copper nitrate samples in the 1900 - 1500 cm^{-1} region as well as the parent SECs. This probably indicates the presence of acetate in the copper coordination environment, which may explain why higher loadings are observed for the acetate samples.

Cu K-edge XANES spectra for copper samples with SECs indicates that copper environment contains only Cu-O in the first coordination shell. The EXAFS data confirmed that the first coordination shell consists of a Jahn-Teller distorted octahedron with a well defined Cu-O₄ square plane with Cu-O distances of 1.95 Å, and longer Cu-O distances that were not always easy to identify with certainty. Although there were weak

Cu...Cu interactions, in comparison to the data from $\text{Cu}(\text{OAc})_2 \cdot \text{H}_2\text{O}$ and $\text{Cu}_2(\text{CO}_3)(\text{OH})_2$ these are not believed to be consistent with the formation of clusters.

The Cu K_α XRF images observed that the structure of the SECs is visible in the images indicating that the copper is closely associated with the BL- SEC or BR-SEC structure.

EPR spectra are consistent with a tetragonal elongated Jahn-Teller distorted octahedron in all of the BL-SEC samples, and is slightly more ordered than in the BR-SEC samples. There was no evidence for dimer or higher cluster formation in the EPR spectra.

All the data from the Cu-SEC complexes indicates that the copper is attached to the SEC with oxygen coordination via carboxylate and possibly phenolic groups. The differences in the spectra of the acetate complexes compared to those derived from chloride and nitrate solutions correlates well with the higher loading observed for the acetate samples, and indicates that there is acetate in the copper coordination environment. In all cases there is no evidence for the formation of clusters.

The second metal studied was iron attached to SECs. A higher iron loading was observed with brown SECs than bleached SECs for all of the iron salts. This may indicate that the whitening method removes some of the functional groups that are involved in the iron coordination. The SEM images show substantial damage to the structure of the SECs in the brown iron-SEC complexes compared with the BL-SEC complexes.

It is possible to divide the UV-vis absorption spectra into two parts: from 5000 to 25000 cm^{-1} , which comprises the bands characteristic of d-d transitions in the Fe(II) (d^6) metal ions (high-spin Fe(III) (d^5) has no spin-allowed transitions), and from 25000 to 50000 cm^{-1} , which is the region where the absorptions $n-\pi^*$ and $\pi-\pi^*$ arising from the SEC functional groups appear. There were slight differences between all the spectra of the iron-BL-SEC complexes, with the complex derived from SEC and solution of $(\text{NH}_4)\text{Fe}(\text{SO}_4)_2$ presenting the highest intensity peak.

Additionally, by applying IR, one can observe the functional groups in the iron-SEC complexes. In contrast to the spectra of the copper complexes, there are fewer new bands in the 1900 – 1500 cm^{-1} region indicating a different mode of coordination of the iron to the SEC.

Fe K-edge EXAFS and FT data recorded of iron salts adsorbed onto both bleached and brown SECs show the Fe-O distance is essentially the same in all of the samples, irrespective of salt or SEC. All of the Debye-Waller factors are very similar, apart from those of BR-SEC and BL-SEC complexes formed from $(\text{NH}_4)\text{Fe}(\text{III})(\text{SO}_4)_2$ solutions which are lower indicating less disorder in the Fe-O coordination environment. The Fe K-edge XANES and ^{57}Fe Mössbauer data indicate that the iron is present as Fe(III) rather than Fe(II).

Similar ΔE_Q and δ values were obtained from the ^{57}Fe Mössbauer spectra for both brown and bleached iron-SEC complexes, but the data for bleached iron-SEC complexes was noisier due to lower iron loading. There was no evidence of magnetic splitting implying that either the iron is magnetically dilute, or any clusters formed are very small.

The overall conclusion from all of the spectroscopic data is that the iron is present as Fe(III) in all of the samples, and that the immediate iron environment is essentially the same in all cases, but with some variation in the longer Fe...Fe distances indicating a range of particle sizes. This may indicate that the iron is not present in the form of isolated octahedral coordination complexes, but as small clusters attached to the SEC surface.

The remaining metals studied were nickel and zinc, and the amount of nickel and zinc in the samples was approximately the same for all stirring times and loadings, but was dependent on the metal salt used. The best attachment rate to the SECs was for acetate compared to chloride and nitrate. The optimal experimental conditions were found to be stirring for three days 0.1 M metal solutions with either 100 mg of SECs in 25 mL of water or 300 mg of SECs in 75 mL of water.

Furthermore, by application of IR and Raman spectroscopy, one can observe the functional groups in the spore metal complexes. Due to the diminished fluorescence of the bleached SEC from *L. clavatum*, Raman spectra could be obtained, but unfortunately there does not appear to be any significant difference in the Raman spectra of the metal loaded SEC compared to the bleached SEC itself. In addition, the IR technique can be used to observe the functional groups of SEC with the metal complexes. It was found that the overall features of the SEC infrared spectra of the Ni-SECs and Zn-SEC complexes were more similar to those of copper than iron. Probably the most important observation is that the IR

spectrum of the acetate samples are different from that of the parent SEC, for nickel and this appears to be the case, but for zinc it is less clear.

The ^{13}C NMR spectra for the zinc acetate with BL-SECs was different in the 35 – 10 ppm region compared to that of zinc nitrate and zinc chloride with BL-SEC. However, the spectra were similar for all zinc salts with BR-SECs.

From all nickel salts with bleached and brown SECs the Ni K-edge XANES data are essentially identical. The Ni K-edge EXAFS data showed that the Ni-O bond length was ca. 2.05 Å with coordination number was six for all the nickel samples onto brown and bleached SECs,. The Zn K-edge XANES spectra were very similar for all the Zn-SEC complexes. The Zn K-edge EXAFS data showed that the local environment around the zinc contains a range of Zn-O distances (2.00 – 2.04 Å) with a coordination number of six.

The Ni K_{α} XRF and Zn K_{α} XRF images showed that the interaction between nickel, zinc and the SECs is similar for all nickel(II) salts and zinc(II) salts with a high correlation between SECs structure and nickel(II) or zinc(II) location. Moreover, the fact that the structure of the SECs is clearly visible in these images indicates that the nickel and zinc are closely associated with the SEC structure.

For the nickel and zinc complexes, the data were more similar to the copper rather than the iron data.

For all the copper, nickel and zinc SEC complexes the structures are based on monomeric coordination type complexes between the metal and SEC surface. The most likely source of coordination of the metals are the carboxylate groups in the sporopollenin structure. The structures of the chloride and nitrate complexes are very similar, but in the case of acetate there is evidence for the presence of acetate ligands in the coordination environment. The higher metal loadings observed for the acetate complexes can be explained by this as the metal does not require so many ligand groups in close proximity on the SEC surface. In the case of iron, the structures appear to be different, and are based on very small clusters of iron oxide or oxyhydroxide particles attached to the SEC surface.

This work also demonstrated that an antibody can be encapsulated and released using sporopollenin exines. The binding properties of the monoclonal antibody were retained,

and this clearly shows that the protein is not denatured. This is an advance in the use of sporopollenin materials as this has not previously been demonstrated.

8.2 Future work

The work described in this thesis acts as a good foundation for further investigations into both fundamental and applied aspects of the interaction of metals with pollen shells. In particular the range of metals could be expanded to include other 3d transition metals, for example cobalt, vanadium, manganese and chromium to see whether the differences for acetate are found throughout the series, and if any other elements behave like iron. In addition the study could be expanded to include the heavier 4d and 5d elements, and metallic main group elements to investigate the effects of size, oxidation state stability and reactivity. This fundamental information could be used to explore their application for metal remediation.

The next step in the biological aspects of this work would be to investigate the longer term release profile of the mAb and to determine a time course for release. It would also be useful to demonstrate that the SEC protects the protein from an acidic environment, such as that encountered in the stomach and gastrointestinal tract. The final part of a future study would be to show a therapeutic response on oral administration of the SEC containing the mAb drug. Additional investigations building on the exploratory biological work could include the encapsulation of metal containing drug molecules and to examine the potential for drug delivery and for its release *in vitro* and *in vivo*. Other areas could include the use of SECs to deliver diagnostic or theranostic metals such as ^{68}Ga .

9. References

1. S. Barrier, PhD thesis, University of Hull, 2008.
2. P. E. Jardine, W. T. Fraser, B. H. Lomax and W. D. Gosling, *J. Micropalaeontol.*, 2015, **34**, 139-149.
3. P. D. Moore, J. A. Webb and M. E. Collinson, in *Pollen analysis*, Blackwell Scientific Publications, 2nd edn., 1999.
4. A. C. Andrada and M. C. Telleria, *Grana*, 2005, **44**, 115-122.
5. J. Brooks and G. Shaw, *Grana*, 1978, **17**, 91-98.
6. A. C. Stevenson and P. D. Moore, *New Phytol.*, 1982, **90**, 327-337.
7. A. Diego-Taboada, S. T. Beckett, S. L. Atkin and G. Mackenzie, *Pharmaceutics*, 2014, **6**, 80-96.
8. J. Brooks and G. Shaw, *Chem. Geol.*, 1972, **10**, 69-87.
9. G. Mackenzie, A. N. Boa, A. Diego-Taboada, S. L. Atkin and T. Sathyapalan, *Front. Mater.*, 2015, **2**, 66.
10. M. Kawase and M. Takahashi, *Grana*, 1995, **34**, 242-245.
11. E. Dominguez, J. A. Mercado, M. A. Quesada and A. Heredia, *Sex. Plant Reprod.*, 1999, **12**, 171-178.
12. P. F. van Bergen, M. E. Blokker, M. E. Collinson, J. S. Sinninghe Damste and J. W. De Leeuw, in *The Evolution of Plant Physiology. From whole plants to ecosystems*, eds. A. R. Hemsley and I. Poole, Elsevier Academic Press, London, 2004, pp. 133-154.
13. P. Blokker, S. Schouten, J. W. de Leeuw, J. S. S. Damste and H. van den Ende, *Planta*, 1999, **207**, 539-543.
14. J. W. de Leeuw, G. J. M. Versteegh and P. F. van Bergen, *Plant. Ecol.*, 2006, **182**, 209-233.
15. J. S. Watson, W. T. Fraser and M. A. Sephton, *J. Anal. Appl. Pyrolysis*, 2012, **95**, 138-144.
16. M. J. Thomasson, D. J. Baldwin, A. Diego-Taboada, S. L. Atkin, G. Mackenzie and J. D. Wadhawan, *Electrochem. Commun.*, 2010, **12**, 1428-1431.
17. I. Feagri and J. Iverson, in *Textbook of Pollen Analysis*, Blackwell London, 1964. .
18. F. Zetzsche and K. Huggler, *Liebig's Ann. Chem.*, 1928, **461**, 89-108.

19. F. Zetsche, P. Kalt, J. Liechti and E. Ziegler, *J. Prakt. Chem.*, 1937, **148**, 267-286.
20. G. Shaw and J. Harborne(Ed), in *Sporopollenin- In: Phytochemical Phylogeny*, Academic Press, London and New York, 1970, ch. 3, pp. 31 -58.
21. J. Brooks and G. Shaw, in *Origin and development of living system*, Academic Press, London and New York., 1973.
22. J. Brooks, M. D. Muir and G. Shaw, *Nature*, 1973, **244**, 215-217.
23. G. Shaw and A. Yeadon, *Nature*, 1968, **220**, 678-679.
24. J. Brooks and G. Shaw, *Nature*, 1969, **223**, 754-756.
25. A. Diego-Taboada, S. L. Atkin, S. Barrier, M. Thomasson and G. Mackenzie, *Innov. Pharm. Technol.*, 2007, 63- 66.
26. S. Barrier, A. Diego-Taboada, M. J. Thomasson, L. Madden, J. C. Pointon, J. D. Wadhawan, S. T. Beckett, S. L. Atkin and G. Mackenzie, *J. Mater. Chem.*, 2011, **21**, 975-981.
27. A. Diego-Taboada, P. Cousson, E. Raynaud, Y. K. Huang, M. Lorch, B. P. Binks, Y. Queneau, A. N. Boa, S. L. Atkin, S. T. Beckett and G. Mackenzie, *J. Mater. Chem.*, 2012, **22**, 9767-9773.
28. I. J. Gomez, W. B. Goodwin, D. Sabo, Z. J. Zhang, K. H. Sandhage and J. C. Meredith, *J. Mater. Chem. C*, 2015, **3**, 632-643.
29. R. C. Mundargi, M. G. Potroz, J. H. Park, J. Seo, E. L. Tan, J. H. Lee and N. J. Cho, *Sci Rep-Uk*, 2016, **6**, 1-14.
30. A. Diego-Taboada, L. Maillet, J. H. Banoub, M. Lorch, A. S. Rigby, A. N. Boa, S. L. Atkin and G. Mackenzie, *J. Mater. Chem. B*, 2013, **1**, 707-713.
31. R. C. Mundargi, M. G. Potroz, J. H. Park, J. Seo, J. H. Lee and N. J. Cho, *RSC. Adv.*, 2016, **6**, 16533-16539.
32. F. Zetsche and O. Kälin, *Helv. Chim. Acta*, 1931, **14**, 517-519.
33. W. J. Guilford, D. M. Schneider, J. Labovitz and S. J. Opella, *Plant Physiol.*, 1988, **86**, 134-136.
34. G. Shaw and D. C. Apperley, *Grana*, 1996, **35**, 125-127.
35. G. Erdtman, *Svensk Botanisk Tidskrift*, 1960, **54**, 561-564.
36. B. Hans-Jörg and P. Stephan, in *Industrial Scale Natural Products Extraction*, Wiley-VCH 2011, pp. 77- 84.

37. E. Dominguez, J. A. Mercado, M. A. Quesada and A. Heredia, *Grana*, 1998, **37**, 93-96.
38. B. G. Baldi, V. R. Franceschi and F. A. Loewus, *Protoplasma*, 1987, **141**, 47-55.
39. K. S. Osthoff and R. Wiermann, *J. Plant Physiol.*, 1987, **131**, 5-15.
40. F. Ahlers, J. Lambert and R. Wiermann, *Z. Naturforsch. C: Biosci.*, 1999, **54**, 492-495.
41. M. Couderchet, J. Schmalfluss and P. Boger, *Pestic. Biochem. Physiol.*, 1996, **55**, 189-199.
42. S. Gubatz, M. Rittscher, A. Meuter, A. Nagler and R. Wiermann, *Grana*, 1993, **32**, 12-17.
43. C. Jungfermann, F. Ahlers, M. Grote, S. Gubatz, S. Steuernagel, I. Thom, G. Wetzels and R. Wiermann, *J. Plant Physiol.*, 1997, **151**, 513-519.
44. S. Herminghaus, S. Gubatz, S. Arendt and R. Wiermann, *Z. Naturforsch. C: Biosci.*, 1988, **43**, 491-500.
45. B. P. Binks, A. N. Boa, M. A. Kibble, G. Mackenzie and A. Rocher, *Soft. Matter.*, 2011, **7**, 4017-4024.
46. H. Tutar, E. Yilmaz, E. Pehlivan and M. Yilmaz, *Int. J. Biol. Macromol.*, 2009, **45**, 315-320.
47. A. R. Hemsley, A. C. Scott, P. J. Barrie and W. G. Chaloner, *Ann. Bot.*, 1996, **78**, 83-94.
48. F. Zetzsche and H. Vicari, *Helv. Chim. Acta.*, 1931, **14**, 62-67.
49. G. Shaw and A. Yeadon, *J. Chem. Soc. Perkin 1*, 1966, **1**, 16-22.
50. G. Shaw and A. Yeadon, *Grana*, 1964, **5**, 247-252.
51. H. Bubert, J. Lambert, S. Steuernagel, F. Ahlers and R. Wiermann, *Z. Naturforsch. C*, 2002, **57**, 1035-1041.
52. S. Barrier, A. Lobbert, A. J. Boasman, A. N. Boa, M. Lorch, S. L. Atkin and G. Mackenzie, *Green. Chem.*, 2010, **12**, 234-240.
53. P. Fawcett, D. Green, R. Holleyhead and G. Shaw, *Grana 10*, 1970, 246- 247.
54. R. Hayatsu, R. E. Botto, R. L. Mcbeth, R. G. Scott and R. E. Winans, *Energy. Fuels.*, 1988, **2**, 843-847.
55. M. Rittscher and R. Wiermann, *Sex. Plant Reprod.*, 1988, **1**, 125–131.

56. M. Rittscher and R. Wiermann, *Sex. Plant Reprod.*, 1988, **1**, 132–139.
57. J. Brooks and G. Shaw, *Grana*, 1968, **8**, 2-3.
58. K. Wehling, C. Niester, J. J. Boon, M. T. M. Willemse and R. Wiermann, *Planta*, 1989, **179**, 376-380.
59. S. Gubatz and R. Wiermann, *Bot. Acta*, 1992, **105**, 407–413.
60. F. Ahlers, J. Lambert and R. Wiermann, *Z. Naturforsch. C: Biosci.*, 2003, **58**, 807-811.
61. J. S. Watson, M. A. Sephton, S. V. Sephton, S. Self, W. T. Fraser, B. H. Lomax, I. Gilmour, C. H. Wellman and D. J. Beerling, *Photochem. Photobio. Sci.*, 2007, **6**, 689-694.
62. R. Wiermann and S. Gubatz, *Int. Rev. Cytol.*, 1992, **140**, 35-72.
63. A. G. Gaonkar, *Microencapsulation in the food industry : a practical implementation guide*, Elsevier Academic Press, Amsterdam, 2014.
64. J. Brooks and G. Shaw, *Nature*, 1968, **219**, 532-533.
65. R. G. Achari, G. Shaw and R. Hollyhead, *Chem. Geol.*, 1973, **12**, 229-234.
66. A. K. Prahl, H. Springstubbe, K. Grumbach and R. Wiermann, *Z. Naturforsch. C: Biosci.*, 1985, **40**, 621-626.
67. G. Mackenzie and G. Shaw, *Int. J. Pept. Protein Res.*, 1980, **15**, 298-300.
68. R. Adamson, S. Gregson and G. Shaw, *Int. J. Pept. Protein Res.*, 1983, **22**, 560-564.
69. G. Shaw, M. Sykes, R. W. Humble, G. Mackenzie, D. Marsden and E. Pehlivan, *React. Polym.*, 1988, **9**, 211-217.
70. I. H. Gubbuk, L. Gurfidan, S. Erdemir and M. Yilmaz, *Water. Air. Soil. Poll.*, 2012, **223**, 2623-2632.
71. A. J. Havinga, *Pollen. et. Spores.*, 1984, **26**, 541-558.
72. U. Brunner and R. Honegger, *Can. J. Bot.*, 1985, **63**, 2221-2230.
73. V. N. Paunov, G. Mackenzie and S. D. Stoyanov, *J. Mater. Chem.*, 2007, **17**, 609-612.
74. B. L. Yule, S. Roberts and J. E. A. Marshall, *Org. Geochem.*, 2000, **31**, 859-870.

75. D. Arrieta-Baez, L. Dorantes-Alvarez, R. Martinez-Torres, G. Zepeda-Vallejo, M. E. Jaramillo-Flores, A. Ortiz-Moreno and G. Aparicio-Ozores, *J Sci Food Agr*, 2012, **92**, 2715-2720.
76. Sporomex, <http://www.sporomex.co.uk/applications>, (accessed 14/06/2014).
77. Kenrico, <http://www.kenrico.com/sporo.html>, (accessed 14/06/2014).
78. S. Barrier, A. S. Rigby, A. Diego-Taboada, M. J. Thomasson, G. Mackenzie and S. L. Atkin, *Lwt-Food Sci. Technol.*, 2010, **43**, 73-76.
79. M. Lorch, M. J. Thomasson, A. Diego-Taboada, S. Barrier, S. L. Atkin, G. Mackenzie and S. J. Archibald, *Chem. Commun.*, 2009, 6442-6444.
80. S. L. Atkin, S. Barrier, Z. G. Cui, P. D. I. Fletcher, G. Mackenzie, V. Panel, V. Sol and X. L. Zhang, *J. Photochem. Photobiol. B*, 2011, **102**, 209-217.
81. S. L. Atkin, S. Barrier, S. T. Beckett, T. Brown, G. Mackenzie and L. Madden, *Coll. Sympos. Series*, 2005, **7**, 307-311.
82. D. H. Robinson and J. W. Mauger, *Am. J. Hosp. Pharm.*, 1991, **48**, S14-S23.
83. L. Brannon-Peppas, *Med. Plastics. Biomaterials*, 1997, **4**, 34-44.
84. V. V. Ranade, *J. Clin. Pharmacol.*, 1990, **30**, 107-120.
85. A. Wakil, G. Mackenzie, A. Diego-Taboada, J. G. Bell and S. L. Atkin, *Lipids*, 2010, **45**, 645-649.
86. S. A. Hamad, A. F. K. Dyab, S. D. Stoyanov and V. N. Paunov, *J. Mater. Chem.*, 2011, **21**, 18018-18023.
87. T. L. Harris, C. J. Wenthur, A. Diego-Taboada, G. Mackenzie, T. S. Corbitt and K. D. Janda, *Chem. Commun.*, 2016, **52**, 4187-4190.
88. R. Partanen, M. Hakala, O. Sjoval, H. Kallio and P. Forssell, *J. Food. Sci.*, 2005, **70**, E37-E43.
89. Z. J. Pan, R. W. van der Hulst, G. N. Tytgat, J. Dankert and A. van der Ende, *Am. J. Gastroenterol.*, 1999, **94**, 1517-1521.
90. M. Ersoz, E. Pehlivan, H. J. Duncan, S. Yildiz and M. Pehlivan, *React. Polym.*, 1995, **24**, 195-202.
91. E. Pehlivan, M. Ersoz, M. Pehlivan, S. Yildiz and H. J. Duncan, *J. Colloid. Interf. Sci.*, 1995, **170**, 320-325.
92. E. Pehlivan, M. Ersoz, S. Yildiz and H. J. Duncan, *Sep. Sci. Technol.*, 1994, **29**, 1757-1768.

93. I. Sargin and G. Arslan, *Int. J. Biol. Macromol.*, 2015, **75**, 230-238.
94. I. Sargin, M. Kaya, G. Arslan, T. Baran and T. Ceter, *Bioresour. Technol.*, 2015, **177**, 1-7.
95. I. Sargin and G. Arslan, *Desalin. Water Treat.*, 2016, **57**, 10664-10676.
96. M. Erzenegin, N. Unlu and M. Odabasi, *J. Chromatogr. A*, 2011, **1218**, 484-490.
97. U. S. Vural, M. Ersoz and E. Pehlivan, *J. Appl. Polym. Sci.*, 1995, **58**, 2423-2428.
98. S. Yildiz, E. Pehlivan, M. Ersoz and M. Pehlivan, *J. Chromatogr. Sci.*, 1993, **31**, 150-152.
99. E. Pehlivan and S. Yildiz, *Sep. Sci. Technol.*, 1994, **29**, 887-895.
100. I. H. Gubbuk, *J. Hazard. Mater.*, 2011, **186**, 416-422.
101. S. J. Archibald, S. L. Atkin, W. Bras, A. Diego-Taboada, G. Mackenzie, J. F. W. Mosselmans, S. Nikitenko, P. D. Quinn, M. F. Thomas and N. A. Young, *J. Mater. Chem. B*, 2014, **2**, 945-959.
102. S. E. Jackson, H. P. Longerich, G. R. Dunning and B. J. Fryer, *Can. Mineral.*, 1992, **30**, 1049-1064.
103. K. E. Espelie, F. A. Loewus, R. J. Pugmire, W. R. Woolfenden, B. G. Baldi and P. H. Given, *Phytochemistry*, 1989, **28**, 751-753.
104. F. Ahlers, H. Bubert, S. Steuernagel and R. Wiermann, *Z. Naturforsch. C: Biosci.*, 2000, **55**, 129-136.
105. S. Wilmesmeier, S. Steuernagel and R. Wiermann, *Z. Naturforsch. C: Biosci.*, 1993, **48**, 697-701.
106. A. R. Hemsley, W. G. Chaloner, A. C. Scott and C. J. Groombridge, *Ann. Bot.*, 1992, **69**, 545-549.
107. A. R. Hemsley, P. J. Barrie, W. G. Chaloner and A. C. Scott, *Grana*, 1993, **32**, 2-11.
108. D. H. Williams and I. Fleming, *Spectroscopic methods in organic chemistry*, McGraw-Hill, London ; New York, 3d edn., 1980.
109. D. A. Weitz, S. Garoff, J. I. Gersten and A. Nitzan, *J. Chem. Phys.*, 1983, **78**, 5324-5338.
110. A. Zumbusch, G. R. Holtom and X. S. Xie, *Phys. Rev. Lett.*, 1999, **82**, 4142-4145.
111. N. P. Ivleva, R. Niessner and U. Panne, *Anal. Bioanal. Chem.*, 2005, **381**, 261-267.

112. K. Maquelin, C. Kirschner, L. P. Choo-Smith, N. van den Braak, H. P. Endtz, D. Naumann and G. J. Puppels, *J. Microbiol. Meth.*, 2002, **51**, 255-271.
113. N. A. Young, *Coord. Chem. Rev.*, 2014, **277**, 224-274.
114. M. Bonnin-Mosbah, A. S. Simionovici, N. Metrich, J. P. Duraud, D. Massare and P. Dillmann, *J. Non-Cryst. Solids*, 2001, **288**, 103-113.
115. M. Bonnin-Mosbah, N. Metrich, J. Susini, M. Salome, D. Massare and B. Menez, *Spectrochim. Acta B*, 2002, **57**, 711-725.
116. L. E. Mayhew, S. M. Webb and A. S. Templeton, *Environ. Sci. Technol.*, 2011, **45**, 4468-4474.
117. J. Prietzel, J. Thieme, K. Eusterhues and D. Eichert, *Eur. J. Soil Sci.*, 2007, **58**, 1027-1041.
118. K. Wovkulich, B. J. Mailloux, B. C. Bostick, H. L. Dong, M. E. Bishop and S. N. Chillrud, *Geochim. Cosmochim. Acta*, 2012, **91**, 254-270.
119. S. Reguer, P. Dillmann and F. Mirambet, *Corros. Sci.*, 2007, **49**, 2726-2744.
120. J. Monnier, D. Vantelon, S. Reguer and P. Dillmann, *J. Anal. At. Spectrom.*, 2011, **26**, 885-891.
121. J. Monnier, D. Vantelon, S. Reguer and P. Dillmann, *Actual. Chimique.*, 2011, 109-112.
122. J. Collingwood and J. Dobson, *J. Alzheimers Dis.*, 2006, **10**, 215-222.
123. J. F. Collingwood, R. K. K. Chong, T. Kasama, L. Cervera-Gontard, R. E. Dunin-Borkowski, G. Perry, M. Posfai, S. L. Siedlak, E. T. Simpson, M. A. Smith and J. Dobson, *J. Alzheimers Dis.*, 2008, **14**, 235-245.
124. J. C. Bridges, M. J. Burchell, H. C. Changela, N. J. Foster, J. A. Creighton, J. D. Carpenter, S. J. Gurman, I. A. Franchi and H. Busemann, *Meteorit. Planet. Sci.*, 2010, **45**, 55-72.
125. H. G. Changela, J. C. Bridges and S. J. Gurman, *Geochim. Cosmochim. Acta*, 2012, **98**, 282-294.
126. S. Bernard, K. Benzerara, O. Beyssac, G. E. Brown, L. G. Stamm and P. Düringer, *Rev. Palaeobot. Palyno.*, 2009, **156**, 248-261.
127. S. Bernard, K. Benzerara, O. Beyssac, E. Balan and G. E. Brown, Jr., *Heliyon.*, 2015, **1**, e00034.
128. R. L. Mössbauer, *Science*, 1962, **137**, 731-738.

129. R. Doerfler, W. Gruber, P. Gütlich, K. M. Hasselbach, O. Leupold, B. Molnar, D. L. Nagy, G. Ritter, H. Spiering and F. Tuczek, *Phys. Rev. Lett.*, 1986, **57**, 2849-2852.
130. G. W. Brudvig, *Method Enzymol*, 1995, **246**, 536-554.
131. J. R. Pilbrow and G. R. Hanson, *Metallobiochemistry, Pt D*, 1993, **227**, 330-353.
132. S. Rada, A. Dehelean, M. Stan, R. Chelcea and E. Culea, *J. Alloy Compd.*, 2011, **509**, 147-151.
133. R. Lopez and R. Gomez, *J. Sol-Gel. Sci. Techn.*, 2012, **61**, 1-7.
134. S. Nikitenko, A. M. Beale, A. M. J. van der Eerden, S. D. M. Jacques, O. Leynaud, M. G. O'Brien, D. Detollenaere, R. Kaptein, B. M. Weckhuysen and W. Bras, *J. Synchrotron. Radiat.*, 2008, **15**, 632-640.
135. B. Ravel and M. Newville, *J. Synchrotron. Radiat.*, 2005, **12**, 537-541.
136. A. Tenderholt, B. Hedman and K. O. Hodgson, *X-Ray. Absorp. Fine Structure-Xafs13.*, 2007, **882**, 105-107.
137. N. Binsted, *Journal*, 1998.
138. J. F. Mosselmans, P. D. Quinn, A. J. Dent, S. A. Cavill, S. D. Moreno, A. Peach, P. J. Leicester, S. J. Keylock, S. R. Gregory, K. D. Atkinson and J. R. Rosell, *J. Synchrotron. Radiat.*, 2009, **16**, 818-824.
139. V. A. Sole, E. Papillon, M. Cotte, P. Walter and J. Susini, *Spectrochim. Acta. B.*, 2007, **62**, 63-68.
140. S. M. Alshehri, H. A. Al-Lohedan, A. A. Chaudhary, E. Al-Farraj, N. Alhokbany, Z. Issa, S. Alhousine and T. Ahamad, *Eur. J. Pharm. Sci.*, 2016, **88**, 158-165.
141. J. Wittborn, K. V. Rao, G. El-Ghazaly and J. R. Rowley, *Ann. Bot-London.*, 1998, **82**, 141-145.
142. G. Bohne, E. Richter, H. Woehlecke and R. Ehwaldi, *Ann. Bot-London.*, 2003, **92**, 289-297.
143. R. C. Mundargi, E. L. Tan, J. Seo and N. J. Cho, *J. Ind. Eng. Chem.*, 2016, **36**, 102-108.
144. R. C. Mundargi, M. G. Potroz, S. Park, J. H. Park, H. Shirahama, J. H. Lee, J. Seo and N. J. Cho, *Adv. Funct. Mater.*, 2016, **26**, 487-497.
145. R. C. Mundargi, M. G. Potroz, S. Park, H. Shirahama, J. H. Lee, J. Seo and N. J. Cho, *Small*, 2016, **12**, 1167-1173.

146. S. M. Alshehri, H. A. Al-Lohedan, E. Al-Farraj, N. Alhokbany, A. A. Chaudhary and T. Ahamad, *Int. J. Pharm.*, 2016, **508**, 135-135.
147. W. T. Fraser, A. C. Scott, A. E. S. Forbes, I. J. Glasspool, R. E. Plotnick, F. Kenig and B. H. Lomax, *New. Phytol.*, 2012, **196**, 397-401.
148. B. Zimmermann, Z. Tkalcec, A. Mesic and A. Kohler, *Plos One*, 2015, **10**.
149. B. Zimmermann and A. Kohler, *Plos One*, 2014, **9**.
150. D. Lin-Vien, N. B. Colthup, W. G. Fateley and J. G. Grasselli, in *The Handbook of Infrared and Raman Characteristic Frequencies of Organic Molecules*, Academic Press, 1991.
151. B. G. Pummer, H. Bauer, J. Bernardi, B. Chazallon, S. Facq, B. Lendl, K. Whitmore and H. Grothe, *J. Raman. Spectrosc.*, 2013, **44**, 1654-1658.
152. F. Schulte, J. Lingott, U. Panne and J. Kneipp, *Anal. Chem.*, 2008, **80**, 9551-9556.
153. V. Joseph, F. Schulte, H. Rooch, I. Feldmann, I. Dorfel, W. Osterle, U. Panne and J. Kneipp, *Chem. Commun.*, 2011, **47**, 3236-3238.
154. S. Seifert, V. Merk and J. Kneipp, *J Biophotonics*, 2016, **9**, 181-189.
155. A. R. Boyain-Goitia, D. C. S. Beddows, B. C. Griffiths and H. H. Telle, *Appl. Opt.*, 2003, **42**, 6119-6132.
156. M. L. Laucks, G. Roll, G. Schweiger and E. J. Davis, *J. Aerosol Sci*, 2000, **31**, 307-319.
157. R. B. Miles, W. R. Lempert and J. N. Forkey, *Meas. Sci. Technol.*, 2001, **12**, R33-R51.
158. M. Sener, D. H. K. Reddy and B. Kayan, *Ecol. Eng.*, 2014, **68**, 200-208.
159. A. Cimen, A. Bilgic, A. N. Kursunlu, I. H. Gubbuk and H. I. Ucan, *Desalin. Water. Treat.*, 2014, **52**, 4837-4847.
160. N. Unlu and M. Ersoz, *J. Hazard. Mater.*, 2006, **136**, 272-280.
161. N. Unlu and M. Ersoz, *Sep. Purif. Technol.*, 2007, **52**, 461-469.
162. A. S. Goggi, H. Lopez-Sanchez, P. Caragea, M. Westgate, R. Arritt and C. A. Clark, *Int. J. Biometeorol.*, 2007, **51**, 493-503.
163. S. Gomez-Salces, F. Aguado, R. Valiente and F. Rodrigues, *Angew. Chem. Int. Ed.*, 2012, **51**, 9335-9338.
164. V. S. Bryantsev, M. S. Diallo, A. C. T. van Duin and W. A. Goddard, *J. Phys. Chem. A.*, 2008, **112**, 9104-9112.

165. M. Benfatto, P. D'Angelo, S. Della Longa and N. V. Pavel, *Phys. Rev. B.*, 2002, **65**.
166. A. Pasquarello, I. Petri, P. S. Salmon, O. Parisel, R. Car, E. Toth, D. H. Powell, H. E. Fischer, L. Helm and A. E. Merbach, *Science*, 2001, **291**, 856-859.
167. M. A. Khan and M. J. Schwingweill, *Inorg. Chem.*, 1976, **15**, 2202-2205.
168. P. De Vreese, N. R. Brooks, K. Van Hecke, L. Van Meervelt, E. Mattheijs, K. Binnemans and R. Van Deun, *Inorg. Chem.*, 2012, **51**, 4972-4981.
169. M. A. Hitchman and T. D. Waite, *Inorg. Chem.*, 1976, **15**, 2150-2154.
170. T. D. Waite and M. A. Hitchman, *Inorg. Chem.*, 1976, **15**, 2155-2158.
171. J. N. v. Niekerk and F. R. L. Schoening, *Acta. Crystallogr.*, 1953, **6**, 227-232.
172. R. L. Martin and A. Whitley, *J. Chem. Soc.*, 1958, 1394-1402.
173. G. Nyberg, *J. Phys. Chem.*, 1971, **75**, 2228-2229.
174. A. T. A. Cheng and R. A. Howald, *Inorg. Chem.*, 1975, **14**, 546-549.
175. P. Sharrock and M. Melnik, *Can. J. Chem.*, 1985, **63**, 52-56.
176. A. Tsybizova, B. L. Ryland, N. Tsierkezos, S. S. Stahl, J. Roithova and D. Schroder, *Eur. J. Inorg. Chem.*, 2014, **2014**, 1407-1412.
177. H. Grasdale and I. Svare, *Acta. Chem. Scand.*, 1971, **25**, 1089-1102.
178. G. Nyberg, *J. Phys. Chem.*, 1971, **75**, 2228.
179. C. W. Reimann, G. F. Kokoszka and G. Gordon, *Inorg. Chem.*, 1965, **4**, 1082-1084.
180. A. T. A. Cheng and R. A. Howald, *Inorg. Chem.*, 1968, **7**, 2100-2105.
181. A. B. P. Lever, *Inorganic Electronic Spectroscopy*, Elsevier, Amsterdam, 1986.
182. G. B. Deacon and R. J. Phillips, *Coordin. Chem. Rev.*, 1980, **33**, 227-250.
183. L. Dubicki and R. L. Martin, *Aust. J. Chem.*, 1969, **22**, 1571.
184. D. A. Edwards and R. N. Hayward, *Can. J. Chem.*, 1968, **46**, 3443.
185. P. D. Meester, S. R. Fletcher and A. C. Skapski, *J. Chem. Soc., Dalton Trans.*, 1973, 2575-2578.
186. A. Engberg, *Acta. Chem. Scand.*, 1970, **24**, 3510-3526.
187. S. Brownstein, N. F. Han, E. Gabe and Y. Lepage, *Z. Kristallogr.*, 1989, **189**, 13-15.

188. B. Morosin, *Acta Crystallographica Section B-Structural Crystallography and Crystal Chemistry*, 1970, **B 26**, 1203-1208.
189. G. Gattow and J. Zemmann, *Acta. Cryst.*, 1958, **11**, 866-872.
190. P. Susse, *Acta. Cryst.*, 1967, **22**, 146-151.
191. F. Zigan, W. Joswig, H. D. Schuster and S. A. Mason, *Z. Kristallogr.*, 1977, **145**, 412-426.
192. S. F. Cheah, G. E. Brown and G. A. Parks, *Am. Mineral.*, 2000, **85**, 118-132.
193. S. Asbrink and L. J. Norrby, *Acta. Cryst. B*, 1970, **B 26**, 8-15.
194. P. Sharrock and M. Melník, *Can. J. Chem.*, 1985, **63**, 52.
195. M. A. Malik, P. O'Brien, F. Tuna, R. Pritchard, J. Buchweishajja, E. Kimambo and E. B. Mubofu, *Dalton Trans.*, 2013, **42**, 14438-14444.
196. J. Svorec, M. Valko, J. Moncol, M. Mazúr, M. Melník and J. Telser, *Transition Met. Chem.*, 2009, **34**, 129-134.
197. B. Kozlevčar and P. Šegedin, *Croat. Chem. Acta*, 2008, **81**, 369-379.
198. J. P. Jolivet, C. Chaneac and E. Tronc, *Chem. Commun.*, 2004, 481-487.
199. S. Ceylan and M. Odabasi, *Artif. Cell. Nanomed. B*, 2013, **41**, 376-383.
200. V. K. Sabirov, *J. Struct. Chem*, 2015, **56**, 698-707.
201. H. Montgomery, B. Morosin, J. J. Natt, A. M. Witkowska and E. C. Lingafelter, *Acta. Cryst.*, 1967, **22**, 775- 780.
202. T. E. Westre, P. Kennepohl, J. G. DeWitt, B. Hedman, K. O. Hodgson and E. I. Solomon, *J. Am. Chem. Soc.*, 1997, **119**, 6297-6314.
203. H. L. Zhang, M. M. Hirschmann, E. Cottrell, M. Newville and A. Lanzirotti, *Chem. Geol.*, 2016, **428**, 48-58.
204. I. Orhan, B. Özçelik, S. Aslan, M. Kartal, T. Karaoglu, B. Şener, S. Terzioglu and M. I. Choudhary, *Phytochem. Rev.*, 2007, **6**, 189-196.
205. R. C. Rosenberg, C. A. Root and H. B. Gray, *J. Am. Chem. Soc.*, 1975, **97**, 21-26.
206. A. D. J. Barnes, T. Baikie, V. Hardy, M. B. Lepetit, A. Maignan, N. A. Young and M. G. Francesconi, *J. Mater. Chem.*, 2006, **16**, 3489-3502.
207. G. J. Colpas, M. J. Maroney, C. Bagyinka, M. Kumar, W. S. Willis, S. L. Suib, N. Baidya and P. K. Mascharak, *Inorg. Chem.*, 1991, **30**, 920-928.

208. L. S. Kau, D. J. Spira-Solomon, J. E. Penner-Hahn, K. O. Hodgson and E. I. Solomon, *J. Am. Chem. Soc.*, 1987, **109**, 6433-6442.
209. G. J. Colpas, M. J. Maroney, C. Bagyinka, M. Kumar, W. S. Willis, S. L. Suib, N. Baidya and P. K. Mascharak, *Inorg. Chem.*, 1991, **30**, 920-928.
210. P. Gallezot, D. Weigel and M. Prettre, *Acta. Cryst.*, 1967, **22**, 699-705.
211. B. Morosin and T. Haseda, *Acta. Crystallogr B.*, 1979, **35**, 2856-2858.
212. J. N. v. Niekerk and F. R. L. Schoening, *Acta. Cryst.*, 1953, **6**, 609-612.
213. J. Mizuno, *J. Phys. Soc. Jpn.*, 1961, **16**, 1574-1580.
214. R. Kleinberg, *J. Chem. Phys.*, 1969, **50**, 4690-4696.
215. W. Clegg, I. R. Little and B. P. Straughan, *Acta. Crystallogr. C.*, 1986, **42**, 1701-1703.
216. H. He, *Acta Cryst. E*, 2006, **62**, m3291-m3292.
217. A. V. Capilla and R. A. Aranda, *Cryst. Struct. Commun.*, 1979, **8**, 795.
218. A. Ferrari, A. Braibanti, A. M. M. Lanfredi and A. Tiripicchio, *Acta Cryst.*, 1967, **22**, 240-246.
219. S. M. Catnach, P. D. Fairclough and S. M. Hammond, *Gut*, 1994, **35**, 441-444.
220. B. F. Choonara, Y. E. Choonara, P. Kumar, D. Bijukumar, L. C. du Toit and V. Pillay, *Biotechnol. Adv.*, 2014, **32**, 1269-1282.
221. K. Park, I. C. Kwon and K. Park, *React. Funct. Polym.*, 2011, **71**, 280-287.
222. C. Y. Dai, B. C. Wang and H. W. Zhao, *Colloid. Surface. B.*, 2005, **41**, 117-120.
223. A. Muheem, F. Shakeel, M. A. Jahangir, M. Anwar, N. Mallick, G. K. Jain, M. H. Warsi and F. J. Ahmad, *Saudi. Pharm. J.*, 2016, **24**, 413-428.
224. S. Gunasekaran, S. Ko and L. Xiao, *J. Food. Eng.*, 2007, **83**, 31-40.
225. S. Gunasekaran, L. Xiao and M. M. O. Eleya, *J. Appl. Polym. Sci.*, 2006, **99**, 2470-2476.
226. Y. C. Chen, T. Smith, R. H. Hicks, A. Doekhie, F. Koumanov, S. A. Wells, K. J. Edler, J. van den Elsen, G. D. Holman, K. J. Marchbank and A. Sartbaeva, *Scientific Reports*, 2017, **7**.
227. K. Ulbrich, K. Hola, V. Subr, A. Bakandritsos, J. Tucek and R. Zboril, *Chem. Rev.*, 2016, **116**, 5338-5431.

228. S. Koutsopoulos, L. D. Unsworth, Y. Nagai and S. G. Zhang, *P. Natl. Acad. Sci. USA.*, 2009, **106**, 4623-4628.
229. M. G. Macey, in *Flow Cytometry Principles and Applications*, Humana Press: Totowa, 2007.
230. K. Nicholson, PhD thesis, University of Hull, 2015.
231. OptoIQ Semiconductor lasers shed new light on flow cytometry, <http://www.optoiq.com/index/photronics-technologies-applications/lfw-display/lfw-article-display/209783/articles/laser-focus-world/volume-40/issue-8/features/optoelectronic-applications-drug-discovery/semiconductor-lasers-shed-new-light-on-flow-cytometry>., (accessed 03/08/2017).
232. Z. Darzynkiewicz, E. Holden, P. Pozarowski, D. Kaur, D. Rew and G. Woltmann, *Cell Imaging Techniques Method and Protocols*, Humana Press: Totowa, 2006.
233. A. Waller, D. Pipkorn, K. L. Sutton, J. J. Linderman and G. M. Omann, *Cytometry*, 2001, **45**, 102-114.
234. J. W. A. Findlay and M. N. Khan, *Ligand-Binding Assays in Drug Development: Introduction and Historical Perspective. In Ligand-Binding Assays*, John Wiley & Sons, Inc, 2009.
235. M. N. Khan, P. D. Dass, J. H. Leete, R. F. Schuman, M. Gunsior and C. Sadhu, *Development of Ligand-Binding Assays for Drug Development Support. In Ligand-Binding Assays*, John Wiley & Sons, Inc., 2009.
236. C. Murdoch and A. Finn, *Blood*, 2000, **95**, 3032-3043.
237. S. Alzahrani, PhD thesis, University of Hull, 2016.
238. T. J. Hubin, J. M. McCormick, S. R. Collinson, N. W. Alcock and D. H. Busch, *Chem. Commun.*, 1998, 1675-1676.
239. L. O. Gerlach, R. T. Skerlj, G. J. Bridger and T. W. Schwartz, *J. Biol. Chem.*, 2001, **276**, 14153-14160.